

Modeling transport processes in run-of-river reservoirs

Stefan Rainer Schäfer

Vollständiger Abdruck der von der TUM School of Engineering and Design der Technischen Universität München zur Erlangung des akademischen Grades eines

Doktors der Ingenieurwissenschaften (Dr.-Ing.)

genehmigten Dissertation.

Vorsitz: Prof. Dr.-Ing. Christian Große

Prüfer*innen der Dissertation:

1. Prof. Dr. sc. techn. Peter Rutschmann
2. Prof. Dr. phil. Nils Rüther
3. Prof. Dr.-Ing. Jochen Aberle

Die Dissertation wurde am 01.07.2022 bei der Technischen Universität München eingereicht
und durch die TUM School of Engineering and Design am 06.09.2022 angenommen.

It must be recognized that a certain amount of practical experience with, or understanding of, river behavior is highly valuable in the correct application of this or any other method of sedimentload determination. Sediment movement and river behavior are inherently complex natural phenomena involving a great many variables. The solution of practical problems cannot be simplified beyond a certain point.

Einstein, H.A. (1950)

Preface

I would like to thank Prof. Dr. sc. techn. Peter Rutschmann for the opportunity to work on exciting projects with great freedom over many years and for his support of this dissertation.

My special thanks go to Prof. Dr. phil. Nils R  ther for his great interest in my work, his encouragement and his valuable advice.

I would also like to thank Prof. Dr.-Ing. Jochen Aberle for taking over the discussion.

To my colleagues at the Obernach Hydraulics Laboratory as well as to my colleagues at the Chair in Munich, I would like to express my thanks for the many years of reliable cooperation and the many interesting conversations.

Mr. Stefan Giehl and Mr. Yannic Fuchs I sincerely thank for the countless discussions and the continued support.

Abstract

Sediment transport processes in river reservoirs during flood events remain a major challenge for the safe operation of reservoirs and dams. Their systematic investigation is extremely complex and, especially in the case of reservoirs predominantly silted up with cohesionless fine sand, this sand makes comparative model experiments in the laboratory difficult due to scale effects. Prediction of bed evolution can also be highly susceptible to error because reliable data sets for calibrating numerical software are scarcely available. This study therefore addresses the methodologic investigation of sediment transport processes during flood discharge in a large laboratory experiment with lightweight sediment in an idealized, elongated river reservoir with online sediment recirculation.

In a two-stage experimental procedure, dynamic equilibrium states of the reservoir bed were first analyzed and then various flood hydrographs were reproduced so that unsteady superposition effects could be distinguished from the natural fluctuations of the reservoir bed in dynamic equilibrium. Thereby, both the measurement accuracy for process description and the accessibility of the measured data for numerical comparative calculations were given equal importance. The detailed data sets on the evolution of the reservoir bed and the course of the sediment transport rate generated in this way made it possible to distinguish morphodynamic processes with high time variability from large-scale morphological processes with low temporal variability and to analyze them separately. In this approach, the reservoir bed passed through the entire evolution from the plane bed of the lower flow regime to the transition zone to the upper flow regime with very high sediment transport rates.

Although the procedures for evaluating the temporal-spatial highly variable reservoir bed could not completely eliminate statistical uncertainties, good agreements of the derived morphological parameters from the laboratory experiment with the literature based predominantly on natural sediments were shown at the process level. At the same time, quantitative differences appeared, especially in bedforms and depending on the flow conditions, presumably due to the inevitable vertical distortion of the spatial force relations when using lightweight sediment. However, these differences were smaller than similarity theory considerations suggested, indicating possibilities for the use of lightweight sediment outside of classical model similarity. In addition, due to the good process similarity, the presented methodology allowed further use of the generated data sets for optimization and, potentially, further development of hydro-morphodynamic software.

Zusammenfassung

Sedimenttransportprozesse in Flusstauräumen während Hochwasser stellen bis heute eine große Herausforderung für den sicheren Betrieb von Stauanlagen dar. Ihre systematische Untersuchung ist extrem aufwendig und besonders bei maßgeblich mit kohäsionslosem Feinsand verlandeten Stauräumen erschwert dieser Sand vergleichende Modellversuche im Labor aufgrund von Maßstabseffekten. Auch die Prognose der Sohlentwicklung ist mitunter stark fehleranfällig, weil kaum verlässliche Datensätze zur Kalibrierung numerischer Programme verfügbar sind. Diese Arbeit befasst sich deshalb mit der methodischen Untersuchung von Sedimenttransportprozessen bei Hochwasserabfluss in einem großen Laborversuch mit Leichtgewichtssediment in einem idealisierten, langgestreckten Flusstauraum mit direkter Sedimentrezirkulation.

In einem zweistufigen Vorgehen wurden zunächst sohdynamische Gleichgewichtszustände analysiert und daran anschließend verschiedene Hochwasserganglinien nachgebildet, sodass instationäre Überlagerungseffekte von den natürlichen Schwankungen der Stauraumsohle im dynamischen Gleichgewicht unterschieden werden konnten. Dabei wurde gleichermaßen Wert auf die Messgenauigkeit zur Prozessbeschreibung und die Zugänglichkeit der Messdaten für numerische Vergleichsrechnungen gelegt. Die so erzeugten detaillierten Datensätze zur Entwicklung der Stauraumsohle und dem Verlauf der Sedimenttransportrate ermöglichten es, morphodynamische Prozesse mit hoher zeitlicher Variabilität von großräumigen, zeitlich gering variablen morphologischen Prozessen zu unterscheiden und getrennt zu analysieren. Die Stauraumsohle durchlief bei diesem Vorgehen die gesamte Entwicklung vom flachen Bett des unteren Fließregimes bis in den Übergangsbereich zum oberen Fließregime mit sehr hohen Transportraten.

Obwohl die Verfahren zur Auswertung der zeitlich-räumlich stark variablen Stauraumsohle statistische Unsicherheiten nicht vollständig beseitigen konnten, zeigten sich auf Prozessebene gute Übereinstimmungen der abgeleiteten morphologischen Parameter aus dem Laborversuch mit der überwiegend auf natürlichen Sedimenten basierenden Literatur. Zeitgleich traten quantitative Unterschiede besonders bei den Sohlformen und abhängig vom Fließzustand auf, die mutmaßlich durch die zwangsläufige vertikale Verzerrung der Kräfteverhältnisse beim Einsatz von Leichtgewichtssediment begründet sind. Diese Differenzen waren jedoch geringer als ähnlichkeitstheoretische Überlegungen nahelegten, was Möglichkeiten für den Einsatz von Leichtgewichtssediment außerhalb der klassischen Modellähnlichkeit aufzeigte. Zudem ermöglichte die vorgestellte Methodik aufgrund der guten Prozessähnlichkeit eine Weiterverwendung der erzeugten Datensätze für die Optimierung und ggf. Weiterentwicklung von hydro-morphodynamischer Software.

Contents

1. Introduction.....	1
1.1. River reservoirs then and now	1
1.2. Challenges in run-of-river reservoirs.....	3
1.3. Research motivation	6
2. Theoretical background.....	8
2.1. Sediment transport mechanisms	9
2.1.1. Modes of sediment transport.....	10
2.1.2. Sediment transport parameters.....	11
2.1.3. Initiation of sediment transport.....	13
2.2. Bedforms in rivers.....	15
2.2.1. Types of bedforms.....	15
2.2.2. Dune migration.....	17
2.3. Physical modeling in river hydraulics.....	21
2.3.1. Limitations of Froude models.....	21
2.3.2. Lightweight sediment in physical modeling.....	24
3. Methodology.....	27
3.1. Research design	28
3.1.1. Hydraulics of the test scenarios.....	29
3.1.2. Properties of the lightweight sediment	31
3.2. Test facility	35
3.2.1. Experiment setup	35
3.2.2. Functional components explained	38
3.3. Methods of data collection.....	43
3.3.1. Bed survey using terrestrial laser scanning	43
3.3.2. Sediment transport measurement	45
3.4. Experimental procedure.....	47
3.4.1. Phase 1: Dynamic bed equilibrium	48
3.4.2. Phase 2: Flood hydrographs.....	51
3.5. Quantification of measurement uncertainty	52
4. Bed evolution in dynamic equilibrium	55
4.1. Data Analysis of steady-state experiments.....	55
4.1.1. Riverbed topography.....	56
4.1.2. Sediment transport.....	69
4.2. Implications of steady-state experiment series	73
4.2.1. Dune dimensions	75
4.2.2. Hydraulic parameters.....	81

4.2.3.	Morphological parameters	87
4.2.4.	Transport functions for sediment transport	93
5.	Morphodynamic processes during flood events.....	98
5.1.	Data analysis of unsteady experiments.....	98
5.1.1.	Continuously monitored raw data.....	99
5.1.2.	Data filtering and post-processing.....	101
5.1.3.	Parameter interdependence.....	105
5.2.	Implications of unsteady experiment series	109
5.2.1.	Scenarios with wide hydrograph peaks.....	109
5.2.2.	Scenarios with pointed hydrograph peaks.....	115
5.2.3.	Comparison with dynamic equilibrium	119
6.	Discussion and applicability	123
7.	Conclusion.....	131
	Bibliography	133
	List of figures	143
	List of tables	149
	List of symbols.....	150
A.	Advances Using Laser Scanning to Determine Riverbed Topography.....	153
B.	Optical Measurement Method for Quantifying Sediment Transport in Physical Experiments	175
C.	Dynamic bed equilibrium data.....	185
C.1.	H = 21.25 cm	185
C.2.	H = 30.00 cm	195
C.3.	H = 35.00 cm	209
C.4.	Dune velocities.....	217

This page is intentionally left blank.

1. Introduction

1.1. River reservoirs then and now

The cultural-historical development of mankind is decisively shaped by living near and dealing with water: reliable drinking water supply, irrigation in agriculture, protection against disease by canalization, trade and transport on navigable waterways, use of water power, culture and customs. Alongside this is the protection of cultural landscapes against the dangers to life and property from heavy rainfall and flooding, bank erosion and wave impact. Hydraulic engineering, thus one of the oldest engineering sciences, enabled the construction, operation and maintenance of a wide variety of structures for all such tasks: canals, distribution networks, river barrages, locks, embankment dams, shipping piers, and many more (Strobl and Zunic 2006; Giesecke et al. 2014).

Significant changes in watercourses over the centuries were mainly due to safety requirements and societal type of use (Minor 2000). While rivers and lakes were initially used mainly for water supply and transportation, their shape and nature became the focus of attention from the 18th century onward. Due to the growing population density in urban areas near rivers, flood protection became more important there and rivers were increasingly modified and constructed according to societal requirements (Meurer 2000). With social progress and technical developments in the 19th century, the view of watercourses changed further: requirements for commercial shipping were added and the demand for electrical energy from hydropower increased rapidly (Radkau 2008).

As a result, corrections were made to the alignment of the watercourses. By straightening the river courses a runtime reduction for flood waves was achieved and thus improved flood routing (DWA 2014; Giesecke et al. 2014). Furthermore, land reclamation and cultivation of agricultural areas in the immediate vicinity of watercourses was promoted, including bank reinforcements and the removal of riparian vegetation. The increased discharge capacity of the elongated watercourses led to increased bed erosion, which in turn had to be counteracted by artificial bed stabilization measures as well as by the installation of hydraulic structures like weirs and dams (Patt 2018). Further strong changes in the shape of the watercourses (morphology) as well as their time-dependent variability (morphodynamics) were caused by hydropower expansion and the associated damming of entire river sections (García 2008).

Anthropogenically unmodified rivers usually are in a morphodynamic equilibrium of erosion and sedimentation processes that occur permanently and with varying intensity. On a long-term average, they have a balanced sediment budget, i.e. an equilibrium of sediment inflows and outflows, and an approximately constant mean bed level (DVWK 1993; DWA 2014). At sufficiently high discharges, the sediments are in constant motion and continuously change the shape of these rivers, while the magnitude of sediment transport is subject to strong seasonal fluctuations and geographic characteristics of the flow regime (Zanke 1982; Strobl and Zunic 2006). In such rivers, extreme flood events may lead to a fundamental reshaping of the river course, as a result of which a new state of morphodynamic equilibrium develops (Becker et al. 2020).

Construction measures in rivers, especially those involving damming, disrupt the river continuum, restrict ecological and sediment continuity, and destabilize the natural interplay of erosion and sedimentation (EU Water Framework Directive 2000; García 2008; Popp and Stein 2022). While large barrages and storage dams impound an entire river valley often up to the valley sides, run-of-river barrages essentially affect the cross-section of the watercourse by means of artificial reservoir banks running parallel to the river (Strobl and Zunic 2006). Due to their limited reservoir widths and lower flow depths, transport-effective flow velocities in the river longitudinal direction are present to a greater extent in run-of-river barrages than in storage dams (Harb et al. 2015). Regardless of this distinction, damming reduces the flow velocity in the affected river section and thus reduces the transport capacity of the flow: hence, solids deposit in the reservoir upstream the barrage and sedimentation builds up over time, leading to a loss of storage capacity and causing operational problems (Annandale 2014).

Although parts of the sedimentations at the reservoir bottom can be removed by occasional reservoir flushings or dredging, the natural sediment budget of the watercourse is severely impacted (Patt and Gonsowski 2011; Patt 2018). Beginning at the head of the reservoir (transition from free flow to backwater), flow velocity continuously slows down and flow turbulence and shear stresses continue to decrease, resulting in a sorting process of sedimented grain fractions with decreasing grain diameter along the reservoir (Morris and Fan 1998). Unlike with storage dams, comparatively less cohesive sediments (silts and clays) settle upstream run-of-river barrages because they remain suspended longer along the impounded reservoir due to their small grain diameters and low settling velocities (Hillebrand 2008; Harb 2016). The small grain diameters in cohesive grain fractions lead to an increased influence of electrochemical forces compared to gravity forces, which result in a more resistant erosion behavior (Raudkivi 1982). As a benchmark for riverbeds without relevant cohesive influence, sediment mixtures with up to 10% clay fraction with a diameter

of $d < 4 \mu\text{m}$ can be considered, and even slightly higher fractions of silt (Van Rijn 1993). However, in addition to the flow conditions in the reservoir, the geology in the catchment and the geographic location of the water body are also relevant for the sedimentation processes (Frings et al. 2019).

In contrast to storage dams, reservoir sedimentation ends much earlier in run-of-river reservoirs because of the higher transport capacity and smaller reservoir volume. Then, a new dynamic equilibrium bed can develop, but with different characteristics than before the barrage was built: the mean bed level is significantly higher, has a lower longitudinal slope, and has different morphological characteristics (DVWK 1993; Kohane 2006; Huber et al. unpublished). The upper layers of the reservoir bed are characterized by the finer grain fractions, deposited there over time after the barrage construction, while most of the coarse bed material remained in the area of the head of the reservoir (Fiedler 2008; Bock et al. 2019). Thus, in reservoirs of run-of-river barrages where grain composition is not significantly influenced by cohesion, there exists a primarily sandy, partially uniform upper bed layer that can be several meters thick and highly mobile, depending on local conditions (Kohane 2000; Kohane 2008).

During a flood, such a reservoir bed can start moving on a large scale, with correspondingly strong effects: massive bed transformations with sometimes high water level fluctuations and wave formation in the reservoir, disruptions of power plant and weir operation with increased wear of water-bearing components and machinery, as well as large sediment fluxes into floodplains and agricultural areas (Neuhold et al. 2009; Wurms 2010; Giesecke et al. 2014). Especially for rivers that are anthropogenically altered by a chain of barrages over a large river section, this leads to major challenges in sediment management, because here the individual consideration of a single barrage is usually not without consequences for the neighboring barrages and strong interdependencies exist (Kottke-Wenzel et al. 2022; Loy 2022; Schmalfuß 2022).

1.2. Challenges in run-of-river reservoirs

Concepts for the implementation of the legally required restoration of sediment continuity according to the EU WFD for such watercourses are still controversial among experts, because in many ways ecological, energy-political, agricultural and social needs are intertwined in addition to purely morphological and morphodynamic requirements, and their respective maximum objectives are often in conflict with each other (Hartmann 2009; Frings 2018; Hauer and Habersack 2022). The successful implementation of legal requirements for sediment continuity is complicated by a partial lack of knowledge of

morphodynamic processes, the immense consequences of which for hydropower are described in detail in Hauer et al. (2018) and Hauer (2020). Until today, sediment transport has to be calculated on the basis of empirical transport models, which are, to the most part, very simplistic. Although these models provide relatively good results for sediment budgeting, they are not able to represent the actual processes in their complexity and high dynamics (Gyr and Hoyer 2006; Haun et al. 2022).

Detailed information on bed development in reservoirs, which can be used to understand the complex processes at the reservoir bed and its response to rapidly and strongly changing hydraulic conditions, e.g. during floods or reservoir flushing, and which can also portray dynamic processes temporally and spatially with the required accuracy, are usually not available to a sufficient extent (Gyr and Kinzelbach 2003; Hager 2018; Ancey 2020a; Ancey 2020b). The acquisition of such data, starting with the water level course along a reservoir and the precise discharge determination, continuing with velocity measurements and the measurement of bed load and suspended sediment concentrations, all the way to the particularly important spatial bed survey and dynamic bed development, is hardly possible to the required extent, especially when these data are most needed: during extreme flood events (Fiedler et al. 2008; Schleiss et al. 2014; Haimann et al. 2018).

Those extreme floods are when strong limitations occur for the implementation of measurement campaigns: heavy water turbidity worsens the conditions of use for the applied measurement techniques (Morgenschweis 2018; Stemmler et al. 2019); high mobility of sediment, especially fine sediment, complicates the temporally as well as spatially consistent measurement of the riverbed (Diplas et al. 2008; U.S. Army Corps of Engineers 2013; Gaida et al. 2019); large reservoir dimensions cause high staff requirements, especially if the riverbed should be measured several times in a short period of time due to high transport activity; wave formation, strong flow and flotsam often represent insurmountable obstacles for the compliance with occupational health and safety standards. These difficulties in data collection, in turn, lead to immediate problems in the use of numerical prediction models: the greater the dynamics of a sediment regime, the more variable and complex prove to be the numerical boundary conditions to be defined, and the sparser and more unreliable are the input variables to be estimated from available data sets (ÖWAV 2011).

Consequently, high-quality data sets are not only needed for an improved process understanding of reservoir bed dynamics: for the calibration and validation of hydro-morphodynamic numerical models, high-quality comparative data are essential. Due to the exponential performance increase of computational fluid dynamics (CFD) in the last

decades, especially due to new possibilities in parallel and high-performance computing, numerical sediment transport simulations can fill knowledge gaps where no measured data are available and have become indispensable as a prognostic tool. In addition to the often time- and personnel-intensive, classical physical model experiments, they offer a much-used alternative, with which, above all, very large-scale investigation areas can be processed cost-effectively.

A major weakness of these numerical models, however, is rooted in their underlying empirical transport equations and the resulting dependence on precise model calibration (ÖWAV 2011; DWA 2021). This in turn is based on a large number of empirical assumptions, for example on turbulence modeling or sediment properties, which must be specifically adapted to the boundary conditions encountered in the respective model and verified by means of comparative calculations (Simons et al. 2000). For reasons of cost efficiency, depth- and turbulence-averaged 2D RANS (Reynolds-averaged Navier-Stokes) models are often used in sediment transport modeling in engineering practice (DWA 2021; Aguirre Iniguez et al. unpublished; Schäfer et al. unpublished). The uncertainties contained therein from the insufficient complexity of the selected numerical model for the processes to be modeled and the deficient state of knowledge in their analytical description lead to a high dependence on high-quality measurement data sets (Wurms 2010). Methods that, like direct numerical simulation (DNS), solve the basic hydraulic equations according to Navier-Stokes numerically without a turbulence model and thus reduce uncertainties from model assumptions, have not yet been explored far enough and, moreover, are hardly technically feasible for the spatial and temporal dimensions of a flood event in the reservoir of a run-of-river barrage, even in the near future (Chan-Braun et al. 2011; Mazzuoli et al. 2020).

To address this problem of availability of reliable data sets for numerical modeling, so-called hybrid models combining the advantages of physical and numerical modeling are often used (Holz and Wundes 1980). In most cases, a physically similar (partial) model of the study area or object is investigated in detail and a numerical model is reliably calibrated for further investigations, based on the measured data which were scaled back to the nature scale (Huber and Liepert 2013; Schneefeld et al. 2017). This approach is very suitable for purely hydrodynamic questions and when the model experiments requires a wider range of scenarios to be investigated, so that numerical model uncertainties can be determined and clearly delimited.

However, for morphodynamic questions, additional limitations occur and especially the grain sizes of the natural sediment limit the similar scaling in the physical model: if relevant parts of grain fractions are reduced to such an extent that they would be classified as silts

or even clays in the physical model, so-called scale effects occur due to over-represented cohesivity of the model sediment as a whole (Yalin 1971; Dorer 1984). The previously described run-of-river reservoirs with fine sand depositions in the upper bed layers are particularly affected by this because even large models with only low downscaling are no longer feasible without scale effects in sediment transport, and the spatial and hydraulic capacities of experimental facilities limit the model size.

The use of so-called lightweight sediments with reduced grain density offers a solution to this, but not without drawback. While lightweight sediments generally allow similar representations of fine-grained and largely cohesionless sediments in the physical model, additional scale effects occur, most notably an inevitable vertical model distortion (Kobus 1978; Ettmer 2007; Hentschel 2007). The different height and length scales in the model change velocity distributions over the flow depth and thus, among other things, the water surface gradient, the development of bedforms and consequently biases the assessment of sediment transport (Kobus 1978; ATV-DVWK 2003). In addition, different time scales for hydraulic and morphodynamic processes occur, so that the temporal transferability of experimental results to nature is also impaired, sometimes even impossible (Hughes 1993; Henry and Aberle 2018). Questions about the quantitative transferability of transport rates and bedforms, especially their dimensions and migration velocities, as well as the interaction of the reservoir bed with unsteady flow conditions can thus hardly be answered reliably. A clear summary of the possibilities and limitations of physical modeling is provided by Green (2014), a full treatise can be found in Frostick et al. (2011).

1.3. Research motivation

For the aforementioned reasons, ongoing research projects are addressing a wide variety of aspects of sediment transport modeling, both numerically and physically. Henning (2013) and Goll (2017) show possibilities in the physical analysis and subsequent numerical modeling of small bedforms in uniformly graded medium to coarse silica sand. Karmacharya et al. (2021) address the interaction of fine sand and lightweight sediment in pressure flushings, and Ettmer et al. (2021) show possibilities for using well graded grain-size distributions of lightweight sediments with different densities. A comprehensive look at the current state of experimental methods offering new opportunities thanks to modern measurement techniques for acquisition and processing of morphological and morphodynamic processes is given by Muste et al. (2017) and Aberle et al. (2017).

Despite the great need for research, one question that has been little addressed experimentally so far concerns the spatial extent and time course of bed transformation

processes in run-of-river reservoirs fully sedimented with predominantly cohesionless fine sediment under variable discharge conditions. Reliable data on the morphodynamic equilibrium conditions occurring there as well as on the influence of flood hydrographs on the reservoir bed are largely unavailable for the reasons explained above. This dissertation therefore presents new findings on bed development in run-of-river reservoirs and on the handling of large volumes of highly mobile lightweight sediment in a laboratory environment at high discharge and high sediment transport rates.

The experimental reservoir bed of uniformly graded polystyrene granules was modeled realistically using recirculating sediment management to systematically investigate the variability of bed structures in dynamic equilibrium from the lower flow regime plane bed to the transition phase and upper plane bed conditions as described in Engelund and Hansen (1967). Subsequently, the influence of different flood hydrographs on sediment transport was analyzed. Special attention was paid to spatially and temporally highly resolved measurement data. At the same time, the availability of the generated data for numerical comparison calculations should be high, in order to allow not only a detailed analysis of the morphodynamic processes in the reservoir, but also have potential for optimization of numerical models.

This dissertation is organized as follows: First, the theoretical background is reviewed, which is necessary for the classification of the methods and data presented in this work. This includes, above all, the basics of sediment transport, dune formation in rivers and the physical modeling of these processes. This is followed by a detailed description of the conceptual design and procedure of the planned experiments as well as the presentation of the measuring systems used and their measurement uncertainties. Afterwards, two parts on the performed physical experiments follow, in which the collected data and their further analysis are shown and correlations are discussed, which can be derived from the data. First, the experiments with steady-state hydraulic conditions in the so-called dynamic bed equilibrium are treated, followed by the experiments with unsteady flood hydrographs. Finally, a discussion of the methods used and the data generated with them follows together with an application case and conclusions about the research objectives are drawn.

2. Theoretical background

The purpose of this chapter is to review the theoretical background relevant to this dissertation. Therefore, the topics of sediment transport and bedforms in rivers will be discussed in the following sections to the extent that they are necessary for the understanding of the presented experimental investigations. For comprehensive and complete coverage of the respective topics and beyond, reference is made to the extensive literature and the "classics" in the field of fluvial hydraulics, including: Hjølström (1935), Shields (1936), Bagnold (1956), Kennedy (1963; 1969), Engelund and Hansen (1967), Graf (1971; 1984), Yalin (1972; 1992), Vanoni (1975), Raudkivi (1982; 1990), Zanke (1982), Hughes (1993), Van Rijn (1993) and others, as well as in the more recent literature, such as Graf and Altinakar (1998), Morris and Fan (1998), Yalin and Da Silva (2001), Julien (2002), Gyr and Hoyer (2006), USBR (2006), Garcia (2008), Dey (2014) and Armanini (2018).

In a further section, the main limitations of physical model similarity are presented, because of their importance for placing the presented experiments with lightweight sediment in the broad field of studies on reservoir sedimentation, even though similarity considerations in the classical sense involving the transfer of model results to nature are not part of this work. For a complete review of the subject matter, again, reference is made to the "classics" in the literature, including Yalin (1971), Kobus (1978), Hudson et al. (1979), Dorer (1984), Dalrymple (1985) and Hughes (1993), and more recently Ettmer (2007), Van Rijn (2007), Frostick et al. (2011), Green (2014), Muste et al. (2017) and Henry and Aberle (2018).

The energy equation of open channel flow, based on the Bernoulli equation, is considered the foundation for the nomenclature of the following sections. Figure 1 gives a concise representation of the required parameters for the calculation of the total energy head H .

$$H = z + h \cos \theta + \alpha \frac{U^2}{2g} \quad (2.1)$$

z	...	Elevation of channel bottom above datum	[m]
h	...	Flow depth	[m]
θ	...	River bed inclination	[-]
α	...	Energy (loss) coefficient	[-]
U	...	Area-averaged flow velocity	[m/s]
g	...	Acceleration due to gravity	[m/s ²]

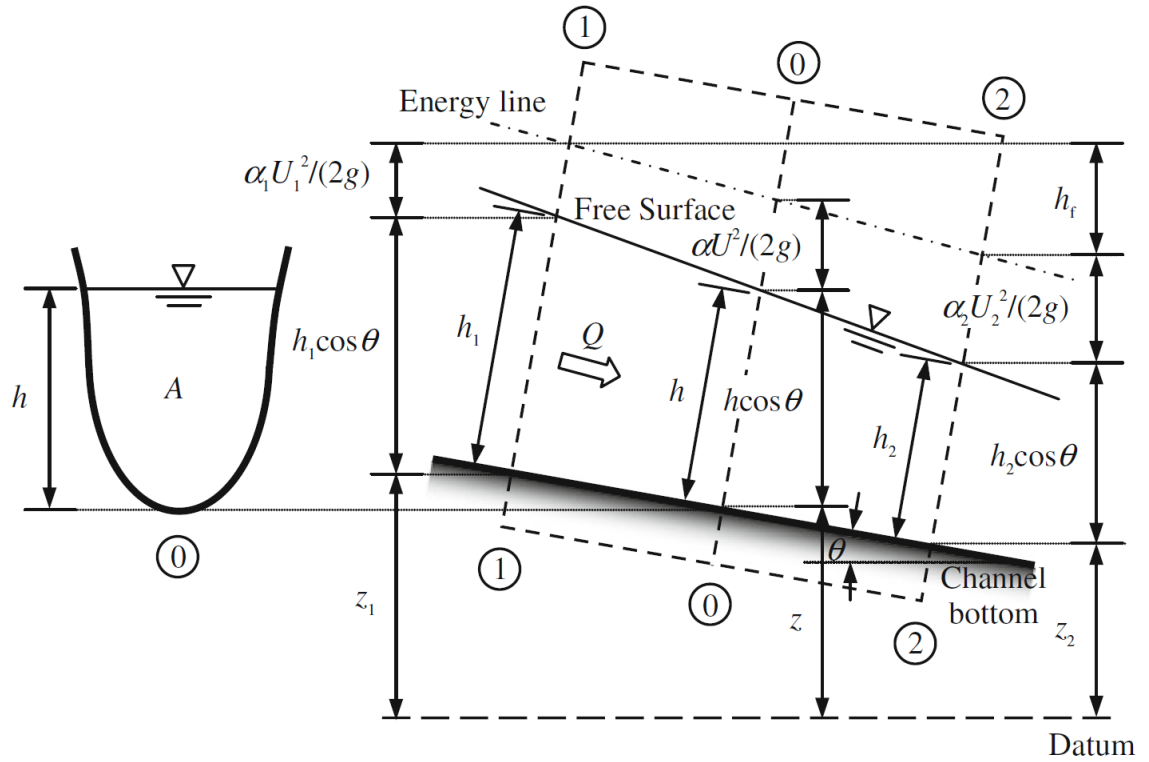


Figure 1: Definition sketch for the derivation of energy equation of a gradually varied steady flow in an open channel (Dey 2014)

Another foundation for the topics to be discussed is the classification of soils and their grain sizes. If no other definition is explicitly referred to in the following, the specifications of DIN EN ISO 14688-1 (2020) apply to this work, which are defined as follows for sands:

- Coarse sand: > 0.63 mm to 2.0 mm
- Medium sand: > 0.2 mm to 0.63 mm
- Fine sand: > 0.063 mm to 0.2 mm.

2.1. Sediment transport mechanisms

Sediment transport mechanisms and morphological processes comprise a wide range of spatial and temporal scales: grain motion is initiated momentarily and the governing processes only takes a few seconds, while bedforms like dunes migrate at much lower speeds and in the scale of hours or days. Changes to the shape of a watercourse occur within years and decades, whole catchments evolve only in geological time scales (Kern 1994; Kleinhans et al. 2015; Henry and Aberle 2018).

When talking about sediment transport, different terms are often used interchangeably, even if they each have a different meaning. The following definitions according to Merkblatt DWA-M 570 (DWA 2018) as well as the respective translation into German (*in italics in brackets*) are used in this work:

- Sediment transport (*Feststofffracht*) in [kg]
- Sediment transport rate (*Feststofftransport*) in [kg/s]
- Sediment load (*Feststofftrieb*) in [kg/(s·m)]

It is important to note that most of the experiments on which the partly semi-theoretical fundamentals of sediment transport are based were not conducted with lightweight sediment, but with natural sediments with a grain density usually in the range of 2.5 - 2.8 kg/m³ (García 2008; Dey 2014). The physical processes underlying the transport of lightweight sediment are the same, but their influence or occurrence may have different relative magnitudes or frequencies (ASCE Task Committee 2000).

2.1.1. Modes of sediment transport

Sediment transport processes can basically be divided into near-bed bedload transport, which mainly involves sands, gravels and larger grains, and far-bed suspended sediment transport, which mainly involves clays and silts, as well as sand under correspondingly high flow impact. Bedload transport comprises several different transport states of individual sediment particles: rolling, sliding and saltating, in which a greater distance is covered per unit time in ascending order. Particles that leave the near-bed layer and enter the far-bed flow, where they can travel significantly longer distances before contacting the bed again, are classified as being in suspension. Sediment particles that are so small that they almost always remain in the water column and do not sink are further differentiated within the suspended load and are referred to as wash-load (see Figure 2). The sedimentation behavior of suspended particles can be described mainly by the settling velocity (Rouse 1938).

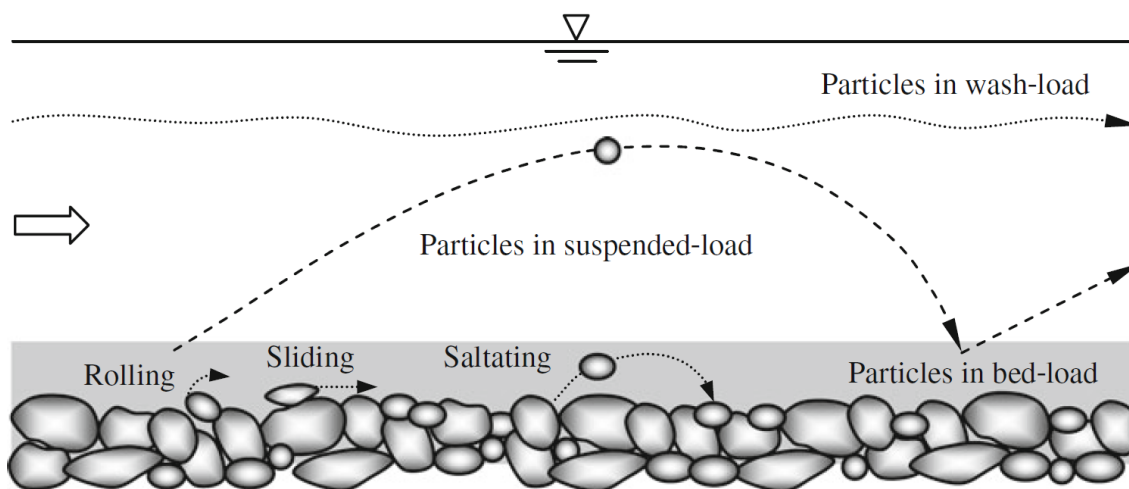


Figure 2: Transport modes of sediment, schematic (Dey 2014)

2.1.2. Sediment transport parameters

A detailed multilayer model for the description of the physical parameters involved in sediment transport was presented in Kaczmarek et al. (2019) (see Figure 3). There, separated by velocity, transport mode and friction, all essential variables involved in sediment transport can be seen, as well as the division of the flow and bed longitudinal section into several layers of different properties or functionality. In comparison to natural sediments, the contact layer will be relatively larger and the grain collision sub-layer smaller for lightweight sediments: due to their lower density, much lower shear stresses are required to pull grains from the dense packing of the grain collision sub-layer into the flow. This agrees with the observation of Zanke (2003), who reported higher relative lift force impact on flow exposed grains due to turbulent velocity fluctuations, which play an even more important role in lightweight sediments. Besides, the outer flow layer is of relatively greater relevance for lightweight sediment, because these particles can more easily reach the outer flow and then travel longer distances, where they are kept in suspension primarily by turbulence.

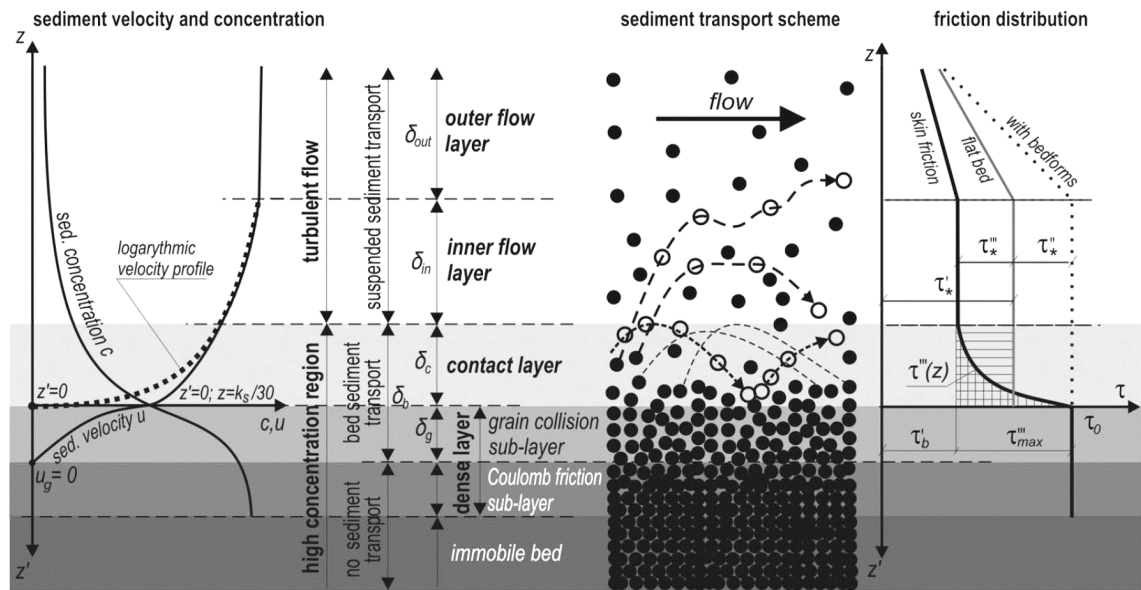


Figure 3: Multilayer structure of sediment transport, schematic (Kaczmarek et al. 2019)

The flow over the more or less loose particles in the contact layer exerts a shear stress on the bed and if the stabilizing resistance of the sediment particles is lower, particle motion sets on. The bed shear stress τ in the flow in proximity of the river bed, following Kaczmarek et al. (2019) located at the top of the contact layer, is traditionally calculated from the bed slope S , which can be replaced by the energy gradient I for steady uniform flow.

$$\tau = \rho g h S \quad (2.2)$$

ρ	...	Fluid density	[kg/m ³]
h	...	Flow depth	[m]
S	...	Bed slope	[-]

Depending on the flow regime and the river bed, τ is typically composed of two or three components, coming from bed skin friction τ' , form drag from bedforms τ'' , and drag of moving sediment particles τ''' ,

$$\tau = \tau' + \tau'' + \tau''' \quad (2.3)$$

A common way to calculate bed shear stress other than from the bed slope is by describing τ as a function of dynamic pressure with the Darcy-Weisbach friction factor λ_D , estimated from the Colebrook-White equation given in Colebrook and White (1937) or from its explicit form in Haaland (1983). Other existing approaches to bed shear stress calculation can be found in the literature, e.g. Chanson (2004) or Dey (2014).

$$\tau = \frac{\lambda_D}{8} \rho u^2 \quad (2.4)$$

$$\frac{1}{\lambda_D^{0.5}} = -0.782 \ln \left[\left(\frac{k_S P}{14.8 A} \right)^{1.1} + \frac{6.9}{Re} \right] \quad (2.5)$$

u	...	Flow velocity	[m/s]
k_S	...	Equivalent sand roughness	[m]
P	...	Wetted perimeter of the riverbed	[m]
A	...	Flow area	[m ²]
Re	...	Reynolds number of the flow	[-]

The determination of k_S depends on many factors, including sediment grading and the presence of bedforms. Typically, k_S can be estimated from the representative sediment size d_m , for which, again, numerous approximations exist. For uniformly graded sediment with uniform grain distribution, $d_m \approx d_{50}$ can be assumed, where d_{50} corresponds to the 50 percent passing in classical sieve analysis (Zanke 2013). The Reynolds number Re of the flow describes the influence of the fluid viscosity on the flow regime with the kinematic viscosity ν . When Re is greater than 500 in open channel flow, which it usually is, then the flow changes from laminar to turbulent (Jirka and Lang 2009).

$$Re = \frac{uR_h}{\nu} = \frac{u\frac{A}{P}}{\nu} \quad (2.6)$$

R_h ... Hydraulic radius [m]

ν ... Kinematic viscosity [m²/s]

The Froude number Fr describes the influence of gravity on the flow via the propagation velocity $c = \sqrt{gh}$ of a gravity wave in shallow water. For $Fr > 1$, the flow velocity is greater than the wave velocity and so-called supercritical flow occurs in the upper flow regime. Otherwise, subcritical flow is present in the lower flow regime.

$$Fr = \frac{u}{c} \quad (2.7)$$

c ... Wave propagation velocity [m/s]

2.1.3. Initiation of sediment transport

For sediment grains to start moving, there must be a minimum of driving forces. These forces must overcome the weight of the sediment particles and the stabilizing effect of surface friction and neighboring particles. A very general representation of this complex problem is shown in Figure 4: Buoyancy-reduced weight force F_G and resistance F_R counteract the driving forces coming from lift F_L and drag F_D .

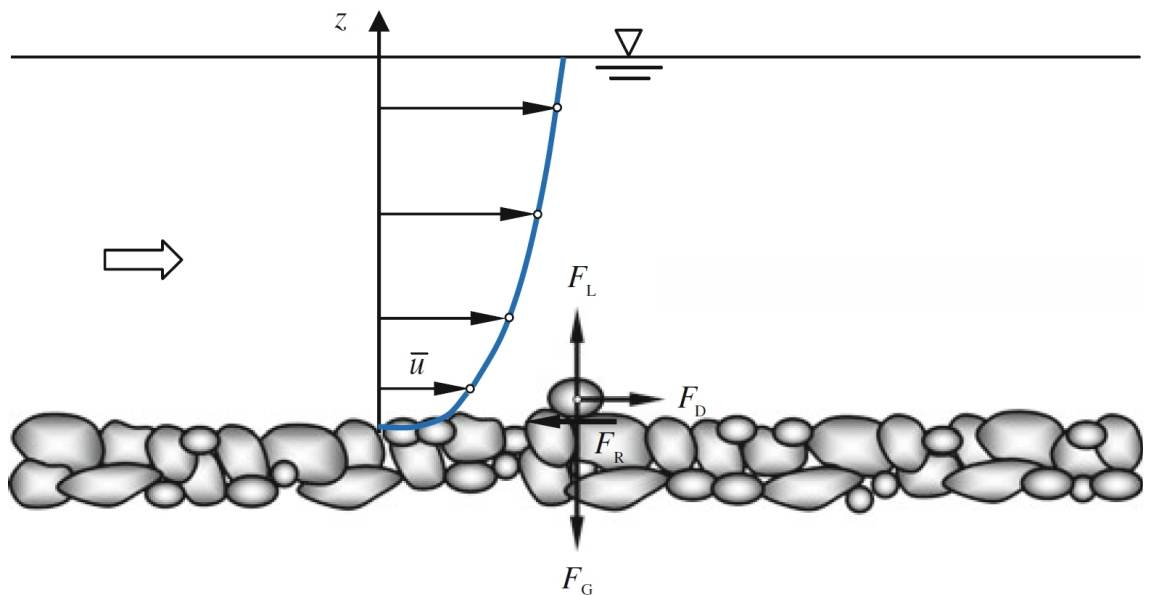


Figure 4: Instantaneous hydrodynamic forces acting on a sediment particle (modified from Dey (2014))

For the description of this most complex problem a variety of approaches exist, which define a threshold value for the initiation of motion and perform a comparison with the existing flow state. Thresholds in those models are deduced from flow velocity or lift force, others

from turbulence and some are probabilistic. A full presentation can be found in Dey (2014). The most wide spread models, however, use shear stress as threshold indicator, the best known of these is the Shields approach (Shields 1936). It was designed to characterize bedload transport of sediments in general, including those of varying density. Shields used two dimensionless parameters for this purpose, the shear Reynolds number Re_*

$$Re_* = u_* \frac{d_m}{\nu} \quad (2.8)$$

u_* ... Shear velocity [m/s]

d_m ... Representative sediment diameter [m]

and the dimensionless shear stress τ^* , with the so called critical dimensionless shear stress τ_c^* for initiation of motion often referred to as Shields parameter θ .

$$\tau^* = Fr_*^2 = \frac{u_*^2}{\rho' g d_m} = \frac{hS}{\rho' d_m} \quad (2.9)$$

Fr_* ... Shear Froude number [-]

ρ' ... Relative density [-]

The shear velocity u_* used in the calculation of Re_* is calculated as follows:

$$u_* = \sqrt{\frac{\tau}{\rho}} = \sqrt{g R_h S} \quad (2.10)$$

The relative density ρ' used to calculate τ^* or Fr_* , respectively, is determined from the material densities of sediment and fluid.

$$\rho' = \frac{(\rho_s - \rho)}{\rho} \quad (2.11)$$

ρ_s ... Sediment grain density [kg/m³]

Shields' approach has been reviewed and extended in a variety of subsequent studies, including Vanoni (1964), Kennedy (1995), Neill and Yalin (1969), Gessler (1970), Brownlie (1981), van Rijn (1984a), and Soulsby and Whitehouse (1997). Because of their definition, the relation of Re_* and τ^* is implicit in Shields' approach, so Figure 5 shows a modified and extended representation of the classical Shields diagram in explicit form, which includes additional information on the flow regime, suspended load, and bedform formation. Instead of Re_* , Re_p is used, the particle Reynolds number.

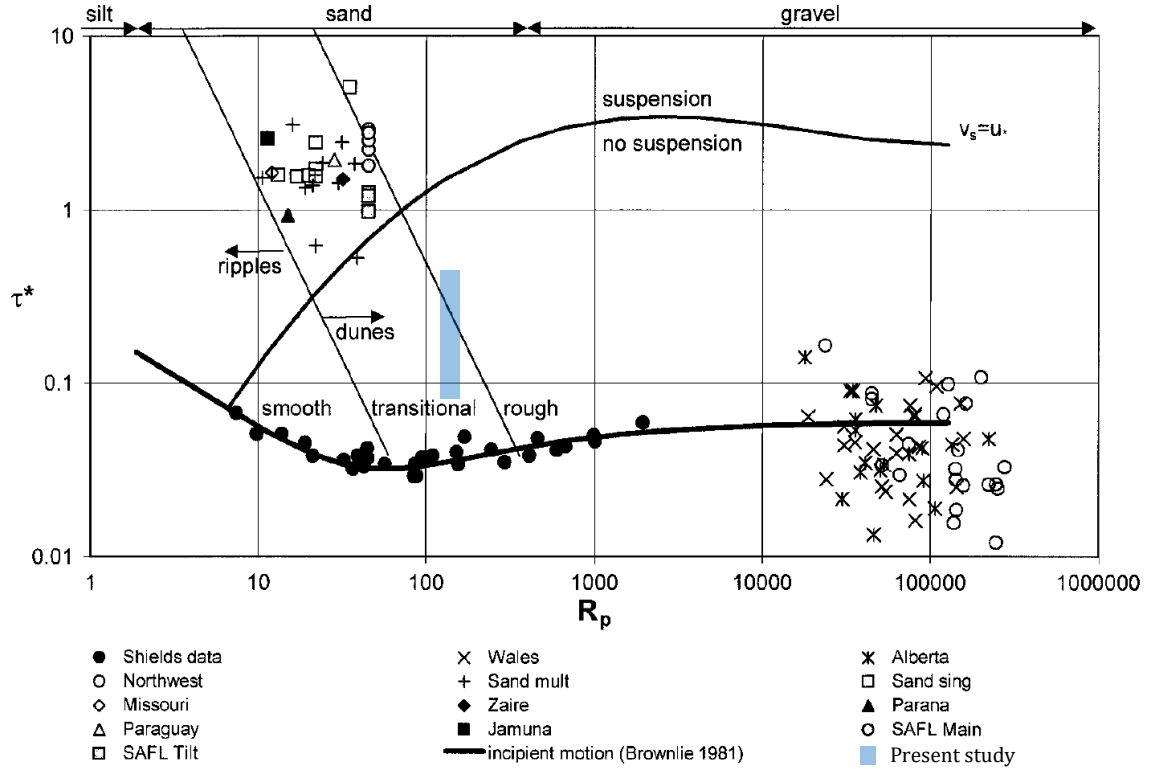


Figure 5: Shields regime diagram (modified from Garcia et al. (2000))

$$Re_p = \sqrt{\rho' g d_m} \frac{d_m}{\nu} \quad (2.12)$$

2.2. Bedforms in rivers

As soon as sediment transport commences, the formation of geometrically similar structures also begins, so called bedforms, which can be regarded as patterns with a repeated sequence in a statistical sense for steady flow conditions. Two groups of parameters mainly influence bedforms: hydraulic factors like flow depth, flow velocity and turbulence, and morphological factors like sediment density, particle size and shape, and bed slope (Kennedy 1969; Best 1988; Gyr and Hoyer 2006). Bedforms are caused by complex sediment transport processes and, at the same time, decisively influence these processes; they are most pronounced in sandy riverbeds (Yalin 1972; Zanke 1982).

2.2.1. Types of bedforms

From a completely flat, primarily sandy bed that starts to move (lower plane bed, $Fr \ll 1$), first smaller ripples, then dunes superimposed with ripples, then larger dunes develop as hydraulic stress continues to increase. After a tipping point (beginning of transition zone, $Fr \lesssim 1$), the dunes lose height again, become elongated, and are finally washed out, so that a new flat bed develops (upper plane bed, $Fr \gtrsim 1$) (see Figure 6). From there, the so-called

antidunes with standing and later breaking waves develop, followed by the formation of chutes and pools (Kennedy 1963; Simons and Richardson 1966; Best 1992).

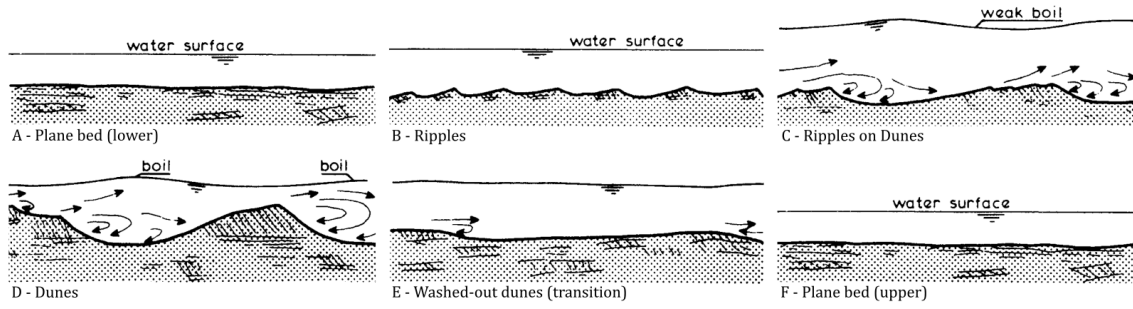


Figure 6: Bedforms according to Simons and Richardson (1966), schematic, modified from Van Rijn (1993)

Most laboratory studies of bedforms have used uniformly graded sands, leading to some limitation in the generality of the findings derived. For example, the tipping point for the onset of the transition to the upper plane bed varies greatly depending on sediment properties, and only few data are available because of the high hydraulic loads required to establish these conditions in experiments. Froude values of as low as 0.5 were recorded for sands with grain sizes below 1 mm according to data from Guy et al. (1966), analyzed for the transition process in Karim (1995). Nevertheless, the upper stage plane bed does only develop under certain circumstances, depending on the sediment properties and the hydraulic stress (Ashley 1990).

The formation of bedforms also very much depends on the dominant grain fractions: In continuously graded sand, the largest bedform height amplitudes occur, that exceeded those in mixtures of sand and gravel by a factor of 3 to 5 according to Núñez-González and Martín-Vide (2010). For coarser gravel, elongated dunes and different types of bars can still be observed (Carling 1999); At the other end of the spectrum, cohesion hinders the formation of bedforms in very fine sediments and large dunes are usually not present in fine sand beds with $d_m \leq 0.2$ mm (Zanke 1982). An important parameter for the assignment of bedforms and bed properties is the dimensionless particle diameter D_* according to Bonnefille (1963), which has no relation to hydraulics and can therefore be used universally.

$$D_* = d_m \left(\frac{\rho' g}{\nu^2} \right)^{1/3} = Re_p^{2/3} \quad (2.13)$$

Since bed and flow are in permanent interaction, the velocity profile above the bed, the local flow turbulence and consequently the resulting shear stress change with the bed roughness. There are different opinions in the literature about the exact extent of this influence (see Figure 7), not least because a direct measurement of the local shear stress is highly

demanding and its interpretation non-trivial (a.o. Harb (2016) and Goll (2017)). The distinctive feature of bedform formation is its stabilizing effect against erosion by a, formally speaking, enormous increase of the overall roughness of the bed via the bedform drag τ'' with increasing hydraulic stress (cf. Armanini (2018)). The different courses of the shear stresses in ripples and dunes are particularly interesting: while Engelund and Hansen (1967) assume an increase of the total shear stress with growing dunes, Raudkivi (1990) expects a shear stress maximum in the transition zone from ripples to dunes, i.e. where ripples tend to exist on dunes.

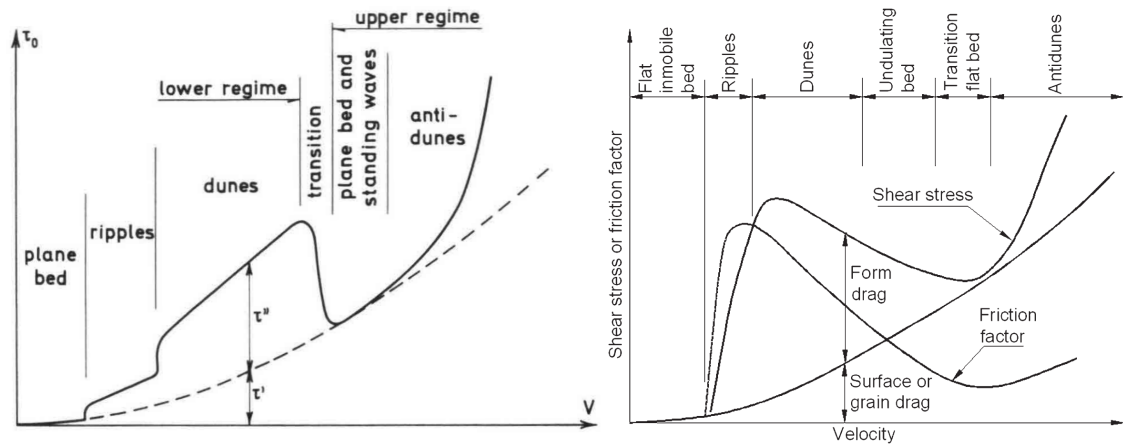


Figure 7: Shear stress and friction over bedforms as a function of velocity: after Engelund and Hansen (1967) (left), after Raudkivi (1990) in Garcia (2008) (right)

2.2.2. Dune migration

In the lower flow regime, dunes influence the flow strongly. While ripples have hardly any effect on the water level and also transport only little material, dunes clearly affect the flow depth of the flow surrounding them. If constant flow conditions prevail over a longer period of time, so-called equilibrium dunes develop. These are in equilibrium with the ambient flow and they show constant average values e.g. for dune height or dune length, while individual dunes may well differ in their shape and also undergo significant changes in shape during migration (e.g. in Henning (2013)). However, since the dune shape reacts only very slowly to the current flow conditions and a constant sediment availability is also required for dynamic equilibrium, equilibrium dunes are rarely found in nature (cf. Hudson (1979), Garcia (2008) and Van der Mark et al. (2008)).

The relevant terms and parameters for the transport of dunes are shown in Figure 8. The dune length λ , which is often referred to as wavelength due to the periodic nature of successive dunes, is measured from the low point of one dune trough to the low point of the next dune trough; the dune height Δ or η_D is measured vertically from the line connecting two dune troughs to the highest elevation of the dune ridge, the dune crest. The area of the

dune facing the flow is called the stoss side; the dune front facing away from the flow is on the lee side. Along the dune ridge, sediment grains are transported downstream at increased velocity and are first deposited in the deposition zone in front of the dune, stabilizing the dune front's angle of repose, and are then reincorporated by the moving dune. In this way, the dune as a whole migrates downstream at low velocity and largely retains its shape.

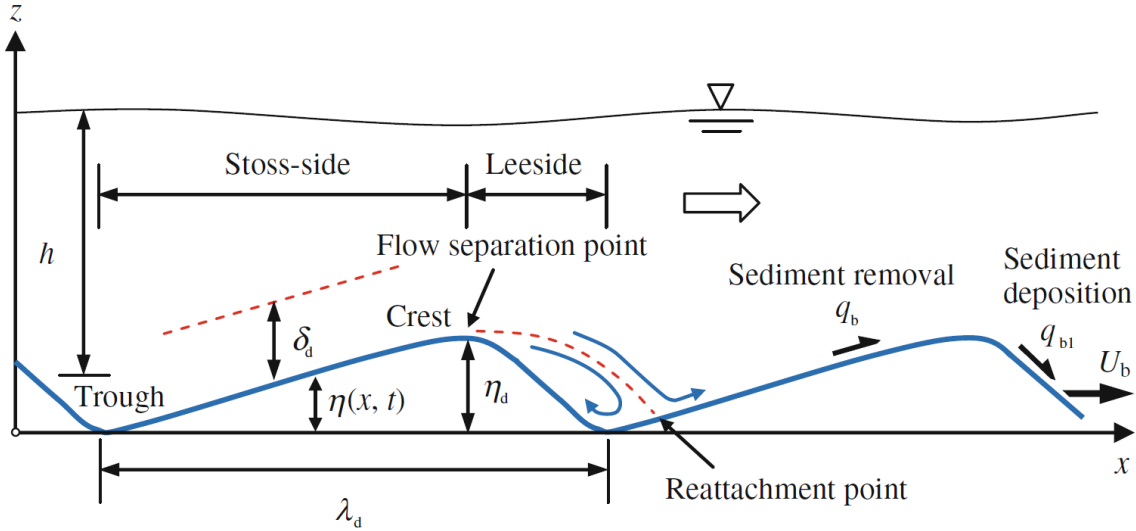


Figure 8: Transport processes of dunes, schematic (Dey 2014)

The velocity distribution above a dune is strongly non-uniform and, depending on the size of the dune, several zones of increased turbulence develop (Engelund and Fredsoe 1982; Bennett and Best 1995; ASCE Task Committee 2002; Best 2005). A lot of sediment is moved in these shear layers, which are marked with number 2 in Figure 9: either a sediment particle goes into suspension there or it gets into the backflow zone on the lee side of the dune. The water level reaches a maximum after the area of the separation zone (number 1) where the reattachment point of the flow can be assumed (cf. Figure 8) and a minimum in the area of the dune crest; at the same time, the flow velocities are at a maximum here (number 5) according to the specific energy in subcritical flow (Chanson 2004; Jirka and Lang 2009; Bollrich 2013). Sediment that is not retained by the backflow is driven up the stoss-side of the dune mainly by turbulence from the reattachment zone onwards, although the shear stresses here are lower than the initiation of motion threshold value (cf. internal boundary layer (number 4) or δ_b) (Zanke 1982; Fredsoe 1982; Dey 2014).

The processes described, however, do not only occur in longitudinal sections as 2D effects but also in three-dimensional dunes, depending on the nature of the flow cross section, the flow conditions and the sediment properties. The decisive factor here is the available bed width, which in morphodynamic studies in experimental channels is often too small for the formation of three-dimensional dunes (Henning 2013). Several studies suggest that under

steady-state equilibrium conditions and sufficiently long experimental times, three-dimensional dunes inevitably form, albeit being less stable in shape and arrangement (Venditti 2005; Coleman et al. 2011; Coleman and Nikora 2011).

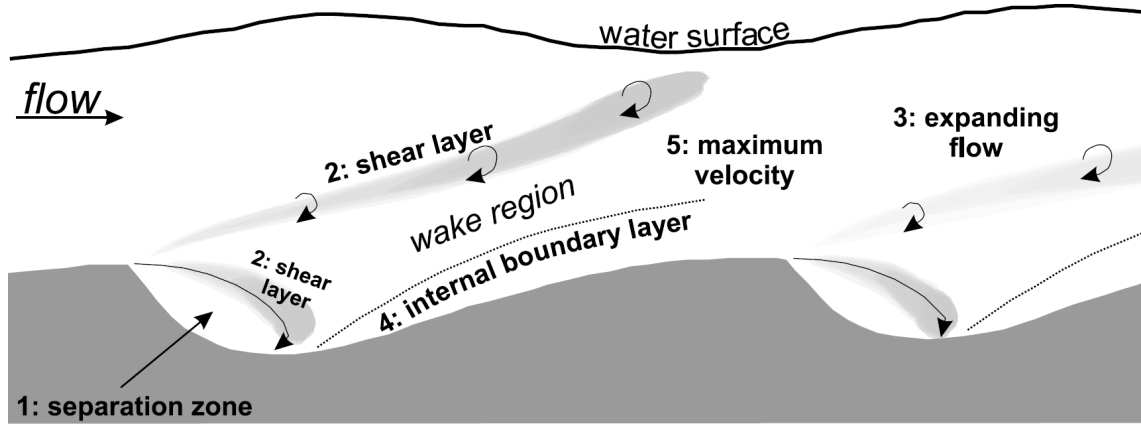


Figure 9: Schematic diagram of the principal regions of flow over asymmetrical, angle-of-repose dunes, schematic (Best 2005)

Notwithstanding this, the understanding of three-dimensional dune development remains limited to this day (Best 2005), and the magnitude of factors such as flow depth and cross-sectional width, two- and three-dimensional flow turbulence, and unsteady flow conditions that are responsible for the development of three-dimensional dunes is not clearly understood (Ashley 1990; Gyr and Hoyer 2006; McElroy and Mohrig 2009). Furthermore, in three-dimensional dunes, superimposed forms of different size scales must also be distinguished (Coleman and Nikora 2011). To describe dunes, formulas are often used that relate dune length and height to flow depth or hydraulic stress under equilibrium conditions (Yalin 1964; Van Rijn 1984b; Flemming 1988; Yalin 1992; Yalin and Da Silva 2001). An exception to this is Fredsoe (1982), who deduced a model to describe the entire development process of a dune after a flow step. A simple approximation for the description of the fully developed dune stage, which is still frequently used today, was made by Yalin (1964) as a function of the mean flow depth h :

$$\lambda = 2\pi h \approx 6h \quad (2.14)$$

Julien and Klaasen (1995) stated for λ/h a value of 6.25. Zanke (1982) compared existing formulas for the estimation of dune height and concluded that bedform height in lowland rivers with sand bed $d_m > 0.2$ mm is of the order of $0.15 < \Delta/h < 0.3$, while Garcia (2008) states for well-developed dunes that $\Delta/h \leq 1/6$.

The relation of dune height to dune length Δ/λ , referred to as dune steepness, was analyzed in various studies (cf. Yalin and Karahan (1979), Shen (1990), Karim (1995) or Carling

(1999)). A functional description with good overall agreement to both field data and laboratory data was presented by Flemming (2000).

$$\Delta = 0.0677\lambda^{0.81} \quad (2.15)$$

Flemming (2000) further showed an exponential correlation of dune length and dune height that accounts for the influence of grain size and suggests self-similarity of dunes across all flow conditions, with limitations being water depth and flow velocity (Figure 10).

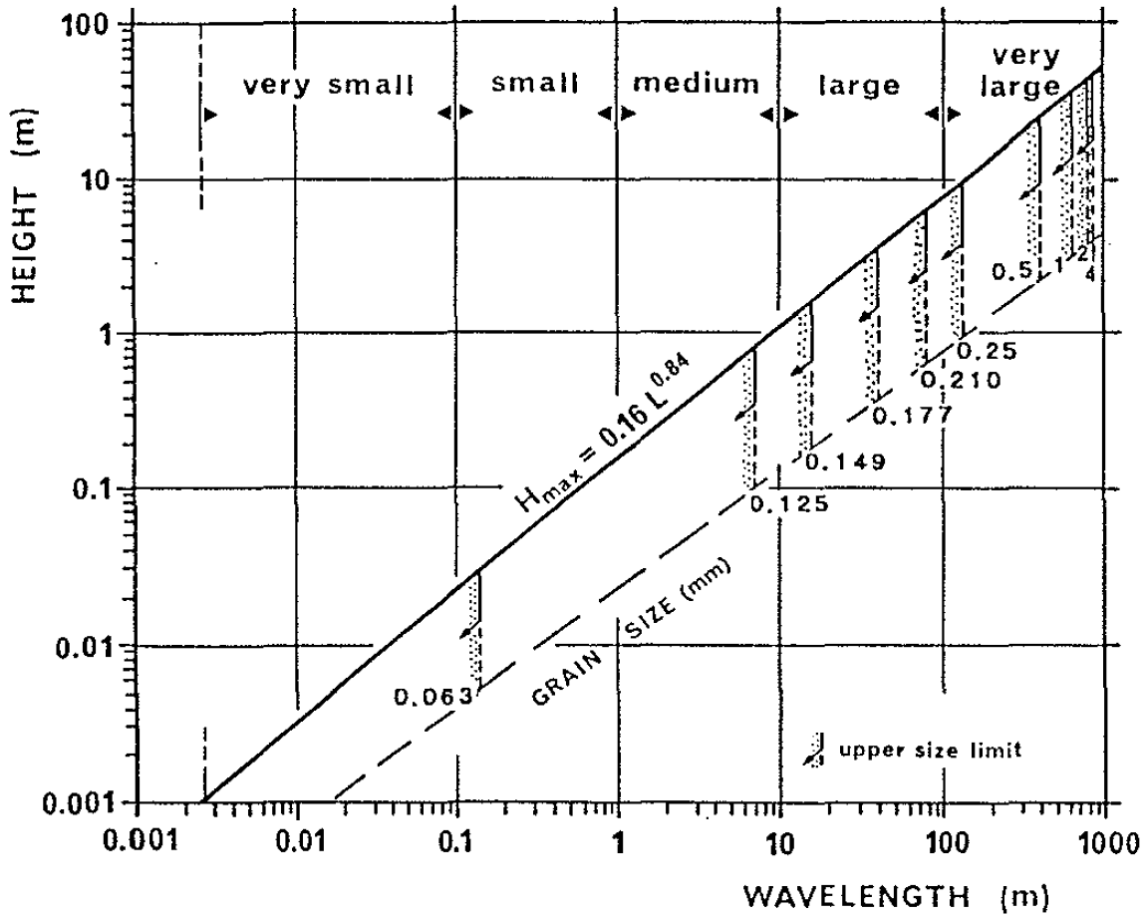


Figure 10: Dune height versus dune length as a function of grain size (Flemming 2000)

Since equilibrium conditions are rarely found in nature and because of the complexity of three-dimensional dune migration processes, application of the existing formulas is often highly inaccurate (Mertens 1995; Julien and Klaassen 1995; Amsler and García 1997; Jerolmack and Mohrig 2005; Van der Mark et al. 2008). Even more so, highly unsteady flow conditions, such as those encountered during floods, are poorly studied, and there is considerable interest in new physical laboratory and field data as well as advances in numerical modeling (ASCE Task Committee 2000; ASCE Task Committee 2002; Schumm 2005; Papanicolaou et al. 2008).

2.3. Physical modeling in river hydraulics

Similarity models, in the broadest sense, are simplified representations of a natural physical object in which all quantities in the model have a predetermined relationship to the corresponding quantities in nature (referred to as prototype in the following), which is specified by one or more model scales. "The requirement for 'similarity' of a model to nature requires geometric, kinematic, and dynamic similarity." (translated from Kobus (1978)). Full dynamic similarity between two geometrically and kinematically similar systems derives from Newton's second law of motion and requires that the relations of all corresponding force vectors in both systems be the same (Frostick et al. 2011).

However, while geometric similarity can usually be well established, physical models with free surface flow, usually implemented as so-called Froude models, are subject to some limitations in representing kinematically and dynamically similar hydraulic and morphological processes; how they are handled determines the quality of experimental results. True similarity in river engineering problems can thus rarely be achieved. The limitations of Froude models can be roughly divided into three categories: Hydraulic limitations, morphological limitations and limitations of the laboratory. The following theoretical considerations are mainly based on Yalin (1971), Kobus (1978), Zanke (1982), Hughes (1993) and Novak et al. (2010), in which the underlying dimensional analyses and their derivations are fully explained.

2.3.1. Limitations of Froude models

The hydraulic limitations include the mandatory fulfillment of the so-called Froude similarity, in which inertial and gravitational forces are correctly represented. However, other forces, e.g. coming from fluid viscosity, surface tension or Coriolis acceleration, are not accurately modeled and thus are subject to scaling effects (Sutherland and Soulsby 2010). In particular, the overestimation of the influence of surface tension and grain friction should be mentioned, which increase strongly with decreasing model dimensions. To minimize the influence of altered grain friction, Reynolds number invariance is required, which is considered to be satisfied when $Re \gtrsim 10^6$. Then, hydraulically rough flow conditions exist in prototype and model, or fully developed turbulent flow (Yalin 1971) prevails. A change in Reynolds number then causes no change in the friction factor λ_D (Chanson 2004; Jirka and Lang 2009).

Maintaining kinematic and dynamic similarity in a physical model with free surface flow in scientific practice is usually complicated by the fact that water is used as the flow medium in prototype and model alike. The requirement of equal length scales, given by

$$\frac{\eta_r}{\rho_r g_r^{1/2}} = L_r^{3/2} \quad (2.16)$$

η	...	Dynamic viscosity	[kg/m·s]
L	...	Length	[m]
Index r	...	Scale number; Relation of nature/field to model	[-]

cannot be observed due to the same fluid densities. In order to maintain dynamic similarity in models with free surface flow, however, the Froude numbers in model and prototype must always be the same: Compliance with Froude's model law

$$Fr_r = \frac{u_r}{\sqrt{g_r L_r}} = 1 \quad (2.17)$$

then inevitably leads to a non-compliance with Reynolds' model law and the Reynolds number of the downscaled model is always smaller than in the prototype.

$$Re_r = \frac{\rho_r u_r L_r}{\eta_r} \neq 1 \quad (2.18)$$

The relatively too high viscosity impact in the model must therefore be compensated for by adjustments elsewhere. Thus, a reduction of the grain roughness reduces the bed roughness and leads to a smaller total friction factor. As a result, the energy line gradient in the model is reduced, at best to the same level as in the prototype. However, as a side effect of this adjustment, velocity distributions over depth are no longer correctly represented due to the change in wall and bed friction.

A deliberate adjustment to geometric similarity in many hydraulic models with free surface flow to compensate for excessive viscous influence in non-rough flow conditions is vertical model distortion. This usually involves exaggerating the model in the vertical, i.e., using a smaller scale number for the vertical dimension than for the horizontal dimensions. In this way, the model is compressed in the longitudinal direction and the longitudinal bed slope is increased, which also increases the Reynolds numbers. The factor of vertical distortion n is defined as follows:

$$n = \frac{L_{rh}}{L_{rv}} \quad (2.19)$$

Index rh ... Horizontal scale number [-]

Index rv ... Vertical scale number [-]

However, the vertical model exaggeration alters the flow conditions in the model even more than the reduction of bed roughness described above. Under these conditions, a direct transfer of the velocity distribution in the flow cross-section to the prototype is no longer possible; likewise, local flow phenomena with vertical velocity components are incorrectly reproduced (Yalin 1971; Jirka and Lang 2009). Since the viscosity of the model fluid is equal to the viscosity in the prototype, turbulent decay processes and viscous damping also occur out of scale (Kundu and Cohen 2002; Dey 2014).

Furthermore, a vertical model distortion is based on some very basic assumptions, most importantly the uniformity of a flow and the ability to describe the flow using mean values. Compliance with the shallow water boundary $h > 5k_s$ (Bollrich (1989) in Martin et al. (2015)) and the validity of the Manning-Strickler equation only in the hydraulically rough region are assumed. Inaccuracies always arise along the way, which is why vertically distorted models must always be calibrated using one or more historical events, which in turn can only be accomplished with the help of high-quality data.

Morphodynamic limitations occur depending on the nature of the sediment encountered in nature. Fine, but still cohesionless grain fractions in the prototype may have to be reduced by scaling to such an extent that they become cohesive in the model. Insofar as these sediment fractions are relevant for the sediment transport processes, corresponding scaling effects occur here due to additional drag forces of the cohesive fractions. For a similar representation of the interaction of sediment and fluid, the grain size scale number d_r and the scale number of the solid densities ρ_r are required additionally, which are related to each other in the following relation:

$$d_r = \Delta \rho_r^{-1/3} \quad (2.20)$$

Together with the length scales L_{rh} and L_{rv} , these scale numbers result in separate time scales for the hydraulic processes and the sediment transport processes. Different morphological processes have different morphological time scales at grain scale and bedform scale, which has to be separated further by vertical and horizontal direction (Yalin 1971). Usually, in practice, morphological models are designed in such a way that next to one hydraulic and one grain time scale a third morphological time scale absorbs the

uncertainties and errors from all of the other chosen scales and for which a calibration at one or more historical event is inevitable (Kobus 1978). Furthermore, Henry and Aberle (2018) refer to an unpublished study showing a fluctuating morphodynamic time scale as a function of flow magnitude in unsteady experiments. For a comprehensive analysis of the influence of time scales, the reader is referred to Henry and Aberle (2018).

In addition to all of the above, limitations in the laboratory include external factors that influence dynamically similar modeling or limit its implementation. Limitations may include the following (list incomplete):

Limitation type	Description
Spatial	Size of laboratory and supporting infrastructure. Accessibility of facilities
Material	Minimum or maximum surface roughness that can be produced Feasibility of construction works
Hydraulic	Discharge capacity Water quality Water supply (natural stream or circulation)
Morphological	Properties of the bed material Sediment supply and removal
Measurement technique	Availability and applicability of measuring equipment and measuring systems
Personnel	Availability of technical and scientific personnel

Table 1: Limitations in the laboratory when performing dynamically similar model experiments

2.3.2. Lightweight sediment in physical modeling

Movable bed models with mostly artificial granulates of reduced density and increased grain diameter compared to the prototype can maintain similarity in both Re_* and Fr_* and allow for a general application of the Shield's diagram and the advancements made in the past (Henry and Aberle 2018). Also, their usage can counteract a possibly too low bed roughness in the model at flow conditions in the hydraulic transition zone between laminar and fully turbulent flow and increase the energy line gradient. The influence of grain roughness on bed roughness, however, is generally secondary in morphological models because the bedforms created by sediment transport processes exert a significantly greater influence on bed roughness.

In most applications, an adjustment of the sediment density in the model inevitably results in a range of scale effects, most importantly a vertical model exaggeration together with the previously described consequences for the transferability of the flow conditions. In addition

to this, sediment transport processes are also affected by model distortion and due to non-similar scaling of particle accelerations, an underestimation of sediment transport rates occurs. Furthermore, particle diameters of lightweight particles are often larger than they should be due to limited availability on the market and due to laboratory limitations in lightweight sediment handling (Hughes 1993). Thus, there is a proportionally reduced flow impact on each individual grain, because the particle resistance to motion increases with the particle volume (hence weight) by the power of 3, while the impact area only increases linearly with the grain diameter.

On the other end of the spectrum, the higher particle diameter leads to increased bed porosity, particles may go into suspension earlier than in the prototype due to local flow turbulence and also bed liquefaction can occur sooner than it would in the prototype (Hughes 1993). Suspended transport, hence, can only be modelled exactly in an undistorted model, but inaccuracies may be accepted for models with mainly bedload (Henry and Aberle 2018). Apart from that, the strong interaction of flow and bed during bedform development is also adversely affected by the vertical model distortion, and so is the sediment load. Shields parameters, which are identical in model and prototype in rough turbulent flow conditions if the model and prototype densities are identical, cannot be directly transferred accordingly. Following this, there is little knowledge how model distortion and the different sediment properties affect bedform shape and kinematics (Henry and Aberle 2018). As a result of the above described, morphodynamic models need to be precisely calibrated to overcome the difficulties of transferring model results directly (Kobus 1978; Muste et al. 2017).

The most widely recognized studies that considered light sediment were performed by Shields (1936) and Meyer-Peter and Müller (1948), although Dittrich et al. (1992) noted that the initiation of motion for particles with densities other than sand is not satisfactorily described there. The introductory remarks of Shen (1990) to the NATO workshop on movable bed physical models are still valid today: "Movable bed models have long been employed to investigate complex hydraulic phenomena. However, the design and usage of models still greatly rely upon experiments and judgments.", and they are even more true for lightweight sediment bed models. Sutherland and Soulsby (2010) pointed out that, in addition to their difficult and expensive generation, the scarcity of high-quality measurement data from field and laboratory studies to date is exacerbated by poor reusability of datasets resulting from too low standards of data management and associated documentation.

Recent research in the field was conducted by Ettmer (2007), Meyering (2012), Ettmer et al. (2015), Link and Ettmer (2018), and Müller et al. (2021), who studied scour development around hydraulic structures such as gates or bridge piers. Mixtures of light sediments to similarly reproduce grain size distributions showed promising results for dynamic similarity in bedform studies, even if geometric similarity cannot be maintained, in studies by Ettmer et al. (2017) and (2021), Hüsener and Hesse (2021), and Orlik and Baumgärtner (2021). Gorricks and Rodriguez (2014) focused on predicting similar dimensions for sand dunes in a physical model solely via the Shields number, Schäfer et al. (2021) presented an approach for direct comparison of prototype and model bedforms in fine sand and lightweight sediment, both studied under laboratory conditions. Petruzzelli et al. (2013) focus on the influence of lightweight sediment properties on the morphodynamic response in general.

3. Methodology

This study focuses on the question of how a lightweight sediment made of polystyrene granules behaves in an elongated run-of-river reservoir of a laboratory experiment under different hydraulic conditions. The purpose is to establish comparability between the riverbed under equilibrium conditions and under unsteady flood discharges and, where appropriate, to draw conclusions about factors influencing bed development under varying hydraulic conditions. Similarity considerations, which are intended to enable transferability of the experimental results to a field site, are not part of this work, but are necessary to describe the experimental conditions in a comprehensible way.

The basis for the design of the experimental run-of-river reservoir were the reservoirs of the Bavarian Inn River. Within the framework of subproject F "Transport processes in reservoirs" of the research project "Retention potential study at the Inn" (Huber et al. unpublished), which was lead-managed by the Chair of Hydraulic and Water Resources Engineering of the Technical University of Munich, the reservoirs of the Bavarian Inn were analyzed in detail and an idealized, standardized elongated run-of-river reservoir was derived. This reservoir was geometrically scaled down and also the discharges characteristic for the Bavarian Inn as well as flood events occurring there were scaled accordingly. The length scale used for this purpose was 1:40. For details on the derivation and selection of the flood events, reference is made to subprojects A, B and F of the retention potential study on the Inn River (Blöschl et al. unpublished; Disse et al. unpublished; Schäfer et al. unpublished).

For the experimental run-of-river reservoir, the occurring flow conditions were analyzed and the largest possible experimental setup was implemented in order to minimize scale effects. Hydraulic similarity was ensured by the fact that the flow conditions occurring in the experiments were in the low range of Reynolds invariance with $Re \gtrsim 10^6$, so that in addition to the geometric similarity, inertia and gravity effects due to bed roughness were also simulated in scale. Assuming a fixed bed, hydraulically similar experiments could have been conducted in the experimental run-of-river reservoir in this way, and a transfer of the experimental results to a prototype in the field would have been possible.

To establish dynamic similarity for an experimental run-of-river reservoir with movable bed too, similar morphological conditions would have been required. However, given the predominantly cohesionless fine and medium sand present in the largely sedimented reservoirs of the Bavarian Inn River, this was not possible: an appropriate lightweight sediment could not be obtained in sufficient quantity due to the specific requirements, and

experimental operation with such a fine lightweight sediment was not feasible. A detailed analysis on this can be found in the report on subproject F of the retention potential study on the Inn River.

For the present study, however, such similarity considerations for the transfer of morphological parameters between experiment and field are only necessary to describe the setup and the boundary conditions of the experimental run-of-river reservoir and they are not investigated any further. Instead, the focus of interest is on the morphodynamic behavior of the lightweight sediment used and its interaction with the flow. The hydraulic conditions in the experimental run-of-river reservoir correspond to those of the Bavarian Inn River and are thus realistically represented for a medium to large water-course with an alpine catchment and fully sedimented run-of-river reservoirs. In these, a morphodynamic bed equilibrium can develop under backwater influence, if discharge conditions remain approximately constant and last sufficiently long.

3.1. Research design

The main goal of the experiments was to generate the broadest possible spectrum of hydro-morphological conditions in the experimental run-of-river reservoir under backwater influence, and to both measure the lightweight sediment bed with high temporal and spatial resolution and continuously record sediment transport. This was accomplished in two experimental phases: Phase 1 considered morphological processes at dynamic bed equilibrium that occurred naturally and unaffected by external factors. Therefore, all parameters that could be influenced during experimental operation were kept constant. After that, in phase 2, the previously considered equilibrium conditions were subjected to varying discharge conditions, which were specified by characteristic flood waves. Compared to the experiments in phase 1, only the discharge was changed over time, all other parameters were set to the same values and, again, kept constant.

To facilitate true dynamic bed equilibrium in the experimental run-of-river reservoir, a so-called online recirculation system for sediment supply was installed, which directly captured the sediment at the end of the reservoir and continuously returned it to the upstream start of the reservoir on a direct path. There it was returned right back into the flow, creating a directly linked dynamic upper and lower boundary condition for sediment transport. With a time lag of below 2 minutes, the sediment transport rate upstream into the experimental reservoir was thus preset to be virtually the same as the rate at which material had previously been discharged at the downstream end of the reservoir. Bedforms that had formed along the reservoir produced varying transport rates in the online

recirculation system according to their shape and size while leaving the reservoir at its downstream end, and were then fed back into the reservoir in the same quantities. This created a bedform dependent temporal variability in sediment supply rates and simulated sediment availability comparable to a naturally occurring situation in the field. This in turn also accelerated the development of bedforms along the reservoir, which further supported the formation of dynamic equilibrium conditions.

The duration of operation varied for each experiment. Both the steady-state experiments in phase 1, due to the duration required to reach dynamic bed equilibrium, and the unsteady-state experiments in Phase 2, due to the duration of the flood events, required several days in continuous operation. Here, the online recirculation system provided an additional operational advantage: the amount of sediment required for experimental operation was limited to the amount that was present in the reservoir at the start of the experiment. Additional sediment for transport out of the water or for a mobilization stretch upstream of the experimental reservoir did not have to be kept aside.

3.1.1. Hydraulics of the test scenarios

All experiments were conducted with the same run-of-river reservoir geometry. The only parameters that were changed were reservoir water level and discharge: In the experiments in Phase 1, they were both set at the start of the experiment and then left unchanged throughout the duration of the experiment; In the experiments in Phase 2, the discharge hydrograph was preset using an automated inflow control system and the water level was held constant using automated weir operation for water level control. A reference water level gauge, referred to as control gauge in the following and located in the end section of the experimental reservoir, served as reference point for the water level in all experiments.

Phase 1: Investigation of dynamic bed equilibrium

In this approach, only the vertical velocity profile was externally influenced by varying water level and discharge, thus indirectly affecting all the coupled parameters used for flow description, while the morphology in form of sediment transport, reservoir bed structures and the corresponding water surface inclination were left to free development. Therefore, three initial water depths at the control gauge and nine discharges were specified, and of the 27 possible combinations, 17 scenarios were investigated in the experimental reservoir. The respective combinations corresponded to realistic scenarios for water depths in run-of-river reservoirs at peak discharges of different return periods between HQ2 and HQ300.

The objective of each experiment was to produce dynamic bed equilibrium in the mobile reservoir bed that was invariant on a time-average basis (cf. Best (1988) and Parker and Wilcock (1993)). For this purpose, each experiment was conducted until all measured parameters reached a statistically stable variability. In particular, the development of the longitudinal water surface gradient and the measured sediment transport in the sediment recirculation were monitored, as well as the migration velocity of the resulting transport structures. Table 2 lists the investigated scenarios as well as those investigated in phase 2. One of the 17 scenarios ("Q409-H30") was attempted but could not be completed because the capacity limit of the sediment recirculation was exceeded in both phase 1 and phase 2.

Discharge [l/s]	Water depth [cm]		
	21.25	30	35
101.7	(1)		
135.5	(1)	(1)	
162.7	(1) (2)	(1) (2)	
180.8		(1)	(1)
193.2	(1) (2)	(1) (2)	
216.9	(1)	(1)	
259.1		(1)	(1)
325.4		(1) (2)	(1) (2)
409.7		(1) (2)	(1) (2)

Table 2: Test scenarios for phase 1: dynamic bed equilibrium, and phase 2: reservoir bed during flood hydrographs

Phase 2: Investigation of morphodynamic processes during flood hydrographs

The influence of flood hydrographs on the reservoir bed was investigated for eight of the 17 scenarios of phase 1. For this purpose, four different hydrographs were used and each of them was used at two flow depths in the experiment. Therefore, each of the four hydrographs is represented twice in Figure 11, but with different durations. The initiation of bed motion along the time axis varied due to the different water depths, and the hydrographs were therefore shortened to the transport-relevant part accordingly.

These hydrographs were then implemented quasi-continuously by an inflow control system with discharge increments of about 4:45 min each, which would correspond to a 30 min interval in the field given a time scale for hydraulics $t_r = L_r^{0.5}$. Shorter discharge increments or fully continuous hydrographs could not be implemented reliably in the test facility: The

discharge fluctuations of the then inadequately damped inflow control process would have had an interfering effect on the water level control in the experimental reservoir, which could then no longer match the slow response of the large water body in the reservoir and the short-term changes of the inflow in a satisfactory way. Weir operation schemes or flushing operations involving deliberate changes to the reservoir water level were not investigated.

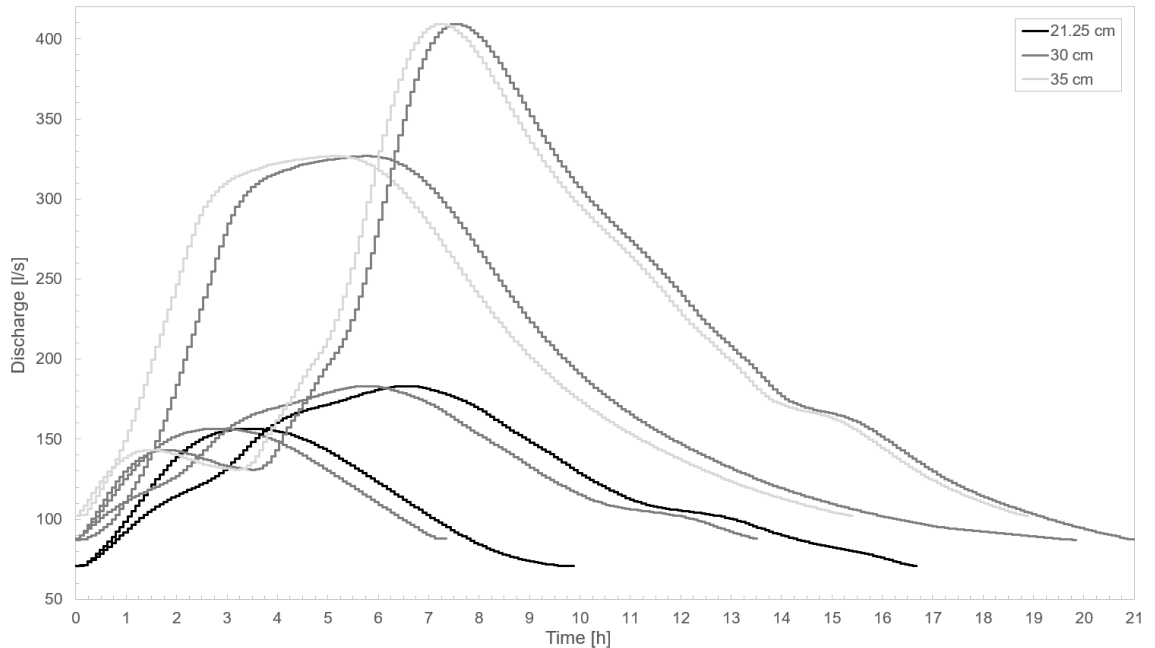


Figure 11: Flood hydrographs for phase 2: reservoir bed during flood hydrographs

3.1.2. Properties of the lightweight sediment

Several factors played a role in the selection of the artificial granulate for use as lightweight sediment. The granulate was supposed to cover a wide range of applications and have good availability. The following factors were considered:

- Procurement and financial cost, especially when large quantities are required
- Physical specifications, e.g. stability of shape, constant density
- Operational aspects, e.g. handling, adhesion to surfaces when wet
- Measurement technique, e.g. need for bright color, opacity (light resistance)

For the present study, the technical requirements of the measurement technique used for bed survey, i.e. terrestrial laser scanning, made the identification of an appropriate lightweight sediment particularly difficult (a description of the bed survey technique will be given in chapter 3.3.1). The large dimensions of the experimental run-of-river reservoir also entailed correspondingly high material required. Thus, for financial reasons only recycled

plastics were considered, most of which, however, are black or brightly colored and often non-opaque.

For a series of tests, various artificial granules were procured that had a density only slightly higher than that of water, and these were tested for physical, operational and measurement requirements. The most suitable materials were thermoplastic polyurethane (TPU), thermoplastic styrene block copolymer (TPE-S), acrylic butadiene styrene (ABS), high impact polystyrene (HIPS) and amorphous polystyrene (PS). The amorphous polystyrene met all requirements and at the same time had the lowest density. It was stable over the long term even after several months of use, did not change in shape, color or density. An initial adhesion between individual particles, which led to the appearance of particle clusters, disappeared after only a few days of testing. Small particle clusters consisting of two to three particles, which occurred only occasionally due to the entrapment of small air bubbles during submerging of the particles, were not stable and dissolved again immediately after the initiation of motion through contact with other particles. Table 3 lists all relevant material properties and shows a material sample.

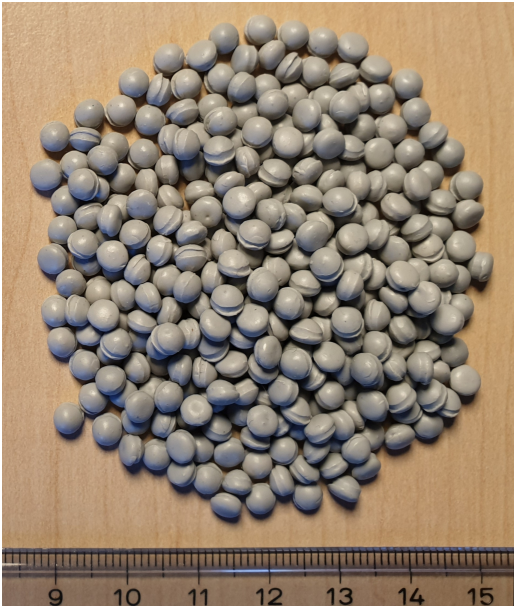
Property	Type/Value	Sample
Material	Polystyrene	
Color	Gray	
Transparency	Opaque	
Shape	Ellipsoidal	
Density	1.05 g/cm ³	
Particle diameter, mean	3.8 mm	
Particle height, mean	3.1 mm	
Shape factor	0.72	
Friction angle (dry)	27.5°	
Friction angle (submerged)	ca. 25°	

Table 3: Properties of the lightweight sediment

The shape or form factor $FF = c/\sqrt{(a \cdot b)}$ describes the deviation of individual sediment grains from spherical shape and is about 0.72 for the chosen polystyrene granules, where a, b, and c are the lengths of the longest, middle, and shortest grain axes in space (Zanke 1982). Natural sediments have a shape factor of $FF \approx 0.7$ (ASCE 1962). In order to obtain accurate information on the nature of the lightweight sediment beyond the usual measure, dynamic

image analysis by means of a CAMSIZER P4 (cf. Retsch Technology GmbH (2012)) was used in addition to classical methods such as sieve analysis and caliper measurement.

The results of the highly accurate grain fraction analysis are shown in Figure 12, left. In addition to the lightweight sediment, a sample of bed material from the uppermost bed layer of one of the upper reservoirs of the Bavarian Inn River was analyzed with the CAMSIZER P4 for comparison, as well as a sample of a commercial quartz sand. Both materials were used at the Obernach Hydraulics Laboratory as part of another research project (Schäfer et al. 2021), and they are used here as a reference to relate the properties of the lightweight sediment to a naturally occurring river sand and an industrially processed quartz sand often used in movable bed physical experiments. However, there is no model similarity between these two reference materials and the lightweight sediment.

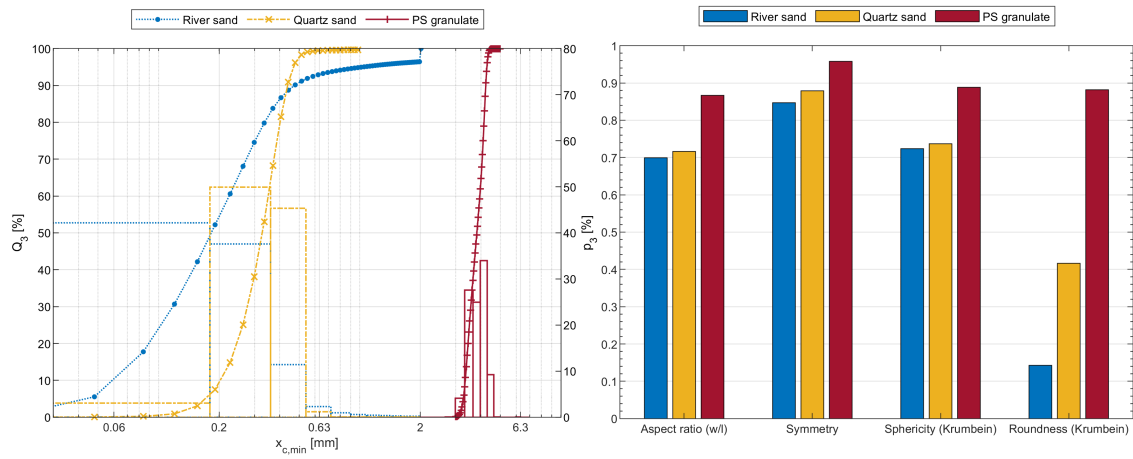


Figure 12: Dynamic image analysis results: sediment grading curves (left), grain shape parameters (right)

In Figure 12, right, four selected parameters for describing the grain shape are shown. The aspect ratio relates the smallest internal width (comparable to the sieve diameter) to the largest direct length (comparable to the largest caliper value). Symmetry is the smallest relation of two radii, which are determined starting from the surface center to the border of the 2D particle projection. The sphericity and the roundness according to Krumbein are used in the geotechnical soil classification to describe the grain shape: the sphericity corresponds to a modified aspect ratio, the roundness to a measure for the angularity, for which the mean diameter of all corner circles is divided by the inscribed circle, i.e. the maximum inner circle. All these shape parameters have a range of values from 0 to 1, where 1 corresponds to a perfect sphere. Further information can be found in Retsch Technology GmbH (2012), Kunz (2014) and Kim (2019).

For the chosen polystyrene granules and water temperatures in the experiment run-of-river reservoir between 5°C and 10°C, the morphological standard values obtained are listed in Table 4. The critical shear stress is calculated after Zanke (2013) with the Shields

parameter: $\tau_c = \theta_c g d_m (\rho_s - \rho)$. The hydromorphological standard values u_* , τ^* and Re_* , which depend on the hydraulic conditions as described in chapter 3.1.1, lie within the ranges given in Table 5. Besides that, the measured particle settling velocity w_f is shown.

D_*	Re_p	Van Rijn (1984a)		Wu and Wang (1999)		Zanke (2013)	
		θ_c	τ_c [N/m ²]	θ_c	τ_c [N/m ²]	θ_c	τ_c [N/m ²]
23 - 25	110 - 127	0.0332	0.0625	0.0320	0.0602	0.0345	0.0649

Table 4: Morphological standard values for the polystyrene lightweight sediment

u_*	τ^*	Re_*	w_f [m/s]
0.012 - 0.029	0.08 - 0.46	34 - 84	0.040

Table 5: Hydromorphological standard value ranges for the present study

A classification of the relation of D_* and Re_* for the description of bedforms to be expected from the experiments after Bonnefille and Pernecker was presented in Vollmers and Giese (1970), cited from Bechteler et al. (1991), and it is shown for the present study in Figure 13.

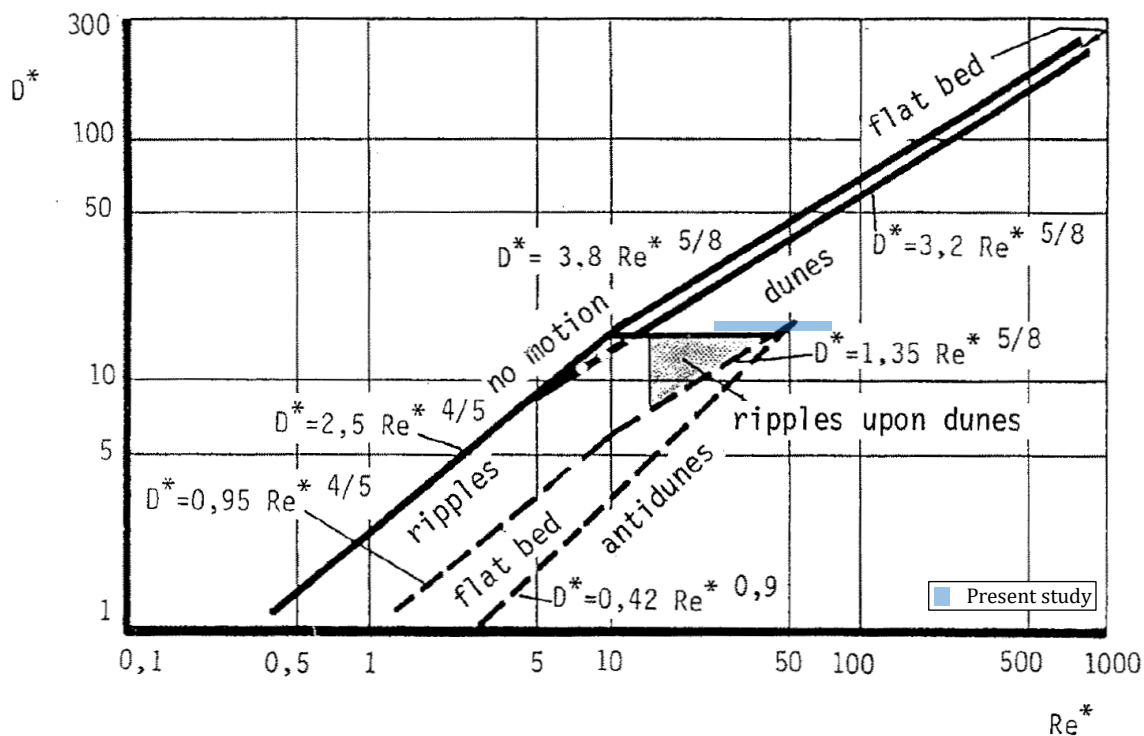


Figure 13: Bonnefille-Pernecker bedform classification diagram after Bechteler et al. (1991), modified

A dynamically similar morphological Froude model, which strictly complied with the condition for grain size scale number d_r and the scale number of the solid densities ρ_r (cf. Eq. 2-20 in chapter 2.3.1) and used the chosen polystyrene granules as lightweight sediment, would still have a vertical model exaggeration of $n = 5.7$. It could be implemented in a situation where a prototype with relatively uniform graded sediment with mean grain

diameter d_{50} of about 1.2 mm, thus classified as coarse sand, and a particle density of $\rho_s = 2.65 \text{ g/cm}^3$ was present. However, such similarity considerations are for illustrative purposes only and their elaboration is not the content of this thesis.

3.2. Test facility

In order to successfully implement the physical investigations of the hydro-morphological processes in run-of-river reservoirs with lightweight sediment outlined above, very high demands were placed on the execution of the experiments. Since polystyrene is only slightly heavier than water and thus very easily mobilized, special care had to be taken both during preparation and execution of experiments. Besides, several developments for measurement techniques and experiment operation were necessary, which exceeded the usual requirements for the setup of a movable bed experiment. Special attention was therefore paid to the configuration of the test facility as a whole as well as to the individual components for flow regulation, operational handling and fully as well as partially automated data acquisition.

3.2.1. Experiment setup

The experimental run-of-river reservoir was integrated into a 110 m long and 8 m wide concrete flume without longitudinal slope. The uppermost 34 m were unobstructed, followed by 7.5 m of flow guiding installations towards the reservoir section, then 57.5 m of straight river reservoir with erodible bed and fixed sloping banks, and finally 11 m of functional structures such as weir, sediment trap and outlet. Two impressions of the test facility in different operational states are shown in Figure 14: dry with plane bed before the start of an experiment (top) and during operation with developed bedforms (bottom). In the center of the pictures is the weir with two simple sluice gates (red), the run-of-river reservoir with movable bed is to the right, the sediment trap with sediment recirculation and outlet are to the left.

A functional classification of the components of the test facility depicted in Figure 14 is provided by Figure 15. All parts essential to execution of the experiments are explained there on the basis of a schematic longitudinal section through the experiment setup. The flow direction in this and all other longitudinal sections of the experiment setup shown in this thesis is from left to right. The water level is shown in blue here and the movable bed in orange. Table 6 is used to explain the numbers in Figure 15.

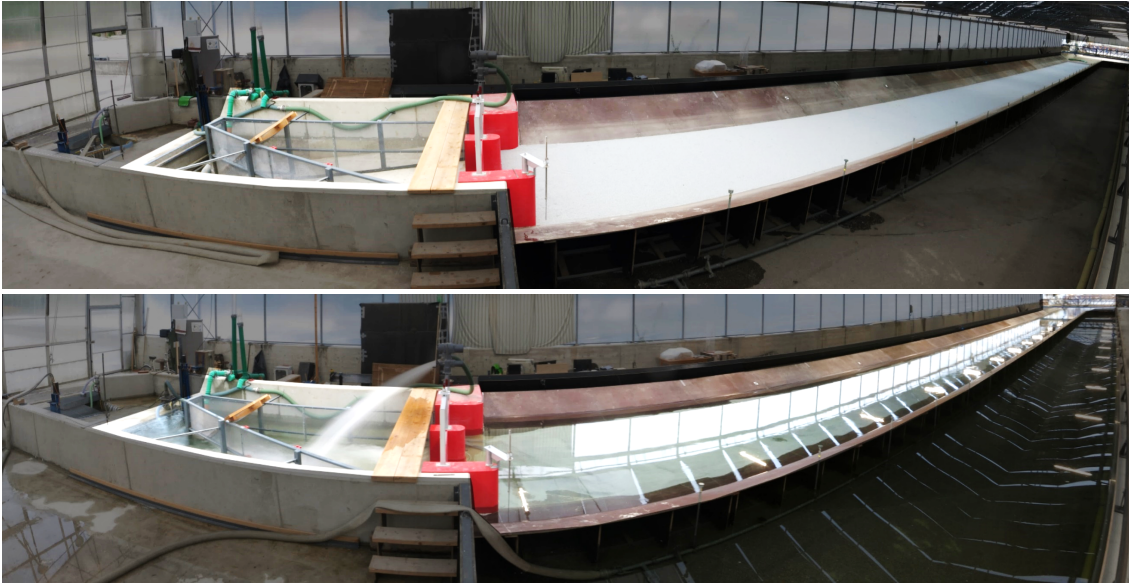


Figure 14: Views of the test facility with a dry river reservoir before the start of an experiment (top) and during operation (bottom), flow coming from the right in both images.

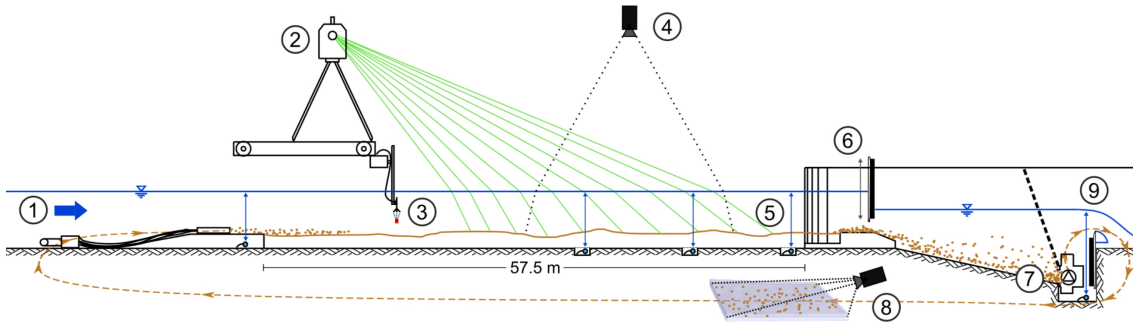


Figure 15: Schematic longitudinal section through the experiment setup with descriptive numbers

#	Description/Function	#	Description/Function
1	Inflow control and sediment supply	2	Bed survey by laser scanning
3	Velocity measurement with ADV probes	4	Ceiling camera for bed monitoring
5	Water level monitoring by pressure sensors	6	Water level control with automatic gate control
7	Sediment recirculation	8	Sediment transport measurement
9	Discharge monitoring via measuring weir		

Table 6: Definition of the descriptive numbers of the schematic longitudinal section through the experiment setup

The positions of the pressure sensors, which are referred to as water level gauges in the following, are given in Figure 16 in a scale plan view of that part of the concrete flume, in which the flow guiding installations, the river reservoir and the weir were located. This figure already contains the color assignments of the water level gauges, which were then used in the following chapters when references are made to the water level gauges. The numbers indicate the distance of the respective water level gauge from the weir along the reservoir centerline. The suffix "rb" indicates water level gauges that were not integrated into the bed along this reservoir centerline, but into standpipes that were built into the solid

right (in flow direction) reservoir bank. This allowed a more accurate measurement of the water level, which was less influenced by morphological phenomena.



Figure 16: Location and labeling of pressure sensors for water level measurement in the river reservoir

For the morphological development of the reservoir bed, a long development distance was required, since fully developed flow conditions (steady-state: $\partial u / \partial t = 0$, uniform: $\partial u / \partial x = 0$ (Dey 2014)), as found in nature, ideally should be present in the experiment too. Depending on the theoretical approach, the literature calls for lengths of up to 80 times the channel width for fully developed flow conditions (cf. Gyr and Hoyer (2006)). In addition to these theoretical requirements, both operational (including flow resistance in the sediment recirculation system growing with distance, cf. generalized Darcy-Weisbach equation as given in Zanke (2013)) and financial (mainly procurement costs of the polystyrene granules) constraints led to a length of the erodible bed of 57.5 m in a straight river reservoir in the present experiments.

Figure 17 shows a schematic cross-section of the experimental run-of-river reservoir, which was constant with these dimensions over its entire length, as can be seen in Figure 16. The three investigated water levels, that were kept constant at the control gauge "P_5rb" during all experiments, are shown as blue lines. Furthermore, the respective reservoir widths at the water surface, the bank slopes and the initial position of the bed surface before the start of each experiment (orange line) are given. Elevation 00.00 cm corresponds to the elevation of both the sediment supply platform upstream of the river reservoir and the weir bottom at the end of the river reservoir: the bed was levelled smoothly to this elevation as initial condition for all experiments.

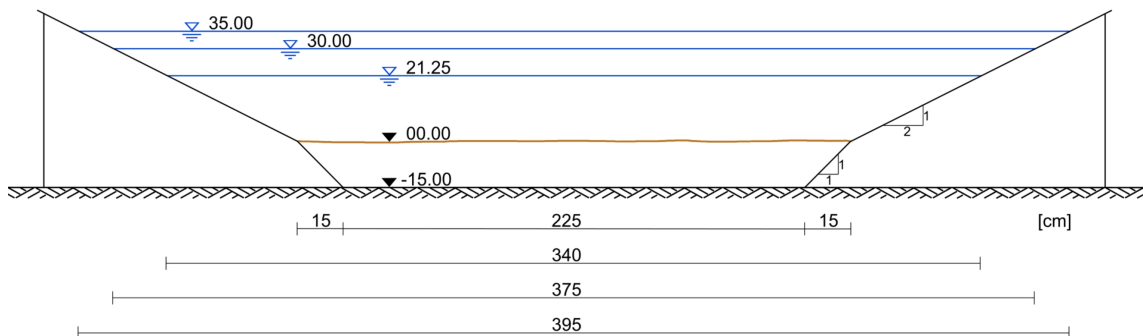


Figure 17: Schematic cross-section of the experimental river reservoir

The thickness of the erodible bed at the start of each experiment was thus fixed at 15 cm. To minimize particle movements due to floating during the filling of the concrete flume, an automatic sprinkler system was installed along the entire river reservoir, which ensured the installation position of the initial bed with local elevation differences of ± 2 mm on particle level.

3.2.2. Functional components explained

The functional components of the experiment setup as shown in Figure 15 are described in detail in the following.

1: Inflow control and sediment supply

The inflow into the concrete flume was controlled by a system of several electric valves and magnetic inductive flow meters (MID). These took water from an elevated tank with a permanently overflowing labyrinth weir and thus a nearly constant water level; fluctuations of the water level were less than 2 mm. An electronic control system for the valves of the inflow pipes based on proportional-integral-derivative (PID) control enabled unsteady operation of the test facility. Flood hydrographs of any shape could be run.

The unobstructed upper part of the concrete flume served to calm the flow. At the transition from this calming section to the less wide river reservoir section, special care was taken to disturb the flow as little as possible, i.e. to generate as few velocity components as possible transverse to the longitudinal direction of flow, in order to obtain the best possible conditions for undisturbed bed development already at the beginning of the reservoir. For these reasons, the influence of the sediment feeder on the velocity distribution in the river reservoir had to be minimized and an equal distribution of the sediment introduced across the reservoir width had to be ensured. Figure 18 shows the transition area into the experimental run-of-river reservoir with the flow calming installations and sediment supply components, i.e. the main pipe with the sediment feeder on the sediment supply platform, in dry conditions and during operation at a medium sediment transport rate.

Via a system of 34 distribution pipes, the sediment was evenly fed into the flow above the sediment supply platform, which was almost completely covered by sediment in the condition shown. The cross-section of the distribution pipes gradually increased from the main pipe to slow down the flow velocity step by step to about 0.3 m/s in the final acrylic pipes and thus adjust it to the velocity level of the free surface flow above the supply platform. The fed sediment was immediately picked up by the flow and evenly transported downstream. Depending on the hydraulic stress and with some randomness, zones with

more or less available sediment per distribution pipe fluctuated slightly. However, these minor differences had no quantifiable effect on bed development and were accepted as natural variations in sediment availability across the reservoir width. At the lower right corner of Figure 18, the formation of a first bedform is already visible.

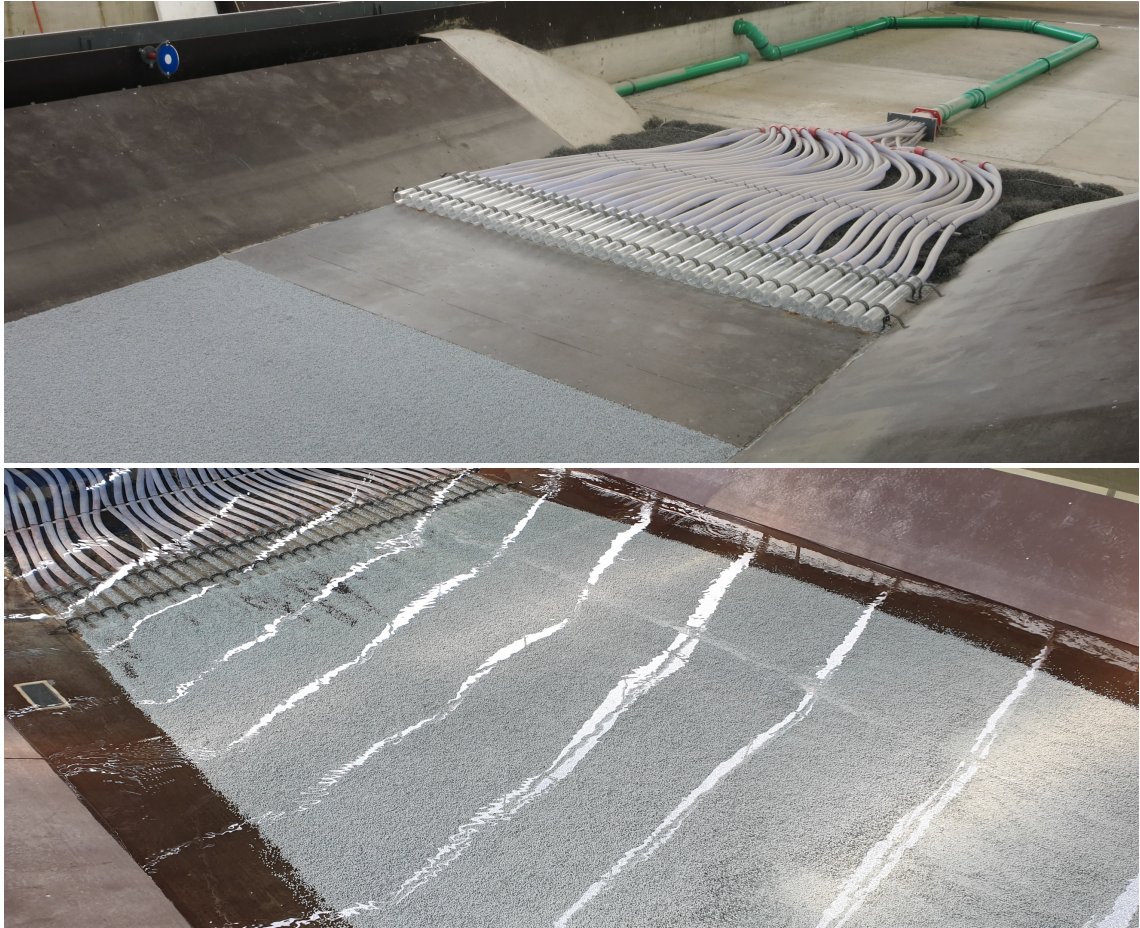


Figure 18: Transition area into the river reservoir with sediment feeder on the supply platform in dry conditions (top) and sediment feeder during operation with medium sediment transport (bottom)

The distance from the sediment feeder to the formation of the first bedforms varied with hydraulic stress and the amount of sediment currently transported through the sediment recirculation in a range of about 1 m to 10 m. Bed erosion directly downstream of the supply platform occurred only when the naturally fluctuating amount of available sediment fell below the transport capacity of the flow for some time. There were no abrupt changes in elevation, but rather a continuous transition from the sediment supply platform to a shallow pan, which refilled when the available amount of sediment increased again. The light stripes in Figure 18, bottom, are reflections of light falling on the water surface from the laboratory ceiling, which have nothing to do with the hydro-morphological events.

2: Bed survey by laser scanning

The measuring cart for bed topography measurements spanned the width of the concrete flume and was movable in longitudinal direction. Figure 19 shows this measuring cart with

the terrestrial laser scanner (the measuring procedure for bed survey will be explained in detail in the following chapter 3.3.1), which was mounted as high as possible and therefore above the bottom chords of the laboratory roof in order to achieve the best possible measuring results. This was unproblematic in that the laser scanner carried out all measurements of an experiment from a fixed position. To move the measuring cart, the laser scanner was demounted. The area measured in the bed survey was defined as the area from reservoir meter 2 to 20 upstream of the weir. Hanging at the base of the measuring cart, one can also see the mounts of the two ADV probes (acoustic Doppler velocimetry) measuring under water. Both laser and ADV measurement procedures were largely automated, but had to be started manually.



Figure 19: Measuring cart with laser scanner and ADV probes during operation

3: Velocity measurement with ADV probes

The velocity measurements with two simultaneously measuring ADV probes were carried out at several points in the reservoir, each above the water level gauges "P_5", "P_10" and "P_15". They were carried out after the bed survey by laser scanning and recorded an estimate for the flow velocity both at a fixed point relative to the initial water depth and, automated by a control process, permanently at a fixed distance of about 2 cm above the assumed bed surface in the center of the reservoir. The measurement data thereby generated were only used for basic checking purposes in this thesis.

4: Ceiling camera for bed monitoring

In addition to measuring the bed topography, a ceiling camera was installed above the reservoir, which made it possible to continuously record a substantial part (12 m length,

entire reservoir width) of the bed also measured by the laser scanner. While the laser scanner could only measure discontinuously and, due to the rotation time of the laser head during the measurement, not instantaneously by definition, the ceiling camera produced photos every 15 seconds during the duration of the experiment. These enabled very good process monitoring in retrospect. Furthermore, the partially redundant information about the bed position could be used for comparison with the laser scan data and additional information about the width development of the bed could be obtained.

5: Water level monitoring by pressure sensors

During the experiments, seven piezoresistive pressure sensors (6 upstream and 1 downstream of the weir) continuously recorded the water levels at selected points in the river reservoir with millimeter precision (cf. Figure 16). They were embedded in the solid bottom of the concrete flume and covered with sediment, separated from the hydro-morphological events in the river reservoir by a fine grid, so that only the hydrostatic pressure was measured. Due to the pore space of the sediment, the measurements were slightly damped, i.e. short-term fluctuations of the order of a second, e.g. due to surface waves, were registered by the pressure sensors only to a reduced extent. However, such fluctuations were not significant for water level monitoring in the experimental river reservoir. Likewise, these short-term fluctuations had no visible effects on morphological processes.

6: Water level control with automatic gate control

At the end of the river reservoir, a weir was installed with two identical weir gates, each 1 m wide, through which the entire discharge was channeled. The weir gates were designed as simple sluice gates, one of which was electrically driven and the other manually adjustable. A control system regulated the gate opening of the electric gate in such a way that during the course of a flood wave the reservoir level was kept constant at the control gauge. Due to the identical design of both weir gates, both the left and right weir gate could be used for automatic control. The construction of a specific stilling basin was not required for the study objectives.

7: Sediment recirculation

After the weir, a sediment trap was installed to separate the sediment from the water (see Figure 20). Therefore, a V-shaped perforated plate barrier was installed on a sloping concrete floor. Sediment that accumulated at the pointed end of the perforated plate barrier was removed there at the deepest point by a submersible pump. At a constant flow rate, the

sediment-water mixture was pumped back upstream to the sediment feeder via a pipeline at high velocity to ensure suspension of the sediment for reliable transport time estimation.

The discharge for sediment recirculation was 17 l/s constant in all experiments and it was permanently provided in the river reservoir. Minor fluctuations in discharge due to the variable sediment load amounted to up to -2.5 l/s during transport peaks and could not be compensated by the submersible pump control system. In relation to the total discharge in the river reservoir, these short-term fluctuations amounted to less than 1 % and were compensated for by the water level controller. The discharges and hydrographs that entered the concrete flume via the inflow control system were reduced by the recirculation basic discharge to meet the required total discharge.

An additional flow jet from above, shown in Figure 20, right, in the lower right corner of the picture, allowed the flow conditions in the sediment trap to be specifically influenced, reduced the retention time of the individual sediment particles in the sediment trap and had a positive effect on the transport performance of the sediment recirculation. In addition, the latency between the flow through the weir at the end of the reservoir and the optical transport measurement (see following section) in the recirculation system was significantly reduced to ≈ 1 min depending on the level of sediment transport. The optimal jet position was identified in preliminary tests and then left unchanged during all of the experiments.



Figure 20: Sediment trap, dry (left) and during operation (right)

8: Sediment transport measurement

Immediately after the sediment-water mixture was pumped out of the sediment trap, it was fed to a measuring device for quantifying the amount of sediment transported through the weir over time. The sediment transport rate was continuously measured there using a calibrated opacity measurement. Due to the constant flow rate of the submersible pump, the transport time of the sediment-water mixture in the recirculation system was known,

which also allowed the amount of sediment fed back into the reservoir to be allocated over time. A detailed description of the sediment transport measurement follows in chapter 3.3.2.

9: Discharge monitoring via measuring weir

Downstream of the sediment trap, an overflow gate was installed, acting as a measuring weir to record the discharge from the river reservoir. It was thus possible to check the time delay and distortion with which the flood hydrograph of the inflow control system arrived at the end of the river reservoir. However, such time delays were in the range of tens of seconds only and hence neglected.

3.3. Methods of data collection

The operation of the physical test facility and the acquisition of measurement data during the experiments required significant in-house developments, as it was not possible to handle the measurement and regulation tasks with conventional solutions available on the market alone. These included in particular the method for bed survey using terrestrial laser scanning and the continuous measurement of sediment transport even at high transport rates. This chapter presents these data acquisition methods used and describes them in detail.

3.3.1. Bed survey using terrestrial laser scanning

The following requirements were specified for the bed topography measurement method, which aimed to detect the bed surface of the river reservoir in three dimensions:

- Measurement of the bed topography during operation (i.e., submerged bed)
- Contactless measurement to avoid disturbing the flow
- Areal measurement of the bed as fast as possible,
- Highest possible spatial resolution

To make this possible, a specific measurement method was developed using a commercially available terrestrial pulse-time-of-flight laser scanner in the visible green wavelength range (532 nm). The scanner had to measure through the water surface during ongoing experimental operation in order to measure the river bed over a wide area. A measurement took only a few minutes, depending on the section to be scanned and the desired measurement point density.

The entire measurement process consisted of three main parts: Positioning via spatial fixed points, scanning of the bed topography and monitoring of the environmental parameters. The duration of a single measurement was about 55 seconds for the section of the riverbed selected in the present study. The terrestrial laser scanner recorded the river bed in radial lines from the fixed position on the measuring cart.

The point clouds generated in this way, were distorted by refraction at the water surface and backscatter under water and had to be rectified by a calibrated post-processing. Here, measurement errors were eliminated as far as possible, so that measurement accuracies of the individual measurements were achieved in the range of grain roughness. For areal analyses, this accuracy could even be increased by means of curve fitting.

Figure 21 gives a schematic representation of the path in air (index a) and water (index w) of a single laser beam emitted from the laser scanner, in cylindrical coordinates ρ and z . The different angles of incidence θ_a and refraction θ_w cause a deflection of the laser beam, which can be described by the refractive index n according to Snell's law:

$$n = \frac{\sin \theta_a}{\sin \theta_w} \quad (3.21)$$

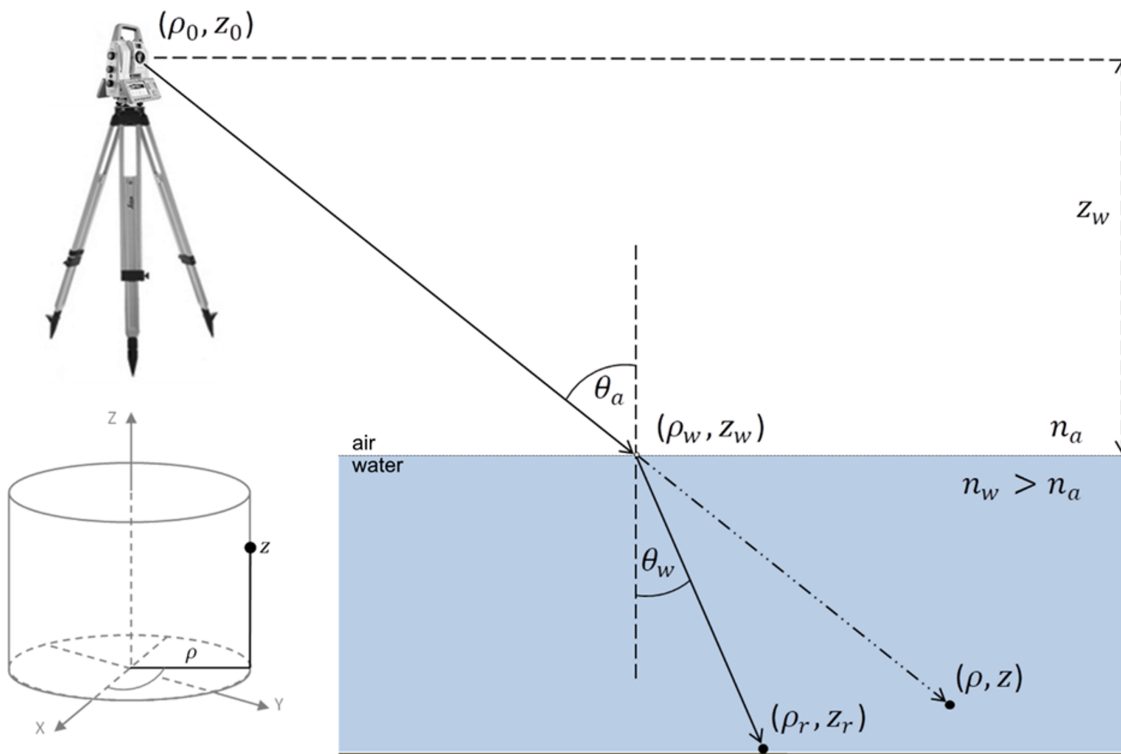


Figure 21: Schematic illustration of laser path in air and water in cylindrical coordinate representation (Schlagenhauser et al. unpublished)

The refractive index is constant and it depends on the properties of the transmission media, the wavelength of the incoming electromagnetic radiation and temperature (Smith et al.

2011). To receive the actual position of the reflecting surface ρ_r and z_r , the point coordinates have to be rectified with a correction model, for example after Smith et al. (2011).

Our in-house investigations, however, showed that the laser beam is additionally affected by scattering in the water body and therefore the correction model of the point cloud should also compensate for an additional signal compromising effect. Thus, we developed an extended correction model which uses an additional scaling factor to compensate for the scattering delay of the distance measurement under water. Physically, this additional scaling factor adjusts the relation of the measured distance over the propagation speed in the water body and increases the measurement accuracy especially in water depths above 10 cm. At lower water depths, scattering effects are only of minor importance.

In this context, a scientific article describing the entire measurement procedure and the extended correction model in detail was written in close collaboration with the author of this thesis and is referred to as Schlagenhauser et al. (unpublished). Unfortunately, this scientific article had not yet been published at the time this paper was written. However, since the content of that scientific article is indispensable for a complete and comprehensible understanding of the measurement data of this thesis, it is included in the appendix in its latest version in chapter A.

The following limitations for the design of the experiments resulted from the laser scanning measurement method:

- Clear water required for high intensities of reflected laser pulses (indicator: visibility to the unaided eye).
- High reflectivity of the scanned surfaces (special requirements for the properties of the lightweight sediment, cf. chapter 3.1.2)
- Low tolerance to surface waves exceeding the unavoidable unevenness of the surface of flowing water.
- No large bed transformations during the measurement in order to retain the character of a snapshot

3.3.2. Sediment transport measurement

The presented measurement method was specifically developed for this study to produce continuous high-quality data of the temporal course of the sediment transport rate in the river reservoir during experimental operation in real-time and with very low computational cost even for high transport rates. The measuring system was supposed to be robust against data spikes and have a low measurement error also when determining the transported

sediment mass. At the heart of the measurement method was a camera-optical gray-scale comparison of individual images from a commercially available industrial camera, which pictured the distribution of sediment particles (here: polystyrene granules) in the surrounding water as they flowed through the so-called measurement field. For each camera image (image frequency 10 Hz), the sediment concentration in the water was first determined at a discrete point in time by means of a gray scale comparison and a previously measured calibration curve, and from this the sediment transport rate was derived. By temporal integration of several successive images, the sediment transport could then be determined for a specific time window. Figure 6 shows the setup of the measurement system schematically.

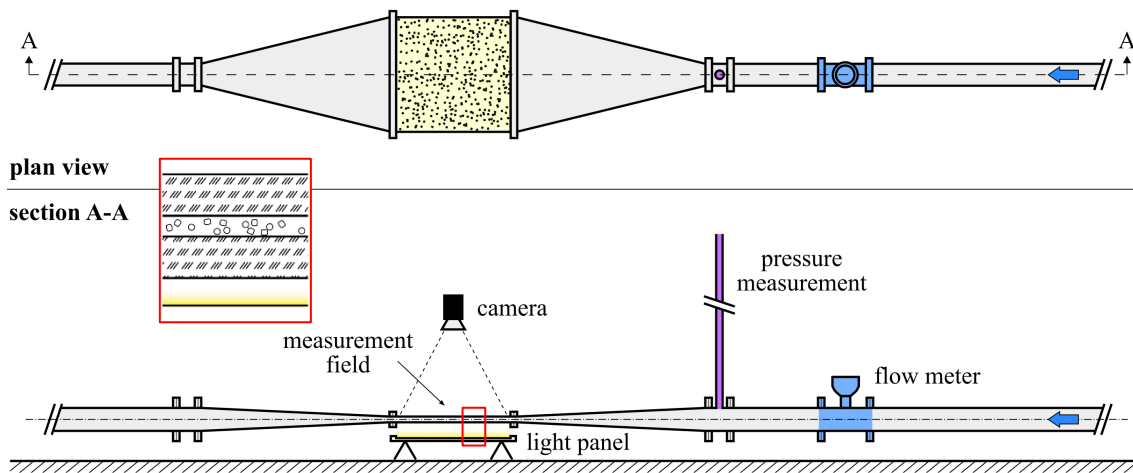


Figure 22: Optical measurement system in plan view and longitudinal section, schematic (modified after Schäfer et al. (2019))

The sediment-water mixture pumped from the sediment trap had to be transported upstream at high velocity to keep all sediment particles in the pipeline fully mixed, i.e. in suspension. This allowed for the assumption that in the measurement window the actual sediment concentration was measured at all times and that there were no delays in mass transport along the pipeline. On the basis of continuous discharge and pressure measurements, the operating conditions for the measuring system were set and kept constant throughout.

A scientific article describing the entire measuring system and the measurement method in detail has been published by Schäfer et al. (2019). Because of its relevance to the investigations dealt with in this thesis, it can also be found in the appendix in chapter B. In addition to the investigations described in the scientific article, further control measurements were carried out after all experiments had been conducted. This was done to ensure that the measuring system worked reliably over the entire period from calibration to the end of the last experiment. For this purpose, predefined amounts of sediment were fed directly into the sediment trap over two different time intervals, covering the entire range of possible sediment transport rates. There was very good agreement between the

measured sediment transport and the fed amounts of sediment, with a measurement error in the low single-digit percentage range (see Figure 23).

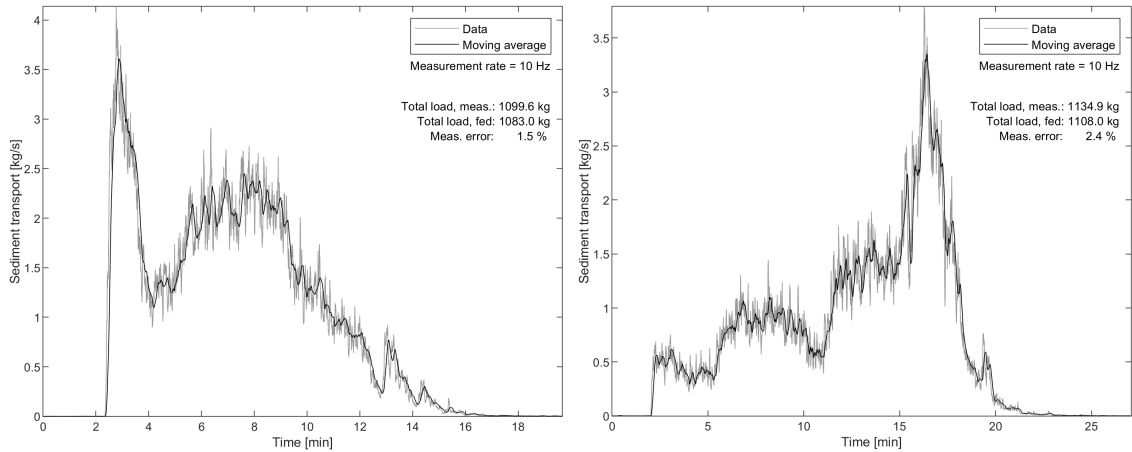


Figure 23: Validation measurements for the sediment transport measurement method

3.4. Experimental procedure

In the following, a step-by-step explanation of the experimental procedure is given and the handling of the generated measurement data is explained. The procedure of all experiments was standardized as far as possible. Differences arose mainly in the duration of the experiment: depending on the required development time for the dynamic bed equilibrium during the steady-state experiments in phase 1 or the length of the hydrograph in the unsteady experiments in phase 2. Reaching the state of dynamic bed equilibrium was assessed during the ongoing experiments based on the migration velocity of the bedforms, the moving average of the measured sediment transport rate, and the evolution of the longitudinal water surface gradient. Table 7 shows all parameters that were recorded during the experiments in both phase 1 and phase 2.

Continuously monitored		Intermittently monitored		
Parameter	Rate [Hz]		Rate [Hz]	
Inflow (upstream)	$\leq 1/2$	Parameter	Phase 1	Phase 2
Discharge (downstream)	1	Ambient temperature	1/60	1/900
Water level in 7 locations	1	Atmospheric pressure	1/60	1/900
Water temperature	1	Bed topography (laser scanning)	1/60	1/900
Weir gate position	1	Flow velocities	1/10	1/10
Sediment transport rate	10	Reservoir photo (ceiling camera)	1/15	1/15

Table 7: Acquired data: continuous (left), demand/discontinuous (right) subdivided into phase 1 and phase 2

The sampling rate or frequency of the respective measured data varied due to the available information of the different measuring devices and the required information density.

3.4.1. Phase 1: Dynamic bed equilibrium

To achieve dynamic equilibrium, each experiment was given 1.5 times the duration required for a bedform assumed to be an equilibrium dune to travel the entire length of the reservoir. This largely ensured that no more influences from the initial plane bed or initial flow depth variations during the start of the experiment were present in the reservoir bed. Following this period of preparation, the main measurements were carried out. The entire procedure of an experiment in phase 1 was structured as follows:

1. Preparation of the initial plane bed
2. Filling of concrete flume and river reservoir
3. Start-up of experiment with discharge below initiation of bed motion
4. Start-up of sediment recirculation
5. Inflow increase to constant target discharge
6. Adjustment of gate positions until constant water level at control gauge
7. Evolution phase of dynamic bed equilibrium
8. Measurement of bed topography
9. Stop of experiment and dewatering

The single steps of the experimental procedure are described in detail in the following.

1. Preparation of the initial plane bed

Before each experiment, a plane bed without longitudinal bed gradient was created in the entire reservoir. The bed material was placed at the level of the sediment supply platform upstream of the reservoir and levelled from there in the direction of flow to the weir bottom. For this purpose, the measuring cart already described was equipped with a grading blade which allowed for high precision levelling and produced identical initial conditions for each experiment.

2. Filling of concrete flume and river reservoir

The small density difference of polystyrene granules and water of only 0.05 g/cm^3 was a challenge, especially during the filling process. Here, the concrete flume slowly filled from the bottom and the surface tension of the rising water simply lifted the granules lying in the upper bottom layer of the reservoir bed. This process was counteracted by setting up a

sprinkler system which, on the one hand, moistened the particles and, on the other hand, reduced the effect of the surface tension by permanently "disturbing" the water surface during the very slow filling process, which lasted several hours. The described procedure ensured that the levelled bed stayed plane on average and within a range of ± 2 mm.

3. Start-up of experiment with discharge below initiation of bed motion

Once the target water level was reached, the discharge in the test facility was slowly increased to a value that did not yet cause any sediment movement. This was necessary to minimize the distance to the target or start discharge so that the start-up of the experiment had as little effect on the bed development as possible. Meanwhile, the various measuring devices were started.

4. Start-up of sediment recirculation

The sediment recirculation had to be started slowly for operational reasons (venting) and carefully brought up to its operational discharge of 17 l/s. The process took about 15 minutes and during this time no sediment was recirculated, as there was no transport in the reservoir yet.

5. Inflow increase to constant target discharge

As soon as all systems were ready to start, the various data recording programs were initiated and then the constant discharge was set at the inflow control system. This process took as short a time as possible (a few minutes depending on the discharge difference between the discharge in step 3 slightly below initiation of motion and the target discharge) to avoid interim conditions.

6. Adjustment of gate positions until constant water level at control gauge

The gate positions were manually adjusted to a previously determined opening value and then only slightly manipulated within the first half hour in order to correct residual deviations of the water level at the control gauge in the low millimeter range. After that, the gate openings remained unchanged, as did all other controlled variables in the test facility, so as not to disturb the development of the dynamic bed equilibrium.

7. Evolution phase of dynamic bed equilibrium

In this phase, the test facility was left to itself and was not otherwise influenced externally. The development of the equilibrium bed required up to 40 hours of continuous operation, depending on the hydraulic stress. Those experiments could not be interrupted during this

time, because the high mobility of the lightweight sediment led to significant changes of the bed forms in the reservoir already in the short phases of stopping and restarting an experiment.

8. Measurement of bed topography

After the dynamic bed equilibrium was reached, a measurement of the bed topography was carried out every minute for 60 to 80 minutes (depending on morphological requirements). The laser scan itself took about 45 seconds, and a further 10 seconds were required internally for controls and data processing. The resolution was chosen as a compromise of measurement duration and sample point density with a sample point spacing of 20 mm horizontally and 5 mm vertically at a distance of 10 m from the laser scanner origin. Due to the radial measurement of the laser scanner, the point cloud density decreased from the scanner towards the weir of the reservoir. Figure 24 shows the scanned area of the reservoir bed.

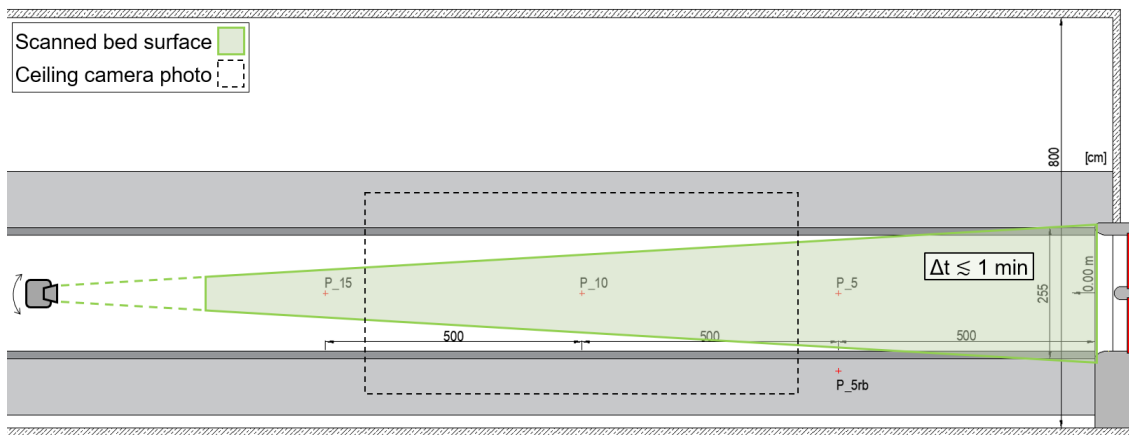


Figure 24: Scanned area of the reservoir bed during measurement of bed topography

During the entire experiment, the ceiling camera generated a photo of the center of the measured study area every 15 seconds for bed evolution monitoring.

9. Stop of experiment and dewatering

When all necessary measurements at the equilibrium bed had been carried out, the experiment was stopped in a short time (inflow was quickly reduced and weir gates closed) and the experimental reservoir was drained very slowly via lateral drainage pipes. This largely preserved the bed topography, but structural changes at grain level with surface cracks and partial sliding of the steep dune fronts could not be avoided. Comparative scans of the dewatered bed without refraction at the water-air phase boundary were thus possible, but the bed changes caused by dewatering did not allow an exact comparison with a scan before dewatering.

3.4.2. Phase 2: Flood hydrographs

In the experiments with unsteady flow, the procedure was slightly different from the procedure in phase 1. There was no preparation time for reaching the dynamic equilibrium, but the bed had to be repeatedly measured during the entire duration of the hydrograph. Since the bed survey by laser scanning was only partially automated and the start of each measurement had to be prepared manually, the measurements could not be carried out with the same frequency as in phase 1 over the long experiment duration. In addition, the amount of data generated in the process would have been hardly manageable. Hence, the procedure of an experiment in phase 2 was structured as follows:

- 1.-4. Same as in phase 1
5. Inflow increase to start discharge of hydrograph
6. Automatic gate control to keep constant water level at control gauge
7. Evolution of the bed depending on the hydrograph
8. Measurement of bed topography
9. Same as in phase 1

The differences in steps 5 to 8 of the experimental procedure in phase 2 are described in detail in the following.

5. Inflow increase to start discharge of hydrograph

As soon as all systems were ready to start, the various data recording programs were initiated and then the hydrograph was started at the inflow control system. This process was smoother for the hydrographs than for the dynamic equilibrium, because the discharge gap between pre-start discharge and hydrograph start discharge was small in call unsteady experiments.

6. Automatic gate control to keep constant water level at control

The gate position of the automated gate was automatically adjusted to the water level measurements at the control gauge 5 meter upstream of the weir. The other gate was manually adjusted as needed to allow for balanced discharge distribution from the reservoir. Fine-tuning of the automatic control system for the sluice gate opening was quite a challenge, but could be solved with the implementation of a feedback control loop using a proportional-integral-derivative (PID) controller (Åström and Murray 2008). The water level at the control gauge could be held constant in the range of 1 to 3 millimeters around

the reference water level, with fluctuations depending on the magnitude of the discharge steps of the inflow hydrograph.

7. Evolution of the bed depending on the hydrograph

The duration of the unsteady experiments was predetermined by the length of the hydrographs, but was usually shortened in the end: when the sediment transport rate tended stably towards zero and the developed bedforms showed no further movements the experiment was terminated, even if the hydrograph was not yet finished. Compared to the plane initial bed, the final bed with morphological structures had a higher transport resistance, so that even at higher discharges no more transport took place there.

8. Measurement of bed topography

During the entire duration of the flood hydrograph, two laser scans were performed every 15 minutes, each 1 minute apart. The scanned area and the resolution were the same as in phase 1, therefore the scan duration was also the same. By carrying out two scans directly after each other, the short-term bed dynamics could also be observed despite the larger time intervals of 15 minutes and thus a comparability to the dynamic bed equilibrium could be established.

Also, just like in phase 1, the ceiling camera generated a photo of the center of the study area every 15 seconds for bed evolution monitoring during the entire experiment.

3.5. Quantification of measurement uncertainty

The exact determination of measurement accuracy in this study is challenging because a multitude of measuring systems interacted. However, the determination of a single overall error is not suitable here, because in the end not only one parameter is analyzed, but a multitude of parameters, whose accuracy in turn depends on the measuring systems that were involved in their recording. For example, the measurement of the water level in the reservoir affects many hydraulic parameters, but also the measurement accuracy of the bed survey, which requires the position of the water level to correct the underwater path of the laser.

In addition, for the determination of a total error per measuring system or measured parameter, it is decisive in which context the measured data are used. A parameter that is used on the basis of a single measured value is strongly dependent on the measurement accuracy, while measured data that can still be compensated by neighborhood comparison

or pooling are not defined by their measurement accuracy alone. The same applies if a large number of measured data can be recorded in a short time sequence and then stabilized by statistical methods. For a further elaboration of this extensive topic, please refer to the corresponding literature (e.g. Coleman and Steele (1995), Muste and Stern (2000), Drosch (2009), Roosh (2014), and Kaloyerou (2018)).

The measurement accuracy shown in Table 8 can be roughly divided into systematic and random errors. The former occur permanently due to the measuring systems used and their application in the test facility and are summarized here as measurement error. Random errors vary from measurement to measurement and are caused by the characteristics of the measured variable and its natural variation: they are summarized in the standard deviation of the individual measurement in Table 8. Random errors are especially high for the sediment transport measurements, but can be compensated by time averaging. The listed values are upper and lower limits on the safe side and measurement values may well lie between these limits for individual measurements within the experiment scenario or time period under consideration.

Measurement technique/instrument	Standard deviation of individual measurement	Measurement error
Inflow metering with MIDs	$\pm 0.005 * Q$	$\pm 0.1 \text{ l/s}$
Water level gauging with piezoresistive pressure sensors	$\pm 0.001 * h$	$\pm 0.5 \text{ mm}$
Topography measuring with terrestrial laser scanner	$\pm 0.006 * h$ (at $h = 35 \text{ cm}$)	$\pm 1.2 \text{ mm}$
Sediment transport monitoring with camera-optical gray-scale comparison	$\pm 0.15 * q_s$	$\pm 0.03 * q_s$

Table 8: Measurement uncertainty of selected measurement procedures

The sediment transport rates were subject to large fluctuations on two different scales: short-term fluctuations came from the distribution of particles along the sediment trap before they reached the submersible pump for recirculation and are reflected in Table 8; long-term fluctuations due to varying amounts of sediment in the sediment trap due to the bedforms in the reservoir are not reflected here and had to be accounted for by the chosen data evaluation method.

An important parameter, which was also subject to strong fluctuations in the experiments, but which is not listed in Table 8 because it could not be measured directly, is the flow depth in the reservoir. It had to be determined from the water level measurements and the bed topography data. Thus, it fluctuated according to the bed elevation above the respective water level gauge and additionally due to the changing water level, which in turn also

depended on the bedform shape (cf. Figure 9). Depending on the resulting flow velocity and the size of the existing bed forms, it changed by several millimeters in some cases even though the water level at the control gauge was constant on average during the entire experiment. The data of the experimental scenarios will be discussed in detail in the following chapters.

4. Bed evolution in dynamic equilibrium

In this chapter, the experiments of phase 1 with steady-state test conditions for the investigation of dynamic bed equilibrium are presented. First, the individual steps for the evaluation of the measurement data of the individual experiments are shown, on which the subsequent analyses of the cumulated results of all experiments are based. This required two separate evaluation processes: that of the bed survey and that of the sediment transport measurement. Afterwards, all experiments of phase 1 are cumulated and presented in comparative illustrations to contrast different hydraulic and morphologic conditions and show interdependencies between parameters. If possible, functional relations are derived. In addition, findings for the quantitative determination of the sediment transport rate are presented.

4.1. Data Analysis of steady-state experiments

The subsequent steps of data analysis for the evaluation of morphological processes under steady-state experimental conditions are described on the basis of two selected experiments, which serve as examples and for explanation of hydraulic and morphologic processes. Thus, in many of the following figures, most of the exemplarily shown data refer to the same two scenarios, referenced to by their discharge and initial water depth as Q162-H21 and Q325-H35. The main difference between these two scenarios is the target water level in the reservoir and thus the flow depth, while the hydraulic stress and the flow regimes are at comparable levels with

- mean shear stresses of about $\tau_{Q162-H21} = 0.63 \text{ N/m}^2$ and $\tau_{Q325-H35} = 0.81 \text{ N/m}^2$,
- mean flow velocities of about $u_{Q162-H21} = 0.28 \text{ m/s}$ and $u_{Q325-H35} = 0.29 \text{ m/s}$,
- and average Froude numbers of about $Fr_{Q162-H21} = 0.2$ and $Fr_{Q325-H35} = 0.155$.

This procedure makes it possible to visualize the effects of the flow depth on morphological processes already during the evaluation of the individual experiments. In the following, when references are made to the reservoir length on the abscissa of a figure, this always refers to the 0.00 reservoir meter at the transition from the moving bed to the fixed weir bottom and thus denotes the distance upstream to the weir. Also, when flow depth is referred to, it means the actual flow depth measured in the reservoir during the experiment, as distinguished from the initial water depth before the start of the experiment and the target water level which was kept at the control gauge.

4.1.1. Riverbed topography

Point clouds from the laser scan measurements used to analyze bed topography were analyzed in three longitudinal sections (see Figure 25): along the reservoir centerline (0.00 m, No. 2), 25 cm orographically to its left (-0.25 m, No. 1), and 25 cm orographically to its right (+0.25 m, No. 3). These longitudinal sections are frequently referred to in the following figures. For all laser scan measurements, the laser scanner was placed upstream and centered above the measurement area as shown in Figure 24.

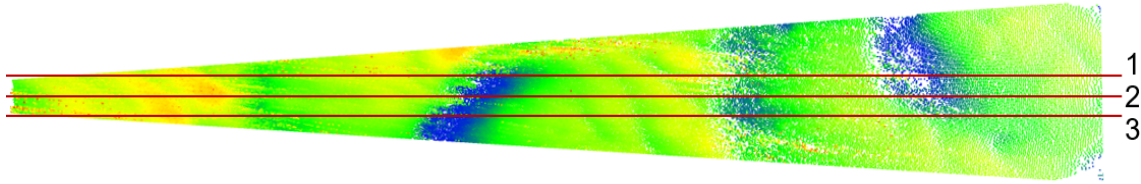


Figure 25: Bed scan with location of the three evaluated longitudinal sections along the reservoir

4.1.1.1. Longitudinal bed sections

Figure 26 shows the three described longitudinal sections through the point clouds of two selected laser scans. Each data point corresponds to a measured sample point from the bed survey and the coloring indicates the allocation to the respective longitudinal section. Bed levels at 0 m equal the elevation of the weir floor and the initial height of the reservoir bed before the start of the experiments.

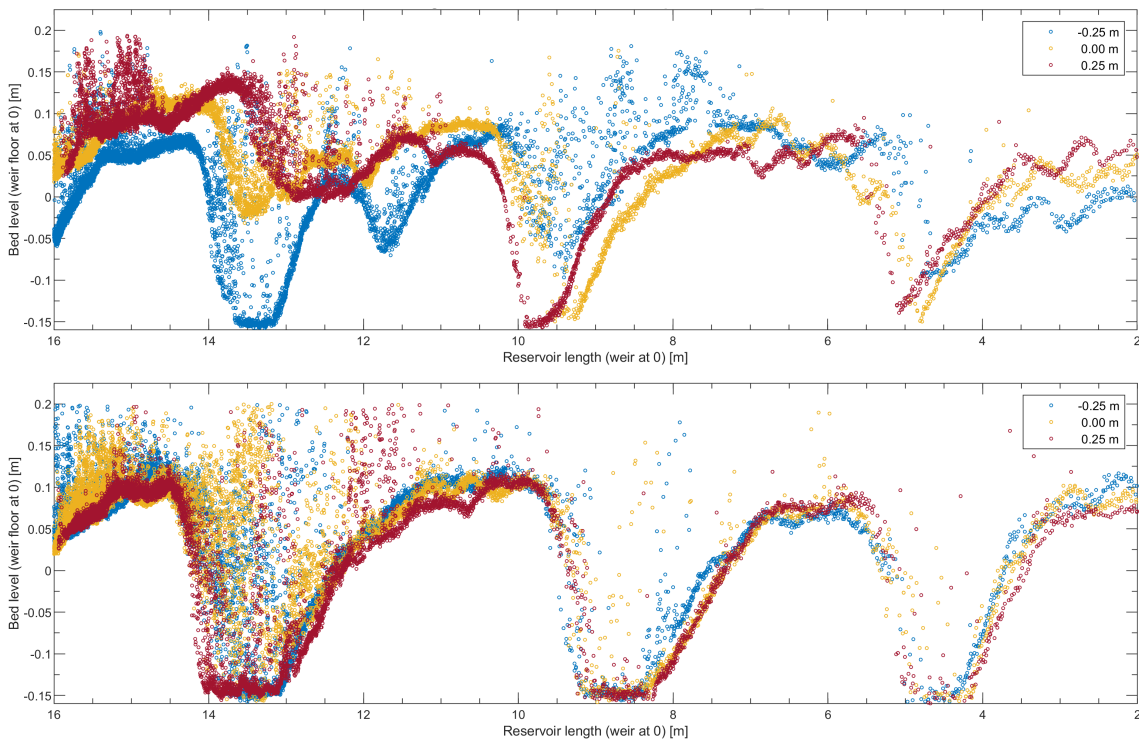


Figure 26: Longitudinal sections 1, 2, and 3 through the refraction-corrected point cloud, exemplary for Q162-H21 (top) and Q325-H35 (bottom)

For experiment Q162-H21 with the lowest of the three water depths of 21.25 cm (top in Figure 26), it can be seen on the one hand that despite the only small distances of 25 cm between the longitudinal sections, a strong three-dimensionality of the bed structures was present (the width of the moving bed was 2.55 m at the beginning of the experiment). However, for experiment Q325-H35 with the highest water level of 35 cm (bottom in Figure 26), this three-dimensionality is hardly visible. This difference is due to the strong dependence of the development of bed structures and bedforms on the flow depth, which will be discussed in detail in chapter 4.2.1.

On the other hand, the location of the actual bed surface is not easily identified everywhere along the longitudinal sections in both experiments. Firstly, the point density of the laser scans varies and decreases towards the weir, which is due to the point grid of the radially measuring laser scanner becoming larger with longer the distance from the laser scanner origin, as well as to the longer path of the laser beam under water, which in turn lead to stronger light scattering and thus increasing point losses. Secondly, depending on the angle of incidence and the slope of the bed surface, it becomes increasingly difficult to detect downstream sloping bed surfaces with greater distance from the laser scanner, which explains the higher point densities near the laser scanner (i.e. upstream) and on the surfaces rising with the flow direction (i.e. dune ridges).

In addition to these measurement technique reasons, there are also areas where sediment was briefly whirled up by the flow and was in the water column at the time of measurement. It can be seen that these swirls are stronger for experiment Q325-H35 with the high water depth, which can be attributed to the larger height differences along the reservoir due to the bed structures and thus stronger local turbulence. To identify the location of the bed surface in the point clouds for further analysis, a gravity center approach was used to determine this location, and outliers (i.e., whirled-up sediment) were removed via a neighborhood comparison and further filtering.

To implement this, all points lying within 20 mm to each side of the longitudinal sections were shifted perpendicularly on the section lines. An active layer thickness of 25 mm was assumed and the expected location of the surface was set at $\frac{1}{4}$ the height of the active layer thickness. Neighboring points were not allowed to have elevation differences greater than 30 mm and a two-step outlier filtering removed clusters of outliers and single point outliers with a moving median. Finally, a smoothing spline was applied and the result of this procedure can be seen in Figure 27 as black lines. These lines represent the identified bed surface in each longitudinal section. In addition to what was previously discussed, it is particularly visible for Q325-H35 with the high water depth that bed elevations of -0.15 cm

were reached. At this elevation was the solid bed of the concrete flume and the mobile sediment was thus completely eroded at these points.

Figure 28 shows the mobile bed in the study area of the reservoir from the perspective of the ceiling camera at the respective time of the laser scans in Figure 26 and Figure 27, namely approximately in the middle of the scan duration, so that a temporal agreement of the ceiling camera photos with the laser scans of ± 5 seconds is given. With the help of the longitudinal sections (colored lines) and the cross sections (white lines) drawn into the photos, it is possible to align the bed elevation profiles from the previous figures with the actual state of the reservoir bed and to better comprehend the morphological situation in the measurement area. On the basis of the top photo in Figure 28, for example, the area of swirled-up sediment particles between 8 and 10 m on the abscissa can be recognized very precisely, which is most visible in Figure 27 (top) for Section 1 (i.e. orographically on the left, blue sample points) and it is not visible at all in Section 3 (red sample points).

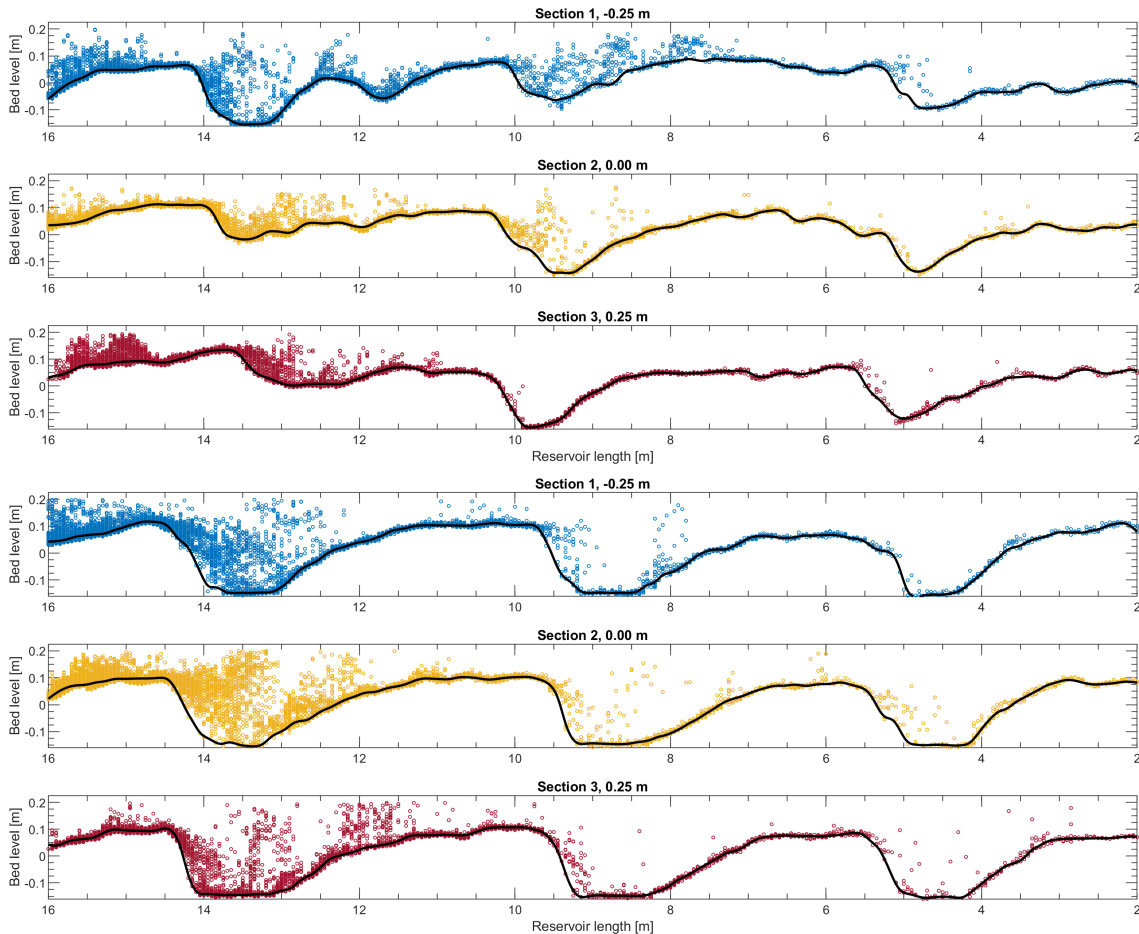


Figure 27: Approximated locations of the bed surface in the 3 longitudinal sections, exemplary for Q162-H21 (top) and Q325-H35 (bottom)

4.1.1.2. Longitudinal bed gradient

With the help of the previously determined position of the bed surface, further evaluations could be made. First of all, an average longitudinal bed gradient per laser scan was to be

determined and from this a time series of the longitudinal bed gradient over the duration of all laser scans. On the basis of the exemplary laser scans in Figure 26 and Figure 27, it could already be seen that the bed elevation varies by up to 30 cm due to the existing bed structures. This is a big challenge for the calculation of a mean longitudinal bed gradient, because the length of the study area of 14 m (only data between 2 and 16 reservoir meters were used) is small in relation to the variations of the bed elevation. The location of individual bedforms has too great an influence on the calculation of the mean longitudinal bed gradient as well as the mean bed elevation to be determined solely from a regression line drawn through the profile of the bed surface.

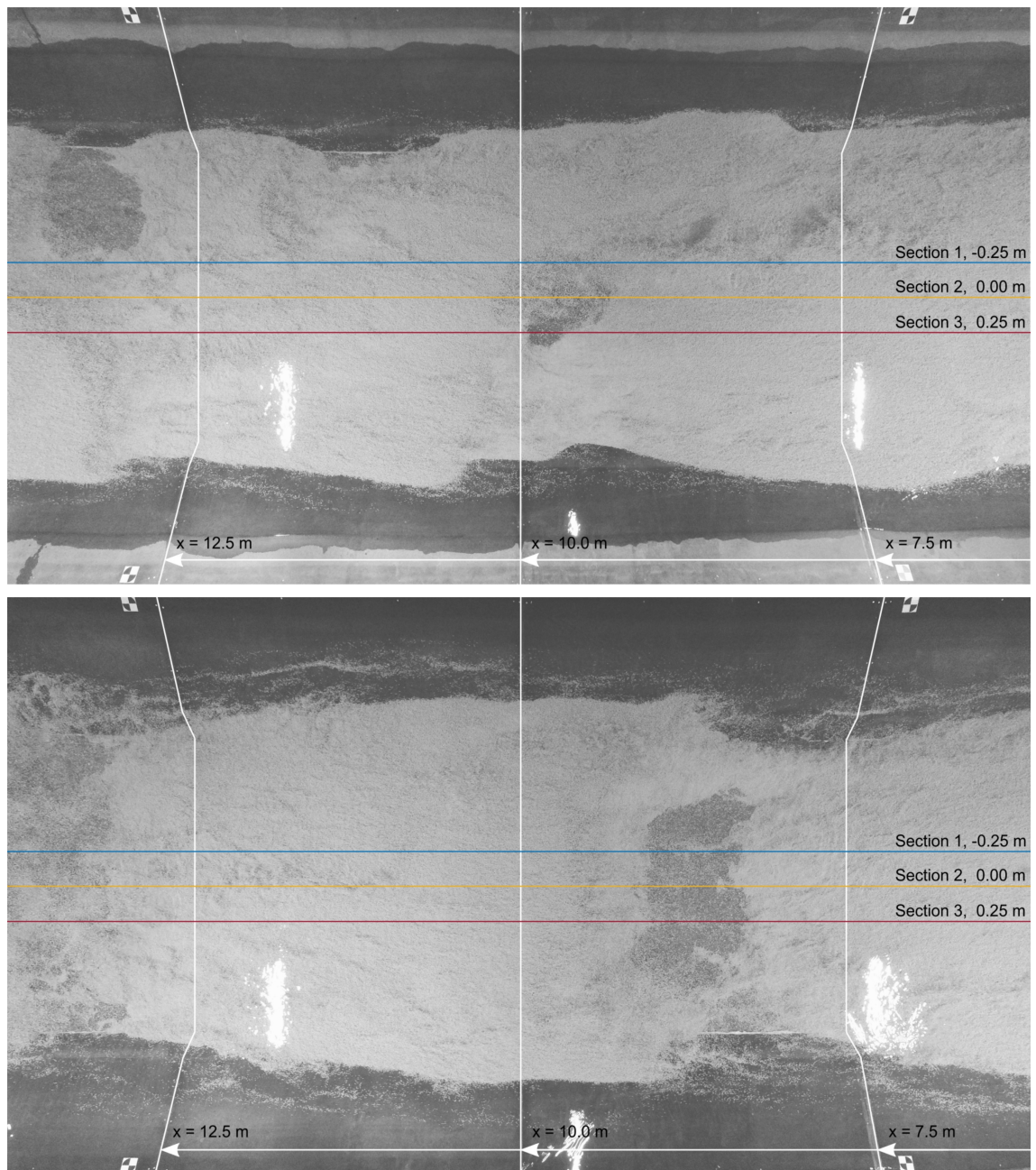


Figure 28: Photos of ceiling camera with position marks and longitudinal sections, exemplary for Q162-H21 (top) and Q325-H35 (bottom)

To reduce this influence, the sample window used to determine a regression line for the mean longitudinal bed gradient is successively shortened within the available study area (i.e. the area between 2 and 16 reservoir meters) and then shifted back and forth within the study area. Because the choice of the length of the sample window also has an influence on the longitudinal bed gradient, a large number of such sample windows were generated and a longitudinal bed gradient is determined for each one. The largest sample window was therefore 14 m long, the smallest half as long at 7 m; additional sample windows were created every 0.5 m in between. All but the largest sample window were then positioned at all possible locations within the largest sample window with a step size of 0.5 m each, and a regression line was determined at each location. The number of longitudinal bed gradients derived for each sample window thus increased as the sample window became smaller, as did the fluctuation range of the longitudinal bed gradients determined (see Figure 29).

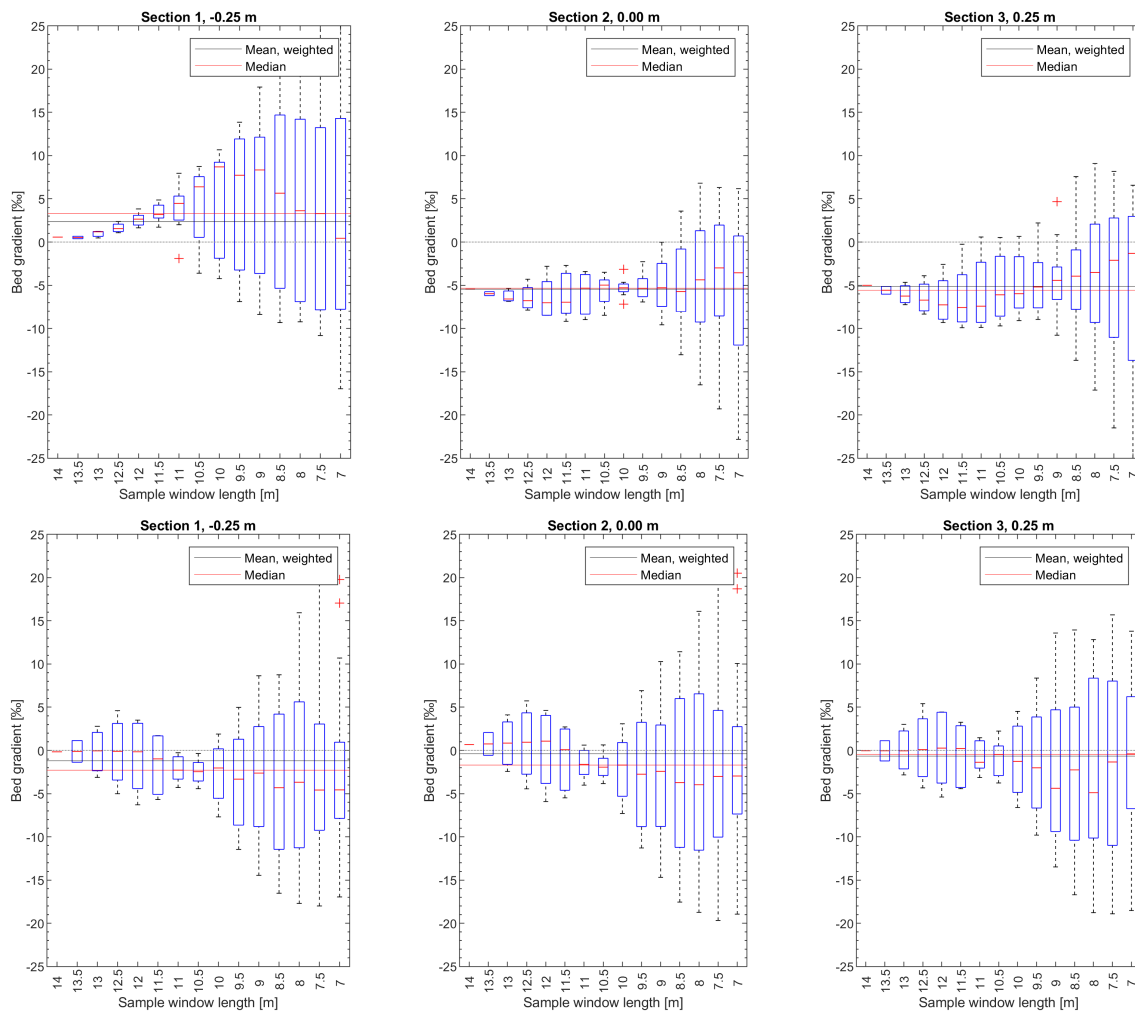


Figure 29: Analysis of the longitudinal bed gradients in the study area for the 3 longitudinal sections, exemplary for Q162-H21 (top) and Q325-H35 (bottom)

For each sample window, the median of the determined longitudinal bed gradients was used and then a weighted average was applied to determine a resulting mean longitudinal bed gradient: The largest sample window was weighted with 50%, the remaining 50% were

evenly distributed among the other sample windows. This process is to a certain extent arbitrary, but it reduces the influence of individual bed structures on the calculation of the longitudinal bed gradient. In Figure 29 (top left, bottom left and center), this effect is well visible: In comparison of the weighted mean with the alternatively used median (fluctuations of the individual values per sample window are not normally distributed), the weighted mean is closer to the median of the largest sample window and thus fluctuates less strongly, while at the same time it still reflects the influences of the smaller sample windows. Negative values indicate longitudinal bed gradients falling with the direction of flow.

Figure 30 shows the corresponding time series of the mean longitudinal bed gradient over the duration of all laser scans. This illustrates the uncertainty in the determination of the longitudinal bed gradient described in Figure 29 in two respects: First, strong fluctuations of the longitudinal bed gradient within short periods of time are indicated, which should also be noticeable in the longitudinal water surface gradient due to their magnitude, especially if the supposed longitudinal bed gradient even increases in the direction of flow in some cases, i.e. positive values of the longitudinal bed gradient are present. However, as can be seen in Figure 31, this was not the case. The longitudinal water surface gradient in Figure 31 (left) varies only in the range of about 0.5 ‰, while the variations of the longitudinal bed gradient are about tenfold.

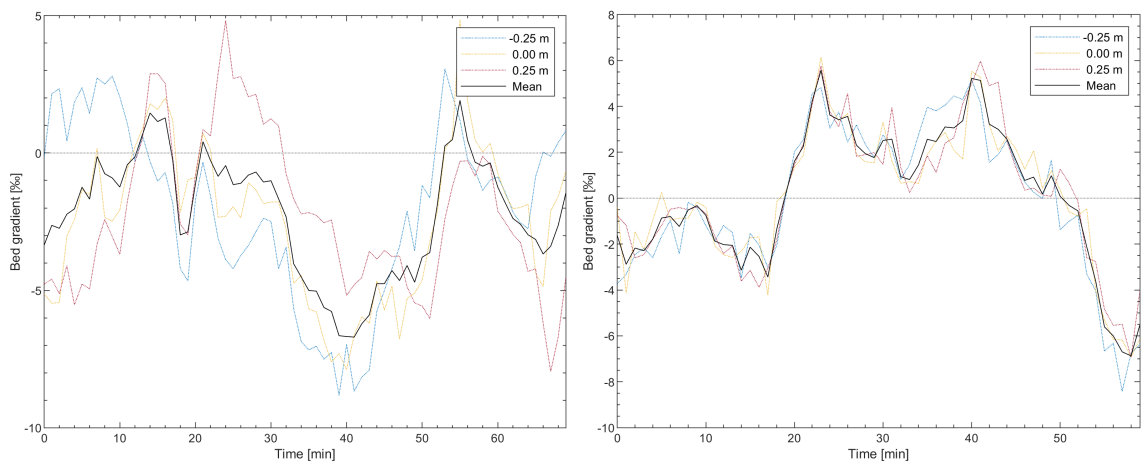


Figure 30: Time series of the longitudinal bed gradient in the study area for the 3 longitudinal sections and averaged, exemplary for Q162-H21 (left) and Q325-H35 (right)

The second factor is the three-dimensionality of the bed structures, which plays a role especially for the experiment with the lowest water depth (Figure 30 left) and makes generalized statements about the longitudinal bed gradient even more difficult, because the different longitudinal sections fluctuate with a significant time offset and, in some cases, even in opposite directions. Therefore, unfortunately, no valid statement for the entire

reservoir could be derived from the longitudinal bed gradients determined with the measurement setup present in the test facility during the experiments.

Thanks to the dynamic equilibrium state of the bed, this problem could be countered with an analysis of the longitudinal water surface gradient. Under normal depth conditions, the longitudinal water surface gradient I_W directly corresponds to the energy line gradient I_E and is assumed constant over time. Hence, it may be equated to the longitudinal bed gradient S . Figure 31, right, shows the averaged longitudinal water surface gradient derived from the control gauge at reservoir meter 5 and the water level gauge at the beginning of the reservoir at reservoir meter 58.

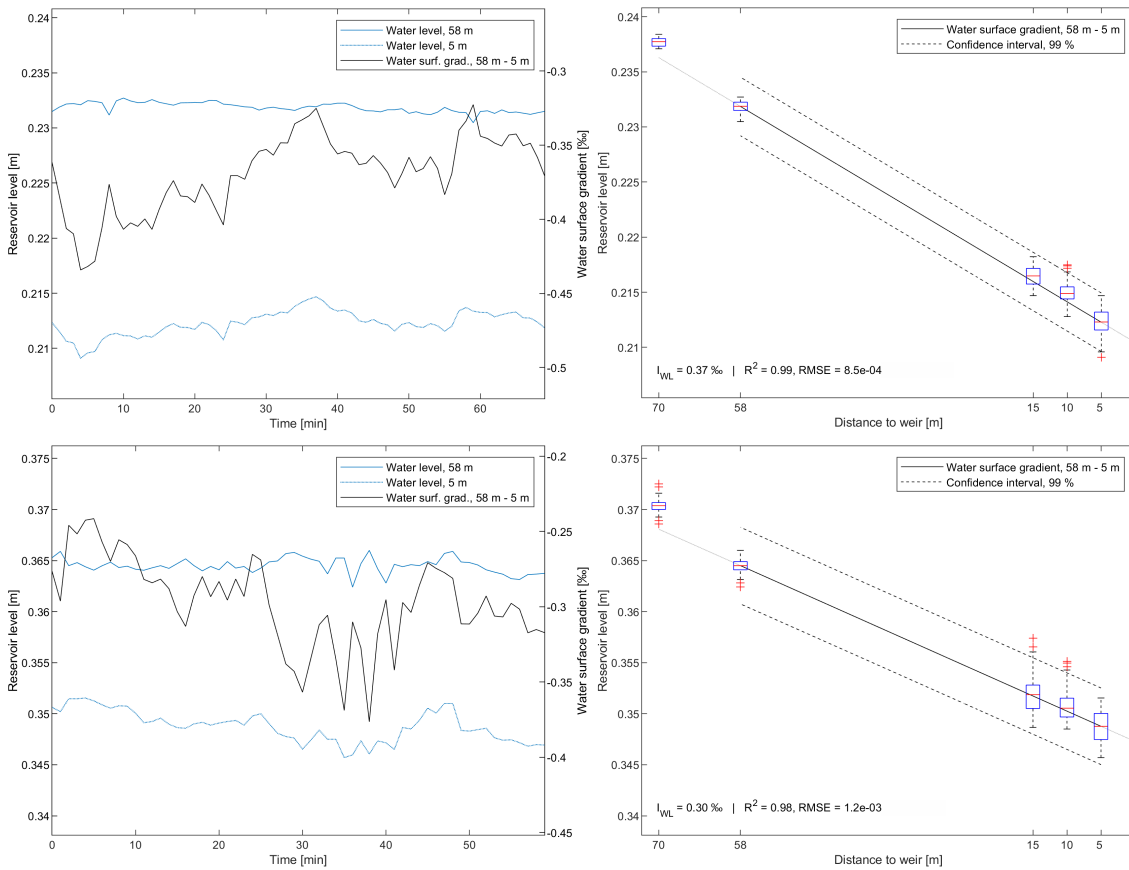


Figure 31: Time series of the longitudinal water surface gradient (left) and averaged longitudinal water surface gradient in the reservoir from water level data (right), exemplary for Q162-H21 (top) and Q325-H35 (bottom)

Also shown are the water levels at the water level gauges along the reservoir centerline at reservoir meters 10 and 15, as well as the water level in the large flume section upstream of the reservoir. Based on the only minor fluctuations of the water levels at the individual water level gauges, the previously made assumptions about normal depth conditions and dynamic bed equilibrium could be considered valid in the present case. In the following, the mean longitudinal bed gradient is therefore assumed to be equal to the longitudinal water surface gradient.

4.1.1.3. Bedform identification

In the next step, the longitudinal sections of the previously identified bed surfaces are examined for the presence of bedforms. For this purpose, the longitudinal sections were first detrended by removing the longitudinal bed gradient from the entire study area (data between 2 and 16 reservoir meters) around the mean bed elevation. In Figure 32 this is shown by the gray line before and the black line after detrending. After that, zero crossing analysis after Nordin (1971) and Mehrdad (1989) was used to detect the highest and lowest points of the bedforms, referred to as dune crests and dune troughs in the following.

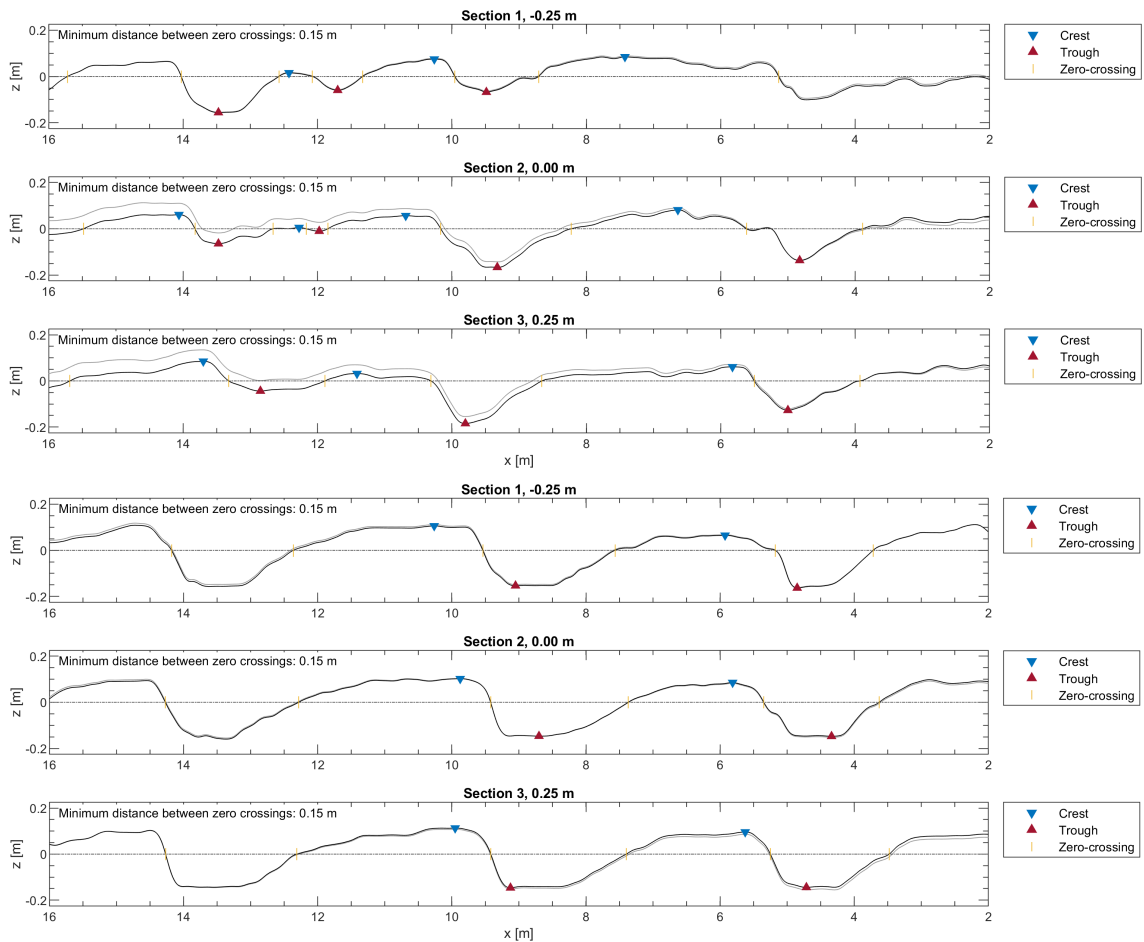


Figure 32: Dune crests and dune troughs along the bed surface in the 3 longitudinal sections after detrending (original bed surface in light gray), exemplary for Q162-H21 (top) and Q325-H35 (bottom)

A number of more advanced methods for the analysis and description of bedforms exist in the literature, for example by using probability density functions to incorporate more features of the dune shape. A detailed study on this topic was carried out by Henning (2013), who dealt with the statistical description of two- and three-dimensional bedforms in uniformly graded coarse sand in the laboratory from the view of modern data analysis methods. Furthermore, powerful open source tools exist, e.g. Bedforms-ATM (Gutierrez et al. 2017) based on wavelet transform, as well as numerical methods for in-depth bedform analysis, for example using Monte Carlo simulation (Reich 2020).

While on the one hand these methods have great potential for more advanced analyses of dune migration processes and shape characteristics, on the other hand they also require a high degree of expert knowledge in the precise setting of the analysis parameters, so that they did not add crucial value to the present study, especially because spatial analyses were not the primary research objective. Nevertheless, the data presented in this study are well suited for further analyses, in particular the identification of multiple bedform classes with different sizes and migration velocities. This could be beneficial if, for example, the classification of the measured lightweight bedforms were to be used for a similarity model study. Our own analysis of longitudinal sections of the bed surface using wavelet decomposition into several frequency ranges showed potential here too, but was not elaborated further in the necessary depth to date.

Due to the high resolution of the bed survey, which resolves height differences of the bed surface in the millimeter range, even very small fluctuations of the bed surface around the zero line were sometimes detected as dune crests or troughs in this procedure, which, however, would not be classified as dunes by manual expert analysis. These ripple-like structures were considered to be insignificant for the governing bedform migration processes and to bias the further analysis of the predominant dunes. They were therefore excluded from the zero-crossing analysis by a manual filter criterion, namely a minimum distance of two consecutive zero-crossings: This threshold was set constant at 15 cm for all experiments. For checking purposes, zero crossing analyses were performed with 10 cm and 35 cm thresholds. Figure 33 only shows scenario Q162-H21 as an example, since no changes occurred in the selected scan of Q325-H35 due to the very large and distinct dunes. Introducing a minimum dune height as an alternative manual filter criterion yielded less accurate filtering due to the often elongated dunes with crests close to the zero line.

For a threshold value of 10 cm (see Figure 33, top), compared to a threshold value of 15 cm (see Figure 32, top) in Section 2, two additional zero crossings were identified between 5 m and 6 m, which would not necessarily be assigned to an independent dune by manual analysis. For a threshold of 35 cm (see Figure 33, bottom), two zero crossings are missing compared to a threshold of 15 cm in Section 2 between 12 m and 12.5 m, which would already have led to an ambiguous decision in manual analysis. The implications of different thresholds in zero crossing analysis are not negligible, hence, but it can be stated in advance to the following analyses that the occurring differences during dune identification do not result in fundamental changes in the correlations derived in general, which is why the threshold value of 15 cm is used in the following.

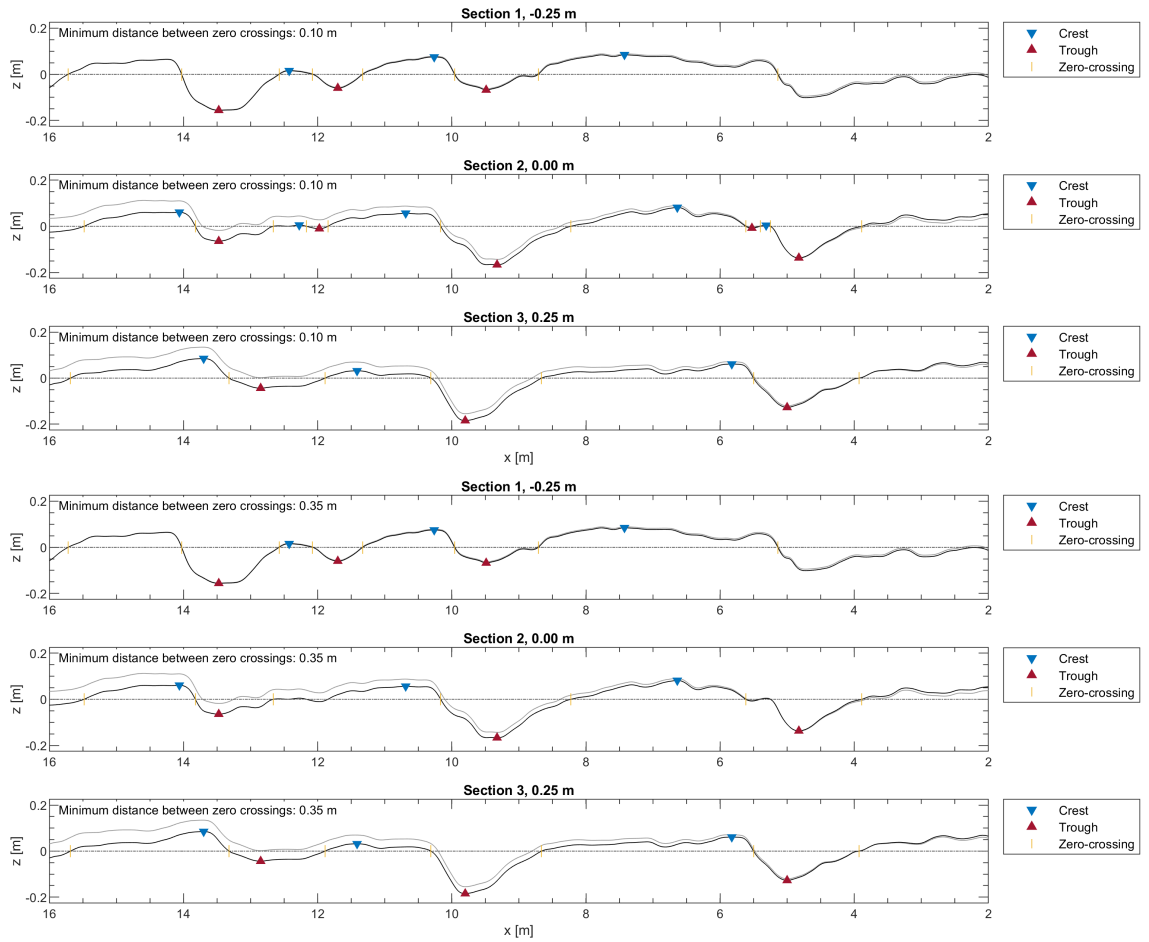


Figure 33: Dune crests and dune troughs along the bed surface in the 3 longitudinal sections with different zero crossing thresholds (un-detrended bed surface in light gray): 10 cm (top), 35 cm (bottom), exemplary for Q162-H21

For the purpose of the present study, the method presented is sufficient to reliably detect the repetitive bed structures that are critical to sediment transport under the hydraulic conditions in the experimental river reservoir. The required statistical robustness of the conclusions thus made was ensured by the large number of created data sets. Accordingly, the presented procedure was applied to all 60 - 80 scans per experiment and dune lengths and heights were determined from the distances between the detected dune crests and troughs. Figure 34 shows all dune lengths and dune heights of all three longitudinal bed sections for the two exemplarily analyzed experiments.

Principal component analysis (PCA) was used to determine the principal axes of the point clouds in Figure 34 to visualize the relation of dune lengths and dune heights by their eigenvalues as a measure of variance. PCA is a multivariate statistical method for dimensional reduction via linear transformation of variables so that as few new variables as possible describe the relevant information, i.e. data. PCA is only reliable if the data are approximately normally distributed; measure of relevance is the variance (Jolliffe 2002). The new variables are called principal components or linear combinations, they are orthogonal and thus uncorrelated. In contrast to linear regression, the error squares are minimized perpendicular to a straight regression line (orthogonal regression) and not along

the ordinate (y-axis) direction (least squares) (cf. Kamke (2014)). Thus, linear regression is more about finding a straight line that best fits the data, depending on the internal data relationships (Henze 2017).

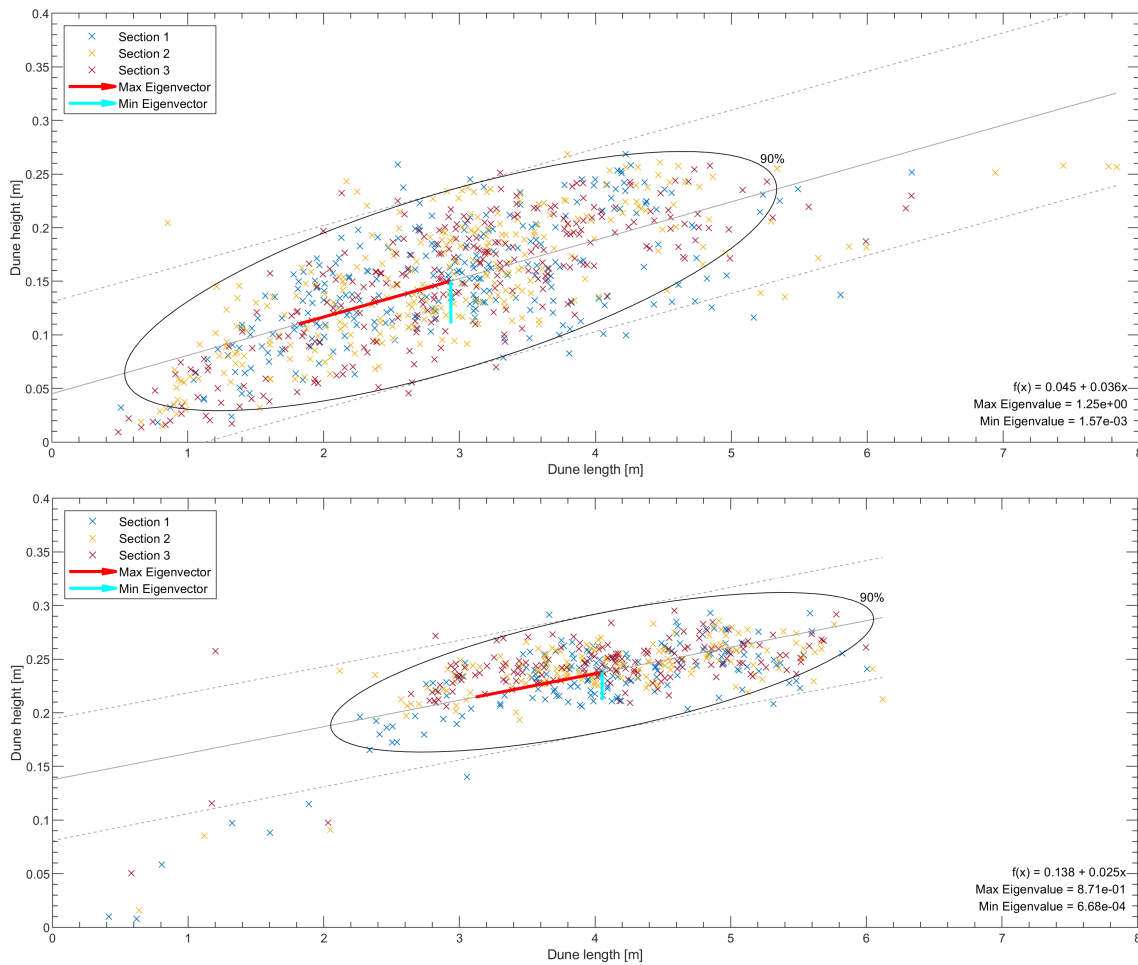


Figure 34: Dune lengths and dune heights of the reservoir bed, exemplary for Q162-H21 (top) and Q325-H35 (bottom)

In this way, the bed structures of all experiments can be compared using only a few statistical variables. In addition, the 90 % error ellipses are shown, which indicate the probability with which a single measurement lies within the respective ellipse, provided that the bed has assumed all possible shapes in the measured period and a normal distribution of the measured values was present, as well as the 90 % confidence intervals of the linear regression in addition. The much larger dispersion of the data points in Figure 34, top, is striking. This is due to the already mentioned stronger three-dimensionality of the bed structures in the experiment with the low water depth as well as to an overall higher variability of the bed structures. Figure 35 shows the data points from Figure 34 again, but separately for each longitudinal section and thus make the individual distributions of the data points comparable.

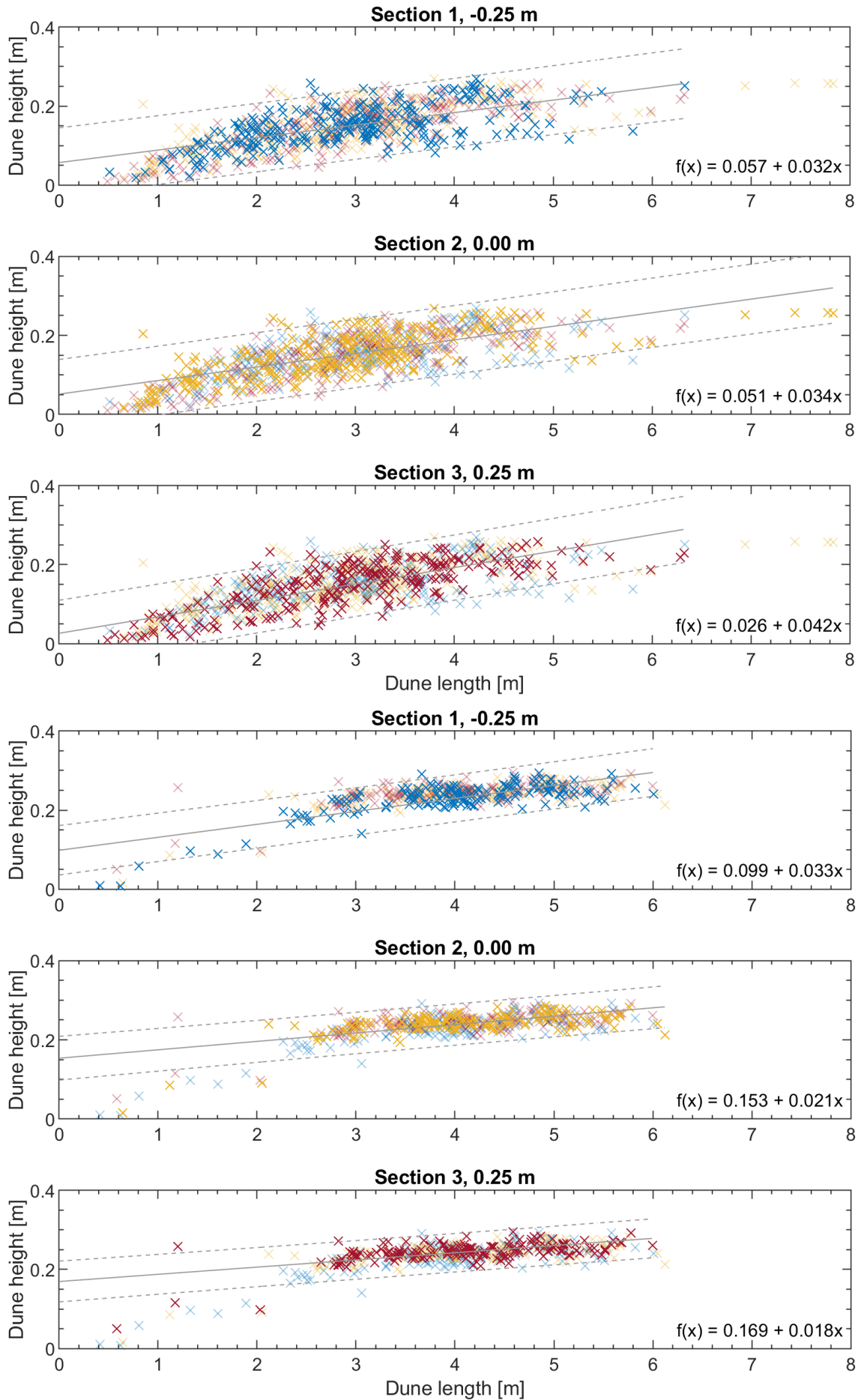


Figure 35: Dune lengths and dune heights of the reservoir bed, section-wise for Q162-H21 (top) and Q325-H35 (bottom)

For both experiments shown here exemplarily, a largely equal distribution of the data points from the three sections can be seen, which is also reflected in very similar regression functions. This can be interpreted as a support for the robustness of the correlations derived in Figure 34. Furthermore, a measure of the migration velocity of the dunes (hereafter referred to as dune velocity) can be derived from the change in position of the dunes in the reservoir from one laser scan to the next.

For this purpose, the following process was followed: For each zero crossing of a selected scan the distance in longitudinal direction to all zero crossings of the previous laser scan was calculated and the smallest positive difference of these distances is used as a measure for the travelled distance of the respective zero crossing from the previous to the selected scan. Because the number and position of the zero crossings sometimes could change considerably from one laser scan to the next, this procedure can only be justified by the large number of random samples, i.e. laser scans, which provide the necessary statistical certainty. In addition, the median was used instead of the mean, which is more robust to outliers. Using dune crests and troughs instead of zero crossings increased the statistical uncertainty because their location varied even more.

Figure 36 shows the distribution of the dune velocity per longitudinal section for the two exemplary experiments, as well as regression lines that can be recognized by means of color assignment. The medians of all values per longitudinal section are given in the text box in the lower left corner. The dashed gray line shows the manually-timed measurement of dune velocity of a single dune traced through the reservoir over a period of 15 to 30 minutes during the ongoing experiments as a reference.

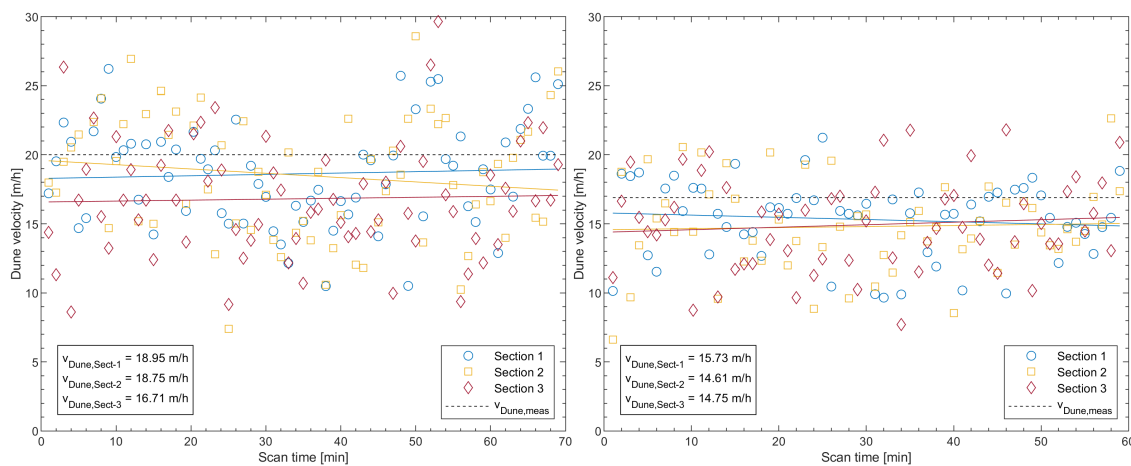


Figure 36: Dune velocities from zero-crossing analysis, exemplary for Q162-H21 (left) and Q325-H35 (right)

The agreement of the calculated dune velocities with the manually-timed measurements is good, although the manually-timed dune velocities were higher in the two examples given. In the other experiments, however, the manually-timed measurement was sometimes also

lower than the calculated values, so there may simply be natural variation in the measurements here due to only a single manually-timed bed structure (cf. chapter C.4 in the appendix). When an average dune velocity was used in the following analyses, it was calculated as the average of the three calculated dune velocities and the manually-timed value in equal parts.

4.1.2. Sediment transport

The time series of the sediment transport measurements for the entire durations of the two experiments already used as examples in chapter 4.1.1, scenarios Q162-H21 and Q325-H35, are given in Figure 37. The raw data of the sediment transport rate recorded with a frequency of 10 Hz as well as a moving average with a window size of 600 readings (about 1 minute) are shown. The time interval during which the bed survey was carried out by laser scanning is highlighted in light orange.

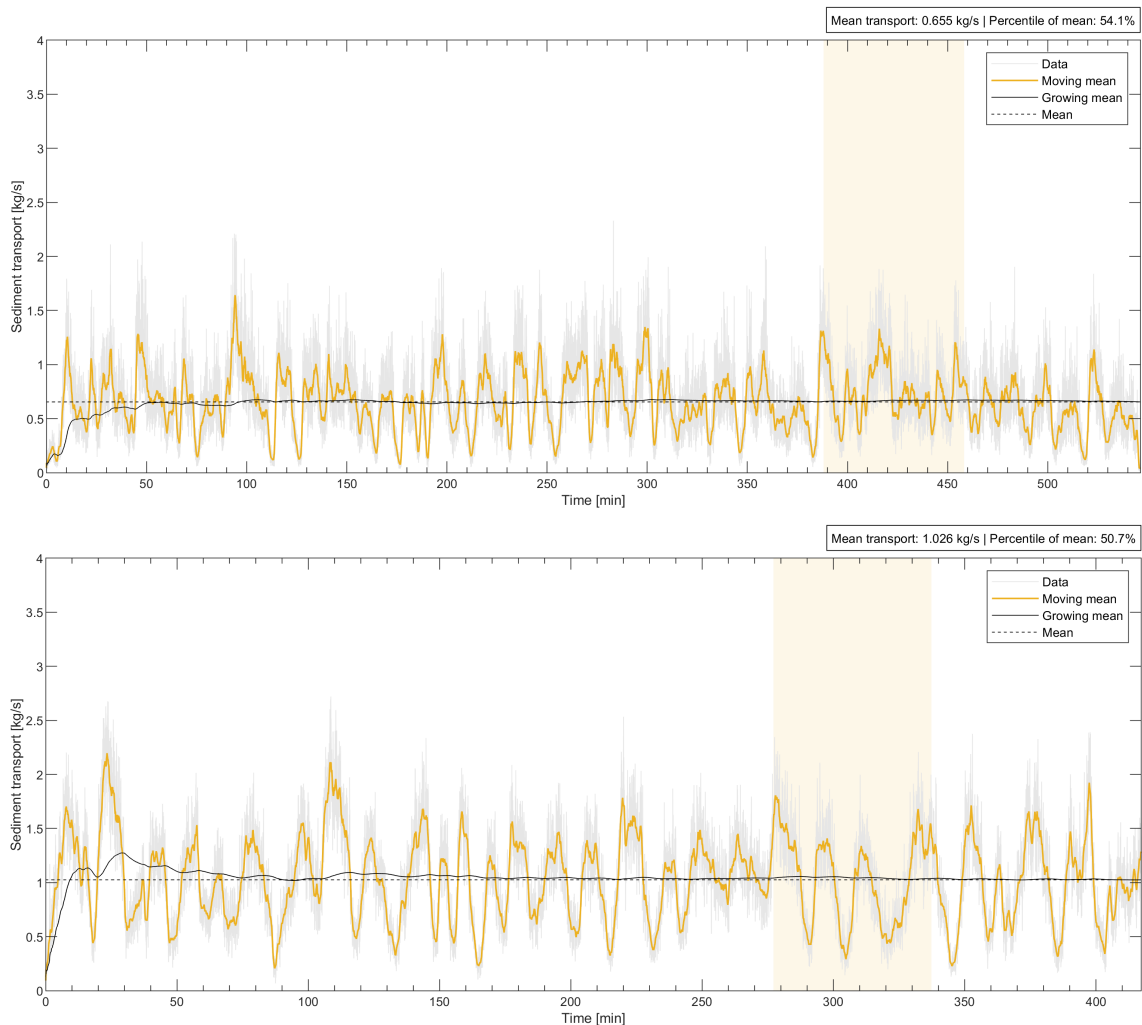


Figure 37: Sediment transport rate time series during the entire experiment, exemplary for Q162-H21 (top) and Q325-H35 (bottom)

The moving average (orange line) shows the course of sediment transport fluctuations, which are directly dependent on the bedforms present in the reservoir. When the front of a

bedform, i.e. dune, was currently passing the weir, the sediment transport measurements increased steeply; if a dune ridge passed through the weir, they decreased slowly. The additionally plotted mean (dashed in black) and the growing mean, which was calculated from the beginning of the experiment (black line) show that the sediment transport rate approaches the overall mean of the experiment very early on and then only fluctuates in the low percentage range depending on the size and distribution of the present bedforms.

When comparing the two experiments, the average sediment transport rate in Figure 37, bottom, is about 1.5 times as large as in Figure 37, top, while the "length" of individual dunes on the time axis does not differ to the same extent. In fact, the lengths are almost the same, which indicates a different bed condition as well as a different dune velocity (cf. also Figure 36). The overall difference in the duration of the experiments is attributed to the fact that reaching dynamic bed equilibrium depended on the hydraulic stress in the river reservoir: The greater the hydraulic stress, the shorter the required duration of the experiment. The minimum duration of an experiment was set to 1.5 times the duration required for a bed structure to travel across the entire reservoir once (cf. chapter 3.4.1.) This ensured that the short-term flushing effects at the beginning of the experiments (which depended on how fast the transition from the flat initial bed to the first stable bedforms took place) no longer had any influence on the bed structures measured by laser scanning.

Figure 38 shows only that time interval on the abscissa, from which the comparative sediment transport parameters were calculated for the analyses following in the next chapter. The time interval is composed of the duration of all laser scans, which took about 60 to 80 minutes per experiment (highlighted in light yellow in Figure 37) and a further 60 minutes directly afterwards. In this way, on the one hand, it is taken into account that the bed structures captured during the laser scanning were recorded with a time offset by the transport measurement procedure, which in turn depended on the hydraulic stress; bed structures were recorded between reservoir meters 2 and 16, the sediment transport measurement took place after the weir. On the other hand, the statistical reliability is increased by a larger time interval, too.

In addition to the time series of sediment transport rate parameters (q_t indicating total measured sediment transport), Figure 38 also shows the water levels (WL) at the reservoir gauges and the discharge (Q). While the hardly visible discharge fluctuations in the per mille range can be neglected, the water levels fluctuate noticeably depending on the existing bed structures. The two uppermost water level gauges are less affected by this. It can also be seen that the control level ("WL, 5 m, rb") and the level in the middle of the reservoir ("WL, 5 m") do not show major differences. Consequently, the influence of the bed

structures on the water level could not be significantly reduced by the standpipe in the right bank for all experiments.

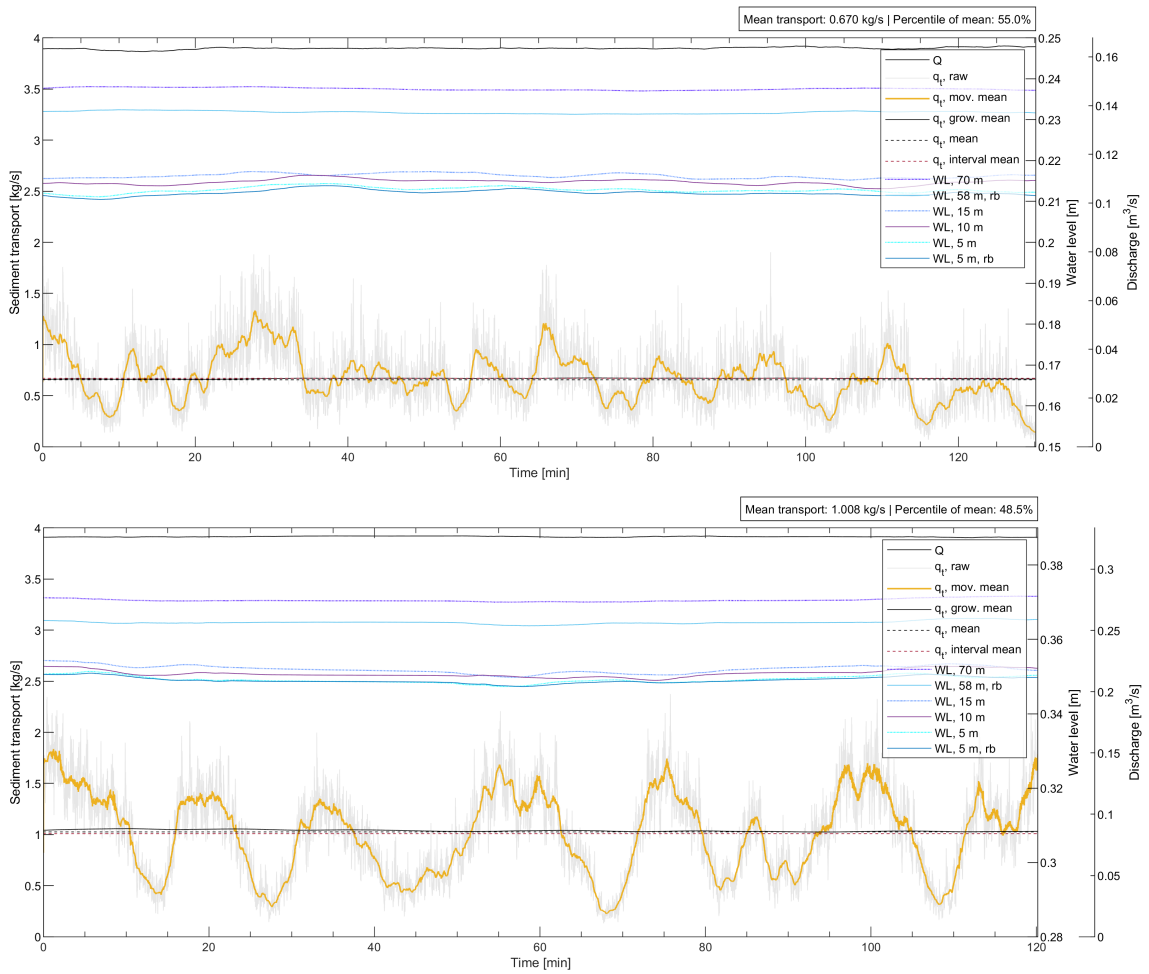


Figure 38: Discharge, water levels and sediment transport rate time series during the bed survey, exemplary for Q162-H21 (top) and Q325-H35 (bottom)

The comparison of the mean sediment transport in both experiments gives an impression of the influence of the bed structures on the quality of the measurement results: While the values of the mean sediment transport are almost identical for both the entire duration of the experiment and for the shorter evaluation interval in Figure 38, top, a slight deviation between the two mean values can be seen in Figure 38, bottom. Also, the growing mean is slightly higher here, which is due to the presence of a large dune passing the sediment transport measurement at the beginning of the bed survey (cf. Figure 37, bottom, at about 280 min). The sediment transport mean of the entire experiment is still influenced by the short-term transport increase at the beginning of the experiment, which can be attributed to the abrupt initiation of bed transformation in the entire reservoir in this case. In absolute terms, however, the differences are of small magnitude and also smaller than the expected total measurement error (cf. chapter 3.5), so that the accuracy of the measurement results of the evaluation interval is considered to be sufficient.

For further analysis of the distribution of the measured data, Figure 39 shows histograms of the sediment transport rate measurements, the calculated means and medians, and also the normal distribution that can be calculated from the means and standard deviations of the measured data of the respective experiment. For Figure 39, left, a slight right skew can be seen with an overall good agreement of the distributions, as a result of which the mean lies somewhat further to the right of the highest bin of the histogram. The median is only slightly closer to the highest bin, which is due to the slightly right-skewed distribution. This, in turn, is due to the nature of the measurement data: the probability of a small measurement value occurring is slightly increased here; moreover, the calculated normal distribution would require negative sediment transport values, which is why this simple comparison with the normal distribution is flawed to some extent.

In Figure 39, right, no right skew is visible and also not indicated by the median, which is almost identical to the mean; instead, there is a negative kurtosis due to the flat-peaked shape of the histogram. This shows that not all cases had an almost normal distribution of the measured values and that in such cases the mean was usually higher than the median. Because the differences between median and mean were small in all experiments, the mean was used for the following evaluations. Furthermore, the use of the mean is obligatory for the analysis of cumulated sediment transport, which are determined from the sediment transport rates during a given time interval.

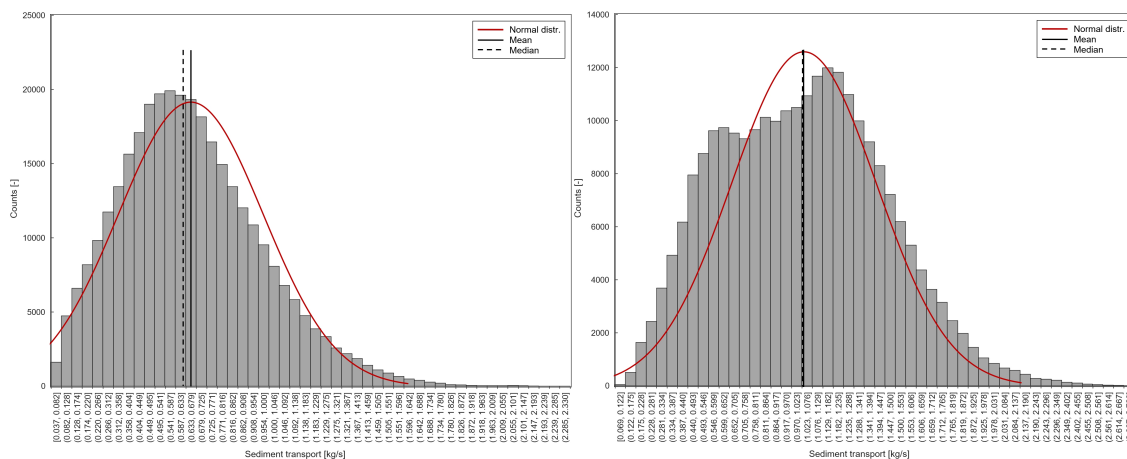


Figure 39: Distributions of sediment transport data, exemplary for Q162-H21 (left) and Q325-H35 (right)

To review the distribution of the measured transport data in all experiments, Figure 40 compares the mean sediment transport to the percentile of the mean of the data series. The percentile of the mean represents the percentage that the mean takes in the population of the measured data. Thus, it can be used as a measure of symmetry of the data distribution and thus describe the location of the mean in the measured data as shown in Figure 39. As the sediment transport rate increases, the percentile of the mean approaches the 50 % line, which is considered a measure of an approximate normal distribution. Kurtosis effects as in

Figure 39, right, are not considered here; however, they are of secondary importance for the comparison of the means. It can be stated: The more sediment transport takes place, the more bed structures can be recorded during the measurement interval, which increases the range of measured data and in turn the statistical certainty of the derived means. Apart from one, all experiments have percentiles of the mean well below 60 %, and they approach the 50 % mark for increasing sediment transport, which can be seen as a confirmation for the applied measurement and data evaluation procedure.

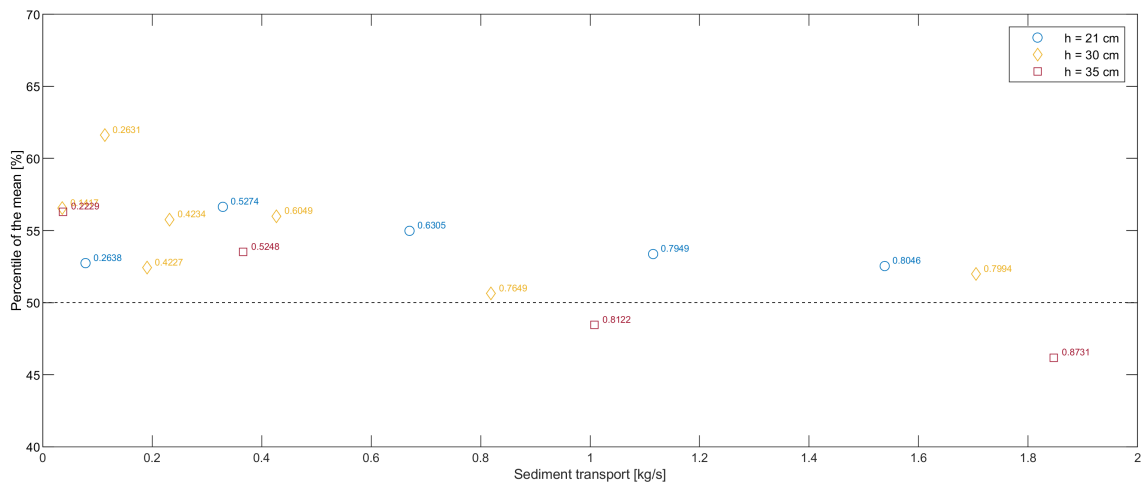


Figure 40: Comparing sediment transport means with percentiles of the means of all steady-state experiments, distinguished by reference water depth

4.2. Implications of steady-state experiment series

In this chapter, all dynamic equilibrium experiments are compared with each other. Mean values are used to reduce the complexity of the measured data. Their goodness of fit is also considered to evaluate the validity of the relationships derived in the comparative mean plots, if any. First geometrical parameters are evaluated, then hydraulic parameters, finally morphological parameters as well as various combinations of these parameters. The aim of these observations is to gain a deeper understanding of the bed transformation processes under steady-state hydraulic conditions as well as knowledge about the influence of flow depth and flow velocity on these transformations. The chosen experimental method provided special conditions for this: Each data point in the following illustrations can be traced back to an independent experiment and was created independently of all other data points. Mutual influences of the measured values between the individual experiments, on which these data points are based, could thus be excluded.

The large number of investigated scenarios makes it possible to analyze lightweight sediment bed parameters under near-natural conditions and under approximate normal depth conditions (the influence of reservoir length on bed evolution was discussed in

chapter 3.2.1). In this way, relationships can be made visible that would be more difficult to identify in common experimental setups, which often suffer from spatial limitations and inflow boundary effects on the bed evolution processes. In particular, the online dynamic sediment supply used in the presented experiments made it possible to generate a much wider range of variation in the bed structures that occurred in the experiments carried out. This, however, also increased the required effort during bed evolution evaluation due to the higher data variance. Therefore, to compare the results of all scenarios, a multi-step data averaging was performed:

1. Hydraulic measurements such as discharge and water levels, which were recorded continuously (approximately 1 Hz), were time-averaged over the duration of one laser scan for bed survey (approximately 1 min).
2. Time-averaged water levels recorded at several longitudinal positions (reservoir meters 5, 10, and 15) were spatially averaged to compensate for local effects of the bed elevation at the measurement points and distributed over a 10 m study reach between the three water level gauges.
3. Mean values obtained for each laser scan were averaged over the duration of the whole bed survey (between 60 and 80 data sets) to produce mean values for each of the total of three longitudinal bed sections.
4. An overall mean per experiment was generated from the three longitudinal bed sections, which are frequently also shown as data points in addition to the overall means in the following figures.

In the experiments conducted, sediment transport occurred primarily as bed transport. Occasionally, sediment grains were picked up by the flow through local eddies and transported in suspension over longer distances before finally settling back down. During experiments with high flow impact on the bed, an active transport layer several centimeters high developed in which sediment grains were transported at high velocities; however, even here sediment grains transitioned to a suspended state only to a very small extent.

The bedforms observed during the experiments grew from the plane starting bed to ripples to dunes, which, depending on the experiment, additionally formed smaller dunes on larger dunes (these were not classical ripples because the dimensions of the smaller dunes were too large) and began to dissolve again at the highest hydraulic stresses. The transition to the upper plane bed could not be observed to the point where all bedforms were completely flushed out, because the amount of sediment in the experimental river reservoir was not high enough to support the formation of an upper flow regime plane bed without any

bedforms. Instead, large gaps formed at the concrete flume bottom that did not carry any sediment anymore and very long dunes with approximately horizontal ridges developed.

4.2.1. Dune dimensions

Figure 41, left, compares the averaged dune heights of all three longitudinal sections of all steady-state experiments with the respective dune lengths. Each data point represents the temporal mean per evaluated longitudinal bed section over the duration of all topography scans, as described previously. The colors and shapes of the data points indicate the target water level per experiment relative to the weir floor, which was used as the reference value for the initial water depth in the reservoir. In Figure 41, right, these points are lighter colored and all shown as crosses for reasons of clarity, but to continue providing additional information about the data spread relative to the overall average values per experiment calculated from the three longitudinal sections and indicated by the other three colored symbols. The additional labels of the mean data points indicate the average shear stress in N/m^2 and serve as a reference for the hydraulic stress in the corresponding scenario in this and most of the following figures.

A positive correlation of dune height and length is visible in Figure 41. Shear stresses also increase along this correlation, showing the expected increase in dune dimensions with increasing hydraulic stress, as described in Fredsoe (1982), Van Rijn (1984b) and Karim (1995) and implicitly visible in Figure 10. Further, a phenomenon becomes apparent that will be considered in more detail in the following chapter 4.2.2: Above a certain level of hydraulic stress, the dune height decreases again, while the dune length continues to increase at a rather constant rate. This is shown in Figure 41, right, for all three water depths at the highest discharge and the highest shear stress, respectively. While dependencies on flow depth and thus the velocity profile across the water column are evident for the dune dimensions, there are no dependencies between the three longitudinal bed sections used for bed topography evaluation, as expected. Figure 41, left, shows the random distribution of the data points coming from the longitudinal bed sections.

The multi-step data averaging reduced the complexity of the hydraulic and morphodynamic process in the experimental reservoir on the one hand and of the large range of measured data on the other hand. The deduced approximations came at the cost of losing data variability, but were necessary to allow for more straightforward data analyses. Thanks to the high data availability, statistical power of many parameters was high and sufficient evidence was provided to conclude whether an effect existed or not. The range of variation of the bedform dimensions can be made explicit by means of error ellipses. In chapter 4.1.1

these error ellipses were already introduced and explained for the individual evaluation of the bedforms during one experimental scenario.

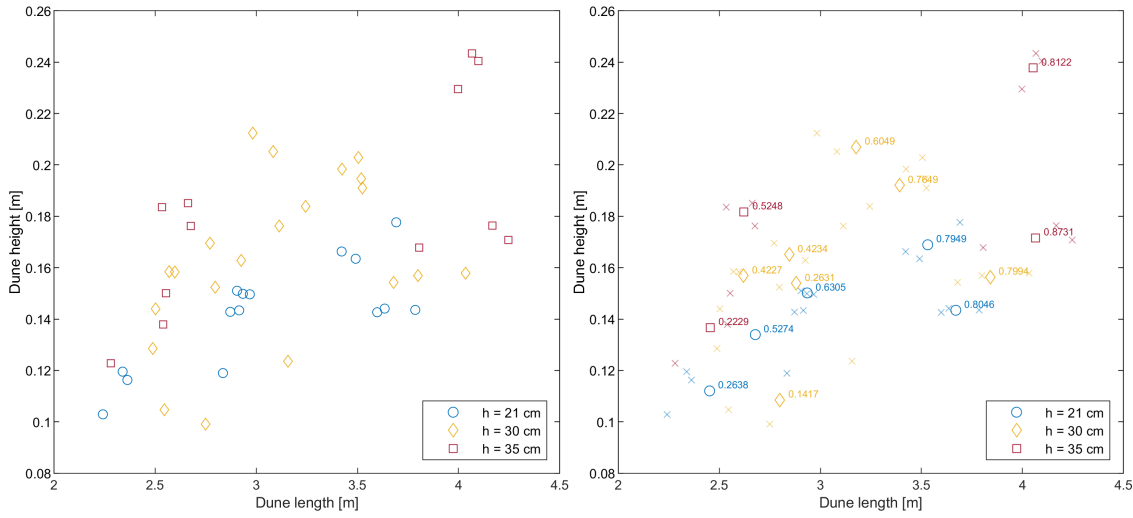


Figure 41: Comparing dune length with dune height of the longitudinal bed sections (left) and of the means per experiment with mean shear stresses in N/m^2 as point labels (right) distinguished by reference water depth

Figure 42 shows the 1 % and 10 % error ellipses for each mean value of a test in order to evaluate the statistical significance of the mean values shown in Figure 41. The error ellipses indicate the confidence interval containing x % of all values in the underlying normal distribution. Two assumptions were made here: the measured dune heights and lengths were normally distributed and measurements were conducted for a sufficiently long time to assume a good approximation to the population of all possible bedforms. Normal distribution could be assumed due to the statistical nature of evolving bedforms in the reservoir, which is also supported by the distribution of the sediment transport rates as given in Figure 39. Reliability of statements about mean bed properties could be reached with the help of statistically robust sample numbers: At least 60 scans per experimental scenario were conducted.

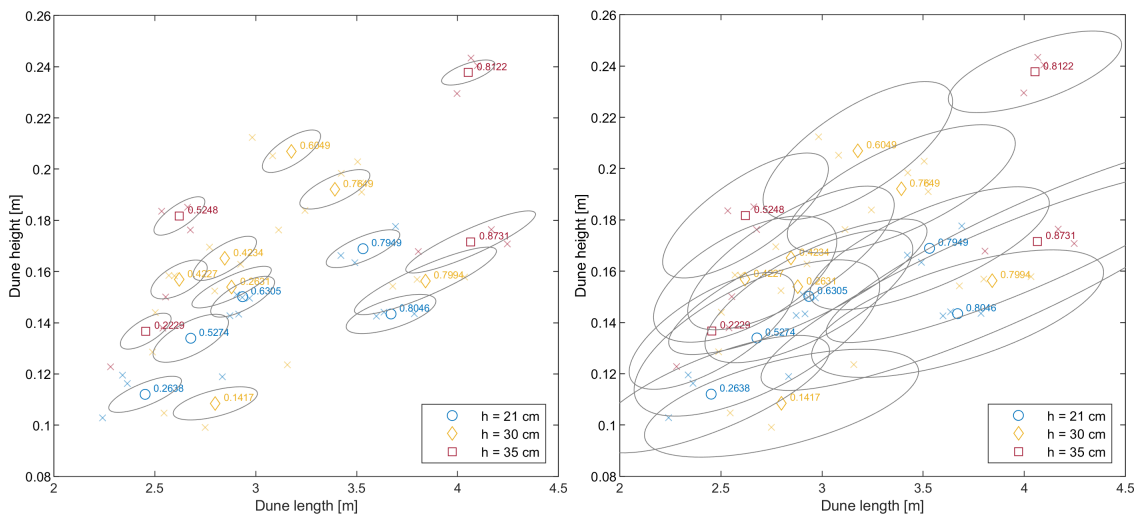


Figure 42: Comparing dune length with dune height, zero crossing threshold 15 cm: 1% error ellipses (left) and 10% error ellipses (right), distinguished by reference water depth; shear stresses as data labels

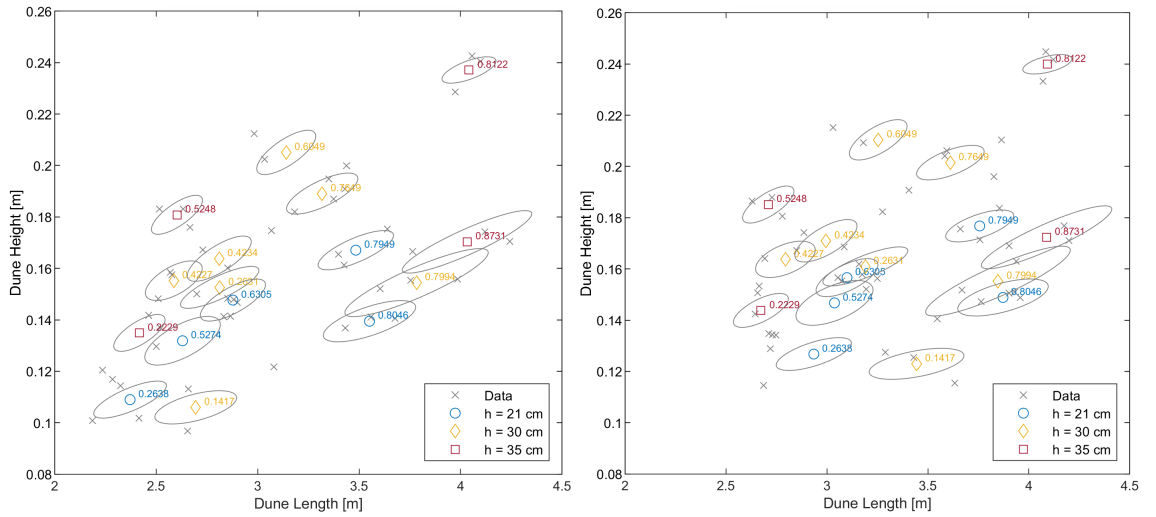


Figure 43: Comparing dune length with dune height, 1% error ellipses: zero crossing threshold 10 cm (left) and 35 cm (right), distinguished by reference water depth; shear stresses as data labels

Assuming this, it becomes clear already for the 10 % error ellipses (Figure 42, right) or from the PCA figures of the individual experiments (cf. Figure 34) that the range of variation of the bedforms in the conducted experiments was very large. This was, on the one hand, due to the freely evolving dunes in the experimental river reservoir and the online recirculation system, but also to some extent due to the chosen procedure of pooling all detected bedforms according to the previously described procedure on the other hand (cf. chapter 4.1.1.3). However, the introduction of a multi-layer model for bedforms would have further increased the complexity of the evaluation and the evaluation process applied in the following, which was supposed to be as straightforward as possible for an appropriate handling of the large amount of data, could not have been applied in the intended way.

To compare the effects of varying the zero crossing threshold to exclude small ripple-like structures from the analysis of longitudinal bed sections, Figure 43 shows the same plot as in Figure 42, left, but for those dune lengths and heights determined with zero crossing thresholds of 10 cm and 35 cm (see also Figure 32 and Figure 33). For a 10 cm threshold, there is almost no change in the derived means compared to the 15 cm threshold in Figure 42. For the 35 cm threshold, the overall distribution of data points appears more compact: while the points with large dune lengths and heights are nearly unchanged, those with smaller mean dimensions are shifted both to the right and upward. This shift is expected and is due to the way the threshold filter works: the larger the threshold, the larger a bed structure must be to be recognized as a dune, and the proportions of smaller bed structures are reduced accordingly. However, the distribution of data points does not change significantly in its structure, so that neighborhood relationships between points are preserved, with a few exceptions of small magnitude. Also, the following analyses and the findings derived from the dune lengths and heights do not change fundamentally, so that the aspect of varying threshold filters does not have to be considered further.

The three different initial water depths of the experiments, which were used as a reference for the different hydraulic boundary conditions, changed during the course of the experiments due to the moving bed with developing bed forms, while the amount of sediment in the reservoir was constant. Flow depth was calculated from the mean of the three gauges in the study area of the experimental reservoir (P_5, P_10, and P_15) and the mean bed elevation from the longitudinal bed sections. However, due to the three-dimensionality of the bedforms, the bed elevations in the longitudinal bed sections varied and so did the derived flow depth. This explains why the mean flow depth in Figure 44, left, varied within a range of 1 cm to 2 cm even in the same reference group, i.e., the experiments with the same initial water depth. In addition, the mean flow depths were slightly higher than the reference water depths in almost all cases, which can be attributed to the water surface gradient in the reservoir caused by the increased flow resistance due to bedforms.

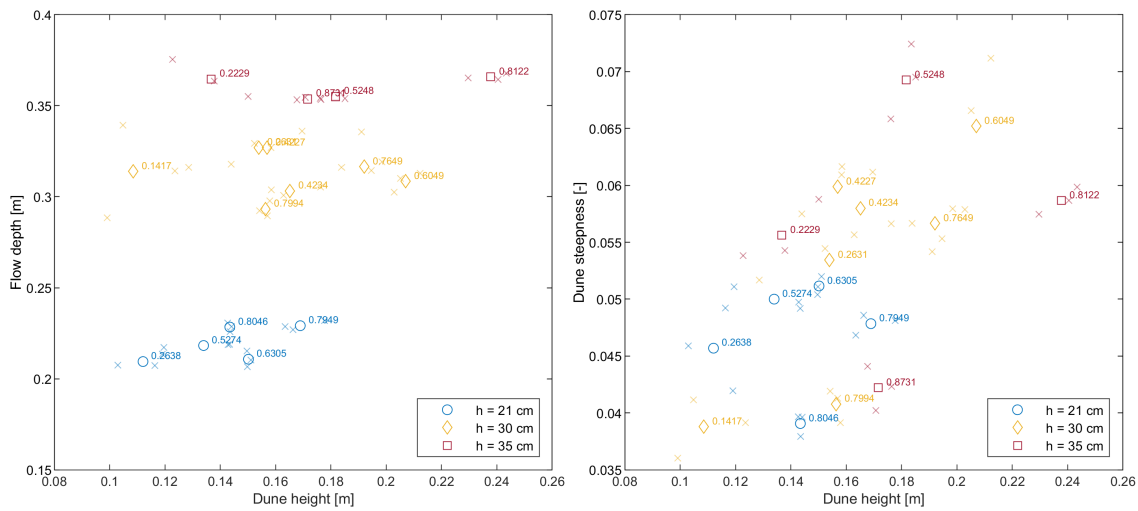


Figure 44: Comparing dune height with flow depth (left) and dune steepness Δ/λ (right), distinguished by reference water depth; shear stresses as data labels

Furthermore, it can be seen from the lighter colored data points representing the data from each longitudinal section, shown as crosses in Figure 44, left, that for the experiments with the lowest hydraulic stresses and apparently independent of flow depth, the data were more widely scattered than for higher hydraulic stresses. This may again be attributed to the higher three-dimensionality of the bedforms at lower hydraulic stress: The bedforms were smaller and the three-dimensionality could develop more easily in the reservoir than with larger bedform dimensions. Figure 44, right, shows the dune steepness Δ/λ compared to the dune height. A positive correlation can be seen that appears to have a linear characteristic, but the data points are relatively widely scattered, so a linear regression function does not provide a very good approximation. Equation (2-15) in chapter 2.2.2 yields values for Δ/λ in the range of 0.05 to 0.06 and is thus well represented in the data in Figure 44, right. Using the relative dune length $\lambda_{rel} = \lambda/h$, which relates the dune length to the prevailing mean flow depth in the reservoir during the experiments instead of the absolute dune length, makes

the positive correlation of dune height and length based on all data points as seen in the previous figures less evident and the data seem more evenly spread (Figure 45 left). However, when the data points are considered separately by initial water depth, positive correlations again become apparent for all water depths. R^2 , the ratio of the model variance and the total variance, and RMSE, the root mean squared error, are also shown as goodness-of-fit measures. Why the linear regression lines shown have different slopes is not clear, but can most likely be attributed to the rather small number of experiments per water depth. A further interpretation of these regressions would have only little additional significance and it is not pursued further.

When, in addition to the relative dune length λ_{rel} the relative dune height $\Delta_{rel} = \Delta/h$ is used, another effect becomes visible via the regression lines separated by initial water depth: the three regression lines very well approximate one underlying linear regression function (Figure 45 right). This shows for all experimental scenarios that mean dune heights grow linearly with mean dune lengths, if height and length are standardized by, and thus independent of, the flow depth. The comparison of Δ_{rel} with λ_{rel} can thus be used as an additional indicator for the dune shape next the dune steepness. This is an important finding for the characterization of dunes: a simple functional relationship between dune length and dune height can be derived, even if the dispersion of the individual data points around the regression line represents a non-negligible residual uncertainty.

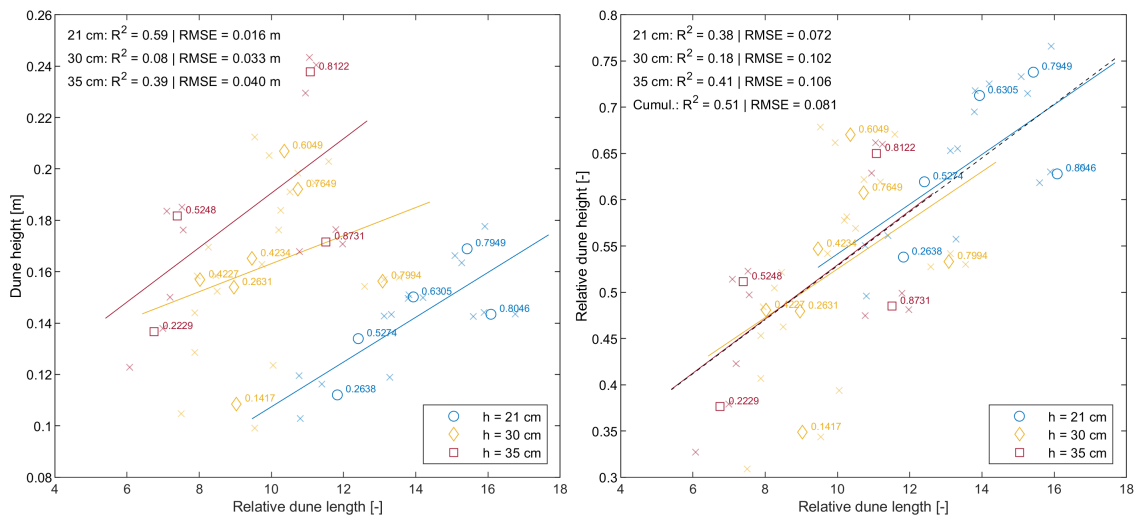


Figure 45: Comparing relative dune length with dune height (left) and relative dune height (right), distinguished by reference water depth; shear stresses as data labels

Notwithstanding what was previously discussed, there also is, to some extent, disagreement with the approach $\Delta_{rel} \leq 1/6$ given in chapter 2.2.2 for natural sediments, because the dune height does not grow linearly with the flow depth, but with a decreasing trend for higher flow depths. Also, in the present data, values for Δ_{rel} are range from 0.35 to 0.74 and according to this are about 2 to 4.5 time higher. Figure 45, right, visualizes this: the data

points for the lowest water depth $h = 21$ cm are separated from the data points for the two larger water depths, and the largest relative dune heights and lengths are shown for the lowest water depth. Relative dunes were thus larger at lower flow depths with otherwise fairly constant dune shape, even though, in absolute terms, bed shear stresses (as can be seen from the numerical data labels) were in the range of the other data. For these two data sets with higher flow depths further differentiation would not be meaningful because the differences of relative dune sizes are too small. Figure 46 illustrates this relationship: the greater the flow depth, the smaller the relative dune lengths and heights tend to be. The regression lines do not represent true correlations and are only used for better illustration, since in this case the dune length or dune height is represented on both axes and was only factorized using constant flow depths.

This phenomenon seems counterintuitive at first sight, but can be explained by the velocity distribution over the flow depth: At comparable mean flow velocity, a lower flow depth results in a velocity profile with larger gradients, or the velocity in the flow direction increases faster from the bed to the water surface than at a higher flow depth. A sediment grain thus moves more quickly from the bed to areas of the water column with increased transport capacity, and more sediment transport occurs as a result. The higher transport velocities above the bed in turn favor the development of stronger turbulence in the lee area of dunes, which leads to a stronger local deepening of the bed in the dune troughs and, at the same time, higher growth of the dune crests due to stronger backflow at the lee front (see also Figure 8 and Figure 9 for comparison). This topic will also be discussed further in the following chapter.

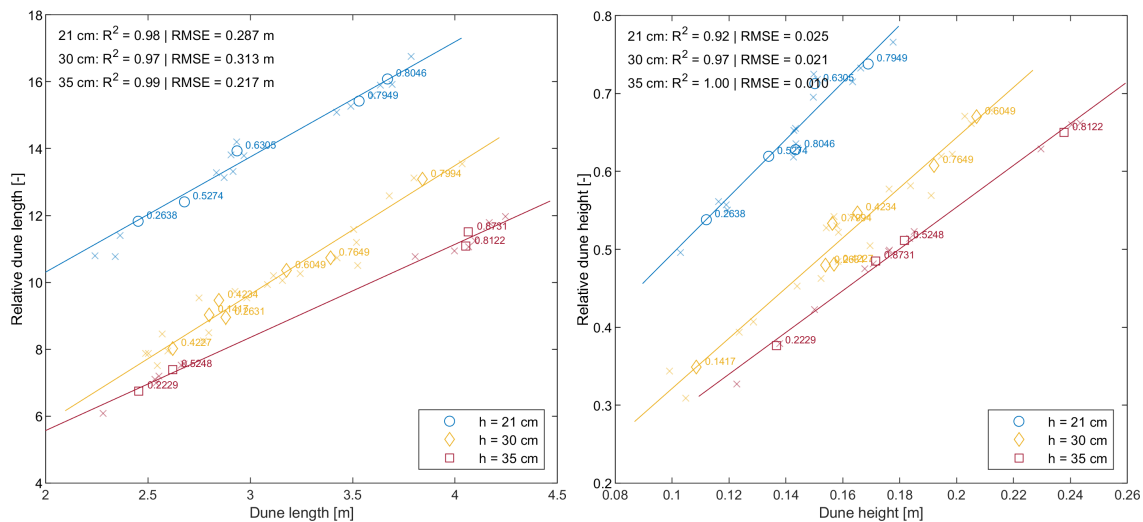


Figure 46: Comparing dune length with relative dune length (left) and dune height with relative dune height (right), distinguished by reference water depth; shear stresses as data labels

Apart from their relevance to the dune evolution process, the visibility of these described correlations in the derived data points can be seen as an indication of the successful

fulfilment of the high requirements for the execution of the experiments and the quality of the measured data as well as the applied methods of data evaluation, which was described in chapter 3. The statistical analyses of the reservoir beds in dynamic equilibrium, which quantifiably show underlying relationships to the bed development here, would have been less meaningful with lower quality data or maybe not even visible. This also supports the assumptions made in chapter 4.1.1.3 for the design of the bedform identification process.

4.2.2. Hydraulic parameters

Hydraulic parameters generally do not describe the bed, but the fluid surrounding it. In the morphological sense, however, these hydraulic parameters determine the condition of the bed decisively due to the permanent interaction between bed and moving fluid. Therefore, to classify the dune dimension in the flow, shear stresses were already used in the previous section to characterize the mean values of the data points. In the following, the hydraulic properties of the flow and its influence on the bed are analyzed in more detail.

Figure 47, left, plots the mean flow velocity u against a parameter referred to as mean flow intensity $\theta_u = u/u_c$ in the following as a multiple of the critical flow velocity u_c , which characterizes the initiation of bed movement. A functional relationship for the initiation of motion of the reservoir bed made from polystyrene granules had been empirically identified for the investigated flow depths h with $u_c = 8.48 \times 10^{-4} h + 7.907 \times 10^{-2}$ in [m/s].

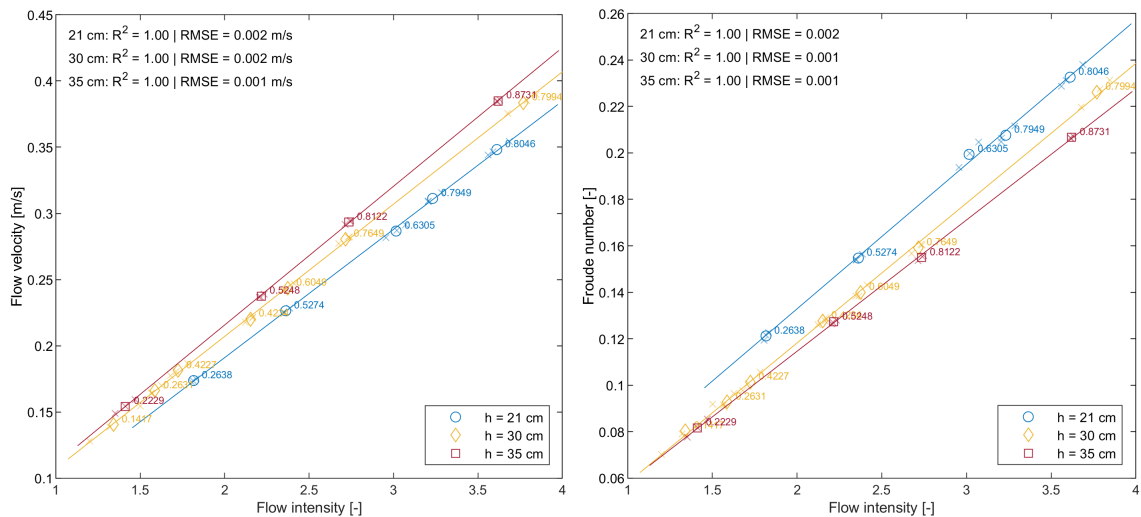


Figure 47: Comparing flow intensity with flow velocity (left) and Froude number (right), distinguished by reference water depth; shear stresses as data labels

Looking at the colored mean values separately by flow depth, it is easy to see that flow depth has little effect on the relation between flow velocity and mean flow intensity: the regression lines are approximately parallel or diverge only by very small angles, and they also lie close together. Their slightly different slopes are due to the only small increase in the critical flow

velocity for the initiation of motion with flow depth. A deeper analysis of these small differences between flow velocity and flow intensity showed no significant influence on other parameters. Since the mean flow intensity is a better comparative parameter because it is dimensionless, it will be used primarily in the following analyses. As an indicator of the variability of hydraulic stress across all experiments, the Froude number is plotted versus mean flow intensity in Figure 47, right. Overall, only low Froude numbers were present. However, due to the low density of the sediment, the Froude numbers alone are not sufficient to provide information about the morphodynamic processes at the bed.

Figure 48 shows what was already visible in figures of the previous chapter by using the shear stress values to label the plotted data points: the dune length correlates positively with the mean flow intensity (and thus also the flow velocity) and an approximately linear correlation can be seen for all data points; when considered individually by flow depth, stronger fluctuations occur, which are especially striking for the highest initial water depth (red data points). For the relative dune length (Figure 48 right), the previously observed gradation by flow depth (e.g., in Figure 44 and Figure 46) is evident regardless of the one red data point that is a bit out of line: For the same mean flow intensities larger relative dune lengths are present for smaller flow depths.

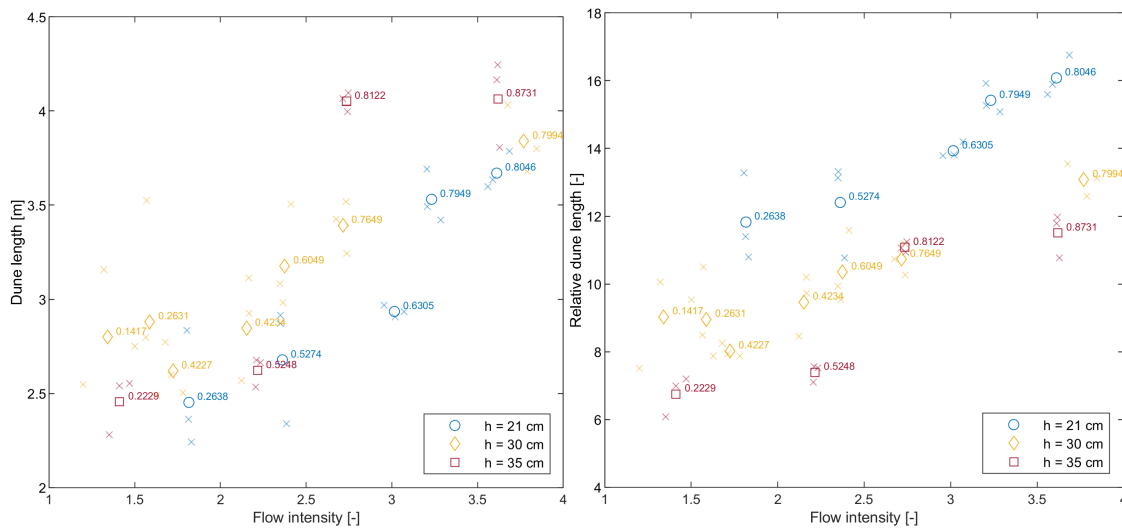


Figure 48: Comparing flow intensity with dune length (left) and relative dune length (right), distinguished by reference water depth; shear stresses as data labels

However, this observation cannot be directly transferred to the dune heights (Figure 49): At a certain mean flow intensity, which depends on the prevailing flow depth, there is a sudden reduction of the dune heights, which were positively correlated with the mean flow intensity up to this point. This process is particularly evident in the relative dune heights (Figure 49 right): for each of the three initial water depths, the data point with the highest mean flow intensity has a significantly lower relative dune height than the next-lowest mean flow intensity.

This sharp bend in the course of the data can be traced back to the beginning transition of the bed to the upper flow regime: the existing bedforms grew in length and height with increasing discharge or mean flow intensity until the point where the shear stresses grew so high that no further height growth was possible. The downstream forces of the flow outweighed the resisting forces of the bed due to turbulence patterns in the flow and backflow effects in the lee areas of the dunes (cf. chapter 2.2) and as a result, washing out of the bedforms began. This process changed the shape of the bedforms, elongated them, and would have resulted in the bed surface becoming mostly flat again if the hydraulic stress had increased further and the sediment volume in the reservoir had not been constant and hence too low for these conditions. However, such high discharge conditions could also not have been investigated in the test facility because of limited sediment recirculation capacity.

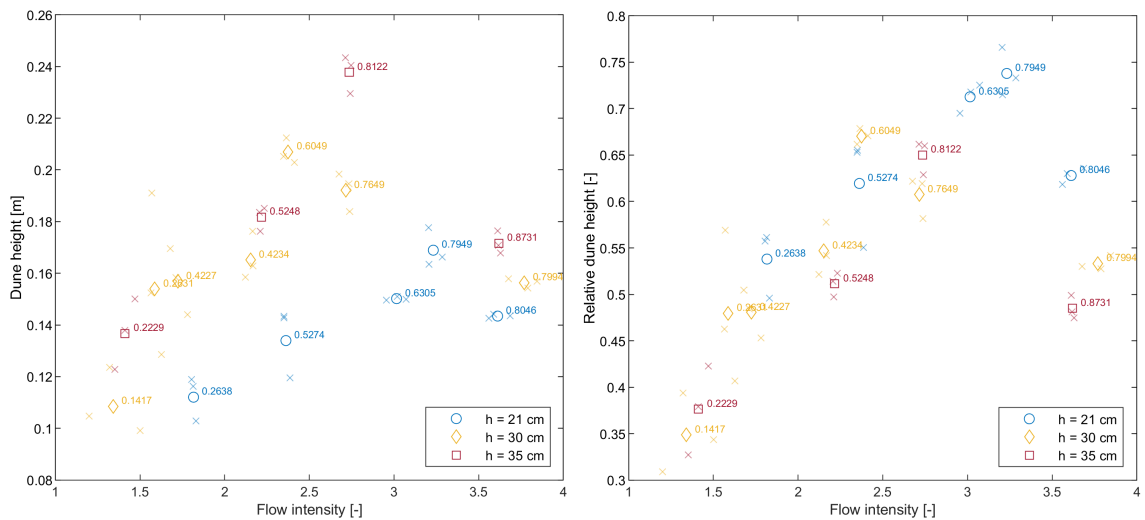


Figure 49: Comparing flow intensity with dune height (left) and relative dune height (right), distinguished by reference water depth; shear stresses as data labels

Using the dune steepness Δ/λ , the described process becomes visible at an earlier stage in Figure 50, left. While for low to medium mean flow intensities an increase of Δ/λ takes place, i.e. the dune height grew more than the dune length, this process reverses visibly as soon as a certain threshold is exceeded, which also depends on the flow depth. In other words, for low flow depths, dunes grew longer before being washed out, but were generally more elongated and not as high in relation as for large flow depths (thus have smaller values of Δ/λ). For the greatest initial water depth, the highest dunes were formed in absolute terms at comparable mean flow intensities, and they were also relatively shorter or more compressed. For high mean flow intensities, however, these differences of Δ/λ balance out again and an approximately linear decrease of Δ/λ takes place, apparently independent of the flow depth and the initial water depth, respectively. Figure 50, right, shows the dune steepness compared to the flow velocity. It is evident here, that there are only few differences to the mean flow intensity, which is more straightforward for analyses however.

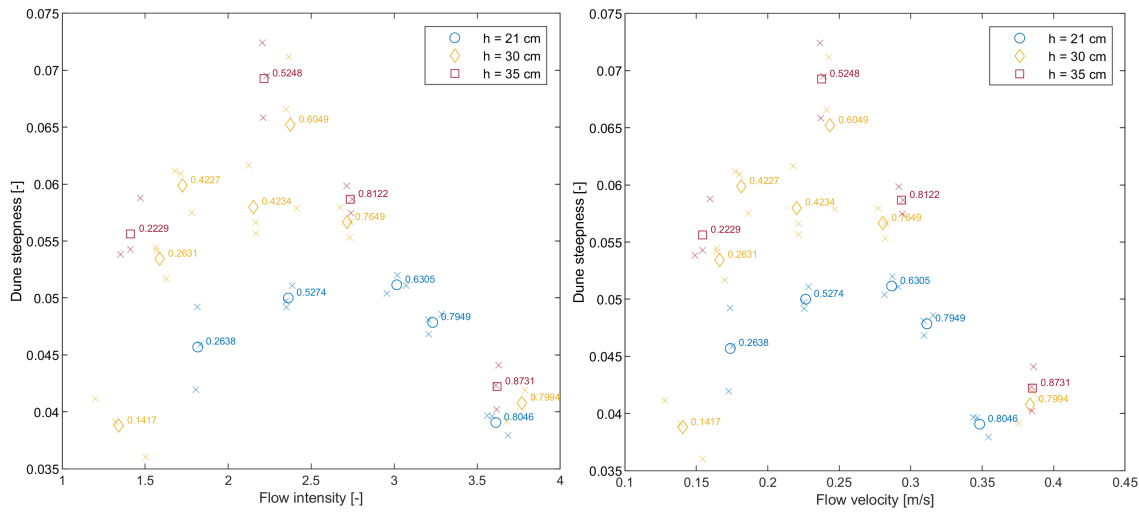


Figure 50: Comparing flow intensity (left) and flow velocity (right) with dune steepness Δ/λ , distinguished by reference water depth; shear stresses as data labels

Following the previous reasoning, Figure 51, left, shows how the longitudinal water surface gradient relates to the relative dune length: At low water surface gradients due to low energy losses from low bed roughness (and thus low shear stresses), lower flow depths resulted in greater relative dune lengths, with otherwise the same water surface gradient. However, with increasing hydraulic stress and correspondingly increasing water surface gradients, this difference visibly disappears. This process can be explained on the basis of the velocity distribution across the flow depth and the changing boundary layer thickness: At high mean flow velocities, the transport capacity of the flow in the immediate vicinity of the bed is high even at great flow depths and the influence of different velocity gradients across the flow depth on sediment transport becomes secondary. Also, for the lowest flow depths, the highest water surface gradients were present. This is due to the relatively higher influence of the bed form roughness on the flow field, resulting in increased flow resistance. For in-depth information on boundary layer theory, refer to the literature, e.g. Kundu and Cohen (2002), Gyr and Hoyer (2006) or Dey (2014).

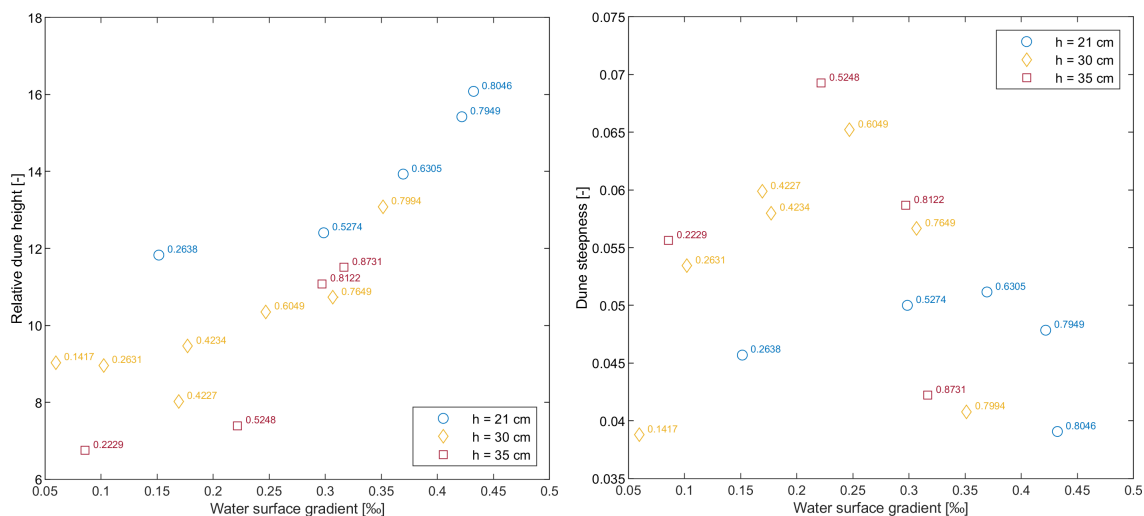


Figure 51: Comparing water surface gradient with relative dune length (left) and dune steepness Δ/λ (right), distinguished by reference water depth; shear stresses as data labels

Figure 51, right, also shows, with respect to the water surface gradient, what was described in Figure 50, left, as a function of mean flow intensity: Bedforms become elongated for high flow velocities, but they remain stable for a longer time, when the flow depth is lower. When analyzing the mean shear stresses, a less clear picture emerges (Figure 52, left). Similar to Figure 49 on the right, the course of the data of the relative dune heights also make a sharp bend at a certain shear stress, but the data points with the largest shear stresses, which already show smaller relative dune heights, are much closer to the data points with the next-smallest shear stress (before the bend) than was the case for the mean flow intensities.

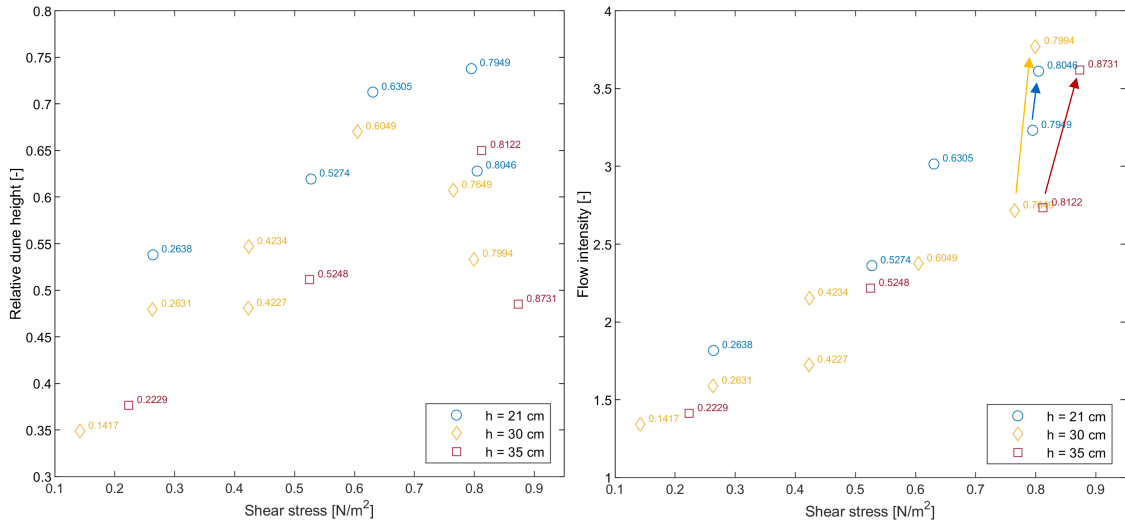


Figure 52: Comparing shear stress with relative dune height (left) and flow intensity (right), distinguished by reference water depth

Figure 52 on the right provides the reason for this: The relation of mean shear stress to mean flow intensity is not continuous. The data points with the highest shear stresses show abruptly higher flow intensities, although the shear stresses are only slightly higher than at the data points with the next-lower shear stresses. Thus, while hydraulic stress increases sharply, in the form of higher discharges and thus higher flow velocities and flow intensities, the calculated mean shear stress changes only marginally. It can be deduced that with the beginning washout of the bedforms in the transition zone to the upper flow regime, the mean bed shear stress as a parameter does not represent the events at the bed well.

The reason for this can be found in the calculation of the bed shear stress from bed slope with $\tau = \rho g h S$. Next to the flow depth, only the bed slope S remains as the only real variable (ρ and g are assumed to be constant). Because normal depth conditions prevailed in all experiments, S could be substituted by the energy gradient I , which is assumed to be equal to the longitudinal water surface gradient I_w . In Figure 53, left, the regression lines separated by initial water depth approximate the data points very well and the enormous transformation processes at the bed starting from shear stresses around 0.8 N/m² do not visibly affect the mean longitudinal water surface gradient, which is why they are not represented in the shear stress.

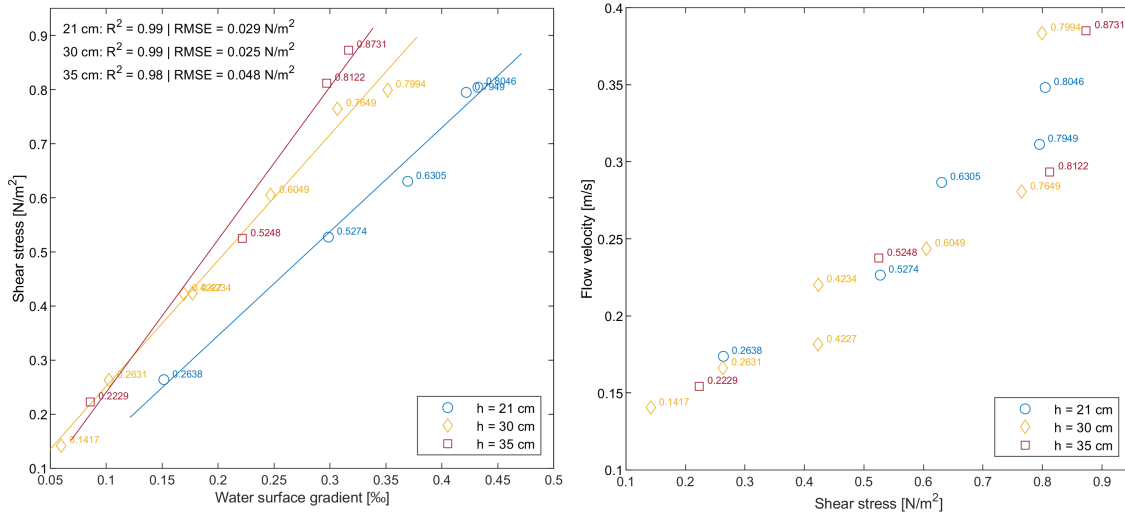


Figure 53: Comparing water surface gradient (left) and flow velocity (right) with bed shear stress, distinguished by reference water depth

This finding in the presented data is, to some extent, contradictory to the assumed course of bed shear stress along the flow regime as given in Figure 7 and in the literature. Figure 53, right, shows the shear stress compared to flow velocity and instead of the expected decline of the bed shear stress with beginning transition to the upper plane bed only a horizontal convergence of the shear stress is visible. This can be due to the, in absolute terms, distinctively lower flow resistance of the lightweight sediment as compared to sand or to the fact that the transition to the upper plane bed was not reached. This, however, does not seem probable given the distinct changes of the courses of parameters presented in the previous figures, e.g. Figure 50 or Figure 52.

Figure 54, left, can be used to support the considerations made. The mean sediment transport rate q_s increases very strongly with increasing mean bed shear stress. At shear stresses around $0.8 N/m^2$, the transport rate increases abruptly, which emphasizes the previously given explanations of the strong transformation of the bed during the transition to the upper flow regime. The bed as a whole is in a large-scale transformation and hardly resists the further increasing hydraulic stress anymore, which is why the mean longitudinal water surface gradients hardly increase any further. In Figure 54, right, however, this abrupt increase is not visible: the sediment transport rate increases rather continuously with flow intensity, even if an increasing tendency for high flow intensities can be detected. Conclusions about the transport state of the bed can thus be better drawn from the flow intensity in the present cases. The flow intensity reflects changes in the sediment transport rate more precisely and remains continuous, especially under high hydraulic stresses.

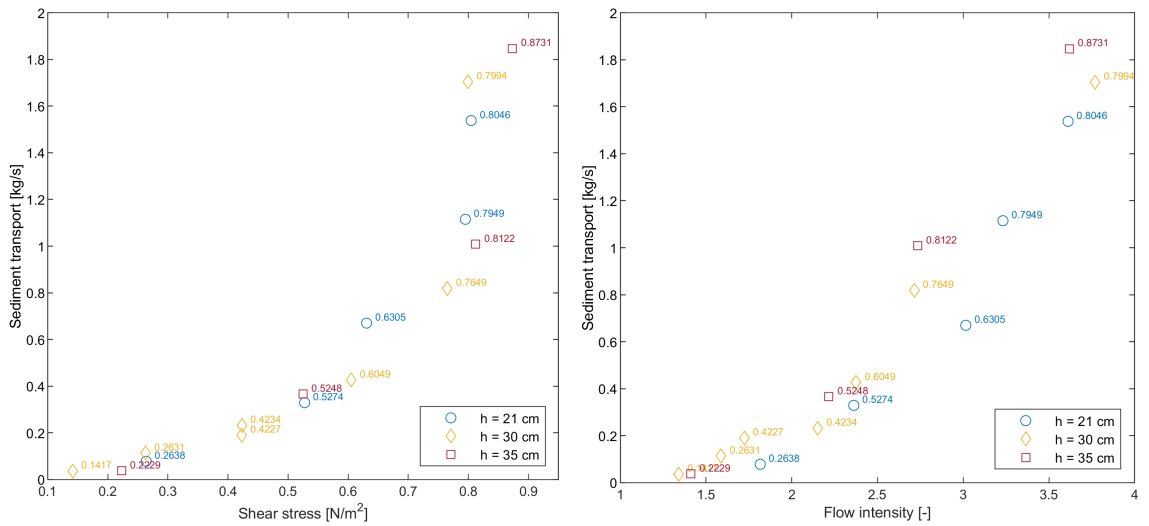


Figure 54: Comparing shear stress (left) and flow intensity (right) with sediment transport rate, distinguished by reference water depth; shear stresses as data labels

4.2.3. Morphological parameters

Morphological parameters are used to describe the processes at the bed and its properties. The main parameters in the following analyses are the migration velocity of the bedforms u_D , referred to as dune velocity, the shear velocity u_* and the shear Reynolds number Re_* .

In Figure 55, the dune velocity is compared with the relative dune length and the relative dune height. As in the previous chapters, the observed gradation by flow depth is particularly evident for the relative dune lengths. One data point from the experiments with the largest flow depth interrupts this gradation in Figure 55, left (as already visible in Figure 48, right), but it cannot be determined exactly whether this data point is an outlier. The data points for other parameters that were also part of this experiment were not identified as outliers in the previous evaluations, so the experiment as a whole was not found to be in error and had to be excluded from the evaluation. It is likely that the relative dune length was slightly biased by the presence of a very large dune upstream of the weir during the data evaluation period, which would also explain the slightly excessive sediment transport rate in parts seen in Figure 54, right.

However, comparative analysis of the ceiling camera photos and all laser scans did not fully explain this increase because many dunes migrated through the surveyed reservoir section within the bed survey period and were recorded by the sediment transport measurement. Instead, it is noticeable that at the same flow intensity in Figure 54, right, the yellow point of the experimental group with 30 cm initial water depth also appears somewhat too high. Thus, it appears that there may be a morphodynamic process leading to increased dune length and sediment transport values shortly before the transition to the upper plane bed, but this cannot be answered with certainty based on the available data. Furthermore, the

comparison of dune velocity with the relative dune heights in Figure 55, right the red data point marked "0.8122" (mean shear stress in N/m^2) does not appear to be an outlier. Regardless of these considerations for a single data point, the steep reduction in dune height at high dune velocities due to high hydraulic stress is again evident for all flow depths.

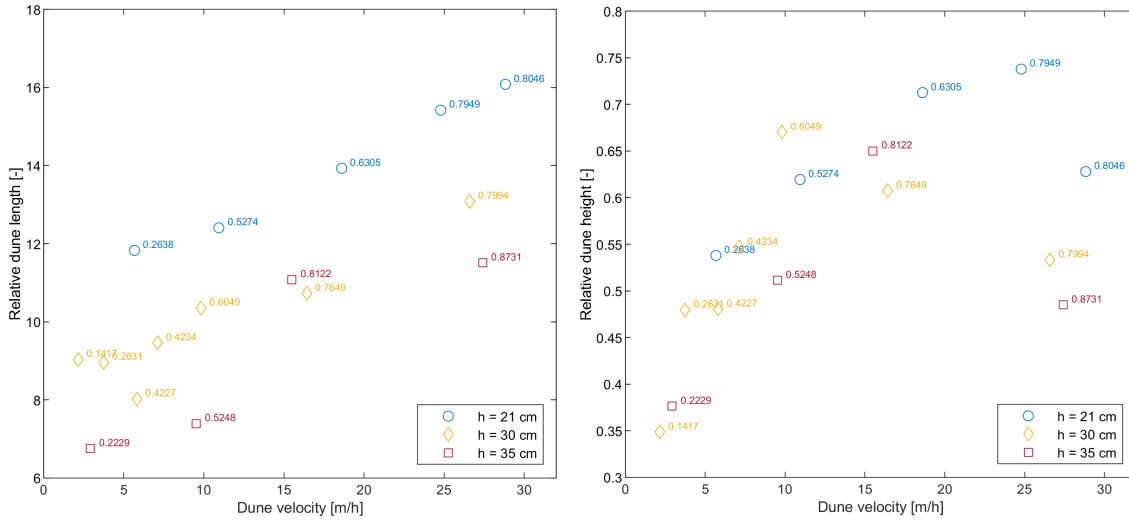


Figure 55: Comparing dune velocity with relative dune length (left) and relative dune height (right), distinguished by reference water depth; shear stresses as data labels

Comparing the dune velocity with the dune steepness in Figure 56, left, shows for the dune velocity what has already been observed for the mean flow intensity in Figure 50, left. For low to medium dune velocities, the dune height increases more than the dune length and this effect increases with the flow depth. As dune velocity continues to increase, this growth in dune height is reversed above a threshold value of dune velocity that varies with the prevailing flow depth. Also, the almost linear decrease of Δ/λ , which is largely independent of the flow depth, can then be observed, so that a strong correlation between dune velocity and flow intensity can be assumed.

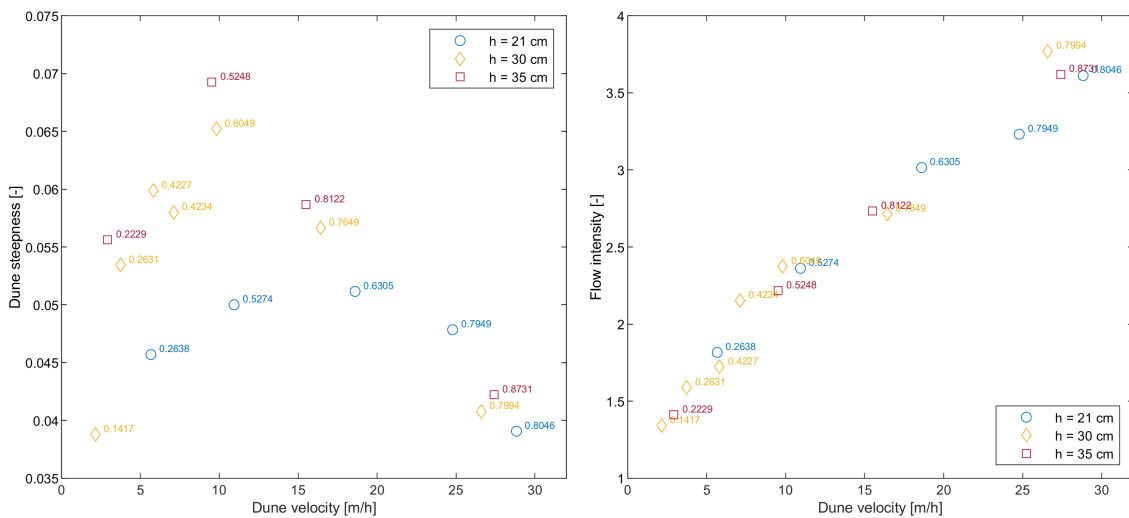


Figure 56: Comparing dune velocity with dune height to length relation Δ/λ (left) and flow intensity (right), distinguished by reference water depth; shear stresses as data labels

To verify this assumption, dune velocity is compared with flow intensity in Figure 56, right and there is a clear positive correlation with a slightly decreasing trend: dune velocity consequently increases more strongly with increasing flow intensity, but this increase is rather continuous and much less abrupt than, e.g., the change of dune heights during the transition to the upper flow regime in the previous chapter or the change of dune steepness versus dune velocity in Figure 56, left. Besides, there is no dependence on flow depth visible when the mean flow intensity is used in Figure 56, right, which is favorable for deriving a generally valid functional relationship. Furthermore, this high correlation explains the high similarity of the two plots in Figure 55 to those in Figure 48 on the right and Figure 49 on the right, in which mean flow intensity was used on the abscissa instead of dune velocity.

If the dune velocity u_D is compared with the relative dune velocity $u_{D,rel} = u_D/u$ (Figure 57, left), which is standardized with the prevailing mean flow velocity u , the distribution of the data points is similar to that in Figure 56 right. The relative dune velocity describes the dune velocity as a multiple of the flow velocity and it increases more slowly with increasing dune velocity. Conversely, the flow velocity, which is in the denominator of the relative dune velocity, increases more than the dune velocity. This proportionality was not apparent in Figure 56, right. There, the hydraulic stress in the form of mean flow intensity is plotted on the ordinate, with flow velocity in the numerator, and yet there is a comparable trend. The reason for this can be found in Figure 57, right: Although the relative dune velocity is approximately linearly correlated with the mean flow intensity, it grows at a much slower rate. This can hardly be seen in Figure 57 on the left by the smaller curvature of the curve of the data points than in Figure 56 on the right, which would correspond to a relatively smaller increase of the dune velocity. The relative dune velocity therefore serves as a comparative parameter for the relation between dune velocity and mean flow intensity.

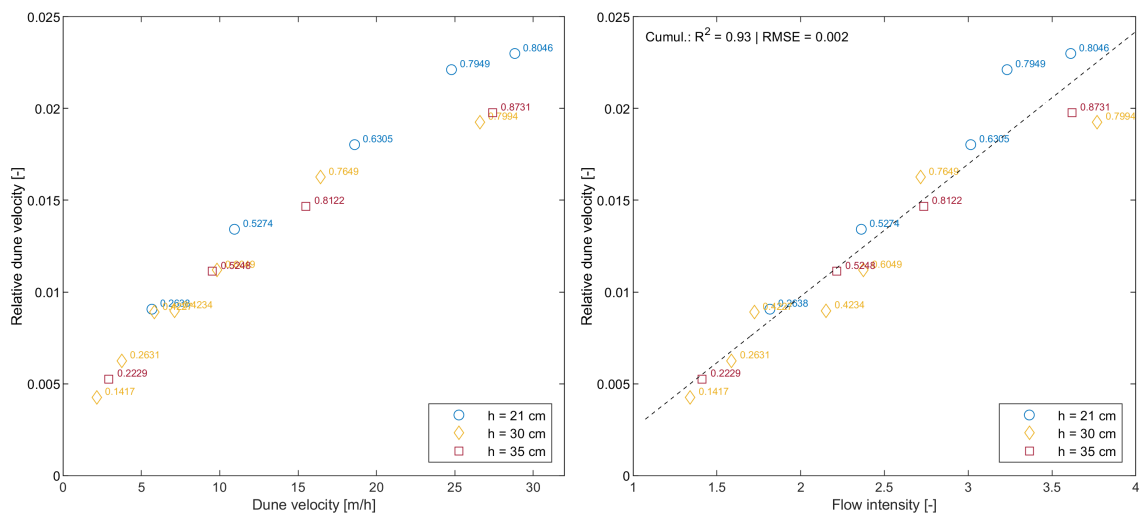


Figure 57: Comparing dune velocity with relative dune velocity (left) and relative dune velocity with flow intensity (right), distinguished by reference water depth; shear stresses as data labels

It should be noted that no further conclusions should be drawn from Figure 57, left, since dune velocity and relative dune velocity are dependent variables and the chosen diagram only served to better illustrate the correlation between flow intensity and relative dune velocity. Besides that, Figure 57, right, shows something else: The influence of the flow depth is also small there, which is why the positive, almost linear correlation of all data points allows to determine first the relative and then the absolute dune velocity via the linear relation shown when the initiation of motion of the bed and the flow velocity are known. Whether this simple factorization has general validity, however, would have to be validated on the basis of further measurement data on dune migration processes.

The sediment transport rate can also be determined from the dune velocity. Figure 58, left shows a stronger, largely homogeneous increase of the sediment transport rate with increasing dune velocity, which seems to follow an exponential curve. Abrupt effects at the beginning of the transition to the upper flow regime are not visible here and the large-scale bed transformations do not affect the transport rate with equally strong fluctuations. However, the flow depth can no longer be neglected when determining the transport rate from the dune velocity: lower flow depths lead to lower sediment transport rates at the same dune velocities. This dependence was not quite so clearly visible in Figure 54, right, even though it can be assumed to be present there, too. Using the relative dune velocity instead, does not really make a difference in this context (Figure 58, right).

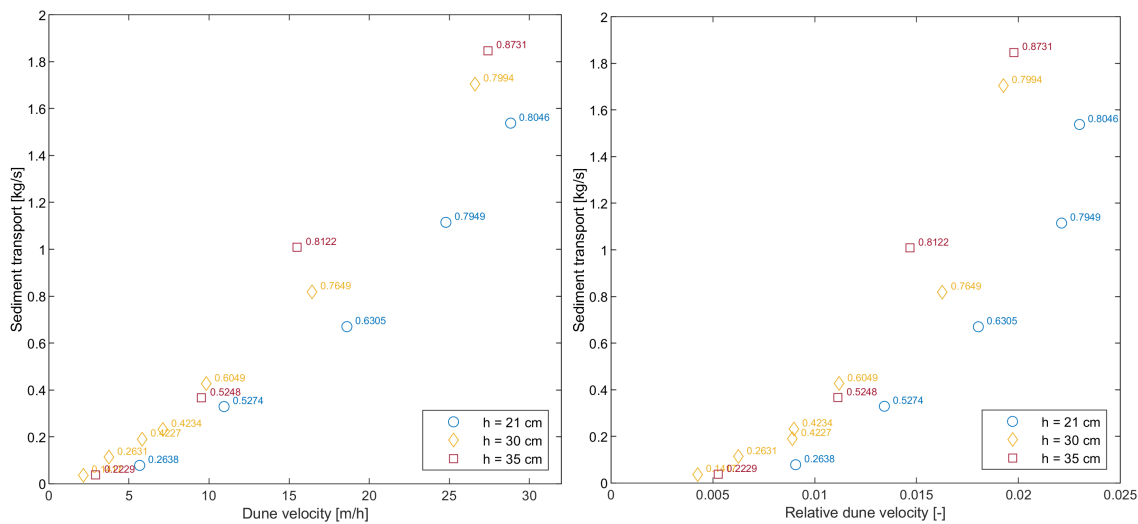


Figure 58: Comparing dune velocity (left) and relative dune velocity (right) with sediment transport, distinguished by reference water depth; shear stresses as data labels

At this point, it should be clearly pointed out that all statements made in this chapter are based on data points that were subjected to a multi-step averaging process in order to reduce the complexity of the actually highly dynamic transport processes and their interaction with the flow to such an extent that they can be analyzed in the selected form of two-dimensional diagrams. Therefore, it cannot be completely ruled out that statements

such as the evaluation of dune velocity and flow intensity for the determination of the sediment transport rate have too low statistical significance, because the absolute differences of the parameter curves are small in some cases. Compared to the relationship shown in Figure 54, left, for the shear stress and the sediment transport rate, where an abrupt increase of the sediment transport rate occurs at shear stress threshold values that are also dependent on the flow depth, the representations in Figure 57 and Figure 58 are, however, quite meaningful and suitable to support the assumptions made before.

In addition to these non-dimensionless diagrams, which are primarily directly applicable to the present investigation and very helpful to gain a better understanding of the governing processes, dimensionless parameters frequently used in the literature will be considered in the following and set in relation to the results obtained so far. Their use allows a classification of the generated measurement data in a larger context, but reduces their direct informative value for the hydraulic and morphological processes which are in fact taking place. In addition, only one bed material was used in the present investigation, which was also uniformly-graded, and the ambient conditions of the experiments were kept constant. Any temperature-related fluctuations in fluid viscosity, surface tension or material densities were considered negligible within the measurement uncertainty of the experiments and compared to the strong averaging of the measured data as described earlier.

When comparing the shear velocity with the shear stress and the flow intensity, it can be seen that the curves of the data points are similar (Figure 59, left). Both data sets were approximated with regression functions and both shear stress and flow intensity increase more strongly with increasing shear velocity. The differences between shear stress and flow intensity at high hydraulic stress, which were discussed in the previous analyses, are no longer obvious (e.g. Figure 52, right). However, the flow intensity varies strongly in comparison with the shear stress. Figure 59, right, shows the linear relations of shear velocity u_* and shear Reynolds number Re_* as well as the shear Froude number Fr_* , which result from the above-mentioned constant conditions of all components required for the calculation of the respective parameters. In Figure 59, left, the curves of the data points do not change when Re_* or Fr_* are on the abscissa accordingly.

In Figure 60, left, Re_* is compared with the dimensionless shear stress τ^* and the dimensionless transport rate q^* , which has the same curve as the non-dimensionless volumetric transport rate q_s in [kg/s] and is calculated as

$$q^* = \frac{q_s}{b\rho_s\sqrt{g\rho'd_m^3}} \quad (4.22)$$

b ... Movable bed width (at beginning of experiment) [m]

Re_* , as well as u_* and Fr_* behave towards τ^* in the same way as towards the shear stress τ and since Re_* and τ^* are both calculated based on the values of τ , their dependency is well visible. The dimensionless transport rate q^* follows a different curve and increases much more strongly above a certain shear velocity threshold. This increase of the transport rate was already described in Figure 53, right, compared to the shear stress and attributed to the reduced flow resistance with strong movement of the bed.

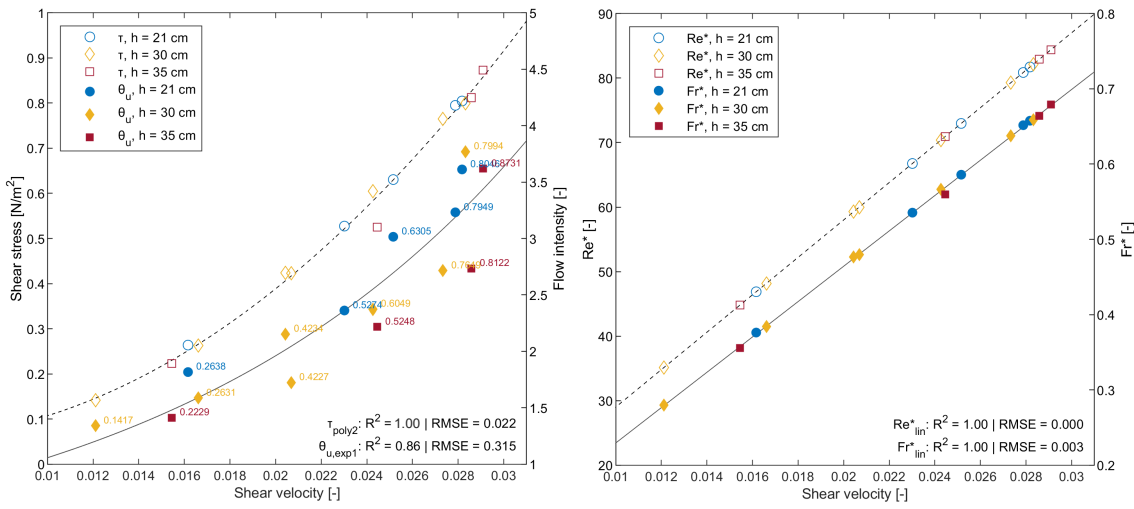


Figure 59: Comparing shear velocity with shear stress and flow intensity (left) as well as with shear Reynolds number and shear Froude number (right)

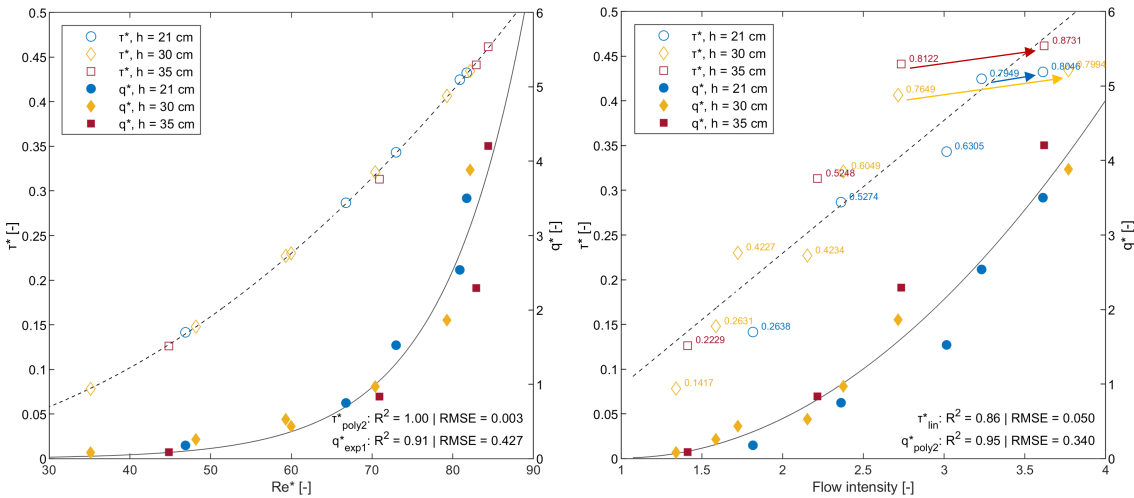


Figure 60: Comparing shear velocity with dimensionless shear stress and dimensionless sediment transport rate (left) as well as sedimentological Reynolds number with dimensionless Shields stress and dimensionless sediment transport rate (right); shear stresses as data labels

Replacing Re_* with the mean flow intensity θ_u on the abscissa in Figure 60, right, the same relationship becomes visible between mean flow intensity and dimensionless shear stress as was already shown in Figure 52 on the right for the flow intensity and the dimensionless

shear stress. Again, the strong abrupt increase in mean flow intensity from a threshold value for the (dimensionless) shear stress when analyzed as a function of flow depth is clearly visible. However, when all data points are analyzed together, an approximately linear relationship can be deduced and the significance of the linear regression is in fact high, thereby highlighting the subtlety of the morphodynamic processes analyzed and how easily they can be overlooked by an inappropriate analysis method. For the curve of the mean flow intensity versus the dimensionless sediment transport rate q^* , the direct relation to the curve of the mean flow intensity and non-dimensionless sediment transport rate q_s shown in Figure 54, right, is clearly visible and the dependence on the flow depth is apparent.

From the previous considerations, it became apparent how challenging the interpretation of the results is, how strongly the fluctuations of individual data points affect possible conclusions, and how easily existing data correlations can be ignored by too simple approximation functions (Figure 60, right, both curves).

4.2.4. Transport functions for sediment transport

The sediment transport rate measurement data can be used to test existing sediment transport functions for their suitability for the polystyrene lightweight sediment used in the experiments. The transport functions, most of which have been obtained at least in part empirically in laboratory and field experiments, have been described in detail many times, among others in Graf (1971), Zanke (1982), Garcia (2008), and Dey (2014). Their application requires not only an understanding of the theoretical principles of the underlying transport processes, but also a great deal of experience in their interpretation, because in most cases the input values are already subject to uncertainties (Patt and Gonsowski 2011). There are different formulas for the separate calculation of bedload and suspended sediment transport as well as their combination as total transport. Depending on sediment properties and flow conditions, the ranges of validity of the different formulas also vary.

Frequently used in engineering practice are the approach according to Meyer-Peter and Müller (1948) for coarser sand and gravel, which has also proven useful for finer sands (cf. Soulsby (1997)), the approach according to Van Rijn (1984a) for sands and bedforms, and the approach according to Engelund and Hansen (1967) as an estimate for the total transport. These approaches are therefore also used for the following analysis. Since the Meyer-Peter and Müller approach tends to overestimate the actual sediment transport, an additional modification of this approach is used according to Wong and Parker (2006). The different approaches have also been widely used in numerical studies, for example Van Rijn

(1984a) in R  ther (2006), Engelund and Hansen (1967) in Goll (2017) and Meyer-Peter and M  ller (1948) and the modification of Wong and Parker (2006) in Mendoza et al. (2017).

The dimensionless sediment transport rates q^* according to these four transport functions are given in the following.

1. Meyer-Peter and M  ller (1948) relation for bedload:

$$q_b^* = 8(\tau^* - \tau_c^*)^{1.5}, \text{ with } \tau_c^* = 0.047 \quad (4.23)$$

2. Meyer-Peter and M  ller relation for bedload, modified after Wong and Parker (2006):

$$q_b^* = 4.93(\tau^* - \tau_c^*)^{1.6}, \text{ with } \tau_c^* = 0.047 \quad (4.24)$$

3. Van Rijn (1984a) relation for bedload:

$$q_b^* = 0.053 \frac{T^{2.1}}{D_*^{0.3}} \quad (4.25)$$

$$T = \frac{\tau_s^* - \tau_c^*}{\tau_c^*} \quad (4.26)$$

T ... Transport stage parameter [-]

τ_s^* ... Dimensionless bed shear stress due to grain friction [-]

4. Engelund and Hansen (1967) relation for total transport:

$$q_t^* = \frac{1}{C_f} 0.05 \tau^{*2.5} \quad (4.27)$$

$$C_f = \left(2.5 \ln \left(11 \frac{R_h}{k_S} \right) \right)^{-2}, \text{ with } k_S = [2, 2.5] d_{50} \quad (4.28)$$

C_f ... Flow resistance, total [-]

Figure 61 compares the calculated values q_m^* from the measured sediment transport rates of the experiments with the results of the selected transport functions and shows power functions of the type ax^b for least squares fitting of the data points. For all four transport functions, the expected positive correlation of the calculated values with the measured values is visible, but all of them show a decreasing tendency for larger values. For transport functions 1, 2 and 4, the impression is that the calculated values even converge towards a maximum value for high measured transport rates. The results of transport functions 2 and 4 are relatively close to each other, but agree with the measured data the least. Only for very low sediment transport rates, agreement is visible, but for increasing sediment transport

rates they significantly underestimate the experimental data. Transport function 1, the original transport function according to Meyer-Peter and Müller (1948), agrees better with the measured data on average and even overestimates them slightly for low sediment transport rates. For higher values from around 1, the course of the fit function falls into a clear underestimation of the measured sediment transport rates. Since transport function 2 is only a moderate factorization of transport function 1 in the mathematical sense and because it shows worse results, it will not be discussed further.

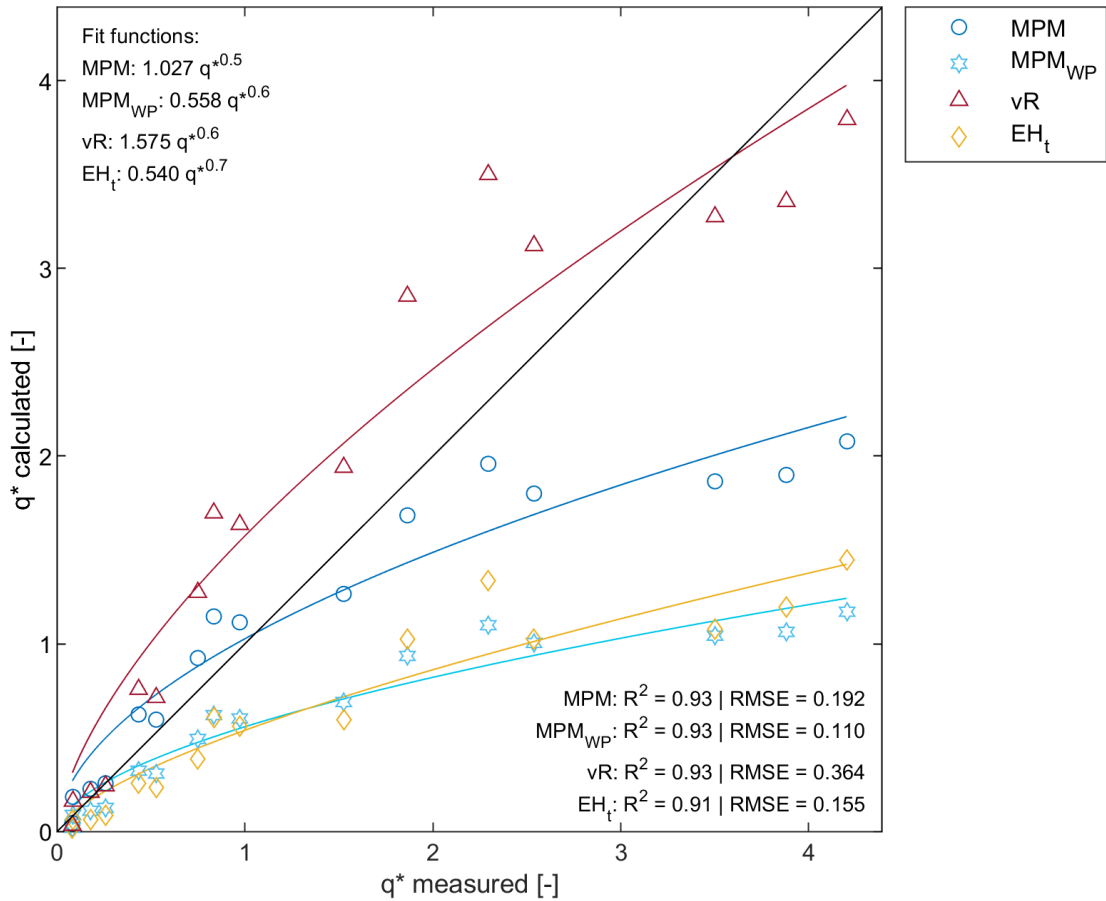


Figure 61: Comparing dimensionless sediment transport rate from the experiments with results of common transport functions

Transport function 3 after Van Rijn (1984a) has a better overall agreement with the measured data, because the non-linearly decreasing trend of the fit function is less pronounced in the range of the measured data, even though this function also tends to underestimate the measured sediment transport rate for very high loads. This, however, cannot be investigated further because even higher sediment transport rates were not available from the measurement data. For the most part, transport function 4 overestimates the measured sediment transport rates instead, starting from up to 100 % below $q_{md}^* \approx 1$ and decreasing to around 0 % for $q_{md}^* \approx 3.5$, before underestimation begins. Using the RMSE coming from $\Delta q^* = q^* - q_{md}^*$ as a measure for assessing the forecast quality, transport function 3 significantly better predicts dimensionless sediment transport rates than the

other transport functions for the range of sediment transport rates measured in the experiments (see Table 9).

#	Transport function	RMSE for Δq^*	RMSE for Δq^*_{cor}
1	Meyer-Peter and Müller (1948)	0.869	0.423
3	Van Rijn (1984)	0.562	0.417
4	Engelund and Hansen (1967)	1.274	0.514

Table 9: RMSE of transport functions compared to measured transport rates before and after correction

For transport functions 1, 3 and 4, the inverse function of the respective fit function was applied as a correction function to the results of the transport function and the results are shown in Figure 62. The filled data points represent the corrected results of the respective transport function and they are dispersed around the diagonal reference line indicating perfect agreement of the measured and calculated transport rates. A data point from Figure 61 that happens to be exactly on the corresponding fit function is moved to the reference line using the correction function. The further the data point is located from the fit function, the more its position may deviate from the reference line after applying the correction function.

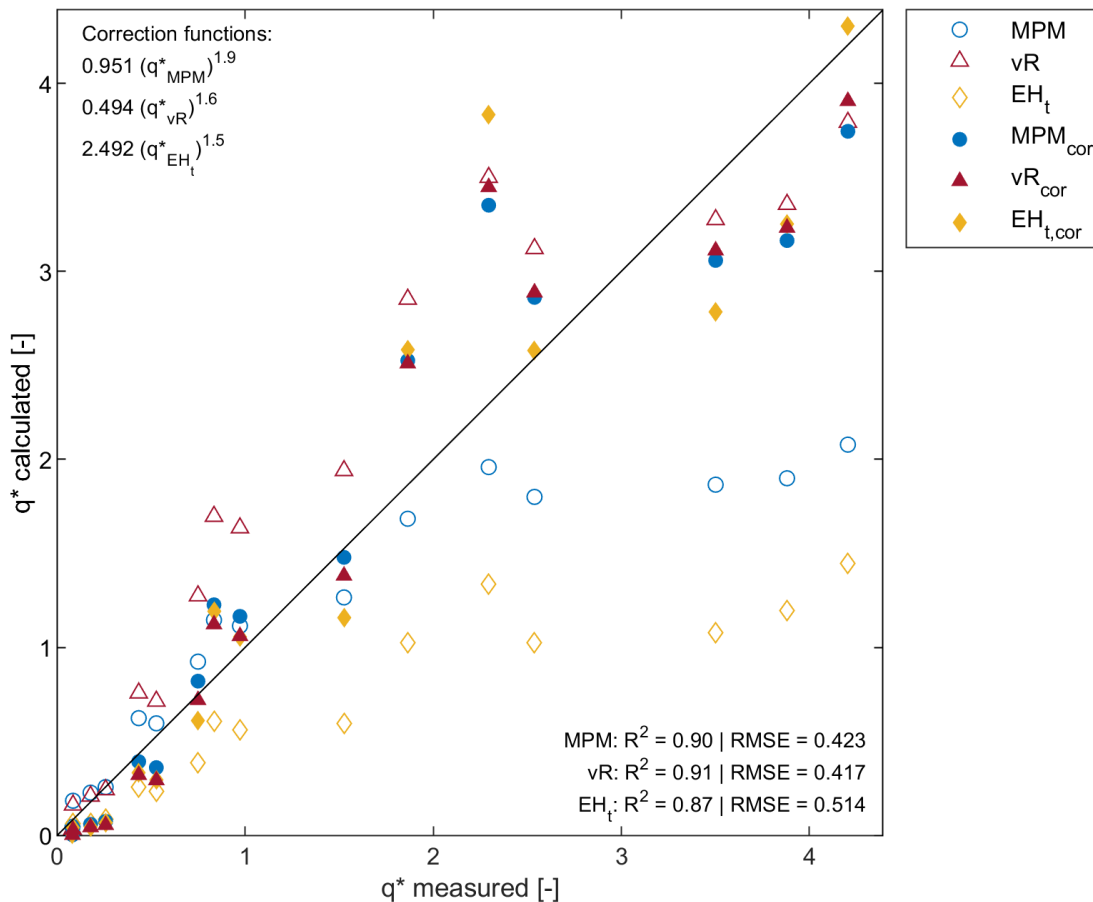


Figure 62: Comparing dimensionless sediment transport rate from the experiments with results of correction functions for common transport functions

Analogous to the previously applied procedure, RMSE values were calculated from the corrected sediment transport rates with $\Delta q_{cor}^* = q_{cor}^* - q_m^*$ (cf. Table 9). RMSEs were improved for all three transport functions to comparable levels around 0.2. Transport function 4, which had by far the highest RMSE, benefited most from the correction function, transport function 3 the least. From visual inspection of the data point trajectories, it can be seen that the chosen procedure is suitable for deriving correction functions for existing empirical transport functions from the measured mean values of the transport rates. These can then be used to improve the prediction of transport rates for the sediment used. Furthermore, it can be stated that transport function 3 after van Rijn (1984a) provides acceptable results for the prediction of mean sediment transport rates in the experiments even without further modification. Nevertheless, it remains unclear how much the deviations of this transport function increase for further rising sediment transport rates.

5. Morphodynamic processes during flood events

In this chapter, the experiments of phase 2 with unsteady flow conditions are presented. In accordance with the previous chapter on the steady-state experiment, the evaluation steps of the measurement data of the individual experiments are presented first and differences in data analysis explained when they occurred. Then, the results of all unsteady experiments are subsequently analyzed and compared with each other. In contrast to the steady-state experiments, it was not possible to generate comparative plots to the same extent for the experiments with flood hydrographs, because this was methodically not possible due to the low number of scenarios, moreover also not reasonable, since each of the experiments had a different characteristic due to the different hydrographs. These differences are referred to at the relevant points.

5.1. Data analysis of unsteady experiments

In the unsteady experiments, one significant change was made to the external boundary conditions compared to the steady-state experiments: The discharge was changed over time and it approximated naturally occurring flood hydrographs from the field (cf. chapter 3.1.1). All seven experiments were conducted in exactly the same way, only the duration of the experiments changed in accordance the length of the respective hydrograph. Consequently, the results of all experiments were also evaluated equally. The subsequent steps of data analysis for evaluating the morphodynamic processes under the unsteady experimental conditions are therefore described exemplarily using a selected scenario, which is referred to in the same manner as in the steady-state experiments: by discharge and initial water depth, but with the suffix "U" for unsteady. The selected experiment for this chapter is one of the two experiments already described in detail in chapter 4.1, scenario Q325-H35-U.

The use of flood hydrographs changed not only the experimental procedure (cf. chapter 3.4), but also the approach to data analysis. Most importantly, the implications of varying inflow on the water level control in the experimental run-of-river reservoir need to be addressed. In its design, the inflow control system could not exactly replicate the specified flood hydrograph of an experiment because the control process had a certain amount of inertia in conjunction with the rather slow-moving large pipe valves. This resulted in inflow fluctuations of up to ± 2 l/s from the specified discharge depending on the size of the respective discharge step that had to be adjusted, but these fluctuations also possessed some residual randomness from the damping of the controller.

To a certain extent, these fluctuations were compensated by the large volume of water in the concrete flume, but they still resulted in slight fluctuations of the water level at the control gauge, to which the very sensitively adjusted water level controller then reacted with an adjusted weir position at the end of the reservoir. This in turn led to water level fluctuations in the order of up to 3 mm, which may have already affected the highly mobile and very sensitive lightweight reservoir bed. However, quantification of these processes was not possible beyond this description due to the limited measurement accuracy of the measurement methods used. Yet, optical observation of the reservoir bed during ongoing experiments as well as the continuously measured sediment transport rate did not indicate such effects and the much larger and continuously happening transformation processes of the reservoir bed due to the quasi-continuous change in inflow predominated during the bed evolution.

Taking these differences in water level control into account, the data analysis is largely the same as for the steady-state experiments. Therefore, the individual evaluation steps and partial results are not discussed here in the same depth as in chapter 4.1, but in case of differences in the evaluation, these are highlighted at the respective points and their effects on the measurement results are discussed.

5.1.1. Continuously monitored raw data

The constantly changing inflows induced a permanent, in its extent varying reaction of the reservoir bed, which in turn led to changes of the water levels as well as the sediment transport rate. A separate assessment of the measured data was therefore not expedient due to the interactions between the different hydraulic and morphological parameters. The continuously recorded measurement data are thus presented and examined together in the following.

In Figure 63, three different types of measured data are plotted over time: discharge, sediment transport rate, and water levels. The black line are data from the inflow measurement, representing the discharge hydrograph; it was filtered with a centered moving average with a window size of 60 seconds. The gray line are the sediment transport rate measurement raw data, superimposed by a centered moving average, also with a window size of 60 seconds (corresponding to about 600 individual measurements) in orange; Plotted in varying shades of blue are water level measurement data, showing the evolution of the water level at various locations in the reservoir, which were also moving average filtered with a window size of 60 seconds. In the following analyses, the focus is on "WL, 58m rb" and "WL, 5m rb", the difference of which indicates, in simple approximation,

the course of the longitudinal water surface gradient I_w over time and thus the energy line gradient I . "WL, 5m rb" is the control gauge used by the water level controller for keeping the reference water level constant by adjusting the gate opening at the weir, "WL, 58m rb" is located at the sediment supply platform at the beginning of the experimental reservoir. The nomenclature of the water level gauges and their positions along the reservoir have already been explained in chapter 3.2.1.

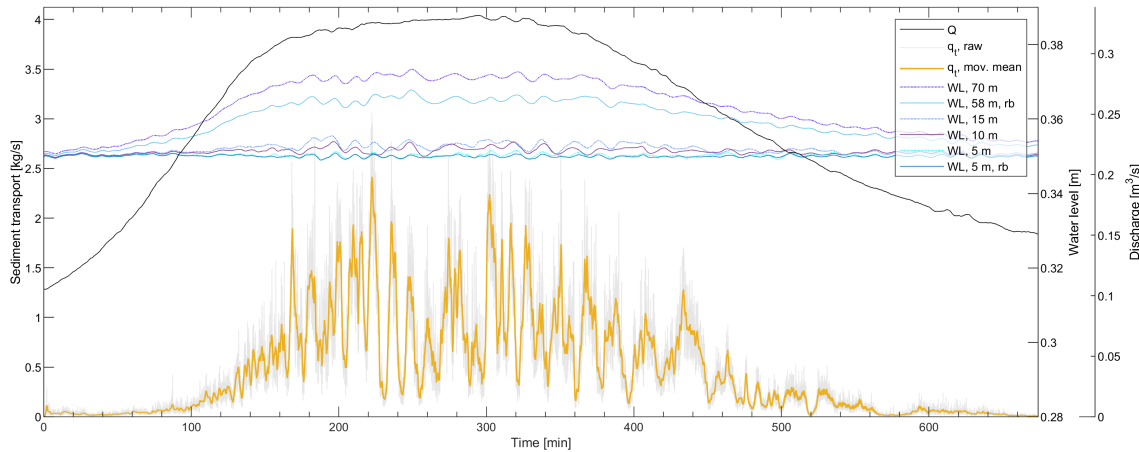


Figure 63: Discharge hydrograph with water levels and sediment transport over time during the full duration of Q325-H35-U

It is clearly visible that the curves of the water levels and the sediment transport rate correlate with the discharge hydrograph. It can be seen that the discharge initially increases largely on its own, until the longitudinal water surface gradient and sediment transport rate also increase noticeably, and above a certain level of discharge a disproportionate increase in both parameters sets in. When the peak plateau of the discharge hydrograph is reached at about 170 min on the abscissa, the longitudinal water surface gradient no longer changes on average, although the discharge continues to increase, albeit at a slower rate.

The oscillations in water levels in this part of the hydrograph were largely induced by variations of the bed elevation at the respective water level gauges, which affected the flow depth. They vary from water level gauge to water level gauge and in places even resemble each other with some temporal offset, which can be attributed to the passage of a larger bed structure from one water level gauge to the next. In addition, variations in water levels were also due to minor fluctuations of the inflow as already mentioned, but their influence on the bed can be considered minor to negligible here: inflow fluctuations were small compared the water level variations in this scenario as can be seen from the respective curves in Figure 63. Besides that, the changes of the sediment transport rate due to changing bedform characteristics occurred at much larger time scales than the very short time fluctuations of the inflow, which were in the order of a few minutes. Discharge fluctuations were hence mostly dissipated by the bed evolution and not visible in the longer-period fluctuations of the sediment transport rate.

With the peak plateau of the inflow hydrograph, the sediment transport rate also reaches a state that could be, on average, described as a plateau too, but with considerably larger fluctuations. These were due to the large bedforms that were present in the reservoir during the high hydraulic stress coming from discharges in the range of the peak of the inflow hydrograph. There is no further increase in the sediment transport rate along this peak plateau, but rather a slight decrease. The transport rate does also not respond directly to the decrease in discharge after the flood peak. Instead, it decreases much slower and moreover with a time delay.

The temporal delay of the sediment transport measurement in the sediment recirculation system plays only a minor role here compared to the inflow and water level measurements, because the relevant morphodynamic processes took place on two different time scales here: On a short time scale, changes in discharge directly led to changes in the transport capacity of the flow, which were also recorded almost immediately by the sediment transport measurement procedure, minus a delay of about 1 minute: this is the maximum time it took for flushed-out sediment to be transported to the sediment transport measurement system, during which peaks of flushed-out sediment were attenuated in the sediment trap similarly to a moving average. Transformation processes of the bedforms took place on a longer time scale which then also affected the transport capacity of the flow, but later and much less abruptly than the changes in discharge. The longitudinal water surface gradient, in comparison, reacts with a similar delay as the sediment transport rate and it also decreases relatively more slowly than the discharge.

5.1.2. Data filtering and post-processing

In order to make the described observations more visible and at least partly quantifiable, different methods for averaging and filtering were applied and parameters combined. In particular, sediment transport rate variations needed to be reduced to identify more general connections between hydraulic and morphological parameters. Figure 64, again, shows the data of the sediment transport measurement superposed with the moving average (MM) with window size 1 minute (cf. Figure 63) as well as another centered moving average filter with window size 10 minutes. In addition, Savitzky-Golay filtering (SG) was applied here with a 4th degree polynomial and a window size of 26 minutes, with the parameters of the filter adjusted by trial and error to fit the characteristics of the data.

Savitzky-Golay filtering after Savitzky and Golay (1964) is a method used to smooth noisy data based on local least-squares polynomial approximation, that reduces noise while maintaining shape and height of waveform peaks (Schafer 2011). It is widely used in signal

processing, but the author of this thesis has not seen its application in hydraulic engineering very often, which is why the process is briefly explained with the help of Figure 65. There, the process of fitting a second-degree polynomial to a predetermined number of input samples (black dots), in this case five, by means of least-squares smoothing in two exemplary locations along the abscissa is illustrated, that in practice is applied to every input sample point. Weighting constants denoted as crosses and their polynomial approximation shown as dotted line are required to receive the least-squares output samples (black circle) for which a shape preserving fit function is deduced. A clear explanation of the method as well as its application is given in Schafer (2011).

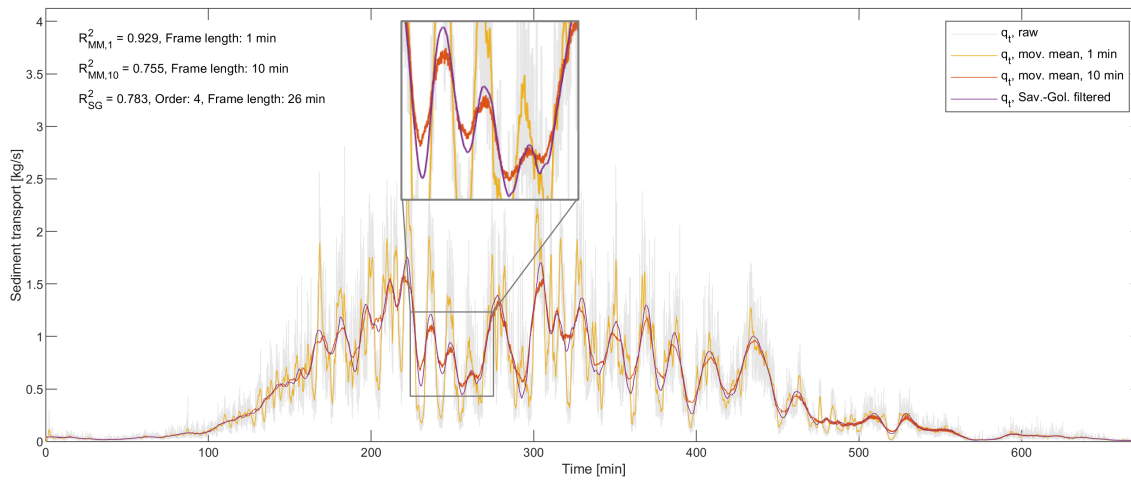


Figure 64: Sediment transport rate over time with moving averages and Savitzky-Golay filtering during the full duration of Q325-H35-U

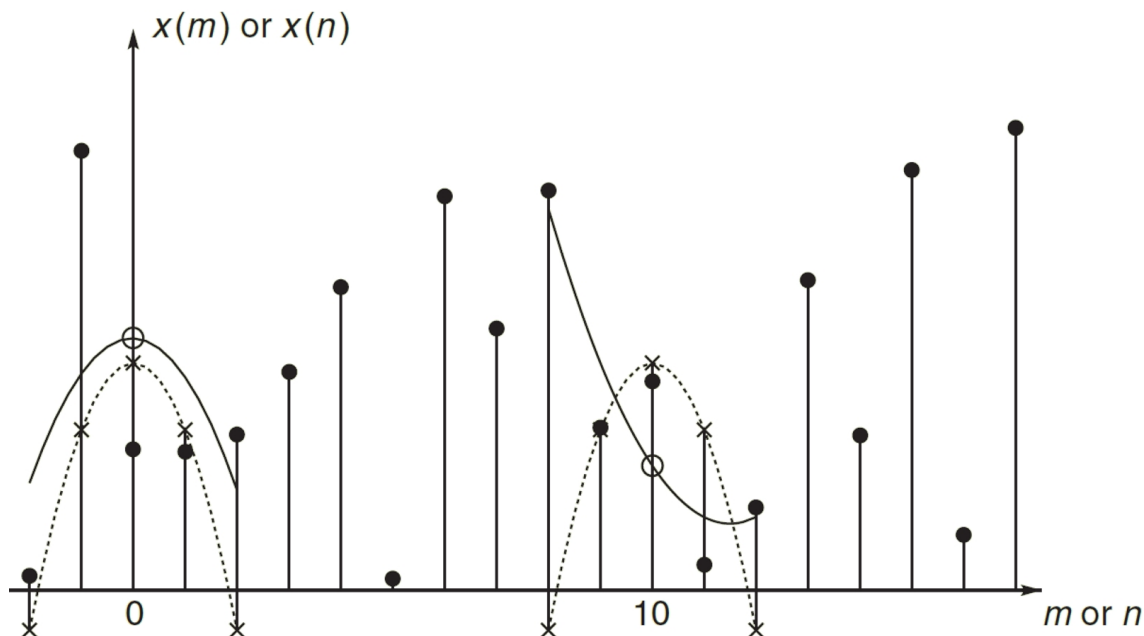


Figure 65: Illustration of least-squares smoothing by locally fitting a second-degree polynomial (solid line) to five input samples after Schafer (2011)

While the 1 minute moving mean values still fluctuated strongly (orange line), oscillations could already be strongly reduced with a larger window size of 10 minutes (red line). In

parts, longer-term oscillations of the sediment transport rate were already completely skipped (e.g. in the section of 170 to 200 minutes on the abscissa) by this moving mean filter, while at the same time the remaining curve still strongly oscillated with a low amplitude, which manifests itself in a varying thickness of the red line when looked at from a certain distance. The Savitzky-Golay filtering successfully counteracted this problem and continues to reproduce the larger oscillations of the transport rate with the selected characteristic. Also, it does not skip the shorter period oscillations like the 10 minute moving average filter and is thus considered suitable for a good visualization of relevant morphodynamic processes that manifest in the sediment transport rate. Consequently, it is used in the following analyses as a trend line for the sediment transport rate.

If the oscillations are to be completely removed and only the fundamental trends of the sediment transport rate time series should be reflected in a figure, the filtering techniques used so far reach their limits due to the large variability of frequencies and amplitudes in of the data oscillations. One solution to this is a transformation of the data from the raw data time-amplitude representation into the frequency domain. There, further information about the data can be revealed from the frequency spectrum which shows all the frequencies that exist in the data time series or the "signal" respectively. This is usually done by applying Fourier transformation. However, when it is important to allocate these frequency (or spectral) components in time, one way to create this time-frequency representation of the data is wavelet transformation.

In the continuous wavelet transform, a finite signal is approximated by using a particular wavelet to represent the signal in question as a combination of all possible scalings (i.e. dilation) of the wavelet in all possible location of the original signal. The wavelet used is itself a short signal in the form of a wavelike oscillation that starts at zero, has a certain signal amplitude, and ends at zero again in a defined time interval, and it is projected onto the original signal at varying frequencies (Polikar 2003). To make this method applicable to filtering techniques, the discrete wavelet transform limits the number of wavelet scalings (i.e., compression or dilation of the wavelet) to certain frequency bands. High-pass and especially low-pass filters are used to decompose the original signal into a finite number of wavelet projections onto the original signal with ever-increasing dilation. The combination of the set of wavelet projections performed in this process results in the filtered signal approximation. Different types of wavelets exist for different types of applications. Figure 66 shows two examples of wavelet decompositions, each with 5 different wavelet scales.

This thesis can only give a very brief introduction the most basic functionalities of wavelet transformation, as the field is wide and the underlying processes too many for an

appropriate presentation here. For more information on wavelet decomposition and the theoretical basis of this complex procedure, see Mallat (1989; 2008), Burke Hubbard (1997), Polikar (2003), and many others.

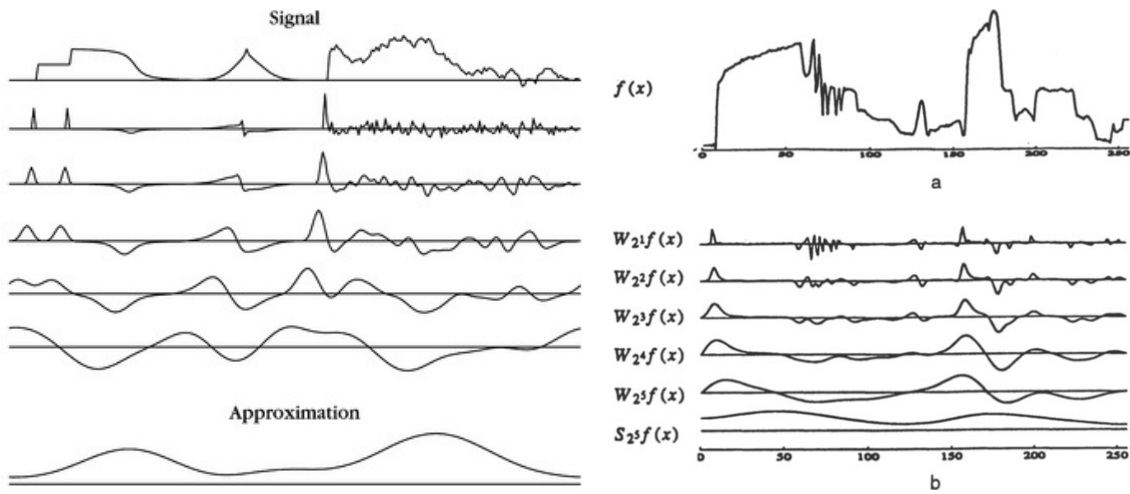


Figure 66: Examples of signal filtering using wavelet decomposition after Mallat (2008) (left) and Burke Hubbard (1997) (right)

In Figure 67, the sediment transport rate raw data and the Savitzky-Golay filtering are presented as well as the two wavelet projections at level 15 and 16 of a wavelet decomposition based on a 6th degree symlet wavelet and Bayes denoising with mean thresholding for the wavelet coefficients as applicable in release R2021a (update 5) of the MATLAB software environment. The two projections are at very low frequency bands and therefore hardly oscillate. For the wavelet projection at level 15, three high points (i.e., maxima of the curve) are still discernible along the entire time series: the first is highest (at about 215 min), and the third of these (at about 440 min) is only just noticeable as a high point. When matching this wavelet projection with the raw data or the Savitzky-Golay filtering, these three high points can also be identified in these stronger oscillating curves, but not very easily and not without many other local curve maxima in between.

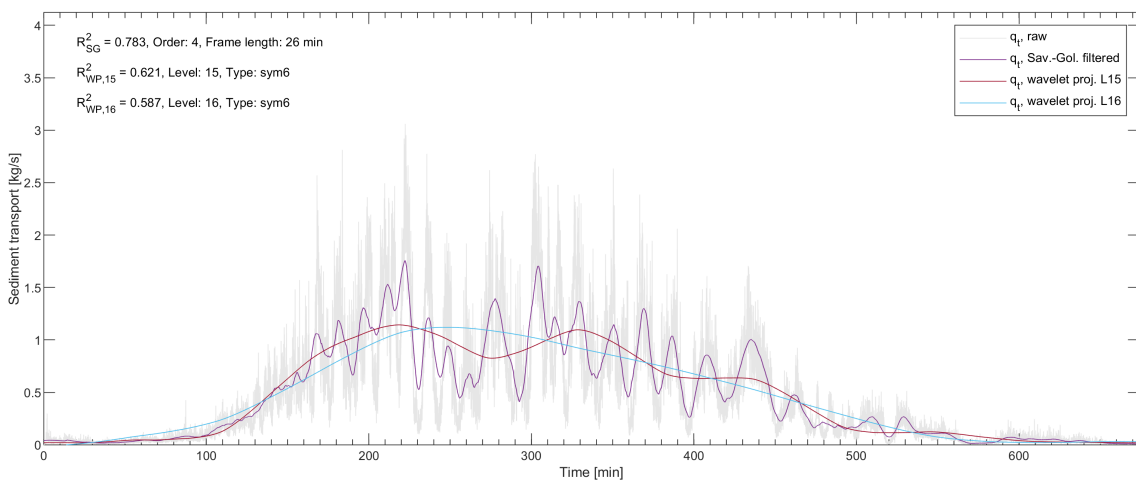


Figure 67: Sediment transport rate over time with Savitzky-Golay filtering and wavelet projections L15 and L16 during the full duration of Q325-H35-U

At level 16, only one maximum is left at about 240 minutes on the abscissa. When comparing with the measured data, this time localization is not obvious and the curves are not well aligned anymore. Instead, the wavelet projection unveils the basic trend of the sediment transport rate development. This procedure can be standardized for the analysis of the time series of sediment transport rate measurement data so that it may be applied in a comparable manner to any unsteady experiment. A unique point along the time series could be defined in the process and used for comparison with other parameters such as the discharge hydrograph.

Following the previously discussed, the presented approach of using individual projection steps of a multilevel wavelet decomposition seems suitable to simplify the curve of the raw data of the sediment transport rate measurement to such an extent that only the fundamental oscillations remain. These findings can then be used to derive information about the temporal course of sediment transport and thus about the general sediment availability in the reservoir, which will be discussed in the next chapter. Furthermore, this process could also be automated by, for example, specifying an allowed number of maxima in the wavelet projection and using an iterative procedure to find the appropriate wavelet level that matches the condition. However, since there are still some more parameters to be set for the wavelet decomposition, such as the type of wavelet used and its symmetry, this process could not be fully automated and run without in-depth expert knowledge.

In general, expert knowledge of the physical processes underlying the measured data is required to successfully fit the particular filter to the data for each of the filtering techniques presented. This process is time-consuming and to some extent subjective, in addition to not being exactly reproducible. To address this issue, automated correlation techniques as used for example in Gutierrez et al. (2017) could be applied, but there are still limitations based on the characteristics of the data. The question, for example, what degree of oscillations of the wavelet projections on the sediment transport rate measurement data is required and at what point characteristic features of the time series are filtered out beyond what the particular question demands, always depends on the individual case and can only be automated to a limited extent, especially for a small number of samples.

5.1.3. Parameter interdependence

For further analysis of the sediment transport rate, Figure 68 shows, in addition to the Savitzky-Golay filtering and the two wavelet projections from Figure 67, the first derivatives of the wavelet projections, representing the gradient of their basic functions and thus indicating at the zero crossing when the basic function shows a maximum (or minimum).

Besides, the discharge hydrograph and its first derivative are given in black. The oscillations of the discharge hydrograph due to the occasional fluctuating inflow control, which are interfering with this kind of analysis by creating many zero crossings of the discharge derivative curve, were largely reduced by a Savitzky-Golay filtering of the discharge hydrograph (window size 10 minutes, 8th degree polynomial).

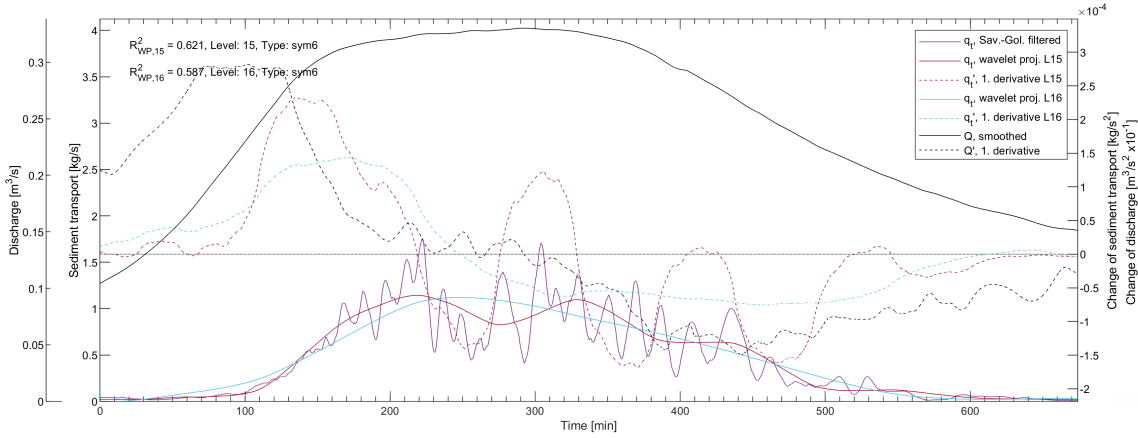


Figure 68: Discharge hydrograph and 1st derivative with filtered sediment transport rate over time, wavelet projections L15 and L16 and 1st derivatives during the full duration of Q325-H35-U

It becomes well visible in this way that for both level 15 (L15) and level 16 (L16) of the wavelet projections the sediment transport rate reaches its peak well before the discharge hydrograph. Using L16 as indicator of the sediment transport rate trend, the transport rate already begins to decrease while the discharge hydrograph still rises slowly along the peak plateau and has not yet reached the actual peak. L15 is also valuable in this context, as it still reflects the time course of the sediment transport rate in, but in a very simplified way, and helps to understand and integrate the information from L16 in the context of the experiments.

With this deepened knowledge of some of the underlying morphodynamic processes in the reservoir during the discharge hydrograph, a comparison can be made to sediment transport processes under steady-state conditions, i.e. to the experiments with dynamic bed equilibrium. If the mean transport rate of the steady-state experiments Q325-H35 is compared with the maximum of the trend of the transport rate (L16 in Figure 68), the unsteady experiment in scenario Q325-H35-U has a maximum sediment transport rate trend about 11 % higher. In combination with even higher values for L15 and the qualitative optical analysis of the measured data as a whole, this can be taken as a clear indication of a flushing effect on the reservoir bed significantly before the discharge peak. This statement is, in a sense, bold, as the uncertainties underlying the measured data and from the introduced filtering and post-processing methods are high in total as has been already described throughout the previous chapters. It is, thus, uncertain whether and how such a statement can be transferred to other situations, but following the presented approach the

result is statistically sound and, given the high data quality, it is also plausible. To support that, in the next chapter the other scenarios are analyzed and a comparison of all experiments is made.

In order to further analyze the measurement data for the assumed flushing effect, Figure 69 combines some more data curves. Next to the discharge hydrograph and the filtered and projected sediment transport rate data, the data of the two water levels at the control gauge, WL_5, and at the beginning of the reservoir, WL_58, are shown, from which the longitudinal water surface gradient can be directly deduced. Besides, three not directly measured data curves are shown, that were calculated from the directly measured data: Flow depth h , mean flow intensity θ_u and shear stress τ . All of them, as has been analyzed in chapter 4.2, were subjected to multi-level averaging to make them suitable for comparison. The curve of the shear stress (orange line) most closely resembles the curve of the longitudinal water surface gradient the most, which can be derived from the difference of the two water level gauges (blue lines) and, more or less directly, seen from the course of WL_58 since WL_5 is close to constant and fluctuates only slightly. However, τ does not reach a comparable horizontal plateau like the longitudinal water surface gradient in the area of the hydrograph peak plateau, but instead continues to increase slightly with the discharge and reaches its maximum at about 270 min, i.e. about 30 minutes after the sediment transport rate and about 30 minutes before the flood peak.

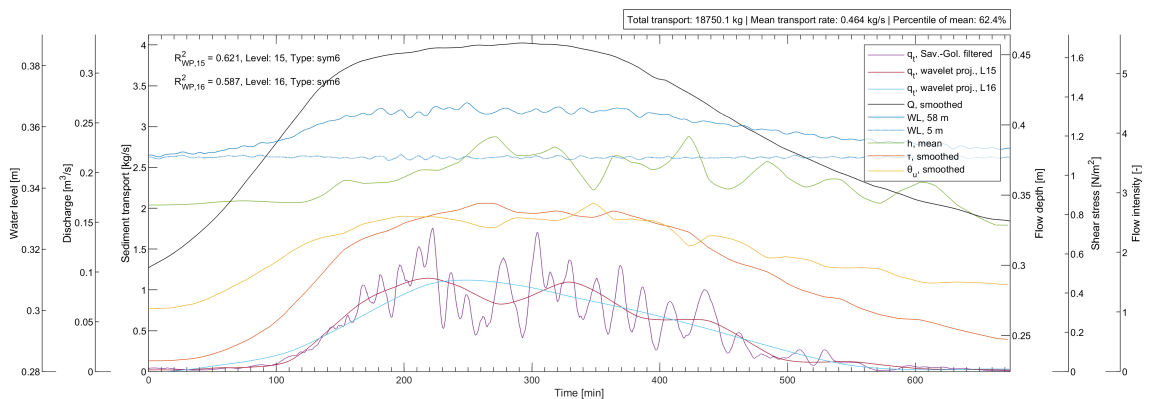


Figure 69: Discharge hydrograph with filtered sediment transport rate over time, wavelet projections L15 and L16, selected water levels, flow depth, shear stress and mean flow intensity during the full duration of Q325-H35-U

This development of the shear stress is depending on the course of the flow depth (green line), which is mainly influenced by the reservoir bed elevation in the vicinity of the water level gauges, since τ was not measured directly, but calculated from the bed slope as introduced in chapter 2.1.1. Consequently, it depends on the energy gradient line equated with the longitudinal water surface gradient and the hydraulic radius of the flow cross section. Thus, if the longitudinal water surface gradient is constant or varies only slightly around a constant mean value (clearly visible along the peak plateau between about 180

and 380 minutes in Figure 69), the flow depth must increase to account for an increase in shear stress.

This is the case in the region between the first and second local maximum of the wavelet projection L15 (approximately between 220 and 330 minutes): the flow depth increases sharply because the previously mentioned flushing effect has eroded the reservoir bed in the downstream part of the reservoir. As a result, the sediment transport rate dropped significantly because less material was present at that time in the study area of the topography scans and the sediment had to be transported again downstream from the sediment supply at the beginning of the reservoir. The bed was thus lower, which led to greater flow depths since the water level was kept constant at the control gauge: the local minimum of the wavelet projection L15 at about 270 min occurs at about the same time as the maximum flow depth. At the second maximum of L15 (approx. 330 min) the flow depth decreases again and the transport rate shows that the mentioned sediment coming from upstream had reached the study area between reservoir meters 2 and 16 again. As mentioned earlier, the second lowest frequency projection of the wavelet decomposition, in this case L15, could be used to represent the variations in sediment transport rate due to time-varying sediment availability.

In the following, the process just described is repeating along the time axis in a weakened form: the sediment transport rate decreases due to decreasing bed elevation and increasing flow depth. However, this is superimposed by the decrease of the discharge hydrograph after the flood peak, which leads to a decrease of the shear stress in spite of again increasing flow depth: The longitudinal water surface gradient is already decreasing at this point. It is remarkable here that both the shear stress and the longitudinal water surface gradient decrease more slowly in relation to the discharge than they had increased in the rising limb. This is due to the altered bed structure after the passage of the flood peak, which has reshaped to match the hydraulic stress and produces increased flow resistance. However, this flow resistance varies greatly depending on the existing bedforms, so it is difficult to draw conclusions about the condition of the bed from the shear stress alone, at least until the flow resistance is not known for each combination of discharge and flow depth, which usually cannot be assumed.

If the curve of mean flow intensity θ_u is considered instead of shear stress, the curve most closely resembles the discharge hydrograph. In the rising limb there is good agreement, likewise the mean flow intensity still increases slightly along the peak plateau, even if the values fluctuate somewhat more strongly, which is related to the flow depth-dependent calculation of the mean flow intensity: Flow depth has the opposite effect here than for shear

stress, so that greater flow depths result in smaller mean flow intensities, e.g., at the maximum flow depth at about 270 min. In the falling limb of the hydrograph, the mean flow intensity decreases only slightly slower than the discharge, which is due to the likewise slower decreasing longitudinal water surface gradient and the slightly higher mean bed position in relation to the longitudinal water surface gradient. Thus, a larger longitudinal water surface gradient in relation to discharge due to higher bed resistance produces slightly higher mean flow intensities.

Furthermore, it is noticeable that the fluctuations of the mean flow intensity in the area of the peak plateau show similarity to the curve of the sediment transport in the form of the wavelet projection L15. The curve of the mean flow intensity represents all three of the local maxima of L15 with only a small time offset and seems to be better suited to represent developments of the sediment transport rate than the shear stress, which was also already found in chapters 4.2.2 and 4.2.3 for the steady-state experiments. It is important to note in this context that the mean flow intensity yields only slight differences to the sediment transport rate even after the passage of the flood peak and the large-scale transformation of the bed at comparable discharges. It is therefore reasonable to assume that a direct relationship can be established between mean flow intensity and sediment transport rate, thereby supporting the findings from the steady-state experiments with dynamic bed equilibrium when comparing shear stress and mean flow intensity.

5.2. Implications of unsteady experiment series

In the following, statements from the previous chapter will be verified by further experiments and differences as well as uncertainties in the analysis will be elaborated on. In contrast to the experiments with dynamic bed equilibrium, no comparative graphical representations are presented. The small number of experiments with at the same time different discharge hydrographs and hydraulic stress levels do not allow for statistically reliable generalized statements. Instead, the experiments conducted are analyzed individually, compared with each other and finally contrasted.

5.2.1. Scenarios with wide hydrograph peaks

Scenario Q325-H30-U used the same hydrograph with the same rather wide peak plateau as scenario Q325-H35-U, that has been elaborated on in detail in the previous chapter, but a lower initial water depth, namely 30 cm instead of 35 cm. The hydraulic stress on the reservoir bed resulting from discharge and water level at the control gauge is thus about 15 % higher at the beginning of the experiment. A major difference to scenario Q325-H35-

U is that this increase in hydraulic stress on the bed caused the reservoir bed to go into transition to the upper plane bed during discharges in the magnitude of the flood peak. This is particularly evident in the interaction of sediment transport and flow depth, which will be discussed below. Besides the different hydraulics, scenario Q325-H30-U was also conducted twice to verify the reproducibility of both the experimental results and the derived findings and referred to as scenario Q325-H30-U-1 and scenario Q325-H30-U-2.

Unlike in the previous chapter, not all evaluation steps are shown and explained in detail, since they were performed exactly the same for all unsteady experiments. The only changes were made during post-processing and concerned the window size of the Savitzky-Golay filtering and the choice of levels for wavelet decomposition to be used for the trend analysis of the sediment transport rate. Figure 70 is therefore arranged in the same way as Figure 69, with the same parameter curves and coloring, but the axes were scaled differently due to the different value ranges of some parameters, in order to make optimal use of the available space for data analysis.

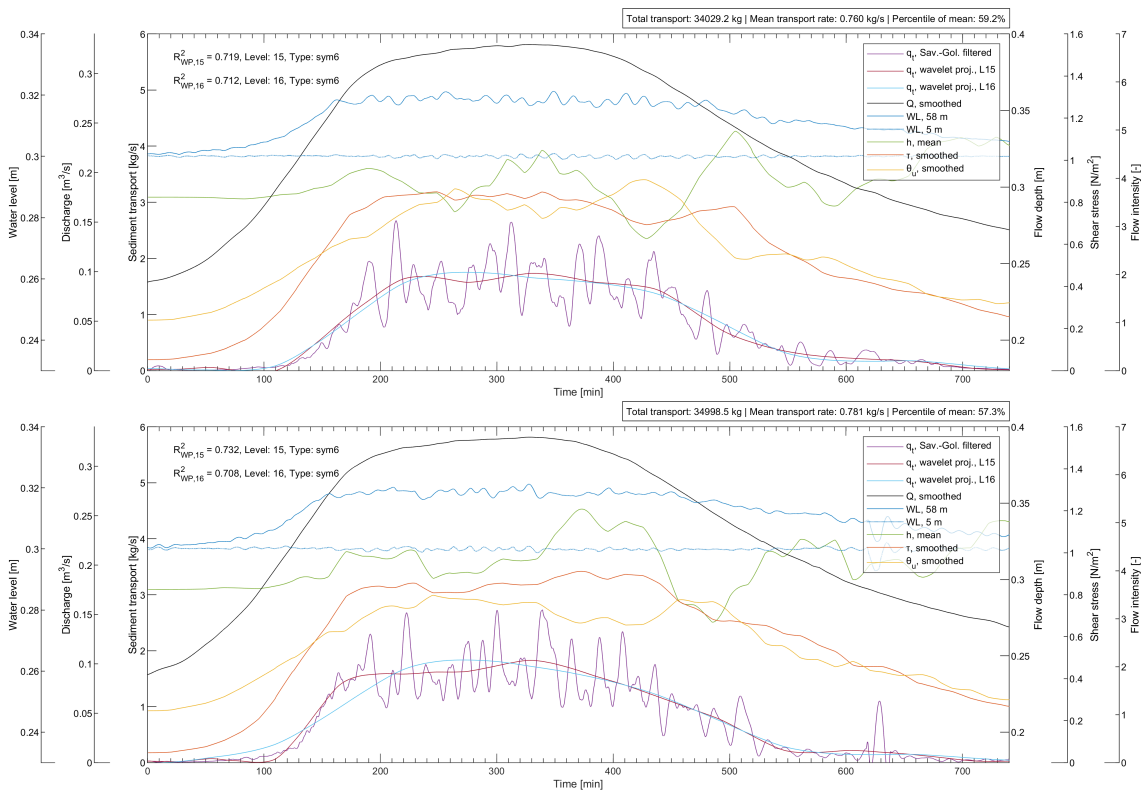


Figure 70: Discharge hydrograph with filtered sediment transport rate over time, wavelet projections L15 and L16, selected water levels, flow depth, shear stress and mean flow intensity during the full duration of Q325-H30-U-1 (top) and Q325-H30-U-2 (bottom)

The curves of the Savitzky-Golay filtered sediment transport rates differ visibly: For experiment 1 (top), the fluctuations show a larger amplitude, i.e. have higher and deeper spikes, and have a somewhat longer period than in experiment 2 (bottom). There, the sediment transport fluctuates back and forth somewhat more frequently and drops somewhat less than in experiment 1. The large influence of the randomness of the smallest

transport processes beginning at grain level and impacting on the overall bed evolution is already evident here. Looking at the wavelet projections in level 15 (again L15), this is reflected in a somewhat stronger formation of local maxima and local minima in experiment 1. The trend of the sediment transport rate defined on the basis of the wavelet projection in level 16 (again L16) of experiment 1 shows a lower maximum of about 5 % (around 280 minutes) compared to experiment 2 (around 270 minutes), which occur with a short time difference of about 10 minutes). Furthermore, the L16 sediment transport trend forms sort of a plateau during the hydrograph plateau, however with a slight decrease as compared to a slight discharge increase, and remains in the range of its peak magnitude longer. After the flood peak, a relatively sudden decrease of the transport rate begins in experiment 1, whereas in experiment 2, an almost continuous transition takes place for the wavelet projection L16 from the trend line's peak of the sediment transport rate.

This randomness of the sediment transport rate (and hence the bed evolution) under otherwise almost exactly identical experimental conditions (minor differences in inflow and water level control have been discussed before and could not be completely eliminated) also has a significant impact on the curves of the other parameters. While the longitudinal water surface gradient is the same in both experiments on average, stronger and longer-period fluctuations are present in experiment 1, similar to the curve of the sediment transport rate. However, these differences are negligibly small in comparison to the differences in flow depth. The flow depth initially increases with the rising hydrograph in both experiments, then decreases in the first section of the hydrograph peak plateau in experiment 1, while it initially remains constant in experiment 2. During the subsequent drop in flow depth in experiment 2 (range between about 260 and 310 minutes), it increases in experiment 1. At about 410 minutes and at about 510 minutes completely opposite extremes occur with flow depth differences between the experiments of up to 7 cm at the same time under the hydrograph.

At this point, it must be pointed out once again that the flow depth curves shown in these figures are very strongly averaged and were calculated from the mean values of the three water level gauges in the study area of the experimental reservoir, each 5 m apart, and the mean bed elevations from topography scanning. When comparing the individual water level gauges, flow depth differences of up to more than 10 cm occurred. Due to the large differences in bed elevation at the respective water level gauges caused by bedforms, averaging over these three water level gauges already compensates for some of these differences and methodically allows for trends to be derived for the experimental reservoir, but the flow depth evolution over the moving bedforms is still only directly comparable in a statistical sense as done for the dynamic equilibrium experiments.

The effects of flow depth on shear stress and mean flow intensity have been discussed for scenario Q325-H35-U already and they are also clearly visible for scenario Q325-H30-U in Figure 70: They most likely lead to the fact that maximum shear stresses are reached much later in experiment 2 than in experiment 1. In experiment 2, this maximum range is already located in the falling limb of the hydrograph and exhibits the highest shear stresses in absolute terms at lower discharges than in experiment 1. The opposite is true for the mean flow intensity: here, absolute maxima are reached in experiment 1 in the falling limb of the hydrograph. In contrast to the previously analyzed scenario Q325-H35-U with the higher flow depth and hence lower absolute hydraulic stress, neither the course of shear stress nor that of the mean flow intensity in scenario Q325-H30-U_H can be directly transferred to the trend of the sediment transport rate.

This phenomenon can be directly attributed to the transition of the reservoir bed into the upper flow regime with so-called undulating dunes, where bed resistance and skin friction are supposed to develop in opposite directions (cf. chapter 2.2.1). If the process of washing out dunes and large bedforms could have been completed and the so-called upper plane bed would have developed in the experiments, lower fluctuations of the sediment transport rate due to the then missing bedforms would have been expected, which would probably have led to a more easily recognizable, direct relationship between shear stress, mean flow intensity and sediment transport rate. However, this was not possible in the present experiments because of the sediment recirculation system capacity and the constant volume of sediment in the reservoir. In combination with the very high transport capacity of the flow, an increasing separation of the available bed material took place over time into longer sections with a very high bed and hardly any morphological structures, which were interrupted by strongly eroded areas where only small sediment accumulations migrated over the solid bottom of the concrete flume. In Figure 70, this can be seen in the ever-increasing fluctuations in flow depth over the duration of the experiment.

The beginning of the transition to the upper flow regime can be recognized from the plateau of the water surface gradient in Figure 70 for both experiments: The gradient rises very quickly at first, but then becomes constant well before the peak plateau of the hydrograph is reached, because a further increase in bed resistance is no longer possible. This can also be seen from the fact that the shear stress in both experiments increases almost exponentially to an initial maximum value of approx. 0.8 N/m^2 (approx. at 200 minutes in each case) even before the peak plateau of the wave and then only fluctuates back and forth to a much lesser extent. Only after the discharge and the longitudinal water surface gradients have already sunk significantly below the values that prevailed when the shear stress plateaus were reached (approx. 510 minutes in experiment 1 and approx. 450

minutes in experiment 2), the shear stress decreases again. For reference to the shear stress threshold of about 0.8 N/m^2 in the dynamic bed equilibrium experiments, cf. chapter 4.2.2, in particular Figure 52 (right) and Figure 54 (left).

The differences between the two experiments mainly come from the different evolution of bedforms described earlier, which in turn is due to the randomness of morphodynamic processes in general, which could not be investigated in greater from the present data unfortunately. The fact that the shear stress remains high for a longer time after the passage of the hydrograph peak has to do with the process of dune formation: in the transition zone to the upper plane bed dune formation no longer takes place and it naturally resumes with sinking hydraulic stress. However, after the hydrograph and due to the long duration of the experiment and recirculation of the sediment, there were already much greater differences in sediment distribution in the reservoir than at the beginning of the experiment. Thus, dune formation resumes even later and at a different level than it stopped under the rising hydrograph.

The fact that the fluctuations of the sediment transport rate in Figure 70 do not correlate more strongly with the fluctuations of the flow depth is due to the extremely high hydraulic stress on the bed in general and to the duration of the experiment: The maximum of the shear stress of about 0.8 N/m^2 is hardly exceeded and maintained for a very long time, almost independently of the flow depth and also of the further increasing discharge. A lot of sediment was permanently in motion in this phase, and the influence of the mean bed elevation on the shear stress was small compared to the high energy line gradient. The active transport layer was several centimeters thick then, so that the permanent activation of such large amounts of sediment acted as an additional flow drag on the water surface gradient as described in chapter 2.1.2 with drag of moving sediment particles τ''' .

For the sake of completeness, it should be written that much longer durations with these high hydraulic stresses would have been necessary to obtain the mentioned sediment separation to an extreme with an almost completely eroded reservoir section. In such a state of separation, average flow depths in the range of approx. 40 - 45 cm could have possibly been achieved, whereas in the present experiments a maximum of only 35 cm was observed. However, since the sections with lower bed elevation were repeatedly overtaken by the sections with higher bed elevation due to their great difference in migration velocity, which was reflected in the sediment transport rate measurement data in the form of the typical fluctuations, it is not clear whether these extreme conditions would occur at all. During the steady-state experiments such developments have not been observed even after 10 hours of experiment operation.

To verify the statements made so far, two more experiments were conducted with rather wide hydrograph peaks, scenario Q162-H21-U (Figure 71) and scenario Q162-H30-U (Figure 72). In scenario Q162-H21-U with the low initial water depth of 21.25 cm, the hydraulic stress does not increase enough to induce a transition to the upper flow regime of the reservoir bed. It can be seen that the statements made for scenario Q325-H35-U (cf. Figure 69) concerning the interdependence between sediment transport rate, flow depth and shear stress as well as mean flow intensity are also valid here: An increased flow depth leads to decreasing sediment transport and increased shear stress (at about 250 minutes) and the mean flow intensity follows the trend of the sediment transport rate, this time given by the wavelet projection at level 15 (L15) due to the shorter experiment duration. Compared to Figure 69, however, there is a slight time lag between the trend of the sediment transport rate and the other curves, which can be explained by the lower migration velocity of the bedforms: It takes a little longer for observations in the study area at reservoir meters 2 to 16 upstream of the weir to be recorded in the sediment transport measurement system downstream of the weir.

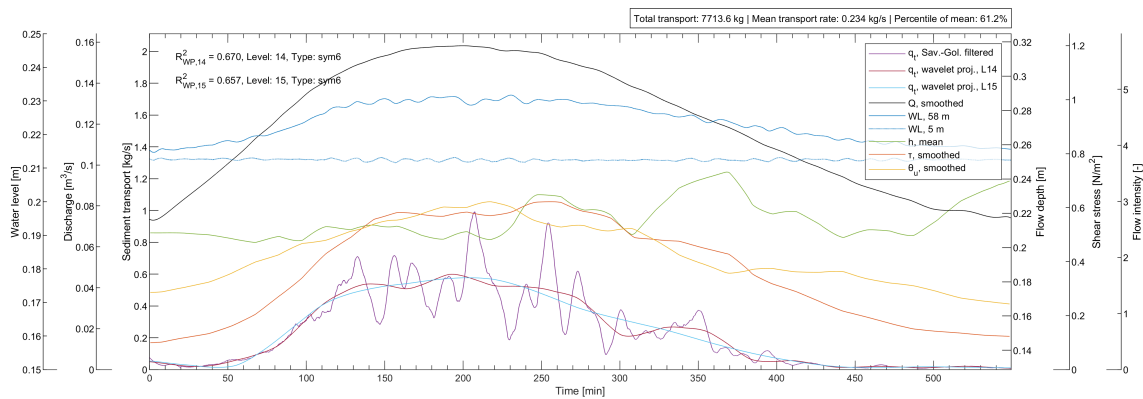


Figure 71: Discharge hydrograph with filtered sediment transport rate over time, wavelet projections L14 and L15, selected water levels, flow depth, shear stress and mean flow intensity during the full duration of Q162-H21-U

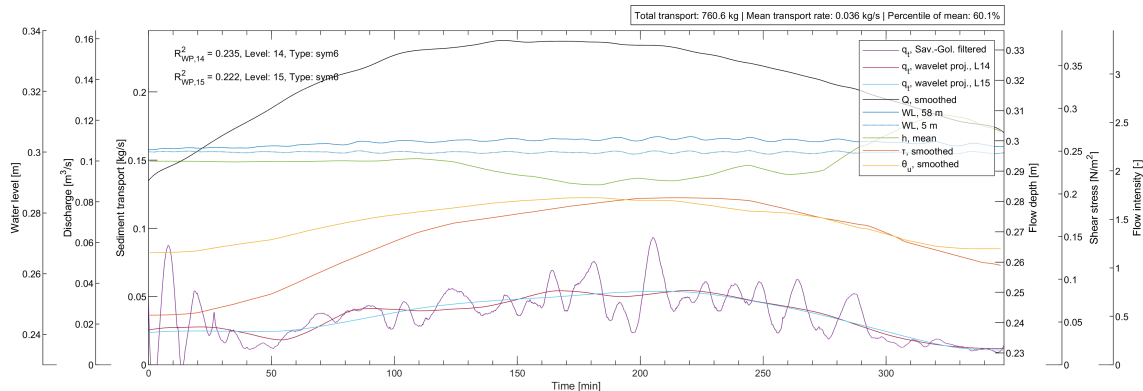


Figure 72: Discharge hydrograph with filtered sediment transport rate over time, wavelet projections L14 and L15, selected water levels, flow depth, shear stress and mean flow intensity during the full duration of Q162-H30-U

In Figure 72, in fact, there is not much happening that needs to be addressed because the hydraulic stresses in scenario Q162-H30-U were simply too low for relevant morphodynamic transformations. The flow depth decreases during the peak of the

hydrograph because initial bedforms have formed in the study area of the reservoir, which have not yet had a noticeable effect on the sediment transport rate due to the low migration velocity. The initial short-term increase in sediment transport was due to the abrupt initiation of movement throughout the reservoir from the plane bed, which always resulted in a brief transport rate peak prior to the formation of ripples. This occurred in all scenarios in both experimental phases, it is only more apparent here due to the low scale of the ordinate axis of the sediment transport rate.

5.2.2. Scenarios with pointed hydrograph peaks

In the experiments described so far, hydrographs with comparatively wide flood peaks were used. The different morphodynamic and hydraulic processes occurring during these hydrographs and their interaction could be adequately reproduced because the bed had, more or less, sufficient time to react to the surrounding hydraulic conditions under the hydrograph peak plateau. For hydrographs with steep peaks this time is not given, which leads to an even stronger overlapping of processes and makes an analysis of the interdependence of the parameters involved more difficult.

Figure 73 therefore shows scenario Q409-H35-U with a hydrograph that has very steep limbs and a short peak duration on the one hand and reaches very high discharges during the hydrograph peak on the other hand. The hydraulic stress on the bed was extremely high during the peak discharge and the highest sediment transport rates and shear stresses of all unsteady scenarios occurred. The sediment transport rate rises almost vertically under the steeply rising hydrograph as does the water surface gradient, similar to the experiments in Figure 70. The simplified time course of the sediment transport rate given by the wavelet projection L15 in this case, reaches its maximum well before the hydrograph peak and by this marks the threshold to the transition zone to the upper flow regime and the beginning of reservoir flushing.

However, due to the simultaneously continuing steep rise of the hydrograph, the sediment transport rate even for L15 remains extremely high (above the maximum of both wavelet projections L15 and L16 in scenario Q325-H30-U of about 1.8 kg/s) for a long period of about 50 minutes (about 370 minutes to 420 minutes on the time axis). All of this happened before the peak discharge of the hydrograph was reached. The shear stress threshold of approx. 0.8 N/m^2 (cf. Figure 70) is also clearly exceeded from about 370 minutes on and the entire reservoir bed was mobilized in a very short time. This then leads first to a collapse of the sediment transport rate and a strong increase of the flow depth under the falling limb

of the hydrograph, before the sediment transport reaches a second peak due to the still very high discharges, however over a shorter period of time.

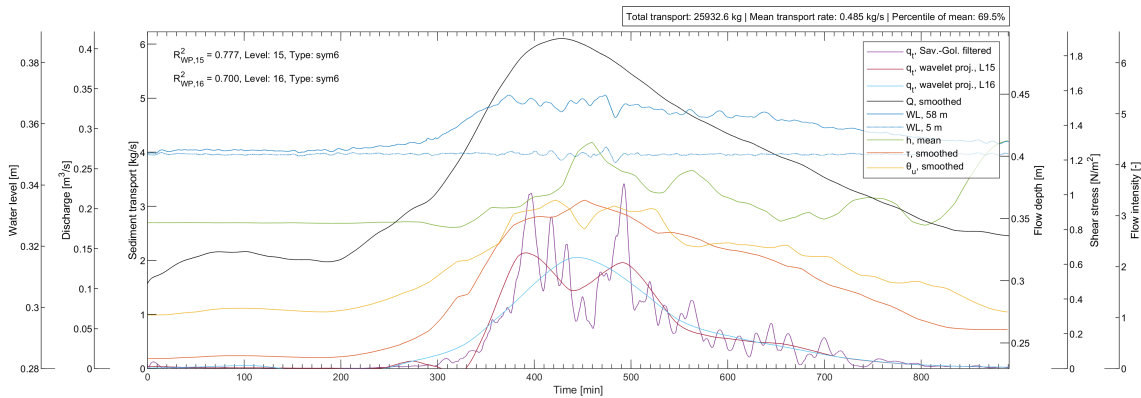


Figure 73: Discharge hydrograph with filtered sediment transport rate over time, wavelet projections L15 and L16, selected water levels, flow depth, shear stress and mean flow intensity during the full duration of Q409-H35-U

The second transport peak is due to a superposition effect from sediment recirculation: A considerable amount of the mobilized sediment, which was transported upstream to the beginning of the reservoir in large quantities during the reservoir flushing preceding the flood peak, already reached the sediment transport measurement system for a second time, at this time due to the very high migration velocity of the bed. This can also be seen in the development of the bed elevation, indicated through the flow depth, which is already sinking again at this point (about 490 minutes), indicating an increase in the amount of sediment upstream of the weir. The water surface gradient, which is slowly decreasing at that time already due to the rapidly sinking discharge, is only partly responsible for the sinking flow depth. The fact that the flow depth during the second peak of sediment transport is nevertheless significantly greater than during the first peak is partly due to the increased bedform resistance after the hydrograph peak and partly to the measurement procedure for the bed survey: The migration velocity of the bed was very high in the area of the flood peak and the bed survey took place only every 15 min, so that the measurement uncertainty was higher here than in the other experiments due to the relatively low sampling rate compared to the extreme dynamic of the reservoir bed.

It should also be mentioned that the water surface gradient does not remain constant over a longer period of time, as initially expected from the other experiments, and only decreases again at significantly lower transport rates than in the rising limb (cf. Figure 69 and Figure 70). Instead, it already decreases during the second transport peak, which can be interpreted as an indication that the permanent activation of large amounts of sediment in the active transport layer during the flood peak has a non-negligible influence on the flow resistance and that it already decreased when the transition zone to the upper flow regime was left by the reduction of the discharge and hence the hydraulic stress. In general, hydraulic and morphodynamic processes strongly overlap and are shifted in their temporal

evolution due to the extremely high rate of change of discharge, and it is very difficult, if not impossible from the presented data, to unravel the individual parts of each of the interdependent parameters.

The scenario with the same hydrograph and the lower initial water depth, scenario Q409-H30-U, could not be completed in the test facility because the sediment trap and recirculation system were clogged due to an overload of transported sediment. The second rather pointed hydrograph was used in scenarios Q193-H21-U and Q193-H30-U. Figure 74 shows the data from the scenario with the lowest initial water depth of 21.25 cm, Q193-H21-U. This experiment was particularly difficult to analyze because the reservoir bed was on the verge of transition to the upper plane bed, but was still in the state of dune formation as could be seen in the pooled analyses of the equilibrium bed experiments in chapter 4.2.

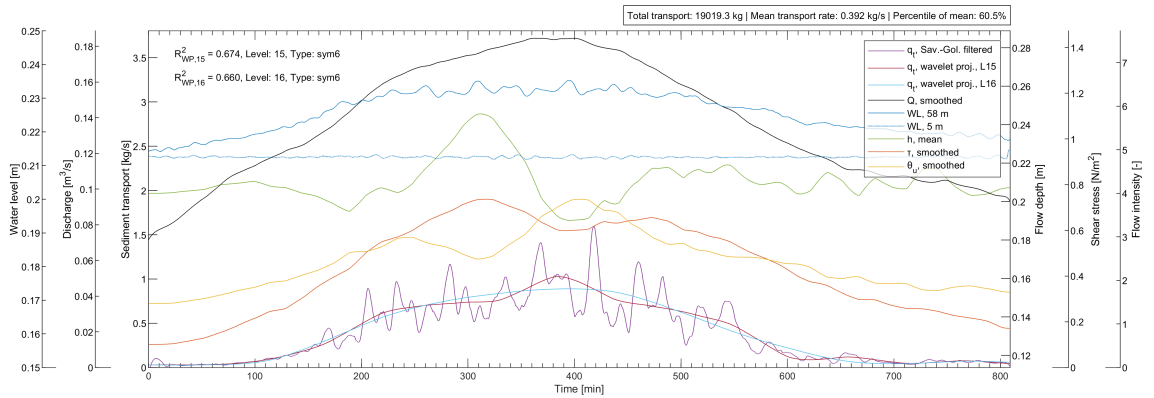


Figure 74: Discharge hydrograph with filtered sediment transport rate over time, wavelet projections L15 and L16, selected water levels, flow depth, shear stress and mean flow intensity during the full duration of Q193-H21-U

In the rising limb of the hydrograph nothing unexpected happens for the first 220 to 230 minutes: the sediment transport rate increases relatively continuously with the increasing discharge and in increasing water surface gradient. From about 220 to 320 minutes on the time axis, however, the lower level wavelet projection L15 stays almost constant for quite a long time, while the discharge continues to increase. Also, the shear stress almost monotonically increases with the discharge, until at a about 0.75 N/m^2 (about 320 minutes) the shear stress starts to decrease again, while none of this seems to affect the sediment transport rate.

This effect was due to a combination of events: A relatively rapid increase in discharge along the rising limb of the hydrograph lowered the mean bed elevation in the study area of the river reservoir during the first stage of the experiment, increasing flow depth and decreasing mean flow intensities (starting at 240 minutes), so that no further increase in the sediment transport rate occurred despite the continued increase in discharge. Meanwhile, bed evolution continued and generated higher flow resistance due to better developed bedforms. As sediment that had been flushed from the reservoir during the first

stage of the experiment, when the initial plane bed had little to no bedforms, re-entered the study area from upstream, the flow depth decreased again, thereby significantly increasing the mean flow intensity and creating a sediment transport peak around the time of the hydrograph peak at around 380 to 390 minutes.

There are two different reasons that explain the monotonic increase of the shear stress: First, it increased with the water surface gradient (up to 230 minutes), and then, just as the surface gradient became constant at slightly below 0.4 ‰ (and thus only slightly below the surface gradient at dynamic equilibrium of slightly above 0.4 ‰), shear stress continued to increase with flow depth from 230-240 minutes on until it almost reached the threshold for transition to the upper plane bed of about 0.8 N/m². However, this did not occur as the flow depth decreased significantly when more sediment from the upstream part of the reservoir reached the study area. A decrease in shear stress with increasing flow velocity due to lower flow depth or higher bed elevation, respectively, sounds like a contradiction, but can be explained with the function for calculating shear stress from bed slope (cf. chapter 2.1.2).

The water surface gradient remains more or less constant during the large changes in flow depth and shear stress, and this is because it is already by definition an averaged parameter. It does not directly respond to local flow fluctuations due to local bedforms because it is formed by the total flow resistance of the bed, which implicitly includes these local variations, to put it simply. Thus, the shear stress calculation performed here is inaccurate to some extent because the flow depth h from the measured data seems to fluctuate too much in the present case: the measured mean flow depth is not the actual mean flow depth because it was measured and averaged at only three locations, and these were apparently not enough sampling locations.

For the sediment transport rate, the local maximum and only peak in L15 appears below the peak of the hydrograph, which is to some extent a coincidence because at that time the sediment availability in the measurement area was high, but also because only at the discharge peak the higher transport rates could have been reached. In addition in this scenario, the peak discharge of the hydrograph is about 4 % lower than in the steady-state experiments to which it is compared, which also explains the lower absolute transport rates in scenario Q193-H21-U compared to Q193-H21. However, the lower sediment transport rate, which does not even have a true peak in trend line L16, is due to the stabilizing bedforms for which the discharge increase along the hydrograph was not rapid enough to overcome them prior to their formation and cause a true flushing effect.

In scenario Q193-H30-U with the higher initial water depth, as in scenario Q162-H30-U, not much that is worth reporting actually happens because the peak discharge of hydrograph is

too low (see Figure 75). An interesting feature is the time lag of the effect of increasing sediment transport under the hydrograph on the flow depth, which does not change much until after the flood peak at about 450 to 550 minutes. Scenario Q193-H21-U in particular shows how challenging it can be to interpret this kind of experimental data and that it is very easy to be misled by investigating only a single measurement parameter, especially under unsteady flow conditions.

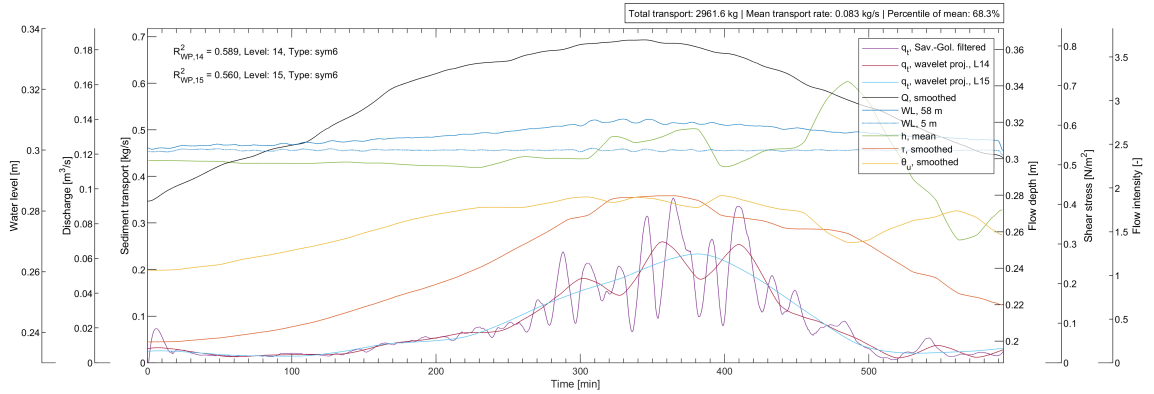


Figure 75: Discharge hydrograph with filtered sediment transport rate over time, wavelet projections L14 and L15, selected water levels, flow depth, shear stress and mean flow intensity during the full duration of Q193-H30-U

5.2.3. Comparison with dynamic equilibrium

Finally, the unsteady flood hydrograph scenarios are contrasted with results from the steady-state experiments of phase 1 (cf. chapter 4) in Table 10. Subdivided by peak width of the flood hydrograph, differences in mean sediment transport rate, mean shear stress and mean flow intensity are listed. For the steady-state experiments, the mean values determined in chapter 4.2 were used (cf. Figure 54) and for the unsteady experiments, the maximum of the largest level wavelet projection per scenario serving as trend line for the sediment transport rate. The difference of these two values was calculated from $\Delta q_s = q_{s,trend,max} - q_{s,mean}$ to make a generalized statement on the difference in bed evolution due to different hydraulic conditions. However, as already discussed, these values can only be viewed as a rough indicator for the actual morphodynamics in the respective scenarios.

In order to associate these values with the course of the hydrograph, the time difference between the hydrograph peak and the sediment transport rate maximum from the wavelet projection $\Delta t_{trend,max} = t_{trend,max} - t_{peak}$ was estimated. Furthermore, shear stress and mean flow intensity at the time of $q_{s,trend,max}$ are listed in Table 10, even though these single values are not highly informative due to the strong fluctuations of these values over time and depending on the local bed elevation. To compensate for the variable time lag between sediment transport rate measurement and data monitoring in the measured reservoir area,

the average shear stress and flow intensity of the 30 minutes prior to the sediment transport rate measurement are also listed.

Scenario		wide peaks					pointed peaks		
		Q325-H35	Q325-H30-1	Q325-H30-2	Q162-H21	Q162-H30	Q409-H35	Q193-H21	Q193-H30
$q_{s,mean}$	[kg/s]	1.01	1.70	1.70	0.67	0.11	1.85	1.11	0.23
$q_{s,trend,max}$	[kg/s]	1.12	1.75	1.83	0.58	0.05	2.05	0.89	0.23
Δq_s	[%]	11	3	8	-14	-53	11	-20	1
$\Delta t_{trend,max}$	[min]	-44	-55	-59	4	64	16	33	37
$\Delta \tau$	[%]	3	3	1	-8	-26	9	-25	-3
$\Delta \tau_{30min}$	[%]	0	4	1	-9	-27	3	-1	-21
$\Delta \theta_u$	[%]	-7	-1	-9	-3	9	-19	18	-17
$\Delta \theta_{u,30min}$	[%]	-5	-3	-8	-4	9	-10	-15	11

Table 10: Comparison of average sediment transport in stationary and instationary experiments

For scenario Q325-H35-U, even though dune formation was still taking place, transport rates rose higher during the flood hydrograph than in the steady-state experiment, despite a broad peak and thus a relatively long time for stabilizing bed transformation processes. A flushing effect occurred under the rising hydrograph limb because the reservoir bed was not yet optimally adapted to the increasing hydraulic stress. This is confirmed by the decreasing sediment transport rate trend during the peak plateau. Shear stresses were about the same although there was less bed resistance, which can be seen from the lower mean flow intensities, but there was more sediment transport and these effects largely cancelled each other out.

For scenarios Q325-H30-U-1 and Q325-H30-U-2, the reservoir bed reached the transition zone to the upper flow regime, and dune formation was largely hindered by the high hydraulic stress. As a consequence, bed resistance did not develop in a comparable manner to Q325-H35-U and the sediment transport rate trend was in the range of the mean sediment transport rates during the steady-state experiment. It was a bit higher, which can be attributed to initial flushing effects and the shorter duration of the hydrograph experiment, but it is below the sediment transport rate in Q325-H35-U. Besides, $q_{s,trend,max}$ varied about 5 % in the two identical experiments, which is why 5 % can be used as an estimate for uncertainty in all of these comparisons. The shear stress was slightly higher

and the flow intensity slightly lower compared to the steady-state experiment, and they are consistent with the findings in scenario Q325-H35-U.

For scenario Q162-H21-U, similar results scenario Q325-H35-U could be expected, since significant dune formation occurred in the steady-state experiment and a flushing effect could have occurred, too, due to the strong increase of discharge in the rising limb of the hydrograph. However, due to the, in absolute terms, only moderate hydraulic stress caused by the relatively small peak discharge of the hydrograph, bed transformation took place without a measurable flushing effect, resulting in lower sediment transport rates and smaller shear stresses than in the steady-state experiment. The processes of flushing due to discharge increase are compensated by bed stabilization in this case.

For scenario Q162-H30-U, with the same hydrograph as scenario Q162-H21-U but higher initial water depth, there was a greater flow depth and thus even smaller hydraulic stress. However, it is interesting to note in Table 10 that the mean flow velocity is about 9 % higher, reflecting the lower total bed resistance due to less bedforms (which needed much longer to form in the steady-state experiments) with higher mean flow velocities.

Scenario Q409-H35-U had the highest sediment transport rates of all experiments. The reservoir bed was in the transition zone to the upper flow regime and, comparable to scenarios Q325-H30-U-1 and Q325-H30-U-2, an approximately equal sediment transport trend would be expected in comparison with the steady-state experiment. However, due to the very high and steep flood peak, a significant flushing effect occurred, and the sediment transport rate was higher. Shear stresses were also higher, but the mean flow velocity was significantly lower, which again can be seen as an indication of lower total flow resistance due to the extreme hydraulic stress in the transition to the upper flow regime and increased flow depths.

For scenario Q193-H21-U, the hydraulic stress was significantly smaller than in scenario Q409-H35-U, and dune formation took place. As a consequence of low sediment availability after a first small flushing effect in the beginning of the hydrograph, bed stabilization through dune development took place even though the discharge was continually increasing. Thus, the sediment transport rate trend maximum is significantly lower, even though higher sediment transport as compared to the steady-state experiment could have been expected. Furthermore, this is also why shear stresses are also lower and mean flow intensity higher during the time of evaluation.

For scenario Q193-H30-U, comparable mean sediment transport rates were observed as a combination of an initial flushing effect and the short duration of the experiment. The

reservoir bed did not have much time to stabilize, while at the same time the hydraulic stress was not high enough to induce an actual flushing effect. This experiment serves as an example for the different time scales in the reservoir. The transformation of the bed is slower than the change of the discharge, and due to the water level control also slower than the change of hydraulic stress on the bed and these processes overlap, however all of this is not visible from the mean values in in Table 10.

6. Discussion and applicability

Flow resistance as a function of flood hydrograph

The following relationships can be derived from the two previous chapters on data evaluation of the dynamic bed equilibrium experiments in phase 1 and the flood hydrographs in phase 2: The reservoir bed transports more sediment after the peak of the hydrograph than before at the same discharges and thereby causes a higher flow resistance due to the better developed bed structures (τ''). Transported sediment also absorbs downstream forces and thereby increases the flow resistance (τ'''). The longitudinal water surface gradient is correspondingly larger, since more potential energy from the water level is required to overcome the increased bed roughness; the shear stresses determined from the water surface gradient are also higher, which can be seen as an indicator of the bed being stabilized against erosion. At the same time, only lower hydraulic stress in the form of flow velocity is required to set the bed in motion, and the flow intensity as well as the critical Shields parameter decrease. This has also been found in other studies, e.g. Chiew and Parker (1994).

This shows that the comparison of the reservoir bed after the hydrograph peak with the initial plane bed at the beginning of the experiments is, so to speak, only an academic special case, because the perfectly plane bed does not exist in nature in general. Our own unpublished investigations on the temporal development of reservoir beds characterized by bedforms after extreme flood events, over which for a longer period of time only a discharge equal to a 2-year flood discharge had flowed, show a continuous reduction of the dimensions of the bed forms towards the smaller equilibrium bedforms typical for the corresponding low discharge. Accordingly, the initial plane bed used, while smoother than typical in nature, was chosen because the slope for an initial bed was not known and the one "correct" initial bed slope did not exist by definition in this case. The specification of an artificial bed roughness would have been inaccurate and, to a certain extent, arbitrary, and would have required considerable additional effort for the implementation in a numerical model. Therefore, the best condition to compare academically was the plane initial bed. All described morphodynamic and morphological processes would have taken place in either case, only with a slight difference at the beginning of the experiments: The water surface gradient would have been higher a little earlier and sediment transport would have started a little earlier, too.

Following the reasoning, less sediment transport takes place along the flat reservoir bed and in the falling limb of the hydrograph the bed transports more material than before,

because the high discharges in the region of the hydrograph peak have created too large bedforms, which then no longer fit the decreasing discharges and need to be transformed again. Due to the bedforms, however, there is a larger energy line and water surface gradient and, as a consequence, the shear stresses are thus significantly higher after the hydrograph than before the hydrograph for the same discharge. This in turn results in more sediment being transported after the hydrograph for the same discharge. The bed has more regions of changing flow velocity due to large bedforms, localized eddy formation due to these velocity changes, and thus an overall increased transport capacity. Thus, the bed transports more sediment after the hydrograph. At the same time, however, the bedforms dissipate more kinetic energy than a flat bed with a comparable mean longitudinal bed gradient, which in turn accounts for the increased energy line gradient. Increased bed roughness thus reduces flow velocity (cf. Manning-Strickler equation with $u = k_{St} R_h^{2/3} I^{1/2}$) and, if discharge and water level at the control level remain constant due to water level control, this increased flow resistance leads to backwatering and buildup of additional potential energy further upstream. As a result, the flow depth upstream is increased in the first instance, but this causes the flow velocity to decrease and sediment to settle along the reservoir until the bed slope is again equal to the water surface gradient on average.

Challenges estimating shear stress

The impression has arisen occasionally in the analysis of the experiments from phase 2 that the shear stress generally increases as the flow depth increases. This is due to the calculation of the shear stress using the bed slope approach and locally and temporarily this increase may indeed occur: higher flow depth equals higher hydrostatic pressure, thus higher shear stress. Globally, however, this is not the case in general. The flow depth and the water surface gradient balance each other out, which, due to the water level control, can only be realized by the water surface gradient, thus the mean bed slope and bed roughness. At constant discharge in subcritical flow, a locally higher flow depth leads to locally lower flow velocities with disproportionately lower flow losses ($\alpha u^2/2g$, cf. Figure 1) at simultaneously higher local shear stress. Viewed over the entire reservoir, however, an overall greater flow depth means a lower energy line gradient, thus less transport and an increasing mean bed elevation, with the consequence that the shear stress also decreases (both energy line gradient and flow depth decrease), although much longer time scales are always assumed here. In the opposite case, the water surface gradient must increase disproportionately for a smaller flow depth to compensate for the losses, and as a result the shear stress increases, even if the hydrostatic pressure on the bed has decreased due to the lower flow depth; but it has just less decreased than the water level gradient or the energy

line gradient. However, since the flow depth was constant on average in all experiments, the shear stress increased on average with the increasing water surface gradient.

If τ is calculated with the formula $\rho C_f u^2$ instead of $\rho g h I$ (both chapter 2.1.1), the relationship between shear stress and flow velocity becomes even clearer. If the flow depth decreases, the flow velocity increases immediately, which is included in the shear stress with the power of two. However, lower flow depths also reduce the roughness C_f medium-term, because bedforms become more elongated, at least in the flow region with dune formation, which explains the decrease in τ in the transition zone in Figure 7. The fact that this was not the case in the experiments with lightweight sediment analyzed here (cf. Figure 53, right) is presumably due to the relatively higher influence of τ''' (thicker transport layer) compared to τ'' (shape roughness). With sand, transport layers are not as thick, presumably, due to vertical distortion in the lightweight sediment experiments, and the bedforms are more stable, in fact, because of their significantly higher relative weight under water (cf. ASCE Task Committee (2000)).

Either way, shear stresses increase with a larger water surface gradient due to the higher bed roughness. If the bed were smooth instead of full of bedforms, the water surface gradient would be smaller, but the flow velocity would still be higher, because the water surface gradient only enters the flow velocity with the root (cf. Manning-Strickler equation), i.e. it has a smaller effect than the roughness. The shear stresses would then be lower due to the smaller water surface gradient and smaller flow depth. In fact, less would have to be transported and it can be assumed that as long as the bed is smooth, the individual particles are exposed to little flow impact. The shear stresses are then indeed low, because there is little impact surface and almost only tangential stress, despite the high flow velocity. However, as soon as the flat bed is "broken up", which always happens sooner or later depending on the level of hydraulic stress, bedforms develop, resulting in a dramatic increase in shear stress, but also a corresponding increase in the water surface gradient due to the increased flow resistance, and the flow depth increases with the flow velocity decreasing.

Stabilizing effects of bedforms

In the hydrograph experiments of phase 2, we can very well see what has just been discussed. Because the initial plane bed cannot persist due to small disturbances in the bed surface, erosion begins at some point. At first uniformly over the entire reservoir, but then local vortices form around the transported particles, causing them to detach and gradually develop the characteristic bedforms. The whole process continues until the dunes are formed in such a way that they are eroded only as little as possible while the hydraulic

energy loss due to friction is minimal: every natural system strives for its lowest-energy state, in this case dynamic bed equilibrium. The respective bed state, which occurs after some time, must therefore be regarded as the one that allows only the least possible transport, i.e. the bed has exactly those bedforms that offer the greatest possible flow resistance. This sounds paradoxical: transport increases through bedform structures, but just the least compared to all other conditions. These bedforms represent the lowest-energy state of the bed because the flat bed with transport cannot exist - it is just not the lowest-energy state: it is a triviality, in fact, but high flow velocities cause little friction losses only when there is little friction. The more sediment is in motion, the more turbulence is present, energy losses rise and so forth. Therefore, sediment transport rates during the hydrograph peak would have to be higher than during dynamic equilibrium because the lowest-energy state could not yet be established.

Evaluation of the methodology

The fact that all these parameter connections can be discussed to this extent at all is due to the high quality of the data and the experimental design. Nevertheless, the results contain many uncertainties, which have already been discussed at the respective points in this thesis. Starting with the measurement accuracy of the individual measuring systems, moving on to the uncertainties resulting from inflow and reservoir control (at least in the unsteady experiments); then to the discontinuous measurement of the reservoir bed, the mean bed surface sections derived from this, the resulting fluctuations in flow depth and the parameters linked to it; then again on to the filtering and post-processing methods used, in particular for the very strongly fluctuating sediment transport rates; through to the derived parameter means, which were used to compare the experiments with each other and which, to a certain extent, can only reflect a small part of the in fact overlapping processes in only a sub-complex manner. In the experiments with dynamic bed equilibrium, however, these process uncertainties played a much smaller role than in the unsteady experiments due to the good statistical analysis possibilities.

It is true that the created data sets offer an immense potential for further in-depth analysis with the wide variety of evaluation measures presented in the literature to date (cf. among others Henning (2013), Gutierrez et al. (2017) or Reich (2020)), but in the present case, and due to the vast amount of data, this was not possible within the scope of only one dissertation. Some of the data have not even been presented here, namely quasi-continuous velocity data coupled with a point measurement of the moving bed below the ADV probes. Hence, it would be of great value if the existing data were analyzed further. They could, for

example, allow more profound conclusions to be drawn about the time dependence of shear stress at local and global scales.

Challenges and opportunities of lightweight sediment

In the presented laboratory experiment, largely only bedload transport occurred. Compared to the field, this is a non-similar simplification, because suspended sediment transport occurs more intensively there at high transport rates. In the experiments, instead, the used lightweight sediment behaved differently in that, although it is generally more mobile, it nevertheless remained near the bed for longer under increasing hydraulic stress and moved forward at high velocity in an active transport layer several centimeters thick, rather than being largely suspended. This effect, however, was only partly due to the relatively smaller flow impact on the single grains due to their off-scale grain diameter, but to the overall altered flow situation due to the vertical distortion.

As a consequence, the ever-present vertical exaggeration of the morphodynamic processes when using lightweight sediment (cf. chapter 2.3.1) is a generally not negligible component in all conducted experiments. This was well visible, for example, in the fact that relative dune heights ($\Delta_{\text{rel}} = \Delta/h$) were significantly higher in the present experiments than for sand dunes (factor 2 to 4.5) coming from the literature. At the same time, and surprisingly, the expected vertical distortion due solely to the definition of the lightweight sediment grain size was given with $n = 5.7$ (cf. chapter 3.1.2), and it is thus about 1.5 to 2.5 times higher than the mean relative dune height in this study would indicate. Furthermore, dune shape, described via the very simple shape parameter dune steepness Δ/λ , was comparable to that in sand dunes from the field and laboratory (cf. chapter 4.2.1). Similar observations of in fact reduced influence of vertical exaggeration on relative dune height in lightweight sediments were made by Gorrick and Rodriguez (2014) and Schäfer et al. (2021), among others.

Based on these findings, it would be highly interesting to carry out further fundamental studies on the actual influence of vertical model exaggeration on sediment transport processes, in which the influence on the sediment transport rate would then be quantified in addition to further statements on bedform evolution. Potentially, such an approach could enable reliable transferability of physical model experiments with large scale numbers, where the previously used approaches of similarity theory would actually not allow it. Similar thoughts on this matter were already expressed by Yalin (1971).

Using the measured data for numerical computations

Notwithstanding these possible developments in physical modeling with lightweight sediments, the results of this present investigation can be directly used for comparative studies with numerical programs. Some examples are the review of the various transport formulas, the numerical representation of bedforms and their temporal variability in terms of statistically random distributions of morphodynamic processes along the reservoir bed, the influence of turbulence models on flow depth and secondary flows in the reservoir cross sections, temporal bedform evolution or the formation and remobilization of sedimentation and erosion zones. In the context of the retention potential study at the Inn (Huber et al. unpublished), calculations with 2D and 3D hydro-morphodynamic numerical models were carried based on the assumption that the cohesionless transport processes of lightweight sediment do not substantially differ physically from those of natural sediments. Thus, findings on the performance and model quality of the numerical programs can be obtained independently of the used sediment.

With the help of the generated experimental data, a detailed analysis of the results quality of the numerical software TELEMAC-2D with the sediment module SISYPHE was carried out. Missing vertical velocity components led to a smoothing tendency of the reservoir bed and thus to the equalization of local bed irregularities in model areas with little transverse flow impact. Temporally variable bedforms did not develop in contrast to the laboratory experiments. Furthermore, the potential and associated effort of setting up and conducting 3D numerical sediment simulations was demonstrated. Unlike TELEMAC-2D, TELEMAC-3D was able to model temporally and spatially random bedforms under otherwise constant boundary conditions (compare e.g. Goll (2017)).

The methodology used in this study with comparison of dynamic bed equilibrium and flood hydrographs can also be applied to any reservoir geometry, but there are additional effects, e.g., secondary currents, sorting processes in more widely graded sediments, stronger water level fluctuations, and so on. Therefore, it is advisable to have knowledge about the dominant morphodynamic phenomena in the slightly less complex straight reservoir and, based on this, to consider more complex flow and boundary conditions. For such an experiment with a more complex reservoir geometry, the results of the conducted physical experiments are shown in Figure 76, as well as for a 2D and a 3D RANS simulation using the TELEMAC-MASCARET software system. The selected plot shows the mean bed surface in the reservoir during a dynamic equilibrium experiment performed in the same test facility and in the same manner as in this study, differing only in the geometry of the investigated reservoir as presented in chapter 3.2. Unlike in the straight reservoir, the reservoir bed in

the curved reservoir developed not only the dunes already known to fluctuate strongly and relatively quickly in time, but also rather permanent areas of erosion and sedimentation that fluctuated much more slowly in size and location.

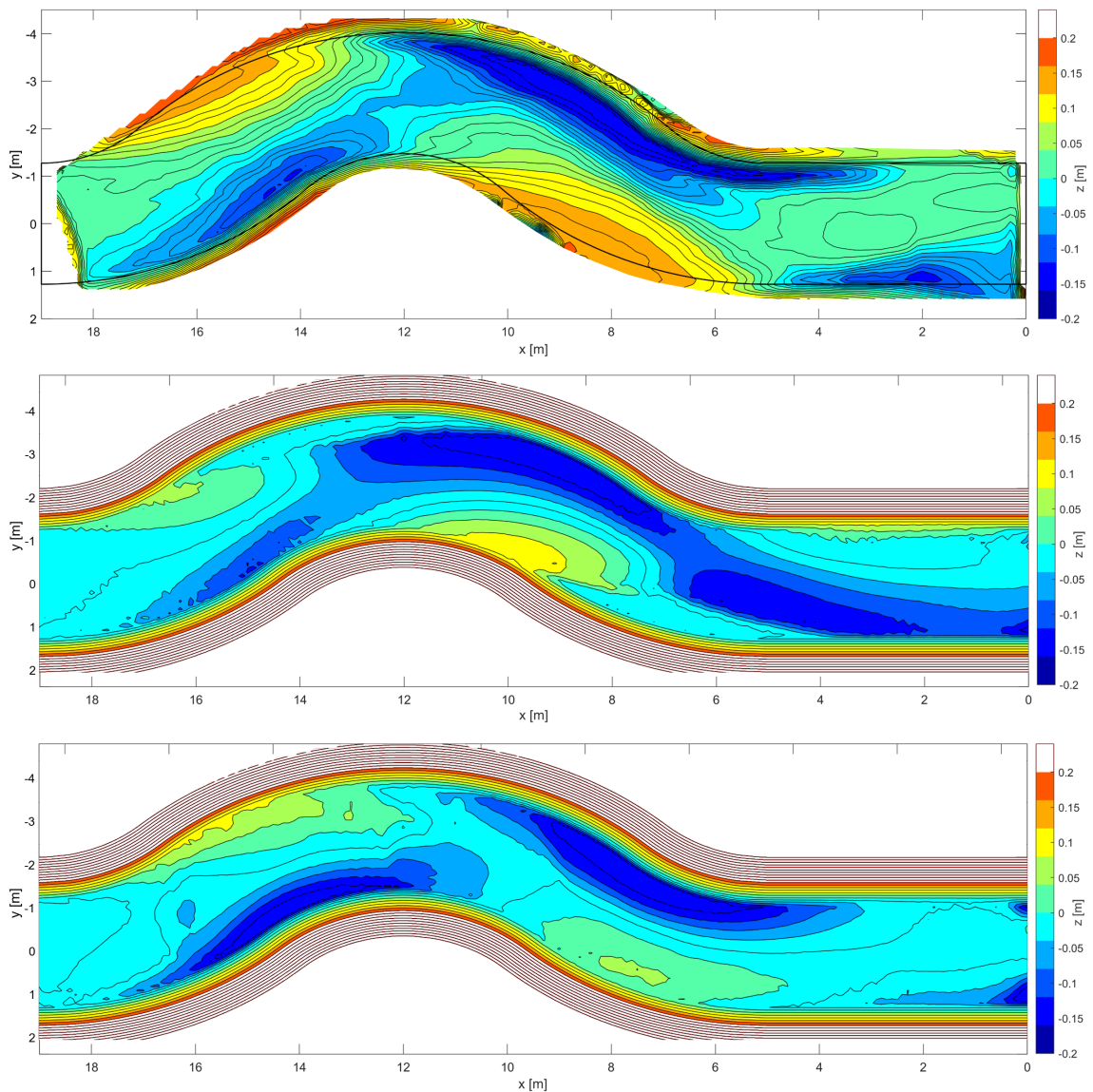


Figure 76: Comparison of the mean bed surface of an experiment with dynamic bed equilibrium in the physical experiment (top), 2D RANS model (center) and 3D RANS model (bottom) (Huber et al. unpublished)

The mean reservoir bed surfaces calculated in the numerical simulations showed good agreement with the measured reservoir beds in some cases, although there were still discrepancies. These could have been reduced to an even greater extent, especially in the 3D model, because the programmatic possibilities for taking relevant morphodynamic processes into account are greater here than in the 2D model, although they are also associated with considerably greater computational effort. Particularly large differences were found in the temporal variability of the bed: This variability was represented to a comparable extent to the measured bed only in the 3D model, while it was increasingly reduced for the 2D model with increasing experiment duration and could only be

reactivated by modified hydraulic boundary conditions. For a detailed analysis of this and other examples, please refer to the report of the retention potential study at the Inn (Huber et al. unpublished), which had not yet been published at the time of writing this thesis.

7. Conclusion

This study presented a methodology to investigate the interaction of hydraulic and morphodynamic processes as they occur in a fully sedimented run-of-river reservoir of a physical laboratory experiment with lightweight sediment. Equal emphasis was placed on measurement accuracy for process description and accessibility of the measured data for numerical comparative calculations. The two-stage experimental concept with experiments on dynamic bed equilibrium and flood hydrographs allowed detailed insights into fundamental bed morphodynamic processes, their influence on morphological bed development and the interdependency of various process parameters important for scientific description. The sediment transport rate, the bed shear stress and the mean flow intensity played a special role in this context and allowed the description of different, partly simultaneous hydraulic and morphodynamic processes.

The high-performance experiment setup allowed the generation of a wide range of hydraulic conditions beyond the usual range of comparable physical experiments, so that high quality data sets could be generated up into the transition region to the upper plane bed flow regime with extremely high transport rates. The use of an online recirculation for the reservoir sediment required a great deal of preliminary work and fine-tuning, but then enabled experimental conditions that would otherwise only be encountered in the field. Further extension of the length of the experimental run-of-river reservoir and measurements of the reservoir bed over a longer distance could have allowed the derivation of a design parameter for required length dimensions for such experiments, but this could not be implemented in the context of the present study due to limitations in the online recirculation. It would have been highly valuable for the ease of implementation of such models, however.

The high data quality of the experiments also made it possible to quantify flushing effects during the rising (and falling) limb of flood hydrographs. Since transferability of the experiments to nature was subject to considerable uncertainties and would only be possible within very narrow limits due to the similarity-theoretical restrictions imposed by the choice of sediment, these observed effects serve to better understand fundamental processes in sediment transport in general as well as to test, verify and, if necessary, optimize numerical models. At this point, however, the online recirculation of the sediment in the river reservoir was also a limiting factor for a close-to-nature description of morphological processes: during the unsteady experiments, various hydraulic and morphodynamic phenomena overlapped with the variable sediment availability caused by the experiment setup with a constant amount of sediment in the reservoir, so that the

evaluation of these experiments was made more difficult and the significance of observations made was reduced accordingly. Nonetheless, it was very valuable to have the methodological ability to at least detect the presence of multiple overlapping effects.

Another advantage of the experiment setup was its modularity, especially for future studies. With relatively little additional effort, the test facility could be used for a variety of other purposes. Under otherwise identical conditions, almost arbitrarily complex geometries could be generated, which then also significantly change the hydraulic and morphodynamic conditions in the river reservoir and thus offer a wide field of research possibilities, especially for the optimization of numerical models. Likewise, the measurements of the ceiling camera for the spatial analysis of the morphological processes in the experimental reservoir, which were not analyzed in detail in this study, as well as the continuous measurements of the flow velocity along the reservoir centerline, which were also carried out during all experiments, offer opportunities for further investigations.

In addition to the classical hydro-morphodynamic numerical computations, the research design of the present study with a wide range of hydraulic and morphodynamic conditions offers great potential for the implementation of machine learning algorithms. There has been a lot of research also in the field of hydraulic and sediment engineering in the recent years, which showed promising results for training so-called artificial neural networks (comprehensive explanations and application examples can be found in Kaveh (2019)). The major advantage of these neural networks over numerical models is their implicitness, which does not require a complete resolution of the physical processes occurring in the experiment or in the field. This implicitness, however, is also their greatest weakness, because the prediction quality of the neural network - its algorithm design and software build are not considered here - depends exclusively on the quality of the training data. Consequently, the more erroneous these data are, the lower is the prediction quality of the neural network. Therefore, the quality and structure of the data of this study seem well suited for machine learning algorithms.

Above all, in the context of the many open questions in the field of sediment transport modeling, lightweight sediments offer immense potential for fundamental process investigations as well as for specific applications, for which, to this day, only a similarity model could provide the necessary answers. There are still many unanswered questions that would allow a reliable quantification of the uncertainties in transferability to nature and thus increase the inhibition threshold to use lightweight sediments in physical experiments. Hopefully, this work will contribute to the re-emphasis of physical experiments with lightweight sediment in the scientific community.

Bibliography

- Aberle J, Rennie CD, Admiraal DM, Muste M. 2017. Experimental Hydraulics: Methods, Instrumentation, Data Processing and Management: Volume II: Instrumentation and Measurement Techniques. 1st ed. Aberle J, Rennie C, Admiraal D, Muste M, editors. CRC Press.
- Aguirre Iniguez D, Bui MD, Rutschmann P. unpublished. Endbericht für Teilprojekt E: Feststoffe am Inn und der Salzach. In: Retentionspotentialstudie am Inn. München.
- Amsler ML, García MH. 1997. Discussions of: Sand-Dune Geometry of Large Rivers during Floods. *Journal of Hydraulic Engineering*. 123(6):582–584.
- Ancey C. 2020a. Bedload transport: a walk between randomness and determinism. Part 1. The state of the art. *Journal of Hydraulic Research*. 58(1):1–17.
- Ancey C. 2020b. Bedload transport: a walk between randomness and determinism. Part 2. Challenges and prospects. *Journal of Hydraulic Research*. 58(1):18–33.
- Annandale GW. 2014. Sustainable water supply, climate change and reservoir sedimentation management: Technical and economic viability. In: Reservoir sedimentation - special session on reservoir sedimentation of the Seventh International Conference on Fluvial Hydraulics (River Flow 2014), IAHR Committee on Fluvial Hydraulics, EPFL Lausanne, Switzerland, 3-5 September 2014.
- Armanini A. 2018. Principles of River Hydraulics. Cham: Springer International Publishing.
- ASCE. 1962. Sediment Transportation Mechanics: Introduction and Properties of Sediment. *Journal of the Hydraulics Division*. HY 4.
- ASCE Task Committee. 2000. Hydraulic Modeling: Concepts and Practice. Ettema R, editor. Reston, VA: American Society of Civil Engineers.
- ASCE Task Committee. 2002. Flow and transport over dunes. *Journal of Hydraulic Engineering*. 128(8):726–728.
- Ashley GM. 1990. Classification of Large-Scale Subaqueous Bedforms: A New Look at an Old Problem. *Journal of Sedimentary Petrology*. 60(1):160–172.
- Åström KJ, Murray RM. 2008. Feedback systems: an introduction for scientists and engineers. Princeton: Princeton University Press.
- ATV-DVWK, editor. 2003. Feststofftransportmodelle für Fließgewässer. Hennef: ATV-DVWK Deutsche Vereinigung für Wasserwirtschaft, Abwasser und Abfall e.V.
- Bagnold RA. 1956. The Flow of Cohesionless Grains in Fluids. *Philosophical Transactions of the Royal Society of London Series A, Mathematical and Physical Sciences*. 249(964):235–297.
- Bechteler W, Vogel G, Vollmers HJ. 1991. Model investigations on the sediment transport of a lower alpine river. In: *Fluvial Hydraulics of Mountain Regions*. Vol. 37. Berlin, Heidelberg: Springer Berlin Heidelberg; p. 179–194.
- Becker I, Egger G, Müller N, Reich M. 2020. Auswirkungen der Ausleitung der Oberen Isar auf die Auenvegetation. 17:28–37.
- Bennett SJ, Best JL. 1995. Mean flow and turbulence structure over fixed, two-dimensional dunes: implications for sediment transport and bedform stability. *Sedimentology*. 42(3):491–513.
- Best J. 1992. On the entrainment of sediment and initiation of bed defects: insights from recent developments within turbulent boundary layer research. *Sedimentology*. 39(5):797–811.

- Best J. 2005. The fluid dynamics of river dunes: A review and some future research directions. *Journal of Geophysical Research*. 110(F04S02):21.
- Best JL. 1988. Sediment transport and bed morphology at river channel confluences. *Sedimentology*. 35(3):481–498.
- Blöschl G, Komma J, Nester T. unpublished. Endbericht für Teilprojekt A: Stochastische Niederschlag-Abflussmodellierung zur Ermittlung des räumlichen Zusammenwirkens der Zubringerwellen. In: Retentionspotentialstudie am Inn. Wien.
- Bock N, Gökler G, Reindl R, Reingruber J, Schmalfuß R, Badura H, Frik G, Leobner I, Lettner J, Scharsching M, Spreitzer R, Thöni M-T. 2019. Feststoffmanagement bei Wasserkraftanlagen in Österreich. *Österreichische Wasser- und Abfallwirtschaft*. 71(3):125–136.
- Bollrich G. 2013. Technische Hydromechanik 1: Grundlagen. 7th ed. Beuth.
- Bonnefille R. 1963. Essais de synthese des lois de debut d'entraînement des sediments sous l'action d'un courant en regime uniform. *Bulletin du Centre de Recherche et d'Essais de Chatou*. 5:67–72.
- Brownlie WR. 1981. Prediction of flow depth and sediment discharge in open channels. Pasadena, CA.: California Institute of Technology.
- Burke Hubbard B. 1997. Wavelets. Basel: Birkhäuser Basel.
- Carling P. 1999. Subaqueous Gravel Dunes. *Journal of Sedimentary Research - J SEDIMENT RES*. 69.
- Chan-Braun C, García-Villalba M, Uhlmann M. 2011. Direct Numerical Simulation of Sediment Transport in Turbulent Open Channel Flow.
- Chanson H. 2004. Environmental hydraulics of open channel flows. Butterworth-Heinemann.
- Chiew Y-M, Parker G. 1994. Incipient sediment motion on non-horizontal slopes. *Journal of Hydraulic Research*. 32(5):649–660.
- Colebrook CF, White CM. 1937. Experiments with fluid friction in roughened pipes. *Proceedings of the Royal Society of London Series A - Mathematical and Physical Sciences*. 161(906):367–381.
- Coleman HW, Steele WG. 1995. Engineering application of experimental uncertainty analysis. *AIAA Journal*. 33(10):1888–1896.
- Coleman SE, Nikora VI. 2011. Fluvial dunes: initiation, characterization, flow structure. *Earth Surface Processes and Landforms*. 36(1):39–57.
- Coleman SE, Nikora VI, Aberle J. 2011. Interpretation of alluvial beds through bed-elevation distribution moments. *Water Resources Research*. 47(11).
- Dalrymple RA, editor. 1985. *Physical Modelling in Coastal Engineering*. 1st ed. CRC Press.
- Dey S. 2014. *Fluvial Hydrodynamics*. Berlin Heidelberg: Springer.
- DIN EN ISO 14688-1. 2020. Geotechnische Erkundung und Untersuchung — Benennung, Beschreibung und Klassifizierung von Boden — Teil 1: Benennung und Beschreibung (ISO 14688-1:2017); Deutsche Fassung EN ISO 14688-1:2018. Beuth Verlag GmbH.
- Diplas P, Kuhnle R, Gray J, Glysson D, Edwards T. 2008. Sediment transport measurements: Chapter 5. In: Marcelo H. García, editor. *Sedimentation engineering: processes, measurements, modeling, and practice*. American Society of Civil Engineers; p. 307–353.
- Disse M, Marcolini G, Willems W. unpublished. Endbericht für Teilprojekt B: Wellenstatistik mittels Copula-Verfahren. In: Retentionspotentialstudie am Inn. München.

- Dittrich A, Rosport M, Badde O. 1992. Untersuchungen zum Stabilitätsverhalten von Gerinnesohlen. Karlsruhe, Germany: Institut für Wasserbau und Kulturtechnik, Universität Fridericiana zu Karlsruhe.
- Dorer H. 1984. Ähnlichkeit bei flussbaulichen Modellen.
- Drosg M. 2009. Dealing with Uncertainties. Berlin, Heidelberg: Springer Berlin Heidelberg.
- DVWK, editor. 1993. Verlandung von Flußstauhaltungen: Morphologie, Bewirtschaftung, Umweltaspekte und Fallbeispiele. Hamburg: Parey.
- DWA, editor. 2014. Sedimentmanagement in Fließgewässern: Grundlagen, Methoden, Fallbeispiele. korrigierte Auflage Januar 2014. Hennef: Deutsche Vereinigung für Wasserwirtschaft, Abwasser und Abfall e.V.
- DWA, editor. 2018. Begriffe aus Gewässermorphodynamik und Flussbau. 1. Auflage. Hennef: Deutsche Vereinigung für Wasserwirtschaft, Abwasser und Abfall e.V.
- DWA, editor. 2021. Mehrdimensionale morphodynamisch-numerische Modelle für Fließgewässer. 1. Auflage. Hennef, Deutschland: Deutsche Vereinigung für Wasserwirtschaft, Abwasser und Abfall e.V.
- Engelund F, Hansen E. 1967. A monograph on sediment transport in alluvial streams. Copenhagen: Teknisk Forlag.
- Engelund FA, Fredsoe J. 1982. Sediment Ripples and Dunes. Annual Review of Fluid Mechanics. 14(1):13–37.
- Ettmer B. 2007. Physikalische Modellierung von Kolkprozessen. In: Wasserbauliches Versuchswesen. Karlsruhe: BAW; p. 107–118.
- Ettmer B, Hentschel B, Link O. 2021. Neue Wege in der experimentellen morphodynamischen Modellierung durch die Verwendung von Kunststoffgranulat-Sieblinien. WASSERWIRTSCHAFT. 111(5):16–22.
- Ettmer B, Hentschel B, Orlik S. 2017. Geschiebetransport im gegenständlichen Modell: Neue Ansätze zur naturähnlichen Abbildung komplexer morphodynamischer Prozesse. In: Kolloquium Wasserbauliche Herausforderungen an den Binnenschiffahrtsstraßen. Karlsruhe: Bundesanstalt für Wasserbau; p. 73–78.
- Ettmer B, Mueller F, Link O. 2015. Live-Bed Scour at Bridge Piers in a Lightweight Polystyrene Bed. Journal of Hydraulic Engineering. 141.
- EU Water Framework Directive. 2000. Directive 2000/60/EC of the European Parliament and of the Council of 23 October 2000 establishing a framework for Community action in the field of water policy.
- Fiedler K. 2008. Erfassung hydromorphologischer Vorgänge bei Hochwasser mit Hilfe von ADCP-Messungen.
- Fiedler K, Strobl T, Zunic F, Matthes H. 2008. Velocity gauging with ADCP in rivers with bedload and sediment transport.
- Flemming B. 1988. Zur Klassifikation subaquatischer, strömungstransversaler Transportkörper. In: Bochumer geologische und geotechnische Arbeiten. Vol. 29. Bochum, Germany; p. 44–47.
- Flemming B. 2000. The role of grain size, water depth and flow velocity as scaling factors controlling the size of subaqueous dunes. Marine Sandwave Dynamics, International Workshop, March 23-24 2000, University of Lille 1, France Proceedings Trentesaux A and Garlan T Ed, 240 pages.:55–61.
- Fredsoe J. 1982. Shape and Dimensions of Stationary Dunes in Rivers. Journal of the Hydraulics Division, ASCE. 108:932–947.
- Frings R, Hillebrand G, Gehres N, Banhold K, Schriever S, Hoffmann T. 2019. From source to mouth: Basin-scale morphodynamics of the Rhine River. Earth-Science Reviews. 196.

- Frings RM. 2018. Sedimentkontinuität als Leitprinzip des Flussgebietsmanagements - Sind wir auf dem richtigen Weg? Hydrologie und Wasserbewirtschaftung / BfG – Jahrgang: 62/2018.:4ISSN 1439.
- Frostick LE, McLelland SJ, Mercer TG, editors. 2011. Users guide to physical modelling and experimentation: Experience of the HYDRALAB network. 1. ed. Leiden, The Netherlands: CRC Press/Balkema.
- Gaida TC, Mohammadloo TH, Snellen M, Simons DG. 2019. Mapping the Seabed and Shallow Subsurface with Multi-Frequency Multibeam Echosounders. Remote Sensing. 12(1):52.
- García MH, editor. 2008. Sedimentation engineering - Processes, Measurements, Modeling, and Practice. Reston, Va: American Society of Civil Engineers.
- García MH, Laursen EM, Michel C, Buffington JM. 2000. The Legend of A. F. Shields. Journal of Hydraulic Engineering. 126(9):718–723.
- Gessler J. 1970. Self-Stabilizing Tendencies of Alluvial Channels. Journal of the Waterways, Harbors and Coastal Engineering Division. 96(2):235–249.
- Giesecke J, Heimerl S, Mosonyi E. 2014. Wasserkraftanlagen: Planung, Bau und Betrieb. Springer-Verlag.
- Goll A. 2017. 3D Numerical Modelling of Dune Formation and Dynamics in Inland Waterways. Karlsruhe: BAW.
- Gorrick S, Rodríguez JF. 2014. Scaling of sediment dynamics in a laboratory model of a sand-bed stream. Journal of Hydro-environment Research. 8(2):77–87.
- Graf WH. 1971. Hydraulics of Sediment Transport. McGraw-Hill Book Comp.
- Graf WH. 1984. Hydraulics of reservoir sedimentation. Lausanne: EPFL.
- Graf WH, Altinakar MS. 1998. Fluvial hydraulics: flow and transport processes in channels of simple geometry. Chichester; New York: Wiley.
- Green D. 2014. Modelling geomorphic systems: scaled physical models. In: Cook SJ Clarke, LE, Nield, JM, editor. Geomorphological Techniques (Online Edition). London, UK: British Society for Geomorphology.
- Gutierrez R, Mallma J, Nuñez-Gonzales F, Abad J. 2017. Bedforms-ATM (Bedforms analysis toolkit for multidimensional modeling).
- Guy HP, Simons DB, Richardson EV. 1966. Summary of Alluvial Channel Data from Flume Experiments, 1956–61. US Geological Survey Professional Paper. 462-I:vii+96.
- Gyr A, Hoyer K. 2006. Sediment Transport: A Geophysical Phenomenon. Berlin u.a.: Springer.
- Gyr A, Kinzelbach W, editors. 2003. Sedimentation and Sediment Transport. Dordrecht: Springer Netherlands.
- Haaland SE. 1983. Simple and Explicit Formulas for the Friction Factor in Turbulent Pipe Flow. Journal of Fluids Engineering. 105(1):89–90.
- Hager WH. 2018. Bed-load transport: advances up to 1945 and outlook into the future. Journal of Hydraulic Research. 56(5):596–607.
- Haimann M, Aigner J, Gmeiner P, Lalk P, Habersack H. 2018. Hochwasser und Feststoffe: vom Sedimenttransport zum flussmorphologischen Raumbedarf. Österreichische Wasser- und Abfallwirtschaft. 70(1):78–89.
- Harb G. 2016. Numerical Modeling of Sediment Transport Processes in Alpine Reservoirs. Verlag der TU Graz.

- Harb G, Badura H, Schneider J, Zenz G. 2015. Verlandungsproblematik bei Wasserkraftanlagen mit niedrigen Fallhöhen. Österreichische Wasser- und Abfallwirtschaft. 67(7–8):315–324.
- Hartmann S. 2009. Sediment Management in Alpine Reservoirs - Recommendations and Best Practice Guide. Neubiberg: Institut für Wasserwesen, Universität der Bundeswehr München.
- Hauer C. 2020. Sediment Management: Hydropower Improvement and Habitat Evaluation. Water. 12:3470.
- Hauer C, Habersack H. 2022. Die Bedeutung und Notwendigkeit der Erfassung der Sedimentdynamik im Spannungsfeld zwischen Ökologie und Wasserkraftnutzung. WASSERWIRTSCHAFT. 112(2–3):18–22.
- Hauer C, Wagner B, Aigner J, Holzapfel P, Flödl P, Liedermann M, Tritthart M, Sindelar C, Pulg U, Klösch M, Haimann M, Donnum BO, Stickler M, Habersack H. 2018. State of the art, shortcomings and future challenges for a sustainable sediment management in hydropower: A review. Renewable and Sustainable Energy Reviews. 98:40–55.
- Haun S, Schwindt S, Wieprecht S. 2022. Physikalische Grundlagen für nachhaltiges Sedimentmanagement von Fließgewässern. WASSERWIRTSCHAFT. 112(2–3):10–17.
- Henning M. 2013. Mehrdimensionale statistische Analyse räumlich und zeitlich hoch aufgelöster Oberflächen von Dünenfeldern [Dissertation]. Braunschweig, Germany: Technische Universität Braunschweig.
- Henry P-Y, Aberle J. 2018. Protocols for scaling morphodynamics in time. Zenodo.
- Hentschel B. 2007. Hydraulische Flussmodelle mit beweglicher Sohle. In: Wasserbauliches Versuchswesen. Karlsruhe: BAW; p. 25–46.
- Henze N. 2017. Stochastik für Einsteiger. Wiesbaden: Springer Spektrum.
- Hillebrand G. 2008. Transportverhalten kohäsiver Sedimente in turbulenten Strömungen - Untersuchungen im offenen Kreisgerinne.
- Hjulström F. 1935. Studies of the morphological activity of rivers as illustrated by the River Fyris. In: Vol. 25. Uppsala: Almqvist & Wiksells; p. 221–527.
- Holz K-P, Wundes R-D. 1980. Hybride Modelle - Ein neuer Weg im wasserbaulichen Versuchswesen. Die Küste, 35.(35):52–56.
- Huber R (editor), Blöschl G, Komma J, Nester T, Disse M, Marcolini G, Willems W, Theobald S, Dickel S, Rutschmann P, Bui MD, Giehl S, Schlagenhauser M, Fuchs Y, Aguirre Iniguez D, Schäfer S. unpublished. Retentionspotentialstudie am Inn - Synthesebericht. Bayerisches Landesamt für Umwelt (LfU).
- Huber R, Liepert T. 2013. Hybrid Model Tests for the Dal HEP (Nile River, Republic of Sudan). In: p. Paper 01c.03, 8 pages.
- Hudson RY, Herrmann FAJr, Soger RA, Whalin RW, Keulegan GH, Chatham J, Hales LZ. 1979. Coastal Hydraulic Models. U.S. Army Corps of Engineers Coastal Engineering Research Center.
- Hughes SA. 1993. Physical Models and Laboratory Techniques in Coastal Engineering. WORLD SCIENTIFIC.
- Hüsener T, Hesse D. 2021. Experimentelle Untersuchungen zu Sedimentablagerungen in einer Flusskrümmung am Mittelrhein. WASSERWIRTSCHAFT. 111(5):23–30.
- Jerolmack D, Mohrig D. 2005. Interactions between bed forms: Topography, turbulence, and transport. Journal of Geophysical Research. 110(F2):13.
- Jirka GH, Lang C. 2009. Einführung in die Gerinnehydraulik. Karlsruhe: KIT Scientific Publishing.
- Jolliffe IT. 2002. Principal component analysis. 2nd ed. New York: Springer.

- Julien PY. 2002. River mechanics. Cambridge; New York: Cambridge University Press.
- Julien PY, Klaassen GJ. 1995. Sand-Dune Geometry of Large Rivers during Floods. *Journal of Hydraulic Engineering*. 121(9):657–663.
- Kaczmarek LM, Biegowski J, Sobczak Ł. 2019. Modeling of Sediment Transport in Steady Flow over Mobile Granular Bed. *Journal of Hydraulic Engineering*. 145(4):04019009.
- Kaloyerou PN. 2018. Basic Concepts of Data and Error Analysis. Cham: Springer.
- Kamke W. 2014. Der Umgang mit experimentellen Daten, insbesondere Fehleranalyse, im Physikalischen Anfänger-Praktikum. Aachen: Shaker.
- Karim F. 1995. Bed Configuration and Hydraulic Resistance in Alluvial-Channel Flows. *Journal of Hydraulic Engineering*. 121(1):15–25.
- Karmacharya SK, Ruther N, Aberle J, Shrestha SM, Bishwakarma MB. 2021. Physical modelling of pressure flushing of sediment using lightweight materials. *Journal of Applied Water Engineering and Research*. 9(3):251–263.
- Kaveh K. 2019. Development of Data Driven Models for Hydromorphology and Sediment Transport [Dissertation]. München: Technische Universität München.
- Kennedy JF. 1963. The mechanics of dunes and antidunes in erodible-bed channels. *Journal of Fluid Mechanics*. 16(4):521–544.
- Kennedy JF. 1969. The Formation of Sediment Ripples, Dunes, and Antidunes. *Annual Review of Fluid Mechanics*. 1(1):147–168.
- Kennedy JF. 1995. The Albert Shields Story. *Journal of Hydraulic Engineering*. 121(11):766–772.
- Kern K. 1994. Grundlagen naturnaher Gewässergestaltung. Berlin, Heidelberg: Springer Berlin Heidelberg.
- Kim Y, Suh HS, Yun TS. 2019. Reliability and applicability of the Krumbein-Sloss chart for estimating geomechanical properties in sands. *Engineering Geology*. 248:117–123.
- Kleinhans MG, Braudrick C, van Dijk WM, van de Lageweg WI, Teske R, van Oorschot M. 2015. Swiftness of biomorphodynamics in Lilliput- to Giant-sized rivers and deltas. *Geomorphology*. 244:56–73.
- Kobus H, editor. 1978. Wasserbauliches Versuchswesen. DVWW Deutscher Verband für Wasserwirtschaft, Arbeitsausschuß „Wasserbauliches Versuchs- und Meßwesen“.
- Kohane R. 2000. Innstaustufe Wasserburg: Berechnung der Wasserspiegellage bei extremem Hochwasser und beweglicher Flußsohle. Landshut: Bayernwerk Wasserkraft AG.
- Kohane R. 2006. Innstaustufe Wasserburg - Strömungs- und Feststofftransportmodellierung, Erläuterungsbericht. Landshut: E.ON Wasserkraft GmbH.
- Kohane R. 2008. Innstaustufe Rosenheim - Strömungs- und Feststofftransportmodellierung, Erläuterungsbericht. Landshut: E.ON Wasserkraft GmbH.
- Kottke-Wenzel B, Jaenicke J, Häckl C. 2022. Sedimentmanagement in Staustufenketten - Notwendigkeit und Herausforderungen am Beispiel der Lech-Stufe 2 Prem. *WASSERWIRTSCHAFT*. 112(2–3):28–32.
- Kundu PK, Cohen IM. 2002. Fluid Mechanics. Second Edition. San Diego, London: Academic Press.
- Kunz K. 2014. Kornformbeurteilung mit dem optischen Partikelmessgerät „Camsizer®“. Bergisch Gladbach: Bundesanstalt für Straßenwesen.
- Link O, Ettmer B. 2018. Similitude of Scour around Bridge Piers. Paquier A, Rivière N, editors. *E3S Web of Conferences*. 40(03026).

- Loy G. 2022. Sedimentmanagement in Staustufen-ketten - Notwendigkeit, Herausforderungen und Umsetzungsbeispiele. *WASSERWIRTSCHAFT*. 112(2–3):45–50.
- Mallat S. 2008. *A Wavelet Tour of Signal Processing*. 3rd Edition. Academic Press.
- Mallat SG. 1989. A theory for multiresolution signal decomposition: the wavelet representation. *IEEE Transactions on Pattern Analysis and Machine Intelligence*. 11(7):674–693.
- Martin H, Pohl R, Aigner D, Bollrich G, Carstensen D, Diersch H-JG, Horlacher H-B. 2015. *Technische Hydromechanik 4: Hydraulische und numerische Modelle*. 3rd ed. Berlin: Beuth.
- Mazzuoli M, Blondeaux P, Vittori G, Uhlmann M, Simeonov J, Calantoni J. 2020. Interface-resolved direct numerical simulations of sediment transport in a turbulent oscillatory boundary layer. *Journal of Fluid Mechanics*. 885:A28.
- McElroy B, Mohrig D. 2009. Nature of deformation of sandy bed forms. *Journal of Geophysical Research*. 114:F00A04.
- Mehrdad MH. 1989. *Bedforms - their measurement, analysis and application* [Ph.D. Thesis]. Washington, D.C., USA: Washington University.
- Mendoza A, Abad JD, Langendoen EJ, Dongchen Wang, Tassi P, Kamal El Kadi Abderrezak. 2017. Effect of Sediment Transport Boundary Conditions on the Numerical Modeling of Bed Morphodynamics. *Journal of Hydraulic Engineering*. 143(4):04016099.
- Mertens W. 1995. Zur Wahl geeigneter Sedimenttransport-Formeln. *WASSERWIRTSCHAFT*. 85(10):486–490.
- Meurer R. 2000. *Wasserbau und Wasserwirtschaft in Deutschland*. Wiesbaden: Vieweg Teubner Verlag.
- Meyering H. 2012. *Effect of sediment density in bridge pier scour experiments* [Dissertation]. Braunschweig, Germany: Technische Universität Braunschweig.
- Meyer-Peter E, Müller R. 1948. Formulas for bed-load transport. In: *Proceedings of the second meeting of International Association for Hydraulic Research*. Vol. 3. Stockholm, Sweden; p. 39–64.
- Minor H-E. 2000. Fliessgewässer im nächsten Jahrtausend, Raumbedarf - Zielkonflikte. *Wasser Energie Luft*. 92(3/4):97–101.
- Morgenschweis G. 2018. *Hydrometrie: Theorie und Praxis der Durchflussmessung in offenen Gerinnen*. Berlin, Heidelberg: Springer Berlin Heidelberg.
- Morris GL, Fan J. 1998. *Reservoir Sedimentation Handbook*. New York: McGraw-Hill Book Co.
- Müller F, Ettmer B, Link O. 2021. Kolkexperimente an Brückenpfeilern unter Sedimenttransportbedingungen mit Polystyrolgranulat. *WASSERWIRTSCHAFT*. 111(5):45–51.
- Muste M (Editor-in-C, Lyn DA, Admiraal DM, Ettema R, Nikora V, Garcia MH, editors. 2017. *Experimental Hydraulics: Methods, Instrumentation, Data Processing and Management: Volume I: Fundamentals and Methods*. 1st ed. CRC Press.
- Muste M, Stern F. 2000. *Proposed Uncertainty Assessment Methodology for Hydraulic and Water Resources Engineering*.
- Neill CR, Yalin MS. 1969. Qualitative definition of beginning of bed movement. *Journal of the Hydraulics Division, ASCE*. 95(1):585–587.
- Neuhold C, Stanzel P, Nachtnebel HP. 2009. Incorporating river morphological changes to flood risk assessment: uncertainties, methodology and application. *Natural Hazards and Earth System Sciences*. 9(3):789–799.
- Nordin CF. 1971. Statistical properties of dune profiles.

- Novak P, Guinot V, Jeffrey A, Reeve DE. 2010. Hydraulic Modelling – an Introduction: Principles, methods and applications. 1st ed. London, UK: CRC Press.
- Núñez-González F, Martín-Vide JP. 2010. Downstream-migrating antidunes in sand, gravel and sand-gravel mixtures. Proceedings of the International Conference on Fluvial Hydraulics - Riverflow 2010.:393–400.
- Orlik S, Baumgärtner C. 2021. Nachbildung von Geschiebeschüttkegeln mit Kunststoffgranulaten. WASSERWIRTSCHAFT. 111(5):31–38.
- ÖWAV. 2011. Fließgewässermodellierung - Arbeitsbehelf Feststofftransport und Gewässermorphologie. Wien: Österreichischer Wasser- und Abfallwirtschaftsverband (ÖWAV) , Bundesministerium für Land- und Forstwirtschaft, Umwelt und Wasserwirtschaft.
- Papanicolaou A (Thanos) N, Elhakeem M, Krallis G, Prakash S, Edinger J. 2008. Sediment Transport Modeling Review—Current and Future Developments. Journal of Hydraulic Engineering. 134(1):1–14.
- Parker G, Wilcock PR. 1993. Sediment Feed and Recirculating Flumes: Fundamental Difference. Journal of Hydraulic Engineering. 119(11):1192–1204.
- Patt H. 2018. Naturnaher Wasserbau. 5. Auflage. Wiesbaden: Springer Vieweg.
- Patt H, Gonsowski P. 2011. Wasserbau. Berlin, Heidelberg: Springer Berlin Heidelberg.
- Petruzzelli V, Garcia VG, Cobos FXG i, Petrillo AF. 2013. On the use of lightweight materials in small-scale mobile bed physical models. Journal of Coastal Research. 165:1575–1580.
- Polikar R. 2003. Making Wavelets, Robi Polikar's "The Wavelet Tutorial" featured by the Science Magazine's NetWatch Department. Science. 300(5621):873–873.
- Popp M, Stein C. 2022. Workshop Sedimentmanagement an Staustufenketten: Handlungsoptionen aus verschiedenen Blickwinkeln. WASSERWIRTSCHAFT. 112(2–3):3–3.
- Radkau J. 2008. Technik in Deutschland. 60486 Frankfurt/Main: Campus Frankfurt / New York.
- Raudkivi AJ. 1982. Grundlagen des Sedimenttransports. Springer.
- Raudkivi AJ. 1990. Loose boundary hydraulics. 3rd ed. Oxford, England, New York: Pergamon Press.
- Reich J. 2020. A Monte Carlo approach to determine the sensitivity of bedform analysis methods.
- Retsch Technology GmbH. 2012. Bedienungsanleitung / Handbuch Korngrößenmesssystem CAMSIZER und CAMSIZER XT. Haan, Germany.
- Rooch A. 2014. Statistik für Ingenieure. Berlin Heidelberg: Springer.
- Rouse H. 1938. Fluid mechanics for hydraulic engineers. McGraw-Hill.
- Rüther N. 2006. Computational Fluid Dynamics in Fluvial Sedimentation Engineering [Ph.D. Thesis]. Trondheim, Norway: Norwegian University of Science and Technology.
- Savitzky A, Golay MJE. 1964. Smoothing and Differentiation of Data by Simplified Least Squares Procedures. Analytical Chemistry. 36(8):1627–1639.
- Schafer R. 2011. What Is a Savitzky-Golay Filter? [Lecture Notes]. IEEE Signal Processing Magazine. 28(4):111–117.
- Schäfer S, Fuchs Y, Rutschmann P. 2021. Ähnlichkeit von Sohlformen bei Sand und Leichtgewichtsgranulat. In: VAW Mitteilungen 262. Zürich, Switzerland: Versuchsanstalt für Wasserbau, Hydrologie und Glaziologie, ETH Zürich; p. 409–418.
- Schäfer S, Huber R, Rutschmann P. unpublished. Endbericht für Teilprojekt F: Transportvorgänge in Stauräumen. In: Retentionspotentialstudie am Inn. München.

- Schäfer S, Schlagenhauser M, Rutschmann P. 2019. Optical measurement method for quantifying sediment transport in physical experiments. In: E-proceedings of the 38th IAHR World Congress. Panama City, Panama: International Association for Hydro-Environment Engineering and Research (IAHR); p. 783–792.
- Schlagenhauser M, Schäfer S, Böcker S, Wiedemann W. unpublished. Advances Using Laser Scanning to Determine Riverbed Topography.
- Schleiss AJ, De Cesare G, Franca MJ, Pfister M, editors. 2014. Reservoir sedimentation - special session on reservoir sedimentation of the Seventh International Conference on Fluvial Hydraulics (River Flow 2014), IAHR Committee on Fluvial Hydraulics, EPFL Lausanne, Switzerland, 3-5 September 2014. Leiden, The Netherlands: CRC Press/Balkema.
- Schmalfuß R. 2022. Sedimentmanagement bei Stauanlagen: Herausforderungen und Lösungen. WASSERWIRTSCHAFT. 112(2-3):65–68.
- Schneefeld C, Heß M, Vollweiler T, Carstensen D. 2017. Hybride Modellierung als effizientes Lösungsverfahren zur Optimierung von Hochwasserentlastungsanlagen. Bemessung im Wasserbau - Klimaanpassung, Untersuchungen, Regeln, Planung, Ausführung.(58):57–66.
- Schumm SA. 2005. River Variability and Complexity. Cambridge: Cambridge University Press.
- Shen HW, editor. 1990. Movable Bed Physical Models. Dordrecht, The Netherlands: Kluwer Academic Publishers.
- Shields A. 1936. Application of similarity principles and turbulence research to bed-load movement. Berlin.
- Simons DB, Richardson EV. 1966. Resistance to flow in alluvial channels. Washington, USA: U. S. Govt. Print. Off.,.
- Simons RK, Canali GE, Anderson-Newton GT, Cotton GK. 2000. Sediment Transport Modeling: Calibration, Verification, and Evaluation. Journal of Soil Contamination. 9(3):261–289.
- Smith M, Vericat D, Gibbins C. 2011. Through-water terrestrial laser scanning of gravel beds at the patch scale. Earth Surface Processes and Landforms. 37(4):411–421.
- Soulsby R. 1997. Dynamics of marine sands. Thomas Telford Publishing.
- Soulsby RL, Whitehouse RJS. 1997. Threshold of Sediment Motion in Coastal Environments. In: Proceedings of Pacific Coasts and Ports '97. Christchurch, N.Z.: University of Canterbury; p. 149–154.
- Stemmler S, Werner CS, Reiterer A. 2019. Development of a time-of-flight laser scanning system for underwater applications. In: Bostater CR, Neyt X, Viallefont-Robinet F, editors. Remote Sensing of the Ocean, Sea Ice, Coastal Waters, and Large Water Regions 2019. Strasbourg, France: SPIE; p. 20.
- Strobl T, Zunic F. 2006. Wasserbau. Berlin [u.a.]: Springer.
- Sutherland J, Soulsby RL. 2010. Guidelines for physical modelling of mobile sediment. In: Proceedings of the third international conference on the application of physical modelling to port and coastal protection. Barcelona.
- U.S. Army Corps of Engineers. 2013. Hydrographic Surveying. USACE Publications.
- USBR. 2006. Erosion and Sedimentation Manual. Denver, Colo.: U.S. Dept. of the Interior, Bureau of Reclamation, Technical Service Center, Sedimentation and River Hydraulics Group.
- Van der Mark CF, Blom A, Hulscher SJMH. 2008. Quantification of variability in bedform geometry. Journal of Geophysical Research. 113(F3):F03020.

- Van Rijn LC. 1984a. Sediment Transport, Part I: Bed Load Transport. *Journal of Hydraulic Engineering*. 110(10):1431–1456.
- Van Rijn LC. 1984b. Sediment Transport, Part III: Bed Forms and Alluvial Roughness. *Journal of Hydraulic Engineering*. 110(12):1733–1754.
- Van Rijn LC. 1993. Principles of sediment transport in rivers, estuaries and coastal seas. Amsterdam: Aqua Publications.
- Van Rijn LC. 2007. Manual sediment transport measurements in rivers, estuaries and coastal seas. The Netherlands: Aquapublications.
- Vanoni VA. 1964. Measurements of critical shear stress for entraining fine sediments in a boundary layer. Pasadena: W. M. Keck Laboratory of Hydraulics and Water Resources, California Institute of Technology.
- Vanoni VA. 1975. Sedimentation engineering. New York : The Society.
- Venditti JG. 2005. Bed form initiation from a flat sand bed. *Journal of Geophysical Research*. 110(F1):F01009.
- Vollmers H, Giese E. 1970. Discussion of “Instability of Flat Bed in Alluvial Channels.” *Journal of the Hydraulics Division*. 96(6):1357–1363.
- Wong M, Parker G. 2006. Reanalysis and Correction of Bed-Load Relation of Meyer-Peter and Müller Using Their Own Database. *Journal of Hydraulic Engineering*. 132(11):1159–1168.
- Wu W, Wang SSY. 1999. Movable Bed Roughness in Alluvial Rivers. *Journal of Hydraulic Engineering*. 125(12):1309–1312.
- Wurms S. 2010. Numerische Modellierung der Sedimentationsprozesse in Retentionsanlagen zur Steuerung von Stoffströmen bei extremen Hochwasserabflussereignissen.
- Yalin MS. 1964. Geometrical Properties of Sand Wave. *Journal of the Hydraulics Division*. 90(5):105–119.
- Yalin MS. 1971. Theory of Hydraulic Models. London, UK: Macmillan.
- Yalin MS. 1972. Mechanics of sediment transport. Oxford; New York: Pergamon Press.
- Yalin MS. 1992. River Mechanics. Oxford; New York: Pergamon.
- Yalin MS, Da Silva AMF. 2001. Fluvial Processes. Delft: IAHR.
- Yalin MS, Karahan E. 1979. Steepness of Sedimentary Dunes. *Journal of the Hydraulics Division*. 105(4):381–392.
- Zanke U. 1982. Grundlagen der Sedimentbewegung. Berlin; New York: Springer.
- Zanke U. 2003. On the influence of turbulence on the initiation of sediment motion. *International Journal of Sediment Research*. 18.
- Zanke U. 2013. Hydraulik für den Wasserbau. Berlin, Heidelberg: Springer Berlin Heidelberg.

List of figures

Figure 1: Definition sketch for the derivation of energy equation of a gradually varied steady flow in an open channel (Dey 2014).....	9
Figure 2: Transport modes of sediment, schematic (Dey 2014)	10
Figure 3: Multilayer structure of sediment transport, schematic (Kaczmarek et al. 2019)	11
Figure 4: Instantaneous hydrodynamic forces acting on a sediment particle (modified from Dey (2014)).....	13
Figure 5: Shields regime diagram (modified from Garcia et al. (2000))	15
Figure 6: Bedforms according to Simons and Richardson (1966), schematic, modified from Van Rijn (1993)	16
Figure 7: Shear stress and friction over bedforms as a function of velocity: after Engelund and Hansen (1967) (left), after Raudkivi (1990) in Garcia (2008) (right)	17
Figure 8: Transport processes of dunes, schematic (Dey 2014)	18
Figure 9: Schematic diagram of the principal regions of flow over asymmetrical, angle-of-repose dunes, schematic (Best 2005)	19
Figure 10: Dune height versus dune length as a function of grain size (Flemming 2000) ..	20
Figure 11: Flood hydrographs for phase 2: reservoir bed during flood hydrographs	31
Figure 12: Dynamic image analysis results: sediment grading curves (left), grain shape parameters (right)	33
Figure 13: Bonnefille-Pernecker bedform classification diagram after Bechteler et al. (1991), modified.....	34
Figure 14: Views of the test facility with a dry river reservoir before the start of an experiment (top) and during operation (bottom), flow coming from the right in both images.	36
Figure 15: Schematic longitudinal section through the experiment setup with descriptive numbers	36
Figure 16: Location and labeling of pressure sensors for water level measurement in the river reservoir.....	37
Figure 17: Schematic cross-section of the experimental river reservoir.....	37

Figure 18: Transition area into the river reservoir with sediment feeder on the supply platform in dry conditions (top) and sediment feeder during operation with medium sediment transport (bottom)	39
Figure 19: Measuring cart with laser scanner and ADV probes during operation	40
Figure 20: Sediment trap, dry (left) and during operation (right)	42
Figure 21: Schematic illustration of laser path in air and water in cylindrical coordinate representation (Schlagenhauser et al. unpublished)	44
Figure 22: Optical measurement system in plan view and longitudinal section, schematic (modified after Schäfer et al. (2019))	46
Figure 23: Validation measurements for the sediment transport measurement method... ..	47
Figure 24: Scanned area of the reservoir bed during measurement of bed topography	50
Figure 25: Bed scan with location of the three evaluated longitudinal sections along the reservoir.....	56
Figure 26: Longitudinal sections 1, 2, and 3 through the refraction-corrected point cloud, exemplary for Q162-H21 (top) and Q325-H35 (bottom).....	56
Figure 27: Approximated locations of the bed surface in the 3 longitudinal sections, exemplary for Q162-H21 (top) and Q325-H35 (bottom).....	58
Figure 28: Photos of ceiling camera with position marks and longitudinal sections, exemplary for Q162-H21 (top) and Q325-H35 (bottom).....	59
Figure 29: Analysis of the longitudinal bed gradients in the study area for the 3 longitudinal sections, exemplary for Q162-H21 (top) and Q325-H35 (bottom).....	60
Figure 30: Time series of the longitudinal bed gradient in the study area for the 3 longitudinal sections and averaged, exemplary for Q162-H21 (left) and Q325-H35 (right)	61
Figure 31: Time series of the longitudinal water surface gradient (left) and averaged longitudinal water surface gradient in the reservoir from water level data (right), exemplary for Q162-H21 (top) and Q325-H35 (bottom).....	62
Figure 32: Dune crests and dune troughs along the bed surface in the 3 longitudinal sections after detrending (original bed surface in light gray), exemplary for Q162-H21 (top) and Q325-H35 (bottom)	63
Figure 33: Dune crests and dune troughs along the bed surface in the 3 longitudinal sections with different zero crossing thresholds (un-detrended bed surface in light gray): 10 cm (top), 35 cm (bottom), exemplary for Q162-H21.....	65

Figure 34: Dune lengths and dune heights of the reservoir bed, exemplary for Q162-H21 (top) and Q325-H35 (bottom)	66
Figure 35: Dune lengths and dune heights of the reservoir bed, section-wise for Q162-H21 (top) and Q325-H35 (bottom)	67
Figure 36: Dune velocities from zero-crossing analysis, exemplary for Q162-H21 (left) and Q325-H35 (right).....	68
Figure 37: Sediment transport rate time series during the entire experiment, exemplary for Q162-H21 (top) and Q325-H35 (bottom).....	69
Figure 38: Discharge, water levels and sediment transport rate time series during the bed survey, exemplary for Q162-H21 (top) and Q325-H35 (bottom).....	71
Figure 39: Distributions of sediment transport data, exemplary for Q162-H21 (left) and Q325-H35 (right).....	72
Figure 40: Comparing sediment transport means with percentiles of the means of all steady-state experiments, distinguished by reference water depth.....	73
Figure 41: Comparing dune length with dune height of the longitudinal bed sections (left) and of the means per experiment with mean shear stresses in N/m^2 as point labels (right) distinguished by reference water depth.....	76
Figure 42: Comparing dune length with dune height, zero crossing threshold 15 cm: 1% error ellipses (left) and 10% error ellipses (right), distinguished by reference water depth; shear stresses as data labels	76
Figure 43: Comparing dune length with dune height, 1% error ellipses: zero crossing threshold 10 cm (left) and 35 cm (right), distinguished by reference water depth; shear stresses as data labels	77
Figure 44: Comparing dune height with flow depth (left) and dune steepness Δ/λ (right), distinguished by reference water depth; shear stresses as data labels.....	78
Figure 45: Comparing relative dune length with dune height (left) and relative dune height (right), distinguished by reference water depth; shear stresses as data labels.....	79
Figure 46: Comparing dune length with relative dune length (left) and dune height with relative dune height (right), distinguished by reference water depth; shear stresses as data labels.....	80
Figure 47: Comparing flow intensity with flow velocity (left) and Froude number (right), distinguished by reference water depth; shear stresses as data labels.....	81
Figure 48: Comparing flow intensity with dune length (left) and relative dune length (right), distinguished by reference water depth; shear stresses as data labels.....	82

Figure 49: Comparing flow intensity with dune height (left) and relative dune height (right), distinguished by reference water depth; shear stresses as data labels.....	83
Figure 50: Comparing flow intensity (left) and flow velocity (right) with dune steepness Δ/λ , distinguished by reference water depth; shear stresses as data labels.....	84
Figure 51: Comparing water surface gradient with relative dune length (left) and dune steepness Δ/λ (right), distinguished by reference water depth; shear stresses as data labels.....	84
Figure 52: Comparing shear stress with relative dune height (left) and flow intensity (right), distinguished by reference water depth.....	85
Figure 53: Comparing water surface gradient (left) and flow velocity (right) with bed shear stress, distinguished by reference water depth.....	86
Figure 54: Comparing shear stress (left) and flow intensity (right) with sediment transport rate, distinguished by reference water depth; shear stresses as data labels.....	87
Figure 55: Comparing dune velocity with relative dune length (left) and relative dune height (right), distinguished by reference water depth; shear stresses as data labels.....	88
Figure 56: Comparing dune velocity with dune height to length relation Δ/λ (left) and flow intensity (right), distinguished by reference water depth; shear stresses as data labels....	88
Figure 57: Comparing dune velocity with relative dune velocity (left) and relative dune velocity with flow intensity (right), distinguished by reference water depth; shear stresses as data labels.....	89
Figure 58: Comparing dune velocity (left) and relative dune velocity (right) with sediment transport, distinguished by reference water depth; shear stresses as data labels.....	90
Figure 59: Comparing shear velocity with shear stress and flow intensity (left) as well as with shear Reynolds number and shear Froude number (right).....	92
Figure 60: Comparing shear velocity with dimensionless shear stress and dimensionless sediment transport rate (left) as well as sedimentological Reynolds number with dimensionless Shields stress and dimensionless sediment transport rate (right); shear stresses as data labels	92
Figure 61: Comparing dimensionless sediment transport rate from the experiments with results of common transport functions	95
Figure 62: Comparing dimensionless sediment transport rate from the experiments with results of correction functions for common transport functions.....	96
Figure 63: Discharge hydrograph with water levels and sediment transport over time during the full duration of Q325-H35-U	100

Figure 64: Sediment transport rate over time with moving averages and Savitzky-Golay filtering during the full duration of Q325-H35-U.....	102
Figure 65: Illustration of least-squares smoothing by locally fitting a second-degree polynomial (solid line) to five input samples after Schafer (2011)	102
Figure 66: Examples of signal filtering using wavelet decomposition after Mallat (2008) (left) and Burke Hubbard (1997) (right)	104
Figure 67: Sediment transport rate over time with Savitzky-Golay filtering and wavelet projections L15 and L16 during the full duration of Q325-H35-U	104
Figure 68: Discharge hydrograph and 1st derivative with filtered sediment transport rate over time, wavelet projections L15 and L16 and 1st derivatives during the full duration of Q325-H35-U.....	106
Figure 69: Discharge hydrograph with filtered sediment transport rate over time, wavelet projections L15 and L16, selected water levels, flow depth, shear stress and mean flow intensity during the full duration of Q325-H35-U	107
Figure 70: Discharge hydrograph with filtered sediment transport rate over time, wavelet projections L15 and L16, selected water levels, flow depth, shear stress and mean flow intensity during the full duration of Q325-H30-U-1 (top) and Q325-H30-U-2 (bottom) ..	110
Figure 71: Discharge hydrograph with filtered sediment transport rate over time, wavelet projections L14 and L15, selected water levels, flow depth, shear stress and mean flow intensity during the full duration of Q162-H21-U	114
Figure 72: Discharge hydrograph with filtered sediment transport rate over time, wavelet projections L14 and L15, selected water levels, flow depth, shear stress and mean flow intensity during the full duration of Q162-H30-U	114
Figure 73: Discharge hydrograph with filtered sediment transport rate over time, wavelet projections L15 and L16, selected water levels, flow depth, shear stress and mean flow intensity during the full duration of Q409-H35-U	116
Figure 74: Discharge hydrograph with filtered sediment transport rate over time, wavelet projections L15 and L16, selected water levels, flow depth, shear stress and mean flow intensity during the full duration of Q193-H21-U	117
Figure 75: Discharge hydrograph with filtered sediment transport rate over time, wavelet projections L14 and L15, selected water levels, flow depth, shear stress and mean flow intensity during the full duration of Q193-H30-U	119

Figure 76: Comparison of the mean bed surface of an experiment with dynamic bed equilibrium in the physical experiment (top), 2D RANS model (center) and 3D RANS model (bottom) (Huber et al. unpublished)..... 129

List of tables

Table 1: Limitations in the laboratory when performing dynamically similar model experiments.....	24
Table 2: Test scenarios for phase 1: dynamic bed equilibrium, and phase 2: reservoir bed during flood hydrographs.....	30
Table 3: Properties of the lightweight sediment.....	32
Table 4: Morphological standard values for the polystyrene lightweight sediment.....	34
Table 5: Hydromorphological standard value ranges for the present study.....	34
Table 6: Definition of the descriptive numbers of the schematic longitudinal section through the experiment setup	36
Table 7: Acquired data: continuous (left), demand/discontinuous (right) subdivided into phase 1 and phase 2	47
Table 8: Measurement uncertainty of selected measurement procedures.....	53
Table 9: RMSE of transport functions compared to measured transport rates before and after correction.....	96
Table 10: Comparison of average sediment transport in stationary and instationary experiments	120

List of symbols

Roman symbols

A	[m ²]	Flow area
b	[m]	Movable bed width
C _f	[-]	Total flow resistance
c	[m/s]	Wave propagation velocity
D _*	[-]	Dimensionless particle diameter
d _m	[m]	Mean/representative sediment diameter
d ₅₀	[m]	50 percent passing of sieve analysis
F _{D,G,L,R}	[N]	Forces coming from drag, weight, lift, resistance
FF	[-]	Shape/form factor
Fr	[-]	Froude number of the flow
Fr _*	[-]	Shear Froude number
h	[m]	Flow depth
I	[-]	Energy line gradient
I _w	[-]	Longitudinal water surface gradient
k _s	[m]	Equivalent sand roughness
k _{St}	[m ^{1/3} /s]	Strickler coefficient
L	[m]	Length
n	[-]	Vertical distortion factor, refractive index (Snell's law)
P	[m]	Wetted perimeter of the riverbed
Q	[m ³ /s], [l/s]	Discharge
q _s	[kg/s], [m ³ /s]	Volumetric sediment transport rate
q [*]	[-]	Dimensionless sediment transport rate
R _h	[m]	Hydraulic radius
Re	[-]	Reynolds number of the flow
Re _p	[-]	Particle Reynolds number
Re _*	[-]	Shear Reynolds number
S	[-]	Bed slope
T	[-]	Transport stage parameter
t	[s], [min]	Time
u	[m/s]	Flow velocity
u _D	[m/s]	Dune velocity
u _{D,rel}	[-]	Relative dune velocity
u _*	[m/s]	Shear velocity
w _f	[m/s]	Particle settling velocity
z	[x,y,z]	Height in cylindrical coordinates

Greek symbols

α	[-]	Energy coefficient
---	-----	--------------------

Δ	[m]	Bedform height, dune height
Δ_{rel}	[-]	Relative dune height
Δt	[s], [min]	Time interval
δ	[m]	Boundary layer height
η	[kg/m·s]	Dynamic viscosity
η_D	[m]	Bedform height, dune height
θ	[-],[°]	Shields parameter, angle of incidence
θ_u	[-]	Mean flow intensity
λ	[m]	Bedform length, dune wavelength
λ_D	[-]	Friction factor, Darcy-Weisbach friction
λ_{rel}	[-]	Relative dune length
ν	[m ² /s]	Kinematic viscosity
ρ	[kg/m ³], [x,y,z]	Fluid density, distance in cylindrical coordinates
ρ_s	[kg/m ³]	Sediment grain density
ρ'	[-]	Relative density
τ	[N/m ²]	Bed shear stress
τ_c	[N/m ²]	Critical bed shear stress
τ'	[N/m ²]	Bed skin friction
τ''	[N/m ²]	Bedform drag
τ'''	[N/m ²]	Moving particle drag
τ^*	[-]	Dimensionless shear stress
τ_c^*	[-]	Critical dimensionless shear stress
τ_s^*	[-]	Dimensionless bed shear stress due to grain friction

Indices

a	Air
b	Bedload
c	Critical
cd	Calculated
cor	Corrected
d	Dune
m	Mean
max	Maximum
md	Measured
min	Minimum
r	Scale number for ratio of nature/field to model, reflecting surface
rh	Horizontal scale number
rv	Vertical scale number
s	Sediment
t	Total load
w	Water
0	Coordinate origin
*	Shear

Acronyms

ABS	<i>Acrylic butadiene styrene</i>
ADV	<i>Acoustic Doppler velocimetry</i>
HIPS	<i>High impact polystyrene</i>
MID	<i>Magnetic inductive flow meter</i>
MM	<i>Moving average, moving mean</i>
PCA	<i>Principal component analysis</i>
PID	<i>Proportional-integral-derivative</i>
PS	<i>Polystyrene</i>
RANS	<i>Reynolds-averaged Navier-Stokes</i>
RMSE	<i>Root mean squared error</i>
SG	<i>Savitzky-Golay</i>
TPE-S	<i>Thermoplastic styrene block copolymer</i>
TPU	<i>Thermoplastic polyurethane</i>
WL	<i>Water level</i>

A. Advances Using Laser Scanning to Determine Riverbed Topography

The following article is referred to as:

Schlagenhauser, M., Schäfer, S., Böcker, S., Wiedemann, W., unpublished. Advances Using Laser Scanning to Determine Riverbed Topography.

Advances Using Laser Scanning to Determine Riverbed Topography

Mathias Schlagenhauser^{a*}, Stefan Schäfer^a, Sebastian Böcker^b, Wolfgang Wiedemann^c

^aDepartment of Civil, Geo and Environmental Engineering, Chair of Hydraulic and Water Resources Engineering, Obernach Hydraulics Laboratory, Technical University of Munich, Munich, Germany; mathias.schlagenhauser@tum.de

^bFormer M.Sc. student at Department of Civil, Geo and Environmental Engineering, Technical University of Munich, Munich, Germany

^cDepartment of Civil, Geo and Environmental Engineering, Chair of Geodesy, Technical University of Munich, Munich, Germany

Schlagenhauser

2012 - 2015: Environmental Engineering, Technical University of Munich, Degree: Master of Science

Since 2015: Research Assistant – Technical University of Munich, Chair of Hydraulic and Water Resources Engineering, Obernach Hydraulics Laboratory.

Schäfer

2010 - 2012: Civil Engineering, Technical University of Munich, Degree: Master of Science

2012 - 2013: Structural Engineer, Bilfinger Construction GmbH, Germany

Since 2013: Research Assistant – Technical University of Munich, Chair of Hydraulic and Water Resources Engineering, Obernach Hydraulics Laboratory.

Böcker

2014 - 2016: Geodesy and Geoinformation, Technical University of Munich, Degree: Master of Science.

Wiedemann:

2010 - 2013: Geodesy and Geoinformation, Technical University of Munich, Degree: Master of Science

Since 2013: Research Associate - Technical University of Munich, Chair of Geodesy.

Advances Using Laser Scanning to Determine Riverbed Topography

Abstract: Terrestrial laser scanning (TLS) enables water-penetrating measurements for bathymetry monitoring in natural river environments and in laboratory experiments. Recent studies show that TLS successfully captures the submerged topography of river beds for water depths of a few decimeters using refraction correction models. With increasing water depths however, backscattering compromises the TLS distance measurement additionally, which results in poor point cloud accuracy.

In this paper, we present an extended correction model to rectify point clouds of submerged river topographies in water depths up to 0.9 meters. An additional scaling factor was derived from identical points in a test setup that was scanned both in dry state and under submerged conditions without knowledge of exact water condition parameters. Using our extended correction model, we achieved an accuracy of about 3 millimeters for the submerged river bed topography in 0.9 meters of water depth and even better in lower water depths.

Keywords: Terrestrial laser scanning (TLS), Bathymetry measurement, Hydraulic modelling, Refraction correction

Introduction

Underwater riverbeds are shaped by processes of aggradation and degradation, which depend on a multitude of parameters, e.g. sediment particle size and composition as well as water depth and flow velocity. During a flood event, river bed shape and elevation are subject to significant dynamic changes. Depending on the river morphology, local erosion and sedimentation processes can act as a limiting factor the discharge capacity of a river section and may even increase the flood risk of the surrounding area (Khouakhi et al. 2019; Reisenbüchler et al. 2019).

As it is very challenging to acquire sufficient data for scientific investigations from the natural environment, hydraulic engineers have been carrying out experiments in scale

model tests for decades. In so called hybrid modelling approaches, these experimental data also support numerical investigations (Rutschmann 2005; Schäfer et al. 2018).

In this context, terrestrial laser scanning (TLS) can provide point clouds of the submerged river topography and increase the quality of hydraulic model experiments as well as of numerical investigations (Deruyter et al. 2015; Friedl et al. 2015; Hodge et al. 2009; Smith et al. 2012; Smith and Vericat 2014). In the course of an experiment, the amount of erosion or deposit of sediments in certain areas of the changing riverbed can be calculated through a time series analysis of the resulting point clouds. The dense point cloud data have accuracies down to a few millimeters for points within a certain distance from the scanner. Besides common surveying engineering, the use of TLS for rapid topography data acquisition has already been considered and put to test for exposed and dry gravel beds in natural environments (Brasington et al. 2012).

Airborne Laser Bathymetry (ALB) provides a method for creating 3D point clouds of (shallow) riverbeds or from a flying platform. Such systems often combine two lasers of different wavelengths: a green, pulsed laser penetrates air and water and captures the submerged bathymetric topography. An additional infrared (NIR) laser which cannot penetrate the water body detects the exact point which separates the air from the water path (Guenther et al. 2000; Mandlbürger et al. 2013).

With accuracies of about 0.1 m in height and 0.1–1 m in position (cf. Mandlbürger et al. 2009), ALB does not meet the requirements for hydraulic models. Nevertheless, the concept of water-penetrating TLS itself is promising enough to be transferred for further laser scanning applications. Smith et al. (2012) provide the basic model to rectify the point cloud data of submerged areas (cf. chapter *Rectification of the submerged point cloud*). In Hodge et al. (2009), Miura and Asano (2013) and Smith and Vericat (2014)

experiments are shown using TLS bathymetry to derive the submerged river bed structure in shallow water, Deruyter et al. (2015) give an example for higher water depths of up to 3 m. Friedl et al. (2018) reconstructed submerged river beds in water depths smaller than 15 cm.

By scanning from air into water, the emitted laser beam travels through two media with different optical density, refracting the laser beam at the boundary layer. This effect has to be considered in order not to distort the results systematically. As our experiments showed, common methods using the Snell's Law for correction only appear insufficient for larger water depths. Backscattering in water additionally compromises the TLS distance measurement, which results in poor point cloud accuracy. So even if the focus of a measurement campaign is only on comparing fully submerged areas, it is necessary to correct the point clouds in order to get accurate results.

A typical application could be a hydraulic model experiment with moving riverbed combined with a numerical simulation. After scanning the riverbed surface through the water, the TLS data need to be corrected for refraction to acquire high quality bathymetry data. Depending on the riverbed topography, point position in alternating water depth is scaled relatively to the scanner origin. Moreover, if the scanner needs to be repositioned between two scans, refraction correction is inevitable to receive the same point clouds due to the different angles of incident at the water surface.

For these reasons, we propose an extended correction model with additional scaling factor, noted as m , which can be derived by analyzing the geometry of a reference object in dry and submerged conditions. It is determined once and is then valid for the same scanning equipment and water conditions.

Instruments and Methods

The measuring range and penetration depth of an electromagnetic signal in water is limited by absorption, scattering and turbidity. The absorption and scattering characteristics of the laser beam shown in Figure 1 are valid for clear fresh water. Due to the higher density of water, they are more pronounced than in air and strongly depend on the emitted wavelength (Hale and Querry 1973; Mobley 1994).

Due to eye safety reasons, most common TLS systems emit a wavelength of about 1550 nm. Such devices hardly penetrate the surface of fresh water and therefore are not suitable for terrestrial laser bathymetry (TLB) (cf. Figure 1). A short wavelength equals more energy. Therefore, a high energy signal can reach objects deeper down below the surface. For example, ALB most often uses green, pulsed lasers with a wavelength around 532 nm (Mandlbürger et al. 2013). Figure 1 illustrates the relation between absorption and penetration for a broad spectrum of wavelengths and a selection of common terrestrial laser scanners.

Suitable scanners for bathymetric usage should have wavelengths within the visible spectrum of light (400 – 700 nm) to allow surface penetration and minimum ranges of several meters into the water body. For our experimentation, we used a *Leica Nova MS60* with a visible red, pulsed laser of 658 nm and a *Leica ScanStation C10* with a visible green, pulsed laser of 532 nm.

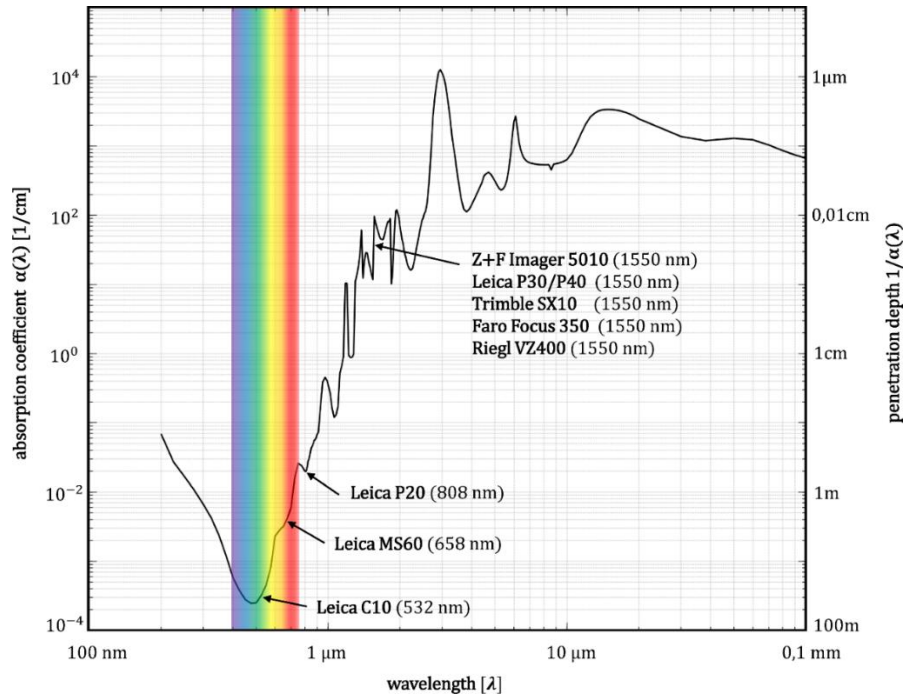


Figure 1. Absorption and penetration depth of electromagnetic waves in clear water: wave length of different TSL systems (Data Source for absorption coefficient and penetration depth: (Hale and Querry 1973) modified by author with instruments wavelengths from manufacturer specifications).

Methodology

TLS is not designed for water-penetrating measurements. As the scanner ignores the medium boundary during data acquisition, the captured point cloud is heavily distorted in the regions covered with water (cf. Figure 2). It requires adaptations and corrections. Otherwise it is not possible to locate the detected changes in the real physical model in an appropriate manner. To rectify the point cloud, we used the calculation scheme referring to Smith et al. (2012). All corrections were applied in post-processing.

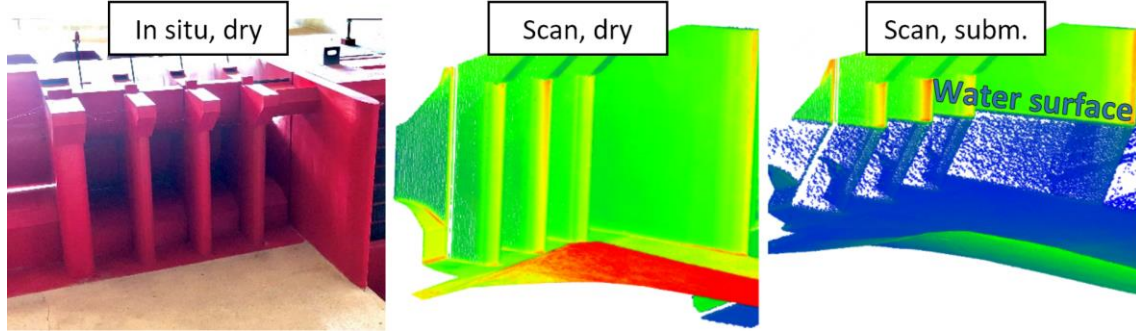


Figure 2. Comparison of point clouds at the intake structure of a model dam (left): scanned with identical setup in dry state (middle) and partly submerged (right) showing the intensity drop (from bright green to blue) and the refraction at the water surface (all blue points in the right plot are submerged points). No correction was performed to the submerged point cloud shown here.

Rectification of the submerged point cloud

Smith et al. (2012) used a 2 D correction method based on a cylindrical coordinate representation and on Snell's law to correct the coordinates of the underwater point cloud. Scanning objects below the waterline from an instrument position ρ_0, z_0 , the emitted laser pulse first passes through the air and strikes the surface of water in an angle of incidence θ_a at the coordinates ρ_w, z_w where the laser beam refracts at the boundary between the two media (cf. Figure 3).

According to Snell's law (Flügge 1956) the relationship between the angle of incidence θ_a and the angle of refraction θ_w is given by the ratio of the refractive index of water n_w and air n_a .

$$\frac{\sin \theta_a}{\sin \theta_w} = \frac{n_w}{n_a} = n, \quad (1)$$

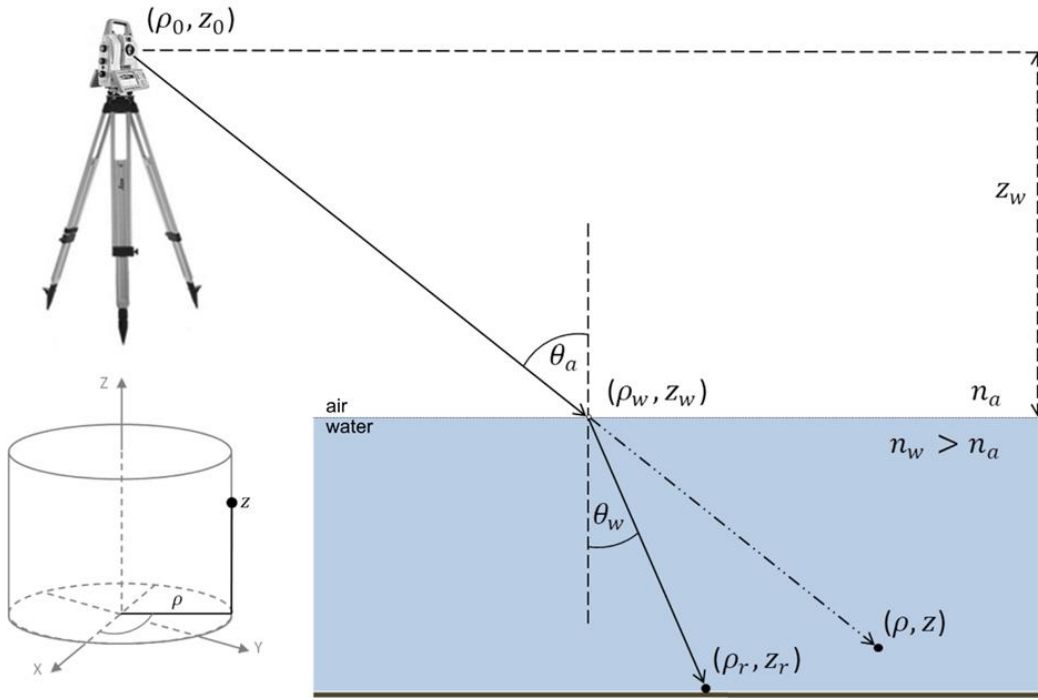


Figure 3. Illustration of laser path in air and water, cylindrical coordinate representation.

The refractive index n describes the ratio in propagation velocity between an electromagnetic wave in a specific medium regarding vacuum conditions. This value depends on the conditions of the related medium and the wavelength of the signal itself. When neglecting the refracting angles, the point cloud will show distortion in submerged areas. Hence, all submerged measurements have to be corrected for the refractive effect individually to get the rectified point coordinates ρ_r, z_r . Furthermore, as TLS is a time-of-flight measurement, the different propagation speed of the emitted electromagnetic wave in each participating medium has to be considered. Because the laser pulse is delayed in water, the distance under water is adjusted with the refractive index.

$$\rho_r = \frac{(\rho - \rho_w)}{n^2} + \rho_w \quad (2)$$

$$z_r = \frac{\cos \theta_w \cdot (\rho - \rho_w)}{n \cdot \sin \theta_a} + z_w \quad (3)$$

In this correction model the most sensitive component is the height of the water surface z_w relatively to the scanner origin z_0 . As it describes the starting point of the submerged laser path, the water level directly relates to the elevation of the submerged point coordinate. Furthermore, a plane water surface is mandatory for this method. An unsettled surface (rough water, wind) will change the path directions of the transferred laser beam according to the orientation of the surface normal at the point of impact at the boundary layer. Without a suitable method to capture the water surface conditions in real time, these effects cannot be compensated for in the correction model presented here.

The refractive index is crucial for rectifying the point cloud under the waterline, as it defines the angle of refraction θ_w in water and the scale factor for submerged distance measurements. To achieve the closest approximation of the medium's conditions, we measured physical parameters of air and water while scanning. In the air, the propagating electromagnetic wave is influenced by atmospheric conditions. The phase refractive index of air n_a can be calculated according to the rules of International Association of Geodesy (Hothem and Rummel 1999). The required physical parameters are: wavelength of the scanning system [nm], temperature of air [K], relative humidity of air [%] and air pressure [hPa].

The refractive index of water n_w is defined by the wavelength of the scanning system [nm], the temperature of water [K] and the specific volume as function of pressure [MPa] and temperature [K]. It can be calculated according to industrial standards of the International Association for the Properties of Water and Steam (IAPWS) (Wagner and

Kruse 1998). With the refractive indices of both media and the reconstructed angle of incidence θ_a the part of the point cloud below the waterline can be rectified according to equations (2) and (3). According to investigations of Smith et al. (2012) and Smith and Vericat (2014) this method has a mean error of less than 5 mm for a water depth of less than 200 mm and no detrimental effect on the precision.

Extended correction model

For our extended correction model, we captured the submerged surface of a fixed reference object by TLS (*Leica ScanStation C10*) at water depths of up to 0.9 m. Within our experiments, we determined significant deviations between the scans of the submerged surfaces corrected with the formulas in chapter *Rectification of the submerged point cloud* and a reference scan, conducted in dry state without water.

Submerged points appear to be lower than the corresponding points of the dry reference scan. This error has also been reported by Friedl et al. (2018) for objects in depths of 0.5 m and 0.72 m, respectively.

Experimental results showed that the TLS laser beam is affected by scattering in the water body and therefore the correction of the point cloud has to compensate for an additional signal compromising effect. In water, scattering of light occurs by the interaction between photons and molecules, such as small-scale density fluctuations, organic and inorganic particles and by the index of refraction itself (Mobley 1994). Besides the absorbing properties of water, the over-all attenuation of an electromagnetic wave can include up to 25 % of scattering (Tönshoff and Kruse 2003). Especially backscattering received as returning signal compromises the distance measurement. Hence, multiple reflections on particles along the laser path appear as signal propagation delay. Moreover, the beam spread in water as well as backscattering

influence the shape of the pulse, which can further reduce accuracy.

In both ways, scattering of the returning signal obviously leads to a misinterpretation of the actual measured underwater distance. The laser pulse travels slower than expected from the refractive index itself and in this way, referring to the scanner origin, the coordinates of a submerged point appear more distant and lower. Therefore, the model described by Smith et al. (2012) was extended by an additional scaling factor m (see Eq. 4 & 5) to compensate for the scattering delay of the submerged TLS distance measurement. Physically, m scales the relation of the measured distance over the propagation speed in the water body.

$$\rho_r = \frac{(\rho - \rho_w) \cdot m}{n^2} + \rho_w \quad (4)$$

$$z_r = \frac{\cos \theta_w \cdot (\rho - \rho_w) \cdot m}{n \cdot \sin \theta_a} + z_w \quad (5)$$

The additional scaling factor m (cf. Eq. 4 & 5) depends on different properties of water conditions like temperature, density, salinity and turbidity. As these parameters cannot be reliably determined from the water itself without a lot of effort, an experimental setup was created to derive the scale factor empirically for the current water conditions. It would also be possible to determine all parameters in equations (4) and (5) from the experiment by including them in the adjustment computation. Since most of them can be easily determined by supplementary measurements, they are not part of the adjustment variables.

Reference Object

A reference object of rectangular bricks was set up to provide a sufficient amount of

unique control points (see Figure 4). The control points were calculated from point cloud data by a semi-automatic intersection of planes fitted to the brick faces. In this way, we generated a total of 45 corrected control points with up to six coordinates on each of the eight different levels. In the submerged scan, control points were located between 0.1 and 0.9 m below the water surface. The incidence angles of the laser beam at the water surface ranged from 66° to 74° for the control point area.

The bright-colored bricks served as ideal objects for underwater scanning. The distance noise on the plane brick faces in the dry reference is about 0.3 mm. The data collected under water shows noise of only 0.6 mm in 20 mm depth and noise of 2 mm in 0.9 m beneath the water surface.



Figure 4. Experimental setup of a reference object to provide object control points (highlighted in red). The measurements were carried out using a *Leica ScanStation C10* even though in this sample image another instrument is shown.

Measurement procedure

First, a scan of the dry reference object and the dry river bed was performed, generating a true scaled reference dataset. Afterwards, the model was filled with clear fresh water

and a second scan of the submerged reference object was performed. Both scans had the same resolution of approx. 3x3 mm at the surface of the reference object.

Furthermore, the level of the water surface relative to the scanner's origin was measured with an accuracy of 0.1 mm to verify a consistent water level during the scanning process. Additionally, all relevant physical parameters for calculating the refraction index of the air and the water according to IAG and IAPWS (cf. chapter *Rectification of the submerged point cloud*) were recorded repeatedly during the scanning process. The mean values of all documented parameters ensured the best approximation for the duration of each individual scan, while parameter fluctuations were kept to a minimum during the measurements.

Results

Comparison of the control points of the two scans (the reference scan in dry state and the submerged scan rectified according to Smith et al. (2012) without the additional scaling factor m gives an impression of the systematically increasing deviation for increasing lengths of the underwater laser path (see Figure 5).

On the condition that the control points should match after the refraction correction, the additional scaling factor m was estimated by least squares adjustment (Gauß-Helmert-Model $f(\hat{b}, \hat{x}) = 0$). The functional model for the adjustment of least squares is given by equations (4) and (5).

In the process, the standard deviations of the parameters water level z_w and both sets of control points were considered. The refractive index itself and its related refraction angles were considered as free from error. The assumed standard deviation value for the control point coordinates was $\sigma_{ref} = 1.0$ mm in dry state and $\sigma_{sub} = 2.0$ mm considering

the higher range noise for the submerged counterparts (for further details compare (Lenzmann and Lenzmann 2005; Neitzel and Petrovic 2008). The standard deviation for the mean value of the water level during the scan process was $\sigma_w = 0.4$ mm.

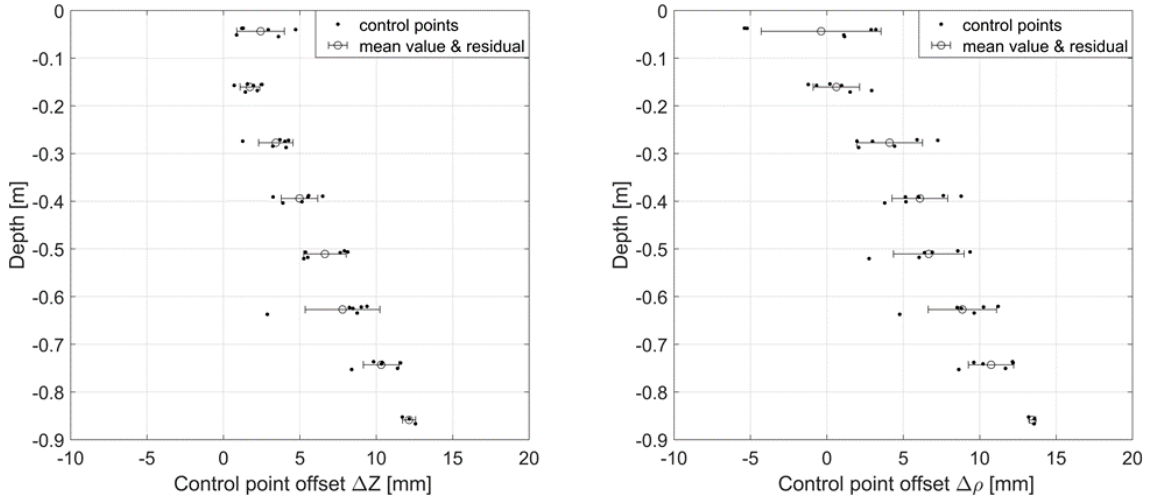


Figure 5. Results for the rectified control points with increasing Depth [m] according to Smith et al. (2012). Control point offset to reference for the components ΔZ [mm] (left) and $\Delta \rho$ [mm] (right) including the mean value and its standard deviation at different water levels.

To evaluate the original versus the modified method, the remaining control point offsets of both procedures were compared. Figure 5 presents the results for the original underwater point cloud correction according to Smith et al. (2012). The control point residuals of both components ($\Delta Z, \Delta \rho$) correlate with increasing depth. In nearly 0.9 m the mean value offset to the reference is about 12 mm for ΔZ and 13 mm for $\Delta \rho$. The shallower a control point, the less severe is the offset due to a considerably shorter laser path in water. For this particular experiment, the 3 D offset in only 100-200 mm water depth was up to 3 mm, which corresponds to earlier observations from Smith et al. (2012, p. 411)

Applying the modified rectification model with the additional scaling factor m

significantly improved the matching of reference and submerged control points, which is depicted in Figure 6. As there is no correlation between offset and water level anymore, the overall mean values for residuals of Z and ρ spread around zero. The residuals of all control points reduce to 2 - 3 mm independent of the water depth.

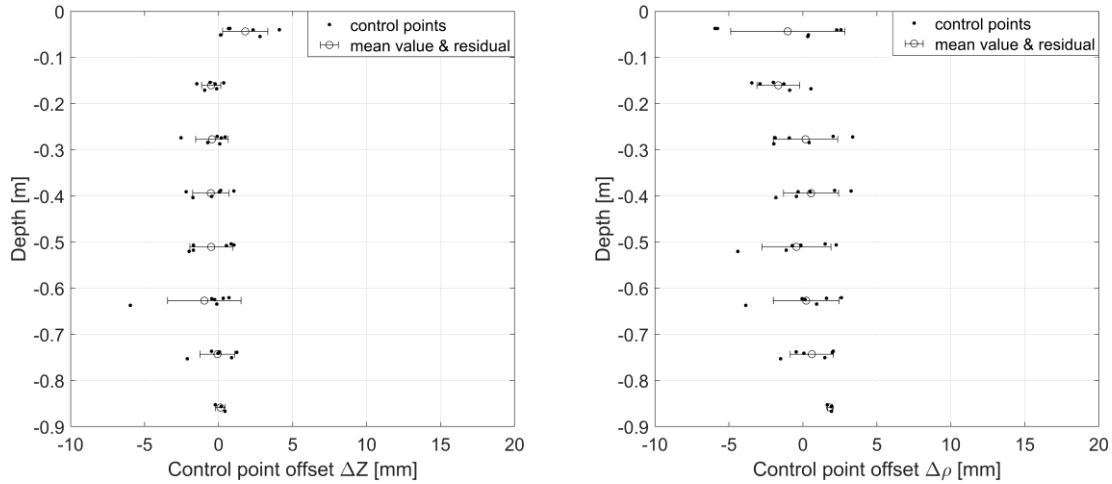


Figure 6. Results for the rectified control points with increasing depth [m] by using the modified equations. Control point offset to reference for component ΔZ [mm] (left) and for component $\Delta \rho$ [mm] (right) including mean value and standard deviation for separate water levels. Overall fit accuracy $Z = 1.2$ mm, $\rho = 2.3$ mm.

By determining the offset between the reference and the rectified underwater point cloud, it was possible to estimate the additional scaling factor m to eliminate the observed error in water-penetrating distance measurement for TLS. The modified correction method provided precise point cloud data even 0.9 m below the water surface. Transferring the results from the control point system back to the whole point cloud confirmed this observation.

Figure 7 shows the point cloud of the reference object with the two different correction methods applied. Depicted in the left image, the rectification of the point cloud was calculated without the additional scaling factor m . The distortion of the point cloud

increased with the water depth, showing deviations up to 15 mm in a depth of 0.9 m. Introducing the additional scaling factor m according to the method presented in this study, limits the remaining deviations to $\pm 2 - 3$ mm and the points in the submerged areas match the reference point cloud much better.

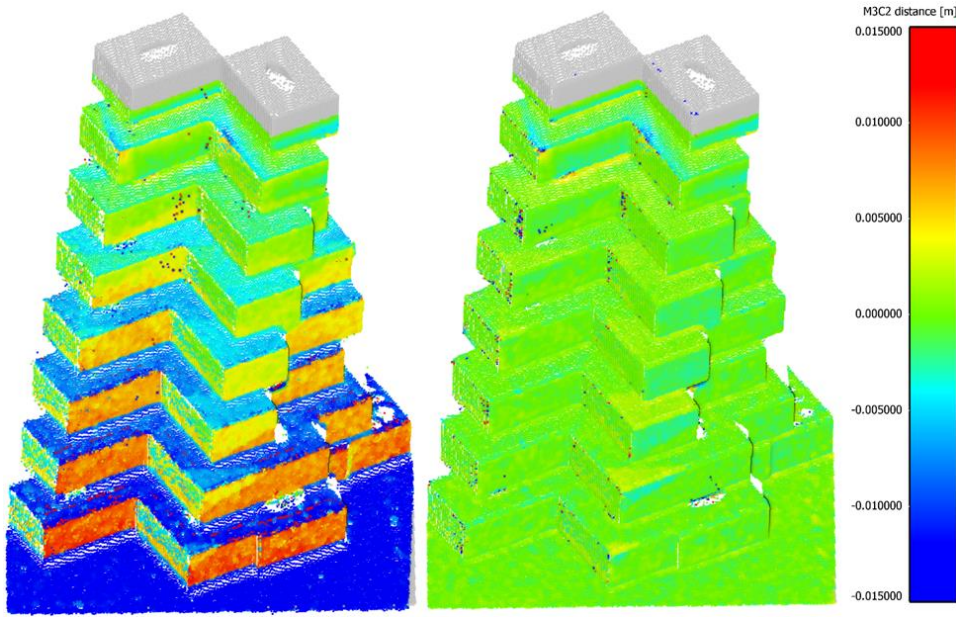


Figure 7. Cloud-to-Cloud distances of the reference scan in dry state and the rectified point clouds of the submerged structure. Left: point cloud rectified according to Smith et al. (2012) only. Right: point cloud rectified with the extended model presented in this study.

Validation tests

For validation, we first subtracted a dry scan point cloud from a corrected underwater point cloud of two trapezoidal PVC prisms (see Figure 8(a)) mounted to the bottom of a laboratory flume (width 0.4 m, length 12 m). The goal was to examine the accuracy of our correction method for surfaces with different orientation and distance from the scanner and for different water levels. For the verification test, the scanner was installed downstream and approx. 3 m above the flume bottom. All prism surfaces were visible to the scanner under dry conditions, horizontal distances to the scanner were approx. 4 m

for prism 1 and approx. 10 m for prism 2. Surfaces 1 of the prisms with 45° inclination were directed towards the scanner, surfaces 3 were directed away from it.

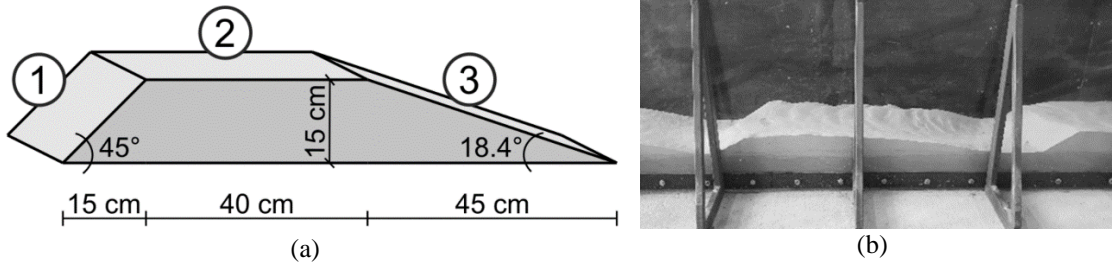


Figure 8. (a): Trapezoidal prism of verification test setup, surface 1 directed towards laser scanner. (b): Bed forms in dry state after flume experiment with movable quartz sand riverbed. TLS measurements conducted from the left in both cases.

Cloud-to-cloud distance with separate distances along x, y and z-axes was utilized for evaluation of the point cloud differences (software used: *CloudCompare* (<https://www.danielgm.net/cc/>)). Differences in the horizontal plane (i.e. x- and y-direction) were below 1 mm and hence neglected. Figure 9 shows the results of the distance calculation (submerged state minus dry state) in z-direction for the prism surfaces as numbered in Figure 8(a) (z-direction along the gravity vector). Prism surface 2-3, the surface of prism 2 facing away from the scanner, was barely detected by TLS in submerged state and hence not evaluated.

In a second step, we applied the method to a flume experiment with movable bed (flume width 0.4 m, flume length 19 m; quartz sand $d_{50} = 0.3$ mm) and realistic bedforms (ripples on dunes), which is shown in Figure 8(b). At the end of the experiment, when bedforms had formed in the flume, two scans were carried out at water levels of approx. 65 cm and 20 cm above the mean bed level, with the transport bodies having heights of about 10 cm. After the flume had been drained very slowly to avoid alterations of the bed shape, a third scan of the dry bed was performed and later used for comparison with the submerged scans in the same manner as applied before to the plastic prisms.

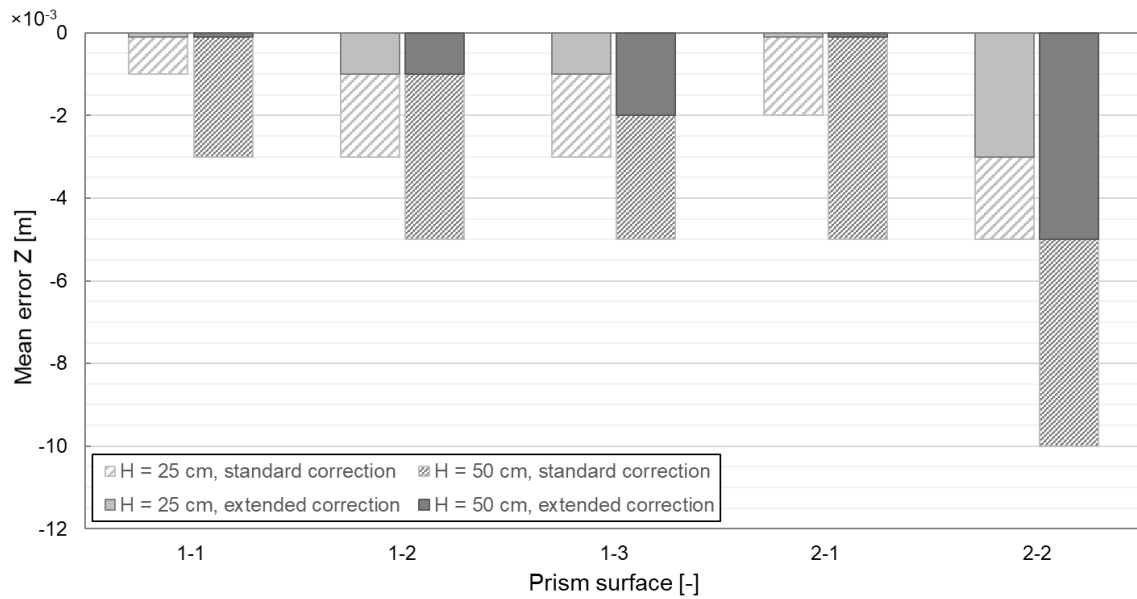


Figure 9. Mean error in z-direction for the trapezoidal prism surfaces in two submerged states: water depths above the prisms were 0.25 m and 0.50 m. Horizontal distances of scanner to prisms: prism 1 approx. 4 m, prism 2 approx. 10 m. Vertical distance of scanner to prisms: approx. 3 m.

Table 1 gives the results for the point cloud differences of the dry and submerged scans after application of the two different correction models: standard refraction correction as described above and modified rectification correction with the additional scaling factor m . The error distribution for all cases shown was almost Gaussian shaped.

Table 1. Mean error and standard deviation of mean error in z-direction for the flume experiment with movable bed in two submerged states.

Water depth during submerged scans	mean / std. dev. [mm]	
	Standard refraction correction	Extended refraction correction
$H_{\text{mean}} = \text{approx. } 0.2 \text{ m}$	-2 / 2	0 / 1
$H_{\text{mean}} = \text{approx. } 0.65 \text{ m}$	-8 / 2	-1 / 2

Summary and outlook

As presented in this study and the mentioned literature, TLS is a suitable method to measure the topography of rivers and hydraulic models under the waterline. The accuracy of point clouds of submerged objects can be improved by an additional scaling

factor for the laser path beneath the water surface. This scaling factor strongly depends on the physical water conditions like temperature, density, turbidity etc. The advantage of the method presented in this paper is that these parameters do not have to be known exactly. Instead, the scaling factor can be estimated from identical control points scanned in dry state as well as under submerged conditions. With this method, point clouds with accuracies better than 3 mm can be captured up to a water depth of approximately one meter with standard TLS equipment.

A restriction for scanning submerged structures with satisfactory accuracy is the need of a smooth water surface. Only in some special cases with a constant water surface slope the effects of an unsettled water surface can be approximated (Miura et al. 2016) As there is no system available to track the water surfaces height and slant for every single scan point in real time, the effects of an unsettled water surface cannot be considered in the correction model and can lead to errors in the rectified point cloud.

References

- Brasington J, Vericat D, Rychkov I. 2012. Modeling river bed morphology, roughness, and surface sedimentology using high resolution terrestrial laser scanning. *Water Resour Res* [Internet]. [accessed 2020 Nov 5] 48(11). <https://doi.org/10.1029/2012WR012223>
- Deruyter G, Vanhaelst M, Cornelis S, Hanne G, Alain DW. 2015. The use of terrestrial laser scanning for measurements in shallow-water: Correction of the 3D coordinates of the point cloud. In: *Inform Geoinformatics Remote Sens Conf Proc*. Vol. 1. Albena, Bulgaria; p. 1203–1210.
- Flügge J. 1956. *Leitfaden der geometrischen Optik und des Optikrechnens*. Göttingen, Germany: Vandenhoeck & Ruprecht.
- Friedl F, Schneider J, Hinkelammert F, Weitbrecht V. 2018. Through-water terrestrial laser scanning in hydraulic scale models: proof of concept. *J Hydraul Res*. 56(4):551–559. <https://doi.org/10.1080/00221686.2017.1372820>
- Friedl M, Weinhold T, Hanke K. 2015. Erfahrungen beim bathymetrischen Einsatz eines “grünen” terrestrischen Laserscanners im Wasserbau. In: Hanke K, Weinhold T, editors. Vol. 8. Obergurgl, Austria: Herbert Wichmann Verlag; p. 207–210.

Guenther G, Cunningham A, LaRocque P, Reid D. 2000. Meeting the accuracy challenge in airborne Lidar bathymetry. In: Proc EARSeL-SIG-Workshop LIDAR. Vol. 1. Dresden, Germany.

Hale GM, Querry MR. 1973. Optical Constants of Water in the 200-nm to 200- μ m Wavelength Region. *Appl Opt.* 12(3):555–563. <https://doi.org/10.1364/AO.12.000555>

Hodge R, Brasington J, Richards K. 2009. In situ characterization of grain-scale fluvial morphology using Terrestrial Laser Scanning. *Earth Surf Process Landf.* 34(7):954–968. <https://doi.org/10.1002/esp.1780>

Hothem L, Rummel R. 1999. IAG Resolutions adopted at the XXIIth General Assembly in Birmingham, 1999 [Internet]. https://iag.dgfi.tum.de/fileadmin/IAG-docs/IAG_Resolutions_1999.pdf

Khouakhi A, Slater L, Wilby R. 2019. Rivers are changing all the time, and it affects their capacity to contain floods. *The Conversation* [Internet]. [accessed 2021 Apr 14]. <http://theconversation.com/rivers-are-changing-all-the-time-and-it-affects-their-capacity-to-contain-floods-126659>

Lenzmann L, Lenzmann E. 2005. Stellungnahme zu dem Beitrag „Zur korrekten Linearisierung von nichtlinearen GH-Modellen“ von Stephan Kupferer. *Allg Vermess-Nachrichten.* 3(112):114. https://gispoint.de/index.php?eID=tx_securedownloads&p=414&u=0&g=0&t=1618310100&hash=7c4dacf6a852a98aebfd4bed121471c8e17ce1bb&file=fileadmin/user_upload/Artikel_Archiv/Volumes_Articles/avn/2005/03/be3cfbc1fe5.pdf

Mandlbürger G, Höfle B, Briese C, Ressler C, Otepka J, Hollaus M, Pfeifer N. 2009. Topographische Daten aus Laserscanning als Grundlage für Hydrologie und Wasserwirtschaft. *Österr Wasser- Abfallwirtsch.* 61(7):89–97. <https://doi.org/10.1007/s00506-009-0095-3>

Mandlbürger G, Pfennigbauer M, Pfeifer N. 2013. Analyzing near water surface penetration in laser bathymetry; A case study at the River Pielach. In: *ISPRS Ann Photogramm Remote Sens Spat Inf Sci* [Internet]. Vol. II-5-W2. Antalya, Turkey: Copernicus GmbH; [accessed 2020 Nov 5]; p. 175–180. <https://doi.org/10.5194/isprsannals-II-5-W2-175-2013>

Miura N, Asano Y. 2013. Green-wavelength terrestrial laser scanning of mountain channel. In: *ISPRS Ann Photogramm Remote Sens Spat Inf Sci* [Internet]. Vol. II-5-W2. Antalya, Turkey: Copernicus GmbH; [accessed 2020 Nov 5]; p. 187–192. <https://doi.org/10.5194/isprsannals-II-5-W2-187-2013>

Miura N, Asano Y, Moribe Y. 2016. Improved correction method for water-refracted terrestrial laser scanning data acquired in the mountain channel. In: *ISPRS - Int Arch Photogramm Remote Sens Spat Inf Sci* [Internet]. Vol. XLI-B8. Prague, Czech Republic: Copernicus GmbH; [accessed 2020 Nov 30]; p. 349–352. <https://doi.org/10.5194/isprs-archives-XLI-B8-349-2016>

Mobley CD. 1994. *Light and water: radiative transfer in natural waters.* San Diego, USA: Academic Press.

Neitzel F, Petrovic S. 2008. Total Least Squares (TLS) im Kontext der Ausgleichung nach kleinsten Quadraten am Beispiel der ausgleichenden Geraden. ZfV - Z Geodasie Geoinformation Landmanagement. 133:141–148. https://www.geodesy.tu-berlin.de/fileadmin/fg261/Publikationen/Neitzel_Petrovic_zfv_3_2008.pdf

Reisenbüchler M, Bui MD, Skublics D, Rutschmann P. 2019. An integrated approach for investigating the correlation between floods and river morphology: A case study of the Saalach River, Germany. Sci Total Environ. 647:814–826. <https://doi.org/10.1016/j.scitotenv.2018.08.018>

Rutschmann P. 2005. Hybride Modelle im Wasserbau. In: Strobl T, editor. Mitt 104 Lehrstuhls Vers Für Wasserbau Wasserwirtsch TU Münch. Vol. 104. Dresden; p. 87–96.

Schäfer S, Schlagenhauser M, Huber R, Minh Duc. B, Rutschmann P. 2018. Trainingsdaten aus dem physikalischen Laborversuch - Ein neuer Ansatz zur Validierung von Sedimenttransportmodellen. In: M³ - Mess Model Manag Hydrol Wasserressourcenbewirtschaftung. Dresden, Germany.

Smith M, Vericat D, Gibbins C. 2012. Through-water terrestrial laser scanning of gravel beds at the patch scale. Earth Surf Process Landf. 37(4):411–421. <https://doi.org/10.1002/esp.2254>

Smith MW, Vericat D. 2014. Evaluating Shallow-Water Bathymetry from Through-Water Terrestrial Laser Scanning Under a Range of Hydraulic and Physical Water Quality Conditions. River Res Appl. 30(7):905–924. <https://doi.org/10.1002/rra.2687>

Tönshoff HK, Kruse U. 2003. Sensorsysteme zur Erfassung von 3D-Objekten unter Wasser. Bonn, Germany: John Wiley & Sons.

Wagner W, Kruse A. 1998. Properties of Water and Steam / Zustandsgrößen von Wasser und Wasserdampf: The Industrial Standard IAPWS-IF97 for the Thermodynamic Properties and Supplementary Equations for Other Properties / Der Industrie-Standard IAPWS-IF97 für die thermodynamischen Zustandsgrößen und ergänzende Gleichungen für andere Eigenschaften [Internet]. Berlin Heidelberg, Germany: Springer-Verlag; [accessed 2020 Nov 5]. <https://doi.org/10.1007/978-3-662-03529-0>

B. Optical Measurement Method for Quantifying Sediment Transport in Physical Experiments

The following article is published as:

Schäfer, S., Schlagenhauser, M., Rutschmann, P., 2019. Optical Measurement Method for Quantifying Sediment Transport in Physical Experiments. In: *E-Proceedings of the 38th IAHR World Congress*. International Association for Hydro-Environment Engineering and Research (IAHR), Panama City, Panama, pp. 783–792.

OPTICAL MEASUREMENT METHOD FOR QUANTIFYING SEDIMENT TRANSPORT IN PHYSICAL EXPERIMENTS

STEFAN SCHÄFER⁽¹⁾, MATHIAS SCHLAGENHAUSER⁽²⁾ & PETER RUTSCHMANN⁽³⁾

^(1,2,3) Obernach Hydraulics Laboratory, Technical University of Munich (TUM), Germany
stefan.schaefer@tum.de

⁽³⁾ Chair of Hydraulic and Water Resources Engineering, Technical University of Munich, Germany

ABSTRACT

The authors present a measurement method that makes it comparatively inexpensive to carry out continuous measurements of sediment transport and display them in real time with very little computing power. The measurement method is part of a system for the continuous diversion or recirculation of sediments discharged from a flume or a laboratory canal. The core of the measurement method is a camera-optical gray value comparison of 8-bit grayscale images of a transparent measuring field, taken with a standard industrial camera. The measuring field consists of two transparent glass plates, one above the other, with a thin film of particle-laden liquid flowing between them (e.g. sand grains or plastic granulate in water). For each image, the concentration of the sediment in the liquid at a discrete point in time is first determined with the help of gray value comparison. The sediment transport \dot{m}_s [kg/s] derives from a calibration function, which was determined in advance from long-term measurements with several constant sediment concentrations. Comparative validation measurements showed measurement errors of around 5 percent for sediment concentrations between 0 and 20 percent.

Keywords: sediment transport; optical measurement; calibration; physical experiments; reservoir management.

1 INTRODUCTION

The quantification of sediment transport is an important task in hydromorphology and of equal importance for geographers, engineers and ecologists. Due to the complexity of sediment transport processes, various forecasting methods have been developed, most of which involve an empirical approach (Yalin, 1972; Zanke, 1982). However, their field of application is mostly limited to specific applications, sometimes only with significant simplifications, so that research on generally valid prediction models is still ongoing (Gyr and Hoyer, 2006; Ancy et al., 2014).

In parallel to theoretical solutions, new measurement methods were continuously developed to quantify sediment transport. In classical methods, which often function very robustly, sediment samples of various sizes are collected over a defined period of time and analyzed later (Van Rijn and Roberti, 2014; Diplas et al., 2008; IAEA, 2005). The greatest weakness of these methods, however, lies in the discontinuous recording of the measurement data. Thanks to great advances in measurement technology and data processing, it has been possible in the recent past to develop non-contact measurement methods with continuous data recording, of which optical and acoustic methods in particular achieve high accuracies (Albayrak et al., 2015; Haimann, 2015; Rüther, 2017; Garcia, 2006).

The range of application of the various measurement methods for hydraulic engineering issues extends from large-scale nature measurements to investigations at grain level and below. At the natural site, the large dimensions of the study area often have a limiting effect, which is why physical laboratory investigations still play an important role in the quantification of sediment transport (Yalin, 1971; Hughes, 1993; Kirkegaard et al., 2011). In the laboratory, complex hydromorphological processes can be simulated under controlled experimental conditions and a large number of different parameters can be recorded simultaneously, reproducibly and with high accuracy.

As part of a research project to investigate sediment transport processes in river reservoirs with predominantly fine sand, a system for the continuous measurement and recycling of solids was developed, which are flushed from the reservoir of a physical laboratory experiment. The discharged solids are collected and fed to a submersible pump, which uses a small proportion of the water flowing through the weir gates to transport the solids back upstream of the reservoir via a pipeline. The measuring field of the optical measuring system presented in this article is integrated into the pipeline and enables continuous measurement of the transport rate. At the same time, the discharged solids can be circulated, which reduces the quantity of solids that would otherwise have to be purchased and stored as supply material for long-term tests without circulation.

At the core of the measurement method is a comparatively simple camera-optical gray value comparison of individual images from a commercially available industrial camera, which depicts the distribution of solid particles (e.g. sand grains or plastic granulate) flowing through a transparent, horizontal measuring field, which is illuminated from below. For each image, the concentration of the solids in the liquid at a discrete point in time is first determined with the aid of the gray value comparison and sediment transport \dot{m}_s [kg/s] is then calculated from the known discharge and the grain density. In contrast to comparable optical methods in which the sediment transport is measured directly in the outlet of the test station (cf. Dhont et al. (2017)), width and flow depth in the test station as well as the amount of mass transported have no direct effect on the quality of the measured values in the measuring field of the measurement method presented.

2 METHODOLOGY

2.1 Optical measuring system

The measuring field consisted of two transparent glass plates arranged horizontally one above the other with a thin sheet of liquid flowing between them. Via a geometric transition element, the liquid flow loaded with solids from the circular pipeline was continuously guided between the glass plates (Figure 1). The transition element was designed to minimize the formation of vortex-inducing flow separation (angle of expansion = 8° , cf. Bollrich (2013)). The sheet between the glass plates was 600 mm x 600 mm in horizontal dimensions and 10 mm high, which was about 2.5 times the height of the largest solid particles to ensure permanent free passage of the measuring field.

The glass plates were illuminated from below so that solid particles created local darkening on their way through the measuring field. An industrial camera was directed at the measuring field from above and depicted the shadows of the solid particles as a gray value image against the otherwise white background. For each pixel of the gray-scale image, the gray-scale value recorded by the camera (8-bit grayscales, value range [0-255]) was compared with a threshold value determined by previous calibration.

Pixels with gray values below the threshold value were assigned the value 0 or white and all others the value 1 or black. In this way, the threshold value comparison transformed the former gray value image into a binary black-and-white image and clearly distinguished for each pixel between the states "black" (= solid particle) and "white" (= no particle). A calibration function was used to assign a solids concentration in the liquid stream to the proportion of black pixels in the overall image.

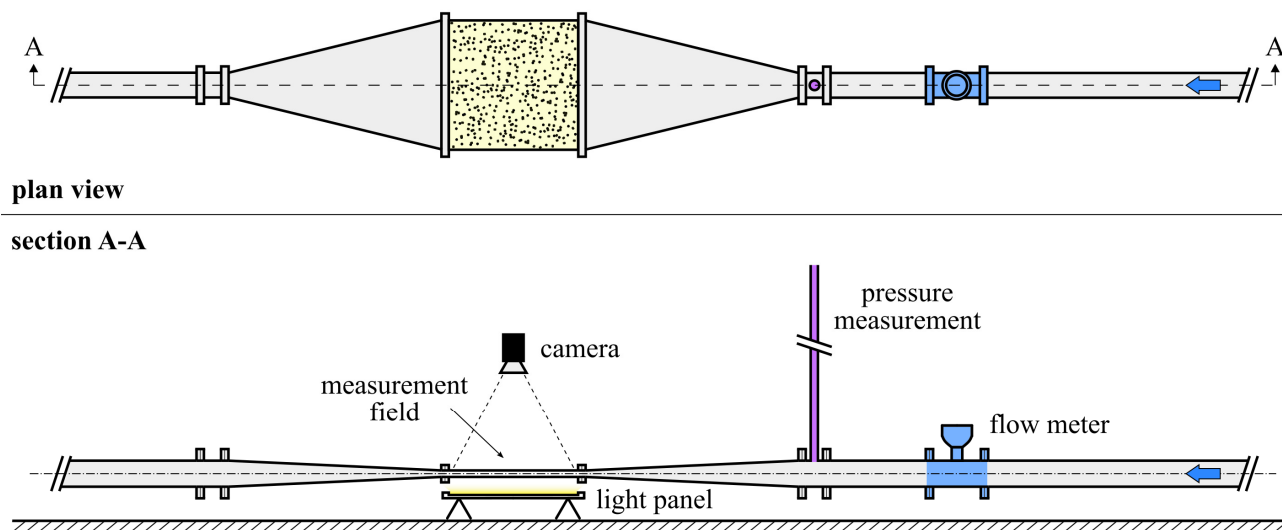


Figure 1. Optical measuring system in plan view and longitudinal section.

2.2 Recirculation system

The optical measuring system was embedded in a system for the continuous recirculation of solids during an experiment. For this purpose, the solids flushed out of the test station were retained in a sediment trap with the aid of an inclined perforated plate. While most of the discharge from the test station flowed through the perforated plate and back into a water reservoir, the solids were collected in a corner of the sediment trap in which there was also the inlet of a dirty water pump (400 V).

This pump had a free passage of grain size up to $\varnothing 10$ mm and a maximum capacity of 38 l/s in the present study. It was regulated by a frequency converter and it transported the fluid-solid mixture into a pipe with a nominal diameter of 100 mm, in which the discharge was first measured by means of an electromagnetic flowmeter (± 0.5 % measurement error (KROHNE Messtechnik GmbH, 2017)). The solid-water mixture flowed past a pressure measurement (± 5 mm measurement error) and was then guided into the measuring field of the

optical measuring system. Afterwards, a DN 100 mm pipeline of variable length led towards the beginning of the test station, where the solids were fed back into the reservoir. Therefor a diffuser was arranged under water, which evenly distributed the solids over the reservoir width. The flow velocity was over 2 m/s in the entire recirculation system and around 2.8 m/s in the measuring field.

2.3 Calibration system

The calibration function was determined from a large number of long-term measurements with solids concentrations kept constant over the duration of the respective measurement. For this purpose, a smaller part of the recirculation system was operated as a closed circuit, within which the system volume and the volume of the solids added were known (Figure 2).

The supply shaft, which was open at the top, was used to add defined quantities of solids to the circuit and thus gradually increase the solids concentration in the system volume. A water-permeable shut-off membrane just above the pipe axis prevented the presence of solid particles in the supply shaft during operation. The pressure level in the measuring system was also controlled by the water level in the supply shaft. With the help of a small additional flow of water into the supply shaft, its upper edge was always slightly overflowed during operation. The shaft height was fitted in advance to set the desired system pressure.

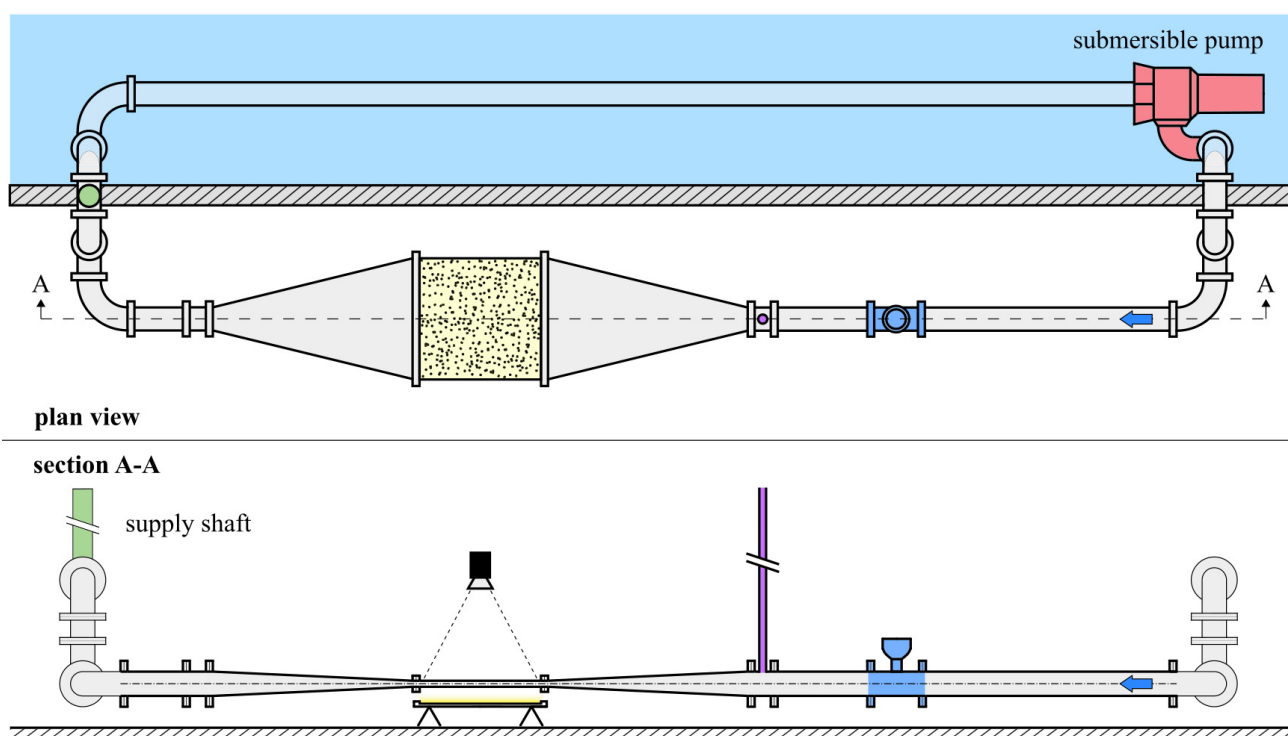


Figure 2. Recirculation system in calibration setup.

3 CALIBRATION OF THE MEASURING SYSTEM

The correlation between gray value and solids concentration was established by calibration measurements. In order to avoid local deposition zones of solids, the greatest possible mixing of solids and liquids had to be ensured during operation. Therefore, flow velocity was chosen so high that the solids were transported at every point with approximately the same velocity as the surrounding liquid. Directional changes in the pipeline course were constructed as streamlined as possible. In this way, systematic errors from the measurement procedure were minimized. Statistical measurement errors, which mainly resulted from turbulent fluctuations in the flow and the statistical distribution of the solid particles in the measuring field, were compensated by long measurement times during calibration.

In the present study, calibration measurements were performed for two uniformly graded lightweight plastic granules with densities of 1.1 and 1.05 g/cm³ and mean grain diameters of 3.7 and 4.1 mm. The calibrated solids concentrations were between 0.5 and 12 % of the system volume. Figure 3 shows the darkening of the measuring field at a concentration of 12 % of the gray granules. Preliminary tests with sand grains were also conducted and showed promising results. However, since sand grains were not used in the physical laboratory experiments that led to the development of the measuring system presented here, no further investigations have been carried out to date.

Several internal and external factors had an influence on the definition of the threshold to distinguish between "particulate" and "no particulate". A gray scale gradient existed from the center to the edge of a solid particle due to scattered light reflected from the side, which was additionally affected by the proportion of fine

air bubbles adhering to the particle surfaces (Raffel, 2007). The identification of the particle edges also depended on external factors like camera settings (e.g. focal length, aperture) and lighting conditions (e.g. absolute brightness of the light panel and its fluctuations, decrease in brightness from the center to the edge of the lens).

The threshold value below which a gray value was defined to be white and above which it was black had to be set so high that fluctuations in lighting conditions did not directly alter the black-and-white distribution in the binary image. Furthermore, the threshold value had to be set sufficiently high that only those pixels were considered black and thus as particles, which actually represented a solid particle. Pixels that were displayed darker due to lower illumination, i.e. in the edge areas of the measuring field, could not be classified as particles. For this reason, only a square of 1700 x 1700 pixels in the center of the measuring field was analyzed.

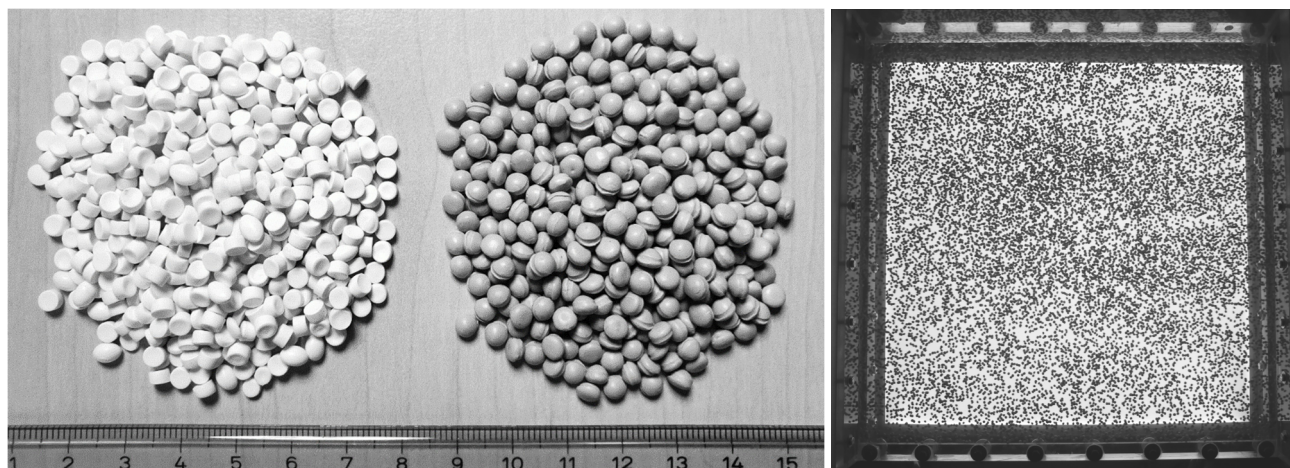


Figure 3. Left: Granules used for calibration. Right: Measuring field during operation (12 % gray granules).

In general, the threshold value should not be set too high because, due to the gray scale difference from the center to the edge of a solid particle, it reduces the black area of a particle and thus the number of black pixels per particle. The lower the proportion of black pixels available for evaluation of the gray value image, the more sensitive the measurement method reacted to concentration fluctuations. For a stable, reliable evaluation process, the highest possible absolute value of pixels evaluated as particles was therefore desirable. All parameters relevant for calibration are presented below.

3.1 Exposure time

For a reproducible approach to image processing, consistently "sharp" images had to be captured. If during the measurements the discharge and thus inevitably the flow velocity had to be varied in order, for example, to increase the transport capacity in the recirculation system for transport peaks with increased pumping performance, a separate calibration function would have to be available for each discharge.

To avoid that, the exposure time would have to be so short during calibration that no relevant movement of the particles would take place within a defined discharge range during exposure. The relevant movement was defined as the proportion of the particle surface at rest that is added by the particle movement during the exposure time and which enlarges the photographed particle surface. The longer the exposure time in relation to the particle motion at a given particle velocity, the more distorted a particle becomes during exposure. Depending on the flow velocity, the same particle would therefore be imaged differently in size or distorted and thus produce a different gray value, which could falsify the measurement result.

In the process described, it is unknown to the authors to what extent an increase in particle area due to particle distortion would lead to an increase in the number of black pixels, and from what point excessive distortion due to residual light would reduce the number of black pixels per particle. This question would have to be verified based on further measurements, which, however, has not been possible with the technical conditions of the measuring system presented so far. For the presented study, the measuring system was therefore operated exclusively with constant discharge.

3.2 Frame rate

Since the analysis of the black-and-white images was done with a statistical approach, the theoretical minimum frame rate depended only on the desired temporal resolution of the concentration variations. However, since perfect mixing could not be guaranteed and the highest possible time resolution was required, the theoretical minimum frame rate in the present study depended on the flow velocity in the measuring field. To ensure continuous measurement, each particle had to be photographed at least once. However, this requirement was not sufficient because a particle at the edge of the image did not provide exactly the same

number of black pixels as in the center of the image. Instead, more black pixels tended to be detected for particles closer to the center of the image than for particles at the edge of the image.

Therefore, two images per particle were chosen as the technically reasonable lower limit for the frame rate, so that each particle was recorded at least twice during the passage of the measuring field. Provided that particles in the measuring field were transported exclusively in the direction of flow and without cross-flow components, e.g. by local turbulence, each particle was recorded between the two following edge cases: in the quarter points of the measuring field or centrally and at the edge. On average, there was a balance between a low black pixel value at the edge and a high black pixel value in the center.

3.3 Camera settings

Components with the following specifications were used for the investigations:

- Camera: IDS USB 3 uEye CP 1;
- Sensor: CMOS 2592 x 2048;
- Lens: Kowa f=16mm/F1.4.

The following camera settings were used for the examinations:

- Evaluated pixels: 1700 x 1700;
- Pixel distance in object plane: 0.28 mm;
- Frame rate: 10 Hz;
- Exposure time: 0.3 ms;
- Aperture: F2.0.

3.4 Lens settings

The aperture was chosen relatively wide with F2.0 to collect as much light as possible at a short exposure time. The resulting low depth of field was not a disadvantage for measurement accuracy because the aperture was kept constant for all investigations and was not varied. Particles were almost equally visible along the 1 cm deep liquid film. For practical reasons, the focal length was adjusted to the surface of the upper glass pane of the measuring field. For this purpose, a so-called calibration field with a defined dot grid was fixed to the edge of the upper pane, which was placed on the upper pane before each new measurement in order to check the camera settings. Because the liquid sheet or the actual measuring plane was lower, the particles to be measured were not as sharp as would theoretically have been possible.

This inaccuracy could have been reduced by lowering the camera by the thickness of the glass plate after calibration with the dot grid. In the present study, however, the camera was not repositioned because the camera mount used could not ensure a single vertical movement without influencing the other spatial axes. The influence of the remaining slight uncertainty on the measurement result could not be quantified in the context of the present study. However, given the high accuracy of the validation measurements, these uncertainties were classified as low.

4 OUTCOMES

4.1 Calibration functions

For the two granules used, measurements with constant solids concentrations were carried out step by step. The box plot in Figure 4 shows how the scattering of the measured black pixels per frame increased with increasing solids concentration: higher boxes with 25 and 75% percentiles and longer whiskers with 1.5-fold interquartile distance. The regression line is used to contrast the non-linear relationship between black pixels and solids concentration.

The entire process was repeated several times to evaluate the reproducibility of the calibration functions and it proved to be very good (cf. right side in Figure 4). The confidence limits are close to the regression function derived from the calibration functions. For the slightly less uniformly graded white granulate, both the distances to the confidence limits were significantly greater and the nonlinearity of the calibration functions more pronounced, which led to a weaker increase in black pixel number with an increase in solids concentration.

4.2 Influence of measurement time

When determining an unknown solids concentration from a single image using the derived calibration function, the resulting measurement error was dependent on the random fluctuation of the recorded black pixel values. In order to quantify this error, the temporal development of the mean values was examined. The left side of Figure 5 shows the temporal development of the mean values at constant solids concentrations during calibration. At the latest after five seconds all mean values were approximately constant.

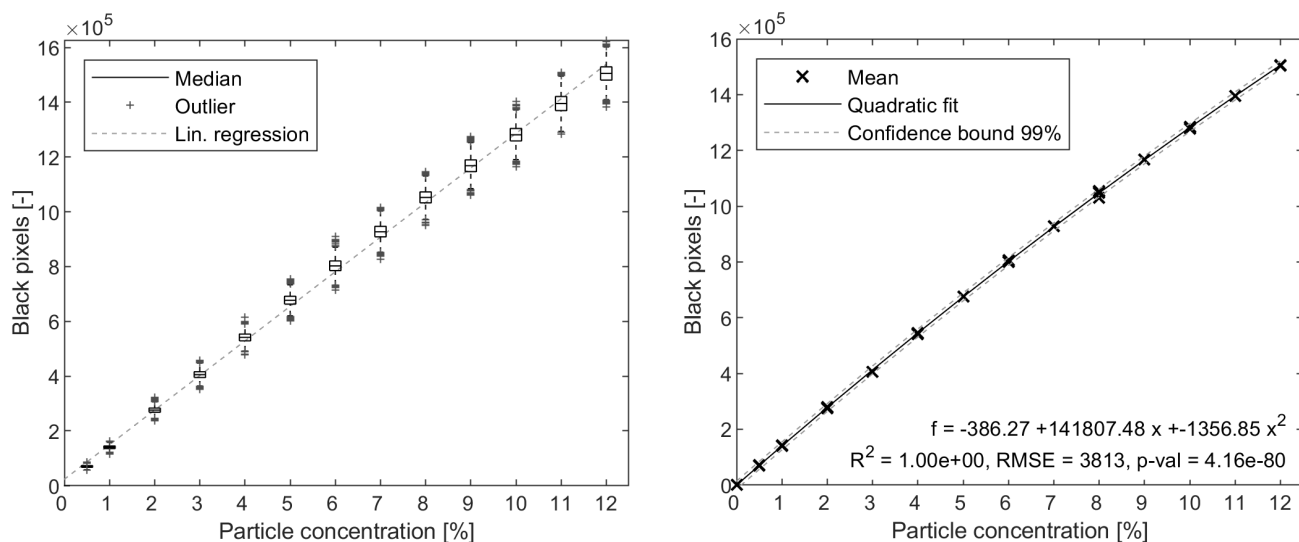


Figure 4. Results of calibration measurements for the gray granules. Left: Box plot of one calibration run. Right: Regression of four calibration runs.

However, this information involves a certain amount of uncertainty because of the fluctuations in the measured values. In order to derive a reliable averaging time, the normalized mean squared error (NMSE), which was defined by González-Castro, et al. (2000) as follows, was also evaluated:

$$NMSE = \frac{(P_T - P)^2}{p'^2} \quad [1]$$

with

- P ... Average black pixel value of a long-term measurement [-];
- P_T ... Average black pixel value of a time series of length T [-];
- p'^2 ... Variance of black pixel values of a long-term measurement [-].

The NMSE is used to evaluate the required measurement time with regard to the temporal randomness of a single measurement. The NMSE normalizes the mean squared error (MSE) using the variance of a data set (here: black pixel values of a long-term measurement) and gives the deviation of the mean value after a certain measurement time from the long-term mean value. Compared to the left side, the right side of Figure 5 shows clear differences between the individual time series, which also show no proportionality to the solids concentration.

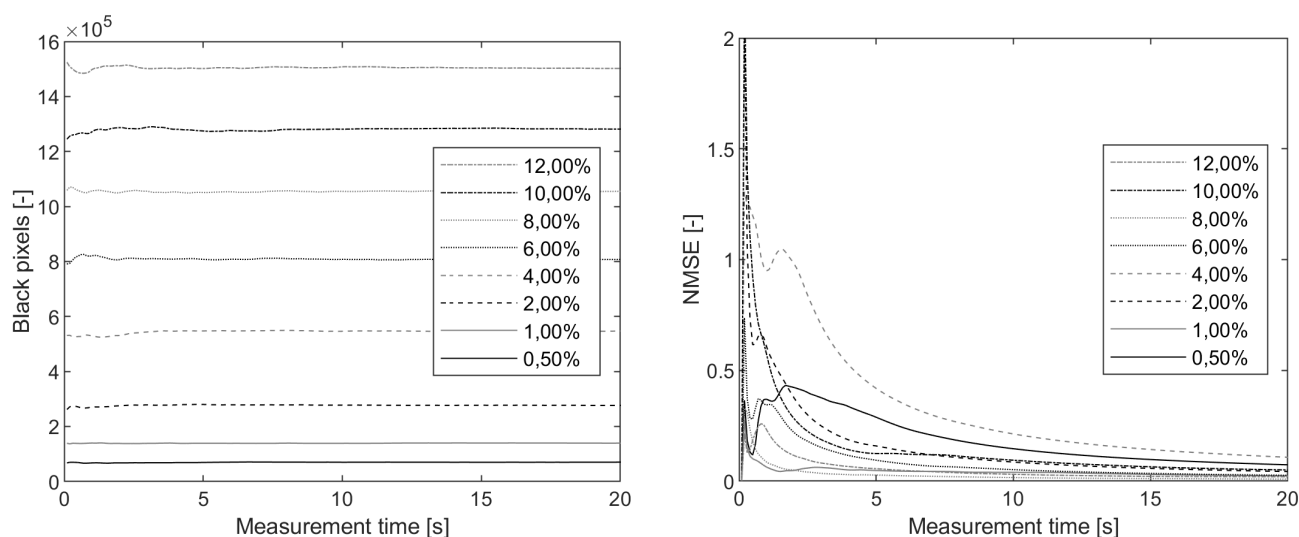


Figure 5. Temporal development of statistical parameters for the gray granules. Left: Mean value development for one calibration run. Right: Corresponding NMSE development.

With a desired NMSE $\leq 20\%$, 10 s were chosen as the minimum required averaging time. The temporal resolution of the measurement method was directly affected by this. Transport processes that took place in shorter time periods could not be recorded with the presented boundary conditions.

4.3 Validation measurements

The accuracy of the derived calibration function was checked by means of validation measurements. For this purpose, defined quantities of solids were fed directly into the inlet of the recirculation system and recorded via the measuring field. Figure 6 shows the measured values recorded at 10 Hz in light gray and a notably simplified data curve of stepwise averaged values with an averaging interval of 10 s in black, where the whole data set was partitioned in steps of the averaging interval. In the given example, each averaging interval had 100 values (10 Hz * 10 s), which explains the jagged curve. For comparison, a moving average curve is given as a dashed line, also with a window length of 10 s, which is smoother due to the larger amount of data points, but which lags in time due to the relatively long averaging interval.

Of the 49.5 kg added in a short time, only 47.3 kg were recorded, which corresponds to an absolute measurement error of $< 5\%$. After subtracting a minor loss during addition, the high peak load is particularly responsible for the measurement error. The solids concentration at the peak was about 17%, which was significantly above the secured calibrated range (12 %). In addition, the peak duration was less than three seconds and thus significantly shorter than the minimum required averaging time. Based on comparable data sets, the calibration function could be extrapolated to cover even higher concentrations. Comparative tests with solids concentrations up to 20% showed good results, but since such peaks did not occur during the operation of the test station in the present study, no additional validation measurements were required.

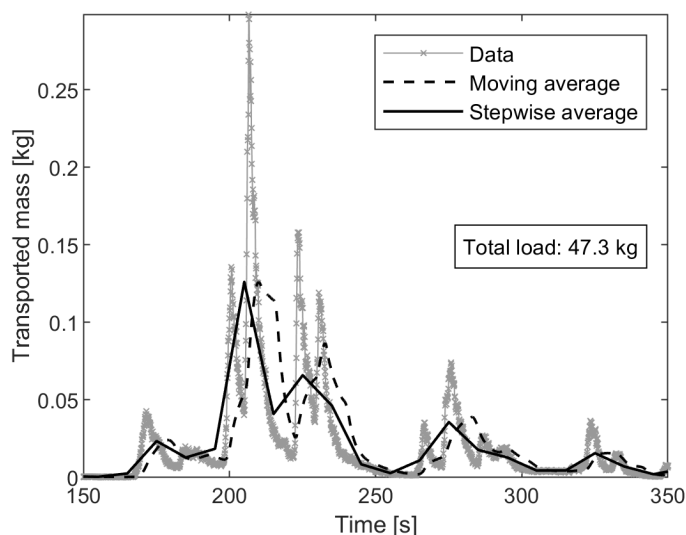


Figure 6. Validation time series with stepwise and moving average of a 49.5 kg sample.

During experiments, the measuring system was operated for many hours without any problems. In experiments with increased sediment transport, up to 10 t of material were transported through the recirculation system and measured. With an experiment duration of 8 hours, this corresponds to an average transport rate of 0.35 kg/s.

5 DISCUSSION

5.1 Uncertainties in the measurement procedure

Solids composition: Depending on the composition of the solids used, the particle sizes and shapes vary, and as a result the measurement uncertainty changes. In the simplest or statistically most reliable case, a single-grain material with perfectly spherical particles, the gray value of two camera images varies only due to the different particle distribution in the measuring field. In the case of solids with less uniform particle distributions and non-spherical particles, the formation of shadow, which is variable due to the orientation and size of the particles, is added as a variable for the proportion of black pixels in the single image. Due to a high variability of the particle geometry of the solids, the statistical uncertainty of a single measurement increases, which could however be compensated by a higher frame rate. An increase in the frame rate generally reduced the statistical uncertainty from the particle geometry and orientation and it is a useful measure with increasing heterogeneity of the solids, as long as no relevant quality losses of the individual images have to be accepted.

Flow conditions: If one could assume perfect mixing of the fluid-solid mixture and assume an equal distribution of the particles in the fluid at all times, a much lower frame rate would also be sufficient to determine the transport rate. In the present study, however, the solid particles used were relatively large and the volume

considered rather small, which led to a high variability of the black pixel number in the measuring field. Furthermore, the particle load of the submersible pump was not constant, which is why the assumption of perfect mixing could not be made. Nevertheless, the mean values became stable within a very short period of time (cf. Figure 5, right). Furthermore, parameters assumed to be constant, such as pump performance, fluctuate and have a direct effect on the measurement result.

System pressure: The system pressure, or more precisely the static pressure level in the measuring field, also had a significant influence on the measurement results. Fluctuations in the static pressure level led to proportionally fluctuating black pixel numbers at constant solids concentrations, even if all other parameters remained constant. The pressure height was regulated by means of a vertical shaft integrated into the recirculation system, originally to dampen fluctuations in pump performance, and subsequently kept constant for all measurements. The following two mechanisms probably played a role here: On the one hand, fine gas bubbles were found on the particle surfaces, which changed their size depending on the system pressure and thus also influenced the scattering of the light coming from the light panel under the measuring field. On the other hand, a slight curvature of the glass plates of the measuring field to the outside, depending on the system pressure, could not be excluded, whereby particles would flow past the camera at a slightly smaller distance than calibrated. However, neither of these mechanisms could be demonstrated in the present study, which is why a final explanation of this phenomenon is still pending.

Camera position: The size of the projected particle surface, that was identified as black by the threshold, varied along the measuring field. The following reasons were identified: A particle in the center of the image was displayed sharper than at the edge of the image, i.e. with a greater gray value gradient at the particle edges, because hardly any scattered light brightened the particle edge due to the vertically incident light rays. A particle at the edge of the image, on the other hand, reflected parts of the light coming from below to the side in the direction of the camera, making the particle edge in this area brighter. Depending on the intensity of the scattered light, pixels in the edge area fell below the threshold for distinguishing between white and black, reducing the particle area imaged as black. In addition, the greater distance of a particle at the edge played a role, because particles further away from the camera occupied fewer pixels, i.e. were imaged smaller. The change of the particle surface was not ideally linear-radial from the center to the edge, but was significantly influenced by the structure of the optical system as well as the installation and alignment of camera and measuring field to each other. For this reason, the camera was permanently installed and fixed so that the height above the measuring field could be reproducibly adjusted and kept constant. The same applied to the orientation of the camera in space.

5.2 Advantages and disadvantages in comparison to other methods

The measurement method is not dependent on the dimensions and transport conditions of the test station, which is why either bed load transport or total transport can be measured. A large spectrum of solids can be measured as long as the solid particles are still large or heavy enough that they can be separated from the surrounding water in the sediment trap. Due to the very small data volume, there is practically no limit to the measurement duration.

Disadvantages of the measurement method are the increased effort involved in preparing and performing the calibration measurements. In addition, there is only little flexibility to making adjustments to the measuring system. A certain calibration function can only be exact if all parameters set during calibration are also set the same during measurement. A change in the discharge in the measuring system would change the relationship between black pixels and solids concentration even if all other parameters were kept constant.

This low flexibility in operation could be improved by a different evaluation method of the camera images, e.g. particle detection. However, particle superposition in the measuring field would lead to measurement errors in a method with particle detection if the transport rate were determined there via the measured number of solid particles. Reducing the height of the liquid sheet in the measuring field to only slightly more than the diameter of a single particle would largely prevent the occurrence of particle overlaps. In these conditions, particle detection would present an alternative to calibrated gray value comparison and the time-consuming calibration measurements would no longer be necessary. In preliminary investigations, however, such a reduction led to the successive blockage of the measuring field and proved to be impracticable.

6 CONCLUSION

The presented measurement method is able to generate high-quality information about the transport of solids during experiment operation in real-time and with very low computing power. The required calibration proved an efficient way to reduce systematic uncertainties in the measurement procedure by implicitly taking them into account in the calibration function. The measurement accuracy achieved in the thin liquid sheet is comparatively high with around 5% and below, while at the same time a wide range of particle loads can be measured (0 - 20%). With further research effort, the remaining uncertainties could be quantified more precisely, which could potentially increase the measurement accuracy even more. Integrating the measurement method into a system for the recirculation of solids can bring financial benefits especially for long-term experiments, since hardly any additional supply material is required.

REFERENCES

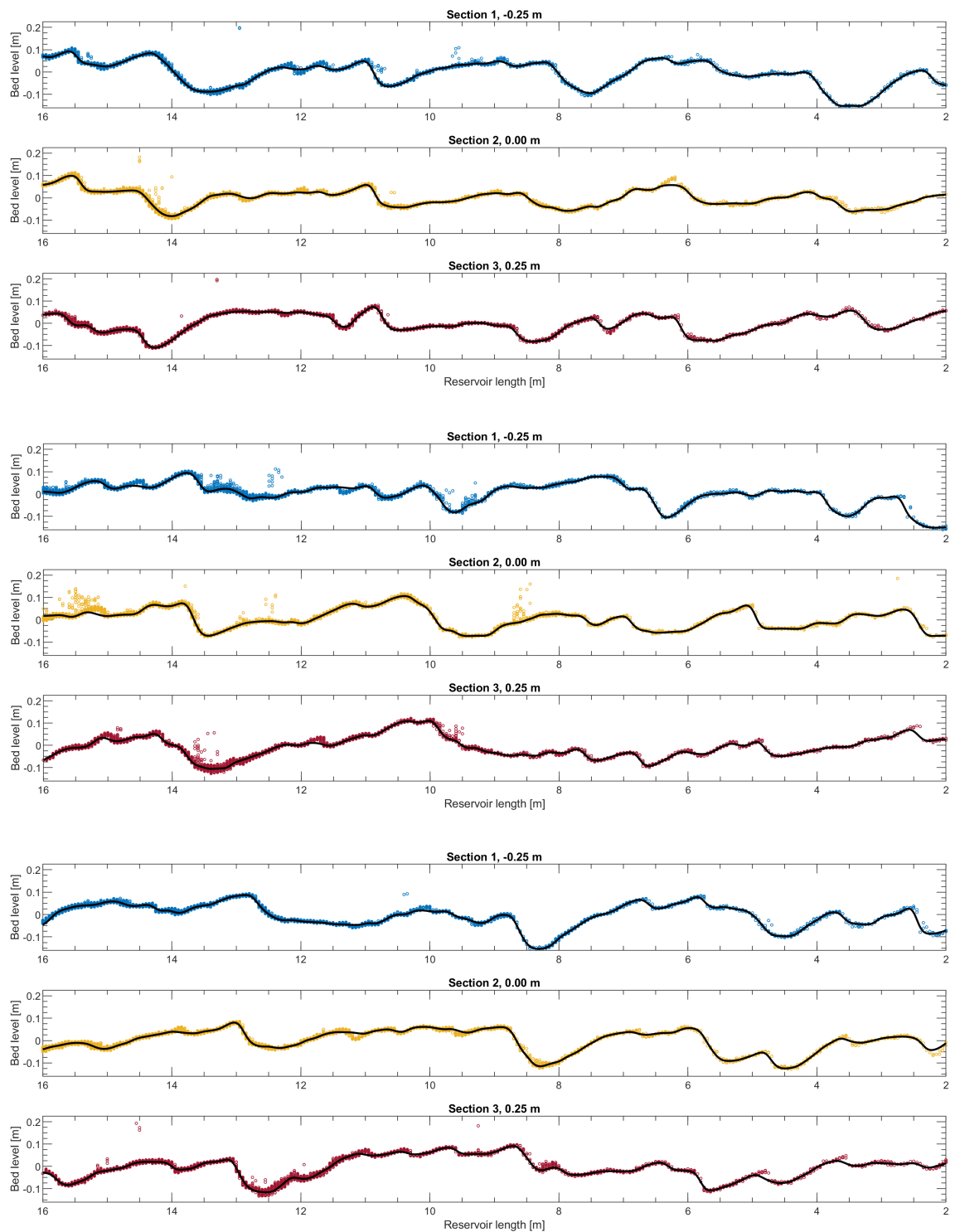
- Albayrak, I., Felix, D., Hagmann, M., Boes, R.M., 2015. Suspended Sediment and Bed Load Transport Monitoring Techniques, in: Dresdner Wasserbauliche Mitteilungen Heft 53. Presented at the 38. Dresdner Wasserbaukolloquium 2015, Technische Universität Dresden, Institut für Wasserbau und Technische Hydromechanik.
- Ancey, C., Bohorquez, P., Bardou, E., 2014. Sediment transport in mountain rivers. ERCOFTAC Bulletin 100, 37–52.
- Bartram, J., Ballance, R., United Nations, World Health Organization (Eds.), 1996. Water quality monitoring: a practical guide to the design and implementation of freshwater quality studies and monitoring programmes, 1st ed. ed. E & FN Spon, London ; New York.
- Bekić, D., Mikoš, M., Babić-Mladenović, M., Kupusović, T., Oskoruš, D., 2015. Review of technical international standards and techniques for sediment monitoring, in: Towards Practical Guidance for Sustainable Sediment Management (SSM) Using the Sava River Basin as a Showcase. Presented at the Workshop on sediment monitoring, Zagreb.
- Bollrich, G., 2013. Technische Hydromechanik 1: Grundlagen, 7th ed. Beuth.
- Dhont Blaise, Rousseau Gauthier, Ancey Christophe, 2017. Continuous Monitoring of Bed-Load Transport in a Laboratory Flume Using an Impact Sensor. Journal of Hydraulic Engineering 143.
- Diplas, P., Kuhnle, R., Gray, J., Glysson, D., Edwards, T., 2008. Sediment transport measurements: Chapter 5, in: Marcelo H. García (Ed.), Sedimentation Engineering: Processes, Measurements, Modeling, and Practice. American Society of Civil Engineers, pp. 307–353.
- García, M.H., 2006. ASCE Manual of Practice 110 - Sedimentation Engineering: Processes, Measurements, Modeling and Practice, in: World Environmental and Water Resource Congress 2006.
- González-Castro, J.A., Oberg, K., Duncker, J.J., 2000. Effect of Temporal Resolution on the Accuracy of ADCP Measurements, in: Joint Conference on Water Resource Engineering and Water Resources Planning. American Society of Civil Engineers, Minneapolis, Minnesota.
- Gyr, A., Hoyer, K., 2006. Sediment Transport: A Geophysical Phenomenon, 2006 edition. ed. Springer, Berlin etc.
- Haimann, M., 2015. Sediment Transport Monitoring and Modelling, in: Towards Practical Guidance for Sustainable Sediment Management (SSM) Using the Sava River Basin as a Showcase. Presented at the Workshop on sediment monitoring, Zagreb.
- Hughes, S.A., 1993. Physical models and laboratory techniques in coastal engineering, Advanced series on ocean engineering. World Scientific, Singapore.
- International Atomic Energy Agency (IAEA), 2005. Fluvial sediment transport: analytical techniques for measuring sediment load. International Atomic Energy Agency, Vienna.
- Kirkegaard, J., Wolters, G., Suterhland, J., Soulsby, R., Frostick, L., McLelland, S., Mercer, T., Gerritsen, H., 2011. Users guide to physical modelling and experimentation, 1. ed., IAHR design manual. CRC Press, Boca Raton etc.
- KROHNE Messtechnik GmbH, 2017. OPTIFLUX 2000 - Technical Datasheet. Duisburg.
- Raffel, M., 2007. Particle image velocimetry: a practical guide. Springer, Berlin.
- Rüther, N., 2017. State of the art of sediment transport measurement techniques in rivers and reservoirs. [WWW Document]. URL <http://folk.ntnu.no/nruther/TVM4155/Lecture14-NR/Sediment%20transport%20measurement%20techniques.pdf> (accessed 4.5.19).
- Van Rijn, L.C., Roberti, H., 2014. Manual Sediment Transport Measurements in Rivers, Estuaries and Coastal Seas - Coastal Wiki [WWW Document]. URL http://www.coastalwiki.org/wiki/Manual_Sediment_Transport_Measurements_in_Rivers,_Estuaries_and_Coastal_Seas#cite_ref-1 (accessed 4.5.19).
- Yalin, M.S., 1972. Mechanics of sediment transport. Pergamon Press, Oxford; New York.
- Yalin, M.S., 1971. Theory of Hydraulic Models. Macmillan Education, Limited, London.
- Zanke, U., 1982. Grundlagen der Sedimentbewegung. Springer, Berlin; New York.

C. Dynamic bed equilibrium data

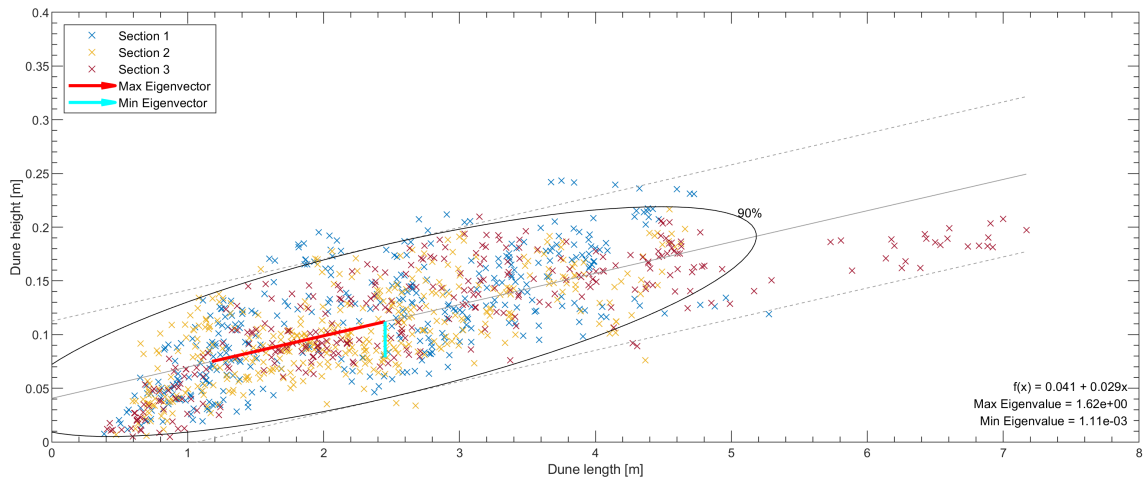
C.1. $H = 21.25$ cm

Q101-H21

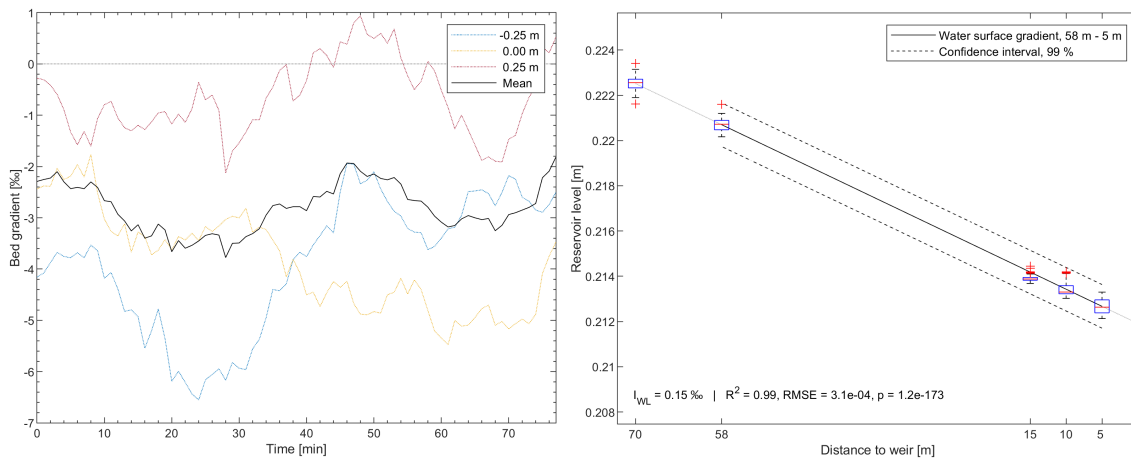
Approximate locations of the bed surface in 3 longitudinal sections after 1, 30 and 60 minutes of bed survey:



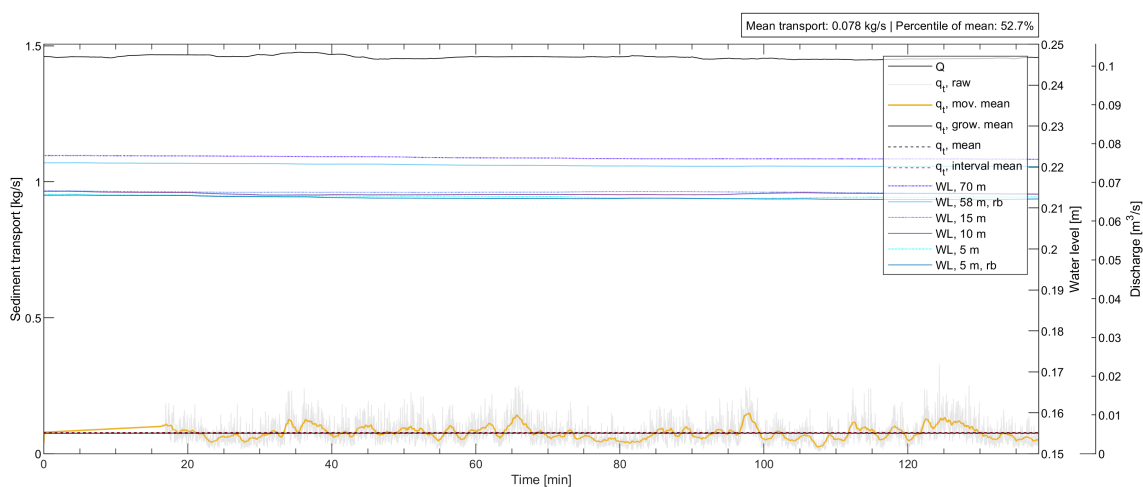
Dune lengths and heights of the reservoir bed:



Time series of the longitudinal bed gradient (left) and averaged longitudinal water surface gradient in the reservoir (right):

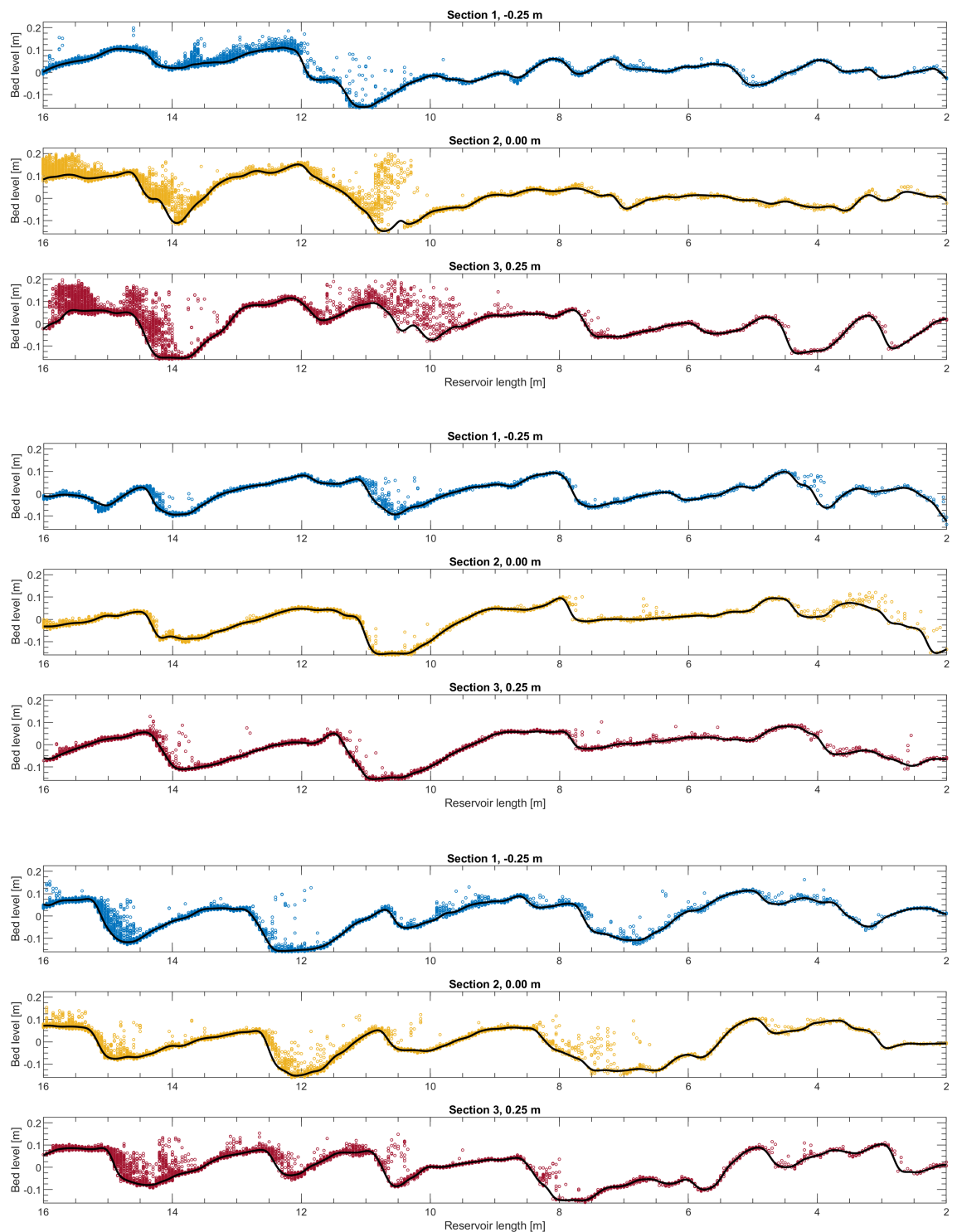


Discharge, water levels and sediment transport rate time series during the bed survey:

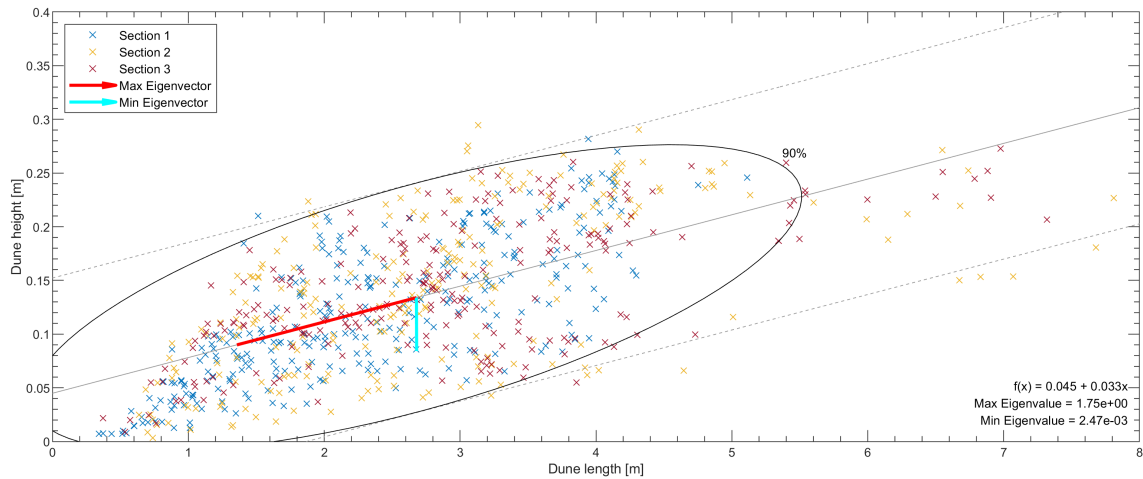


Q135-H21

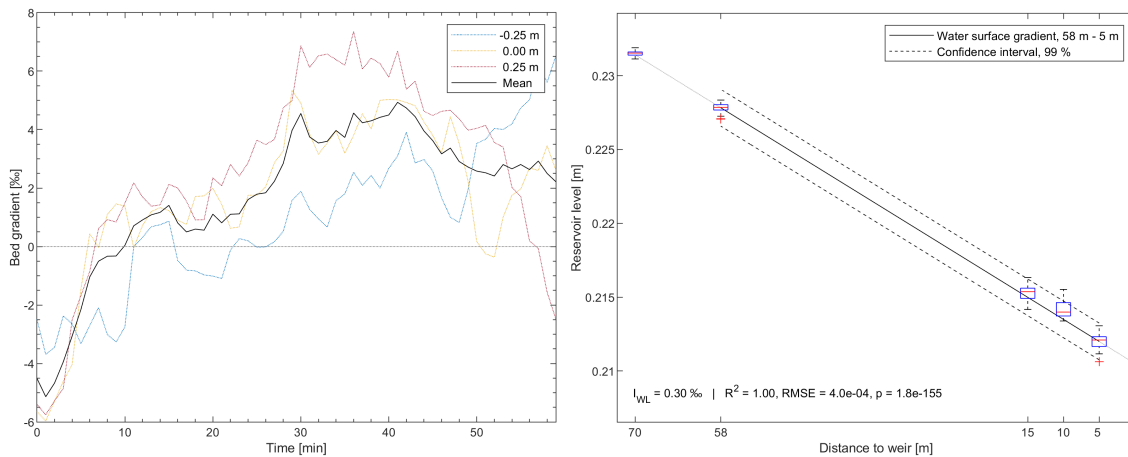
Approximate locations of the bed surface in 3 longitudinal sections after 1, 30 and 60 minutes of bed survey:



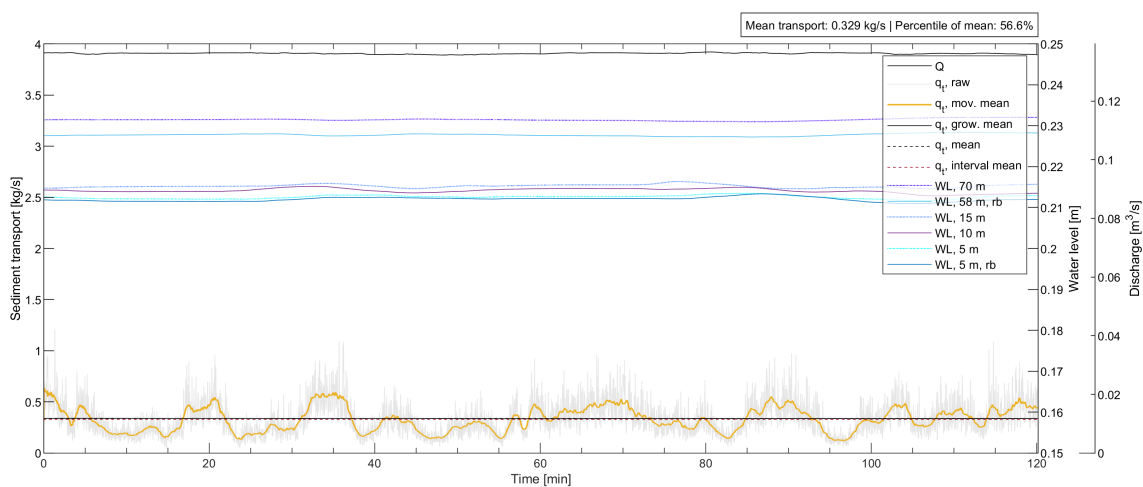
Dune lengths and heights of the reservoir bed:



Time series of the longitudinal bed gradient (left) and averaged longitudinal water surface gradient in the reservoir (right):

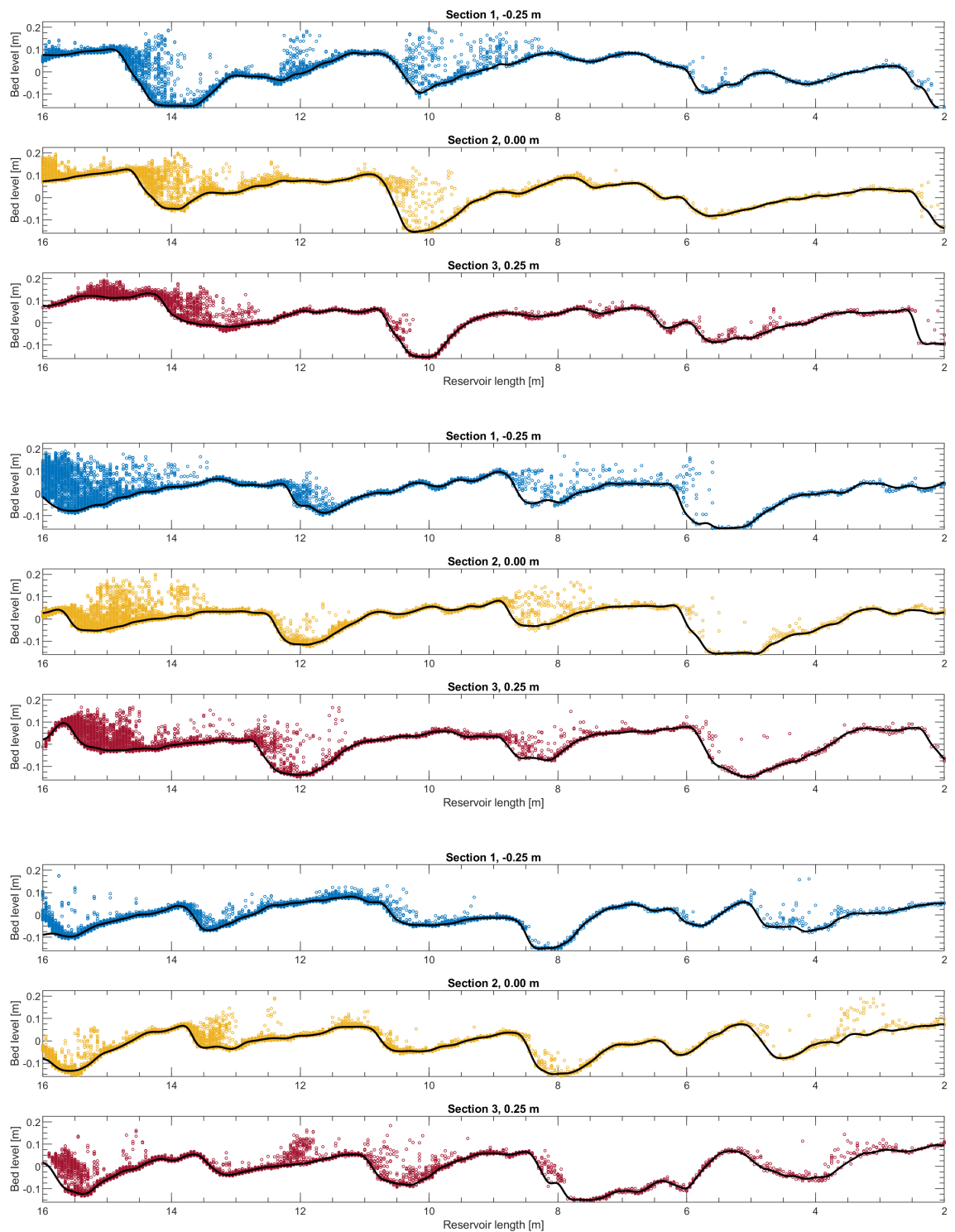


Discharge, water levels and sediment transport rate time series during the bed survey:

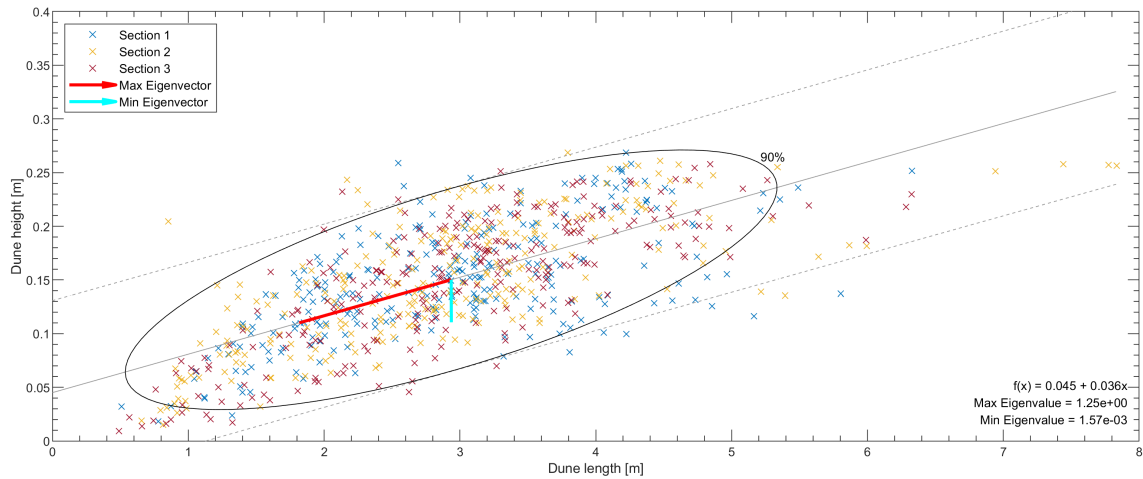


Q162-H21

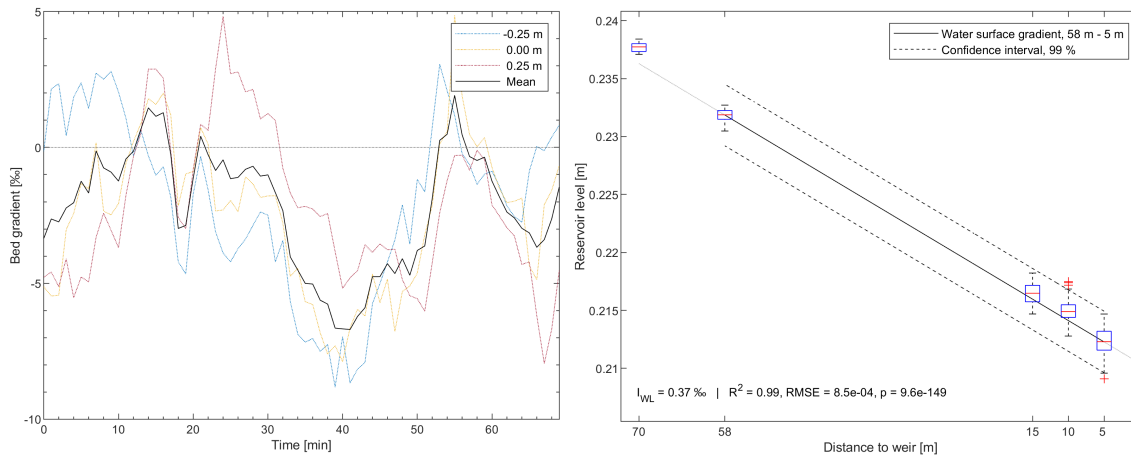
Approximate locations of the bed surface in 3 longitudinal sections after 1, 30 and 60 minutes of bed survey:



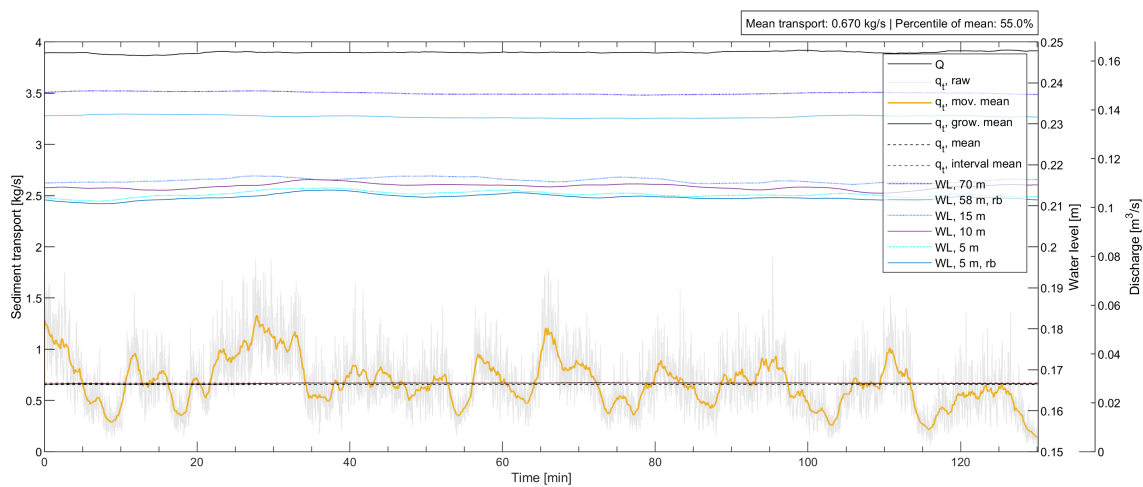
Dune lengths and heights of the reservoir bed:



Time series of the longitudinal water surface gradient (left) and averaged longitudinal water surface gradient in the reservoir (right):

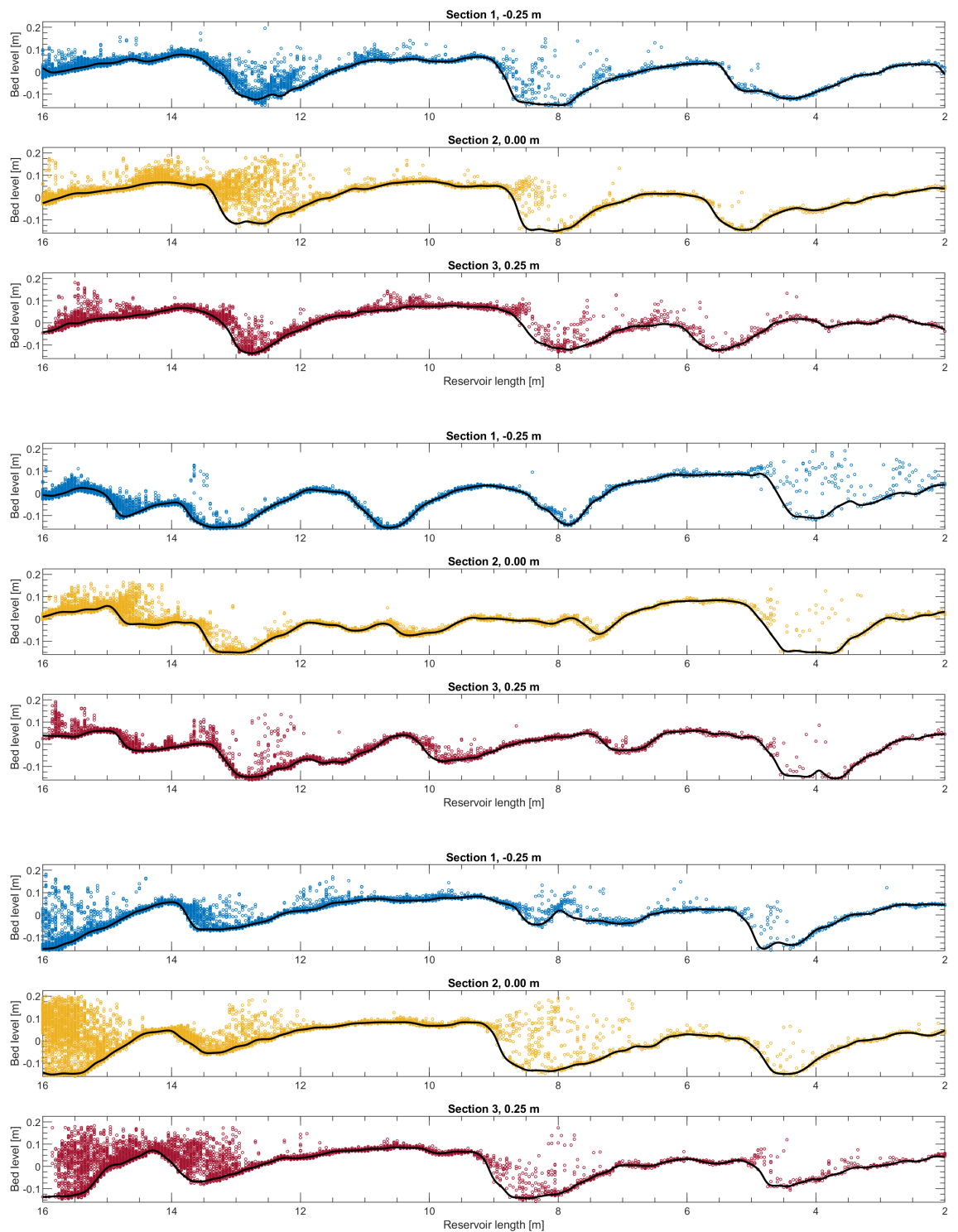


Discharge, water levels and sediment transport rate time series during the bed survey:

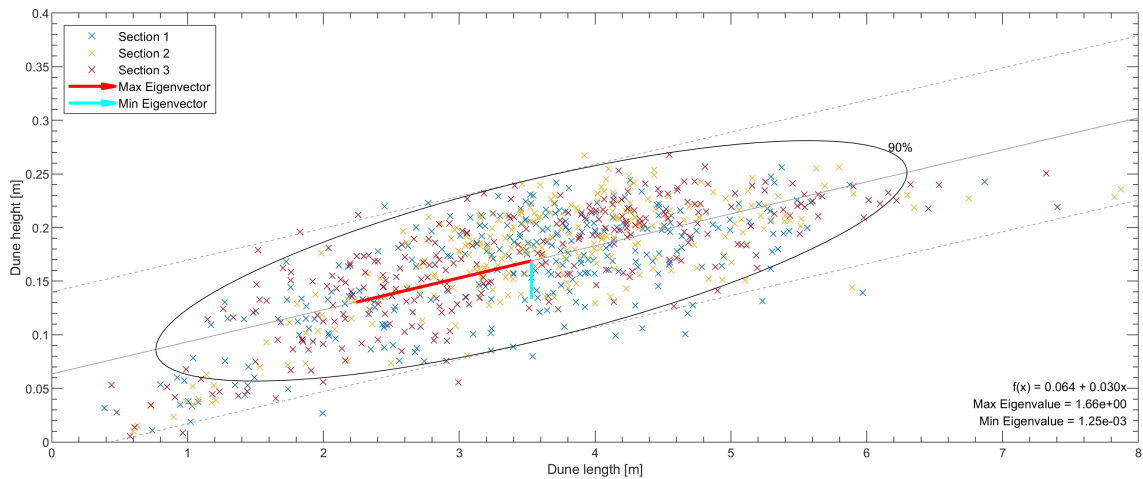


Q193-H21

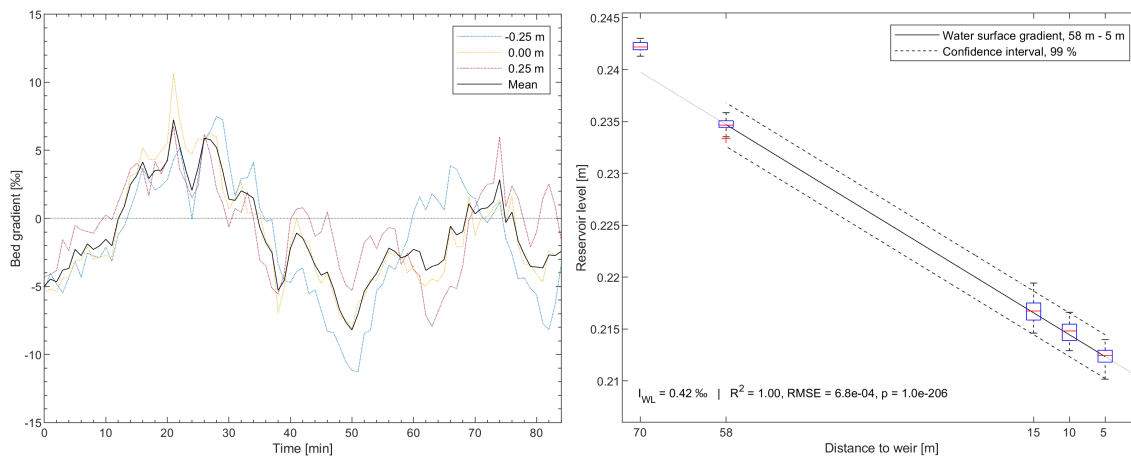
Approximate locations of the bed surface in 3 longitudinal sections after 1, 30 and 60 minutes of bed survey:



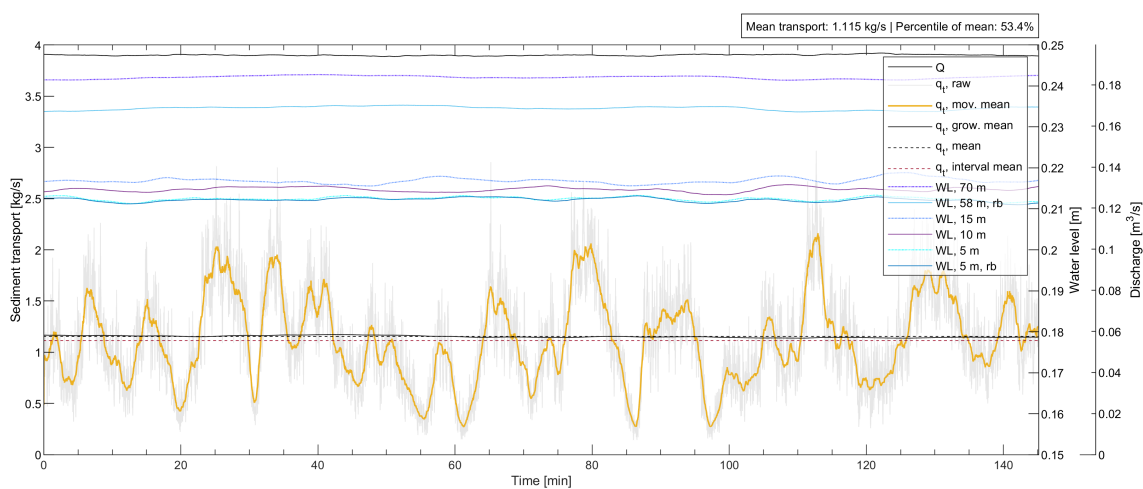
Dune lengths and heights of the reservoir bed:



Time series of the longitudinal bed gradient (left) and averaged longitudinal water surface gradient in the reservoir (right):

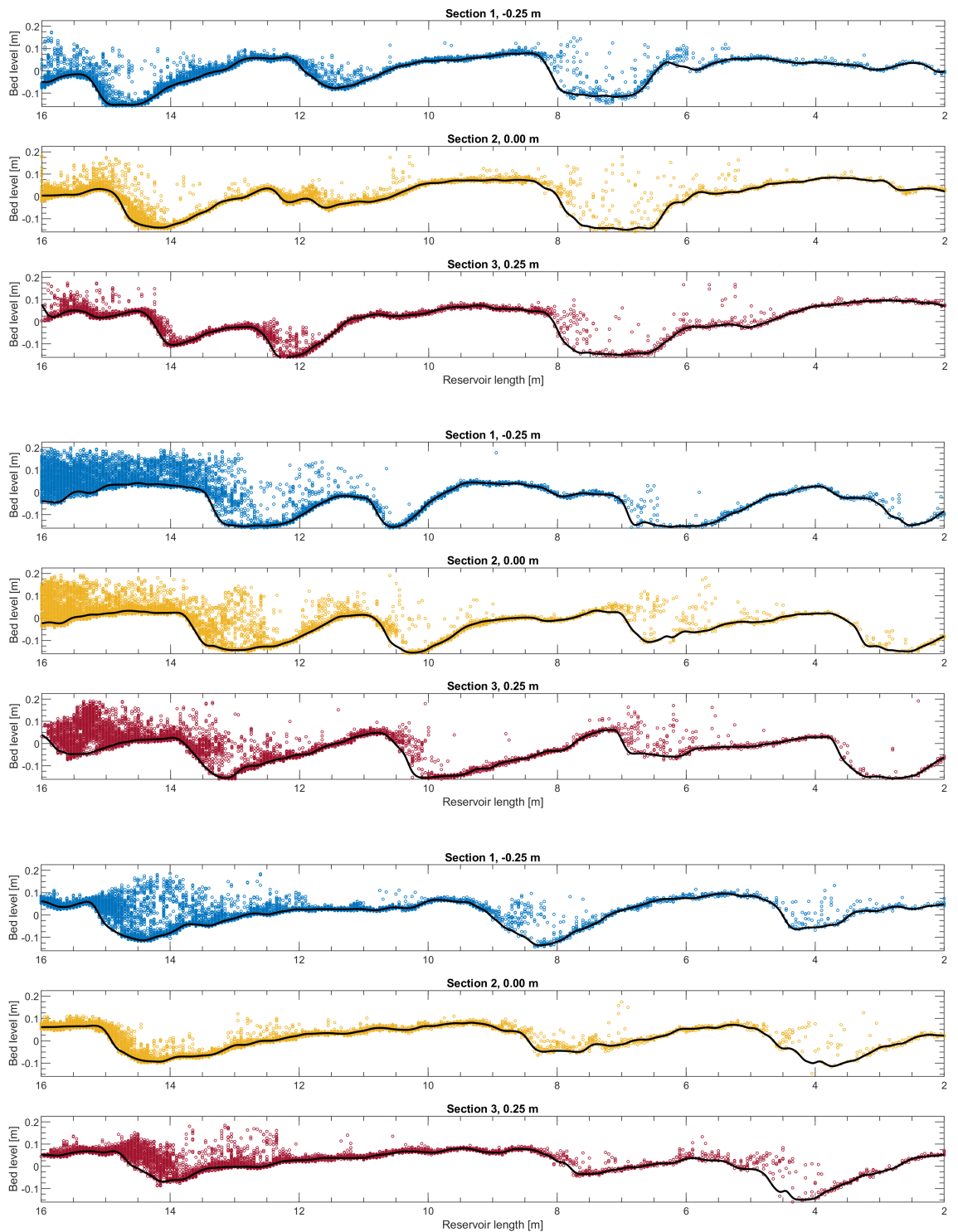


Discharge, water levels and sediment transport rate time series during the bed survey:

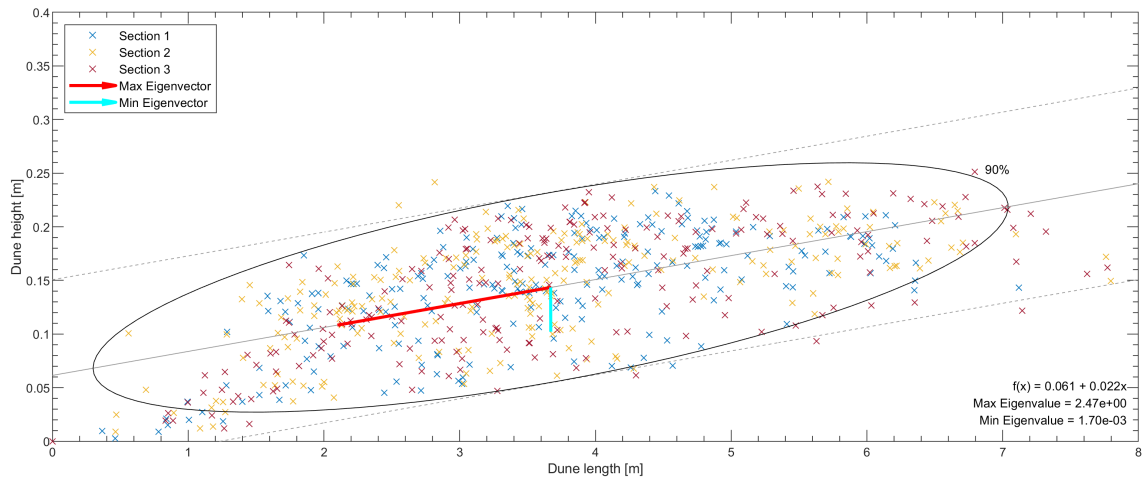


Q216-H21

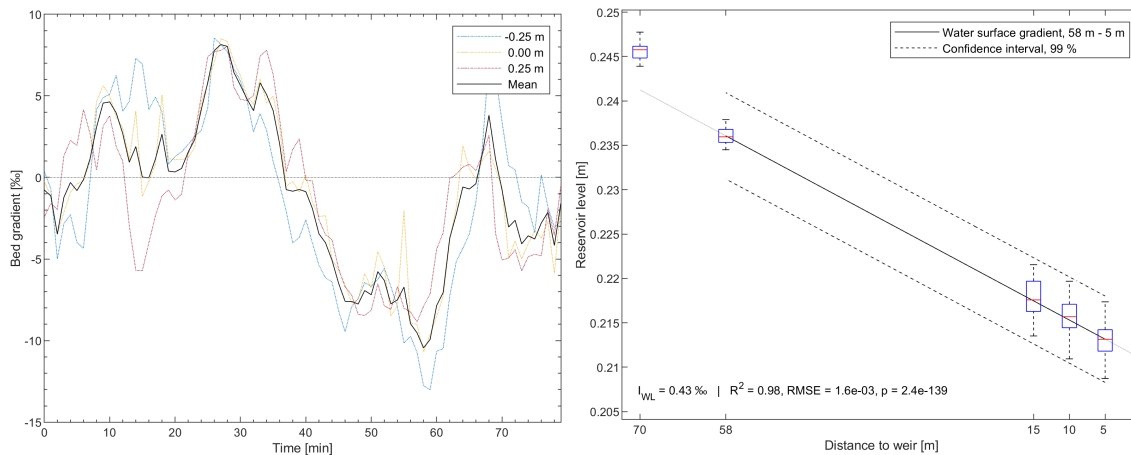
Approximate locations of the bed surface in 3 longitudinal sections after 1, 30 and 60 minutes of bed survey:



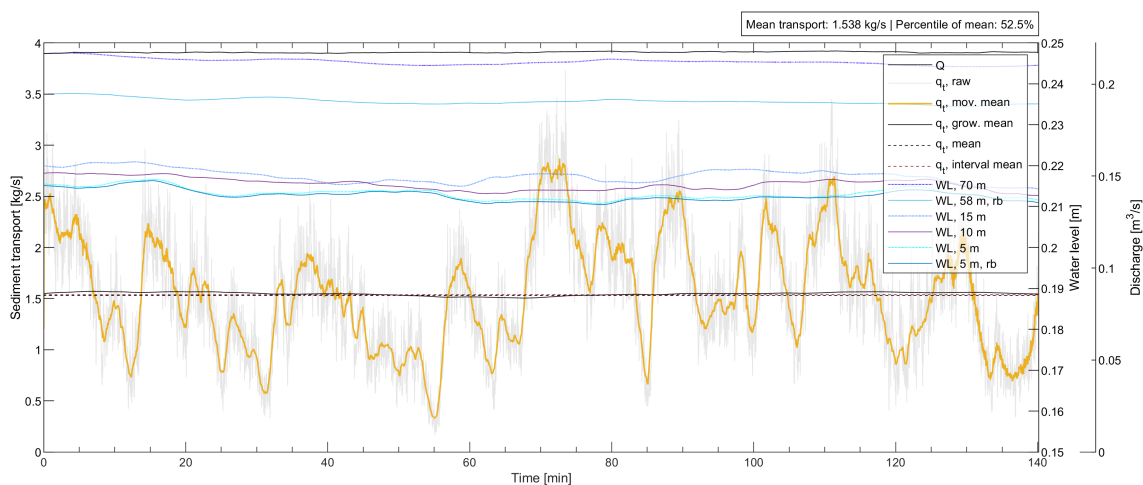
Dune lengths and heights of the reservoir bed:



Time series of the longitudinal bed gradient (left) and averaged longitudinal water surface gradient in the reservoir (right):



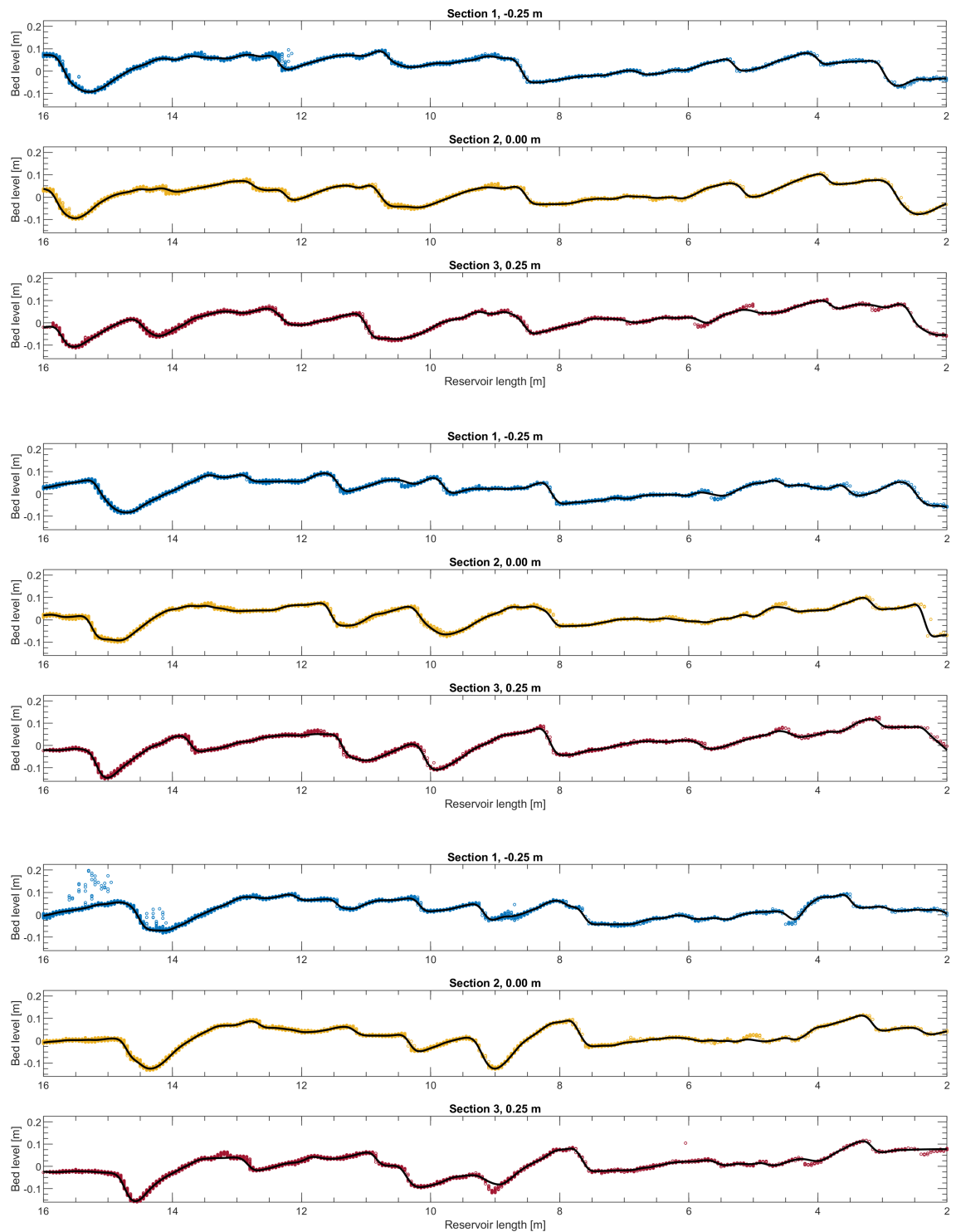
Discharge, water levels and sediment transport rate time series during the bed survey:



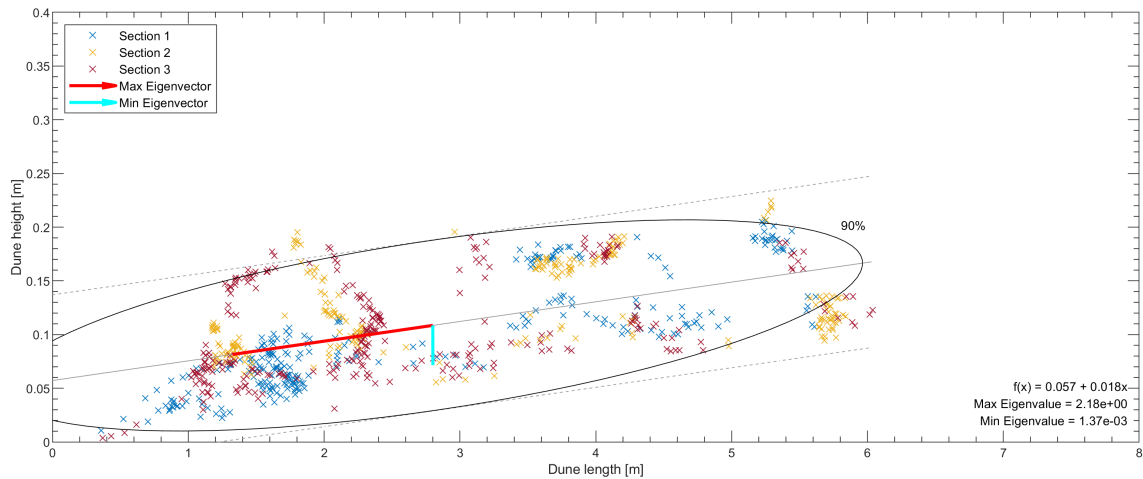
C.2. $H = 30.00$ cm

Q135-H30

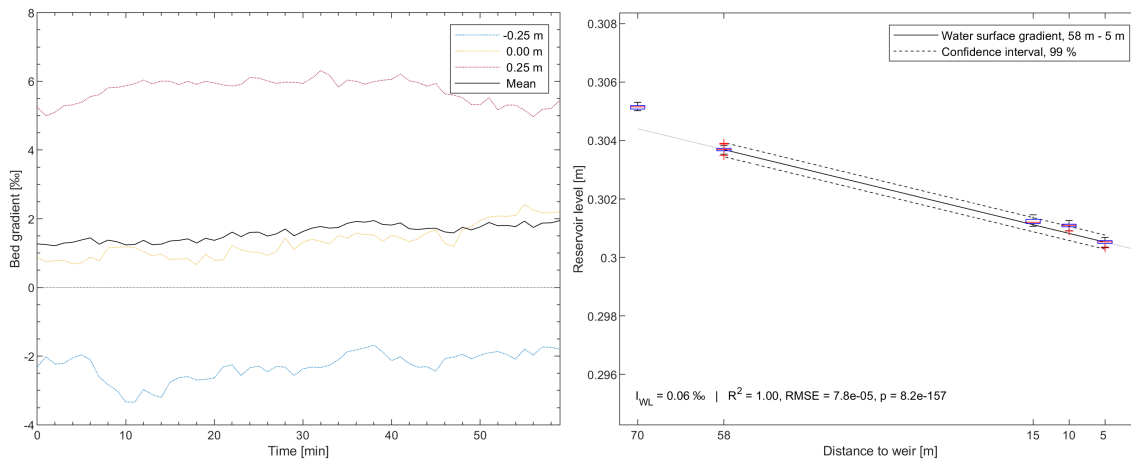
Approximate locations of the bed surface in 3 longitudinal sections after 1, 30 and 60 minutes of bed survey:



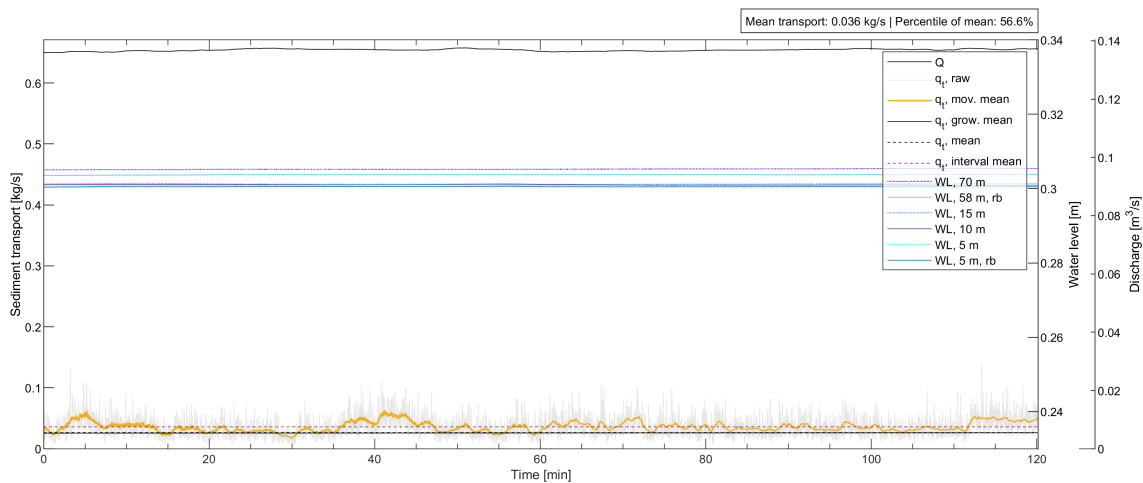
Dune lengths and heights of the reservoir bed:



Time series of the longitudinal bed gradient (left) and averaged longitudinal water surface gradient in the reservoir (right):

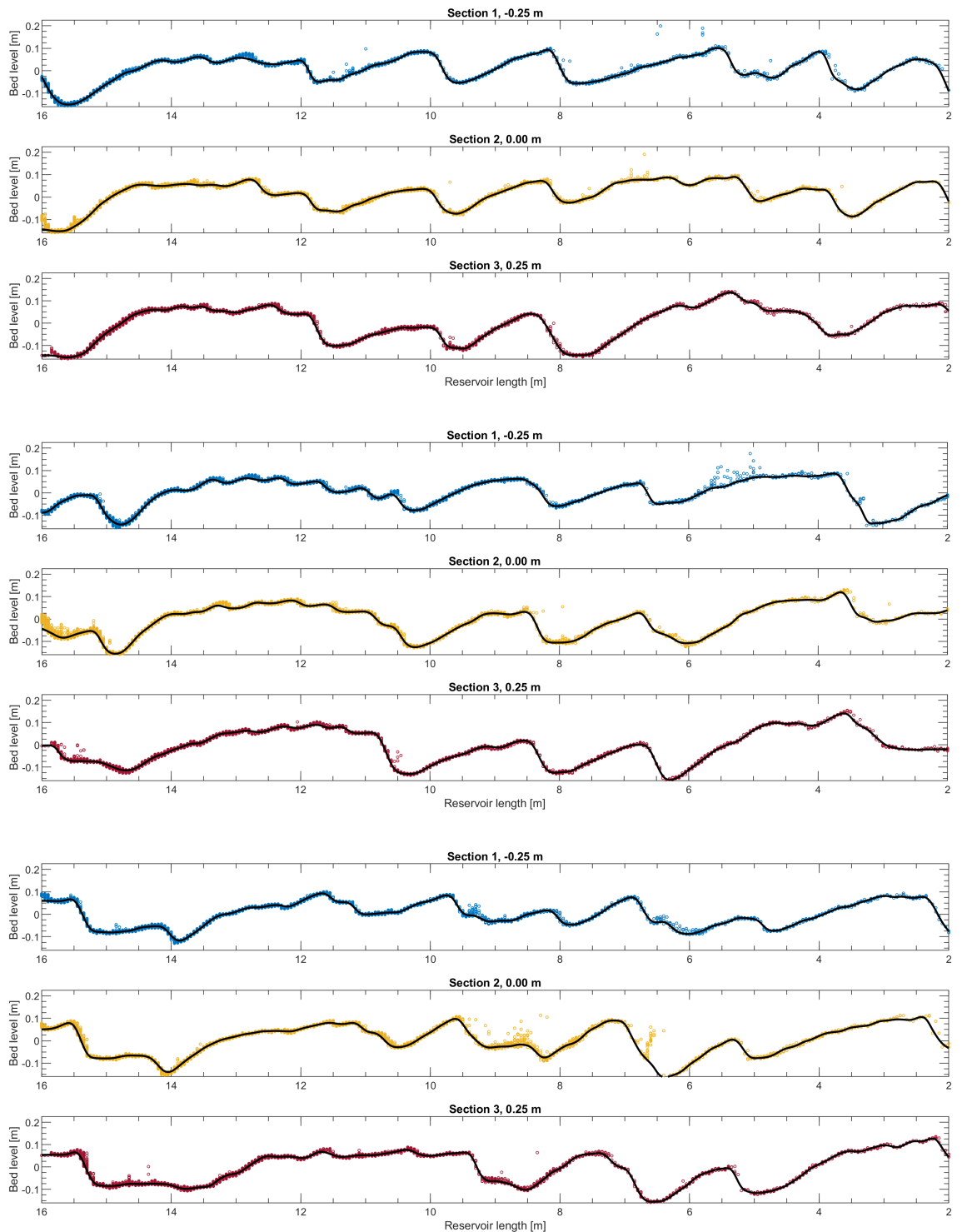


Discharge, water levels and sediment transport rate time series during the bed survey:

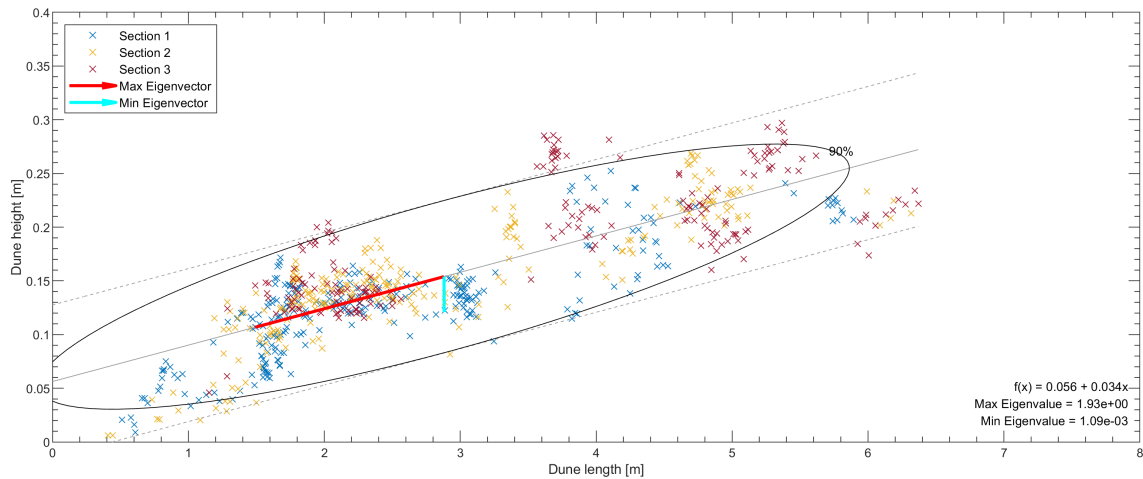


Q162-H30

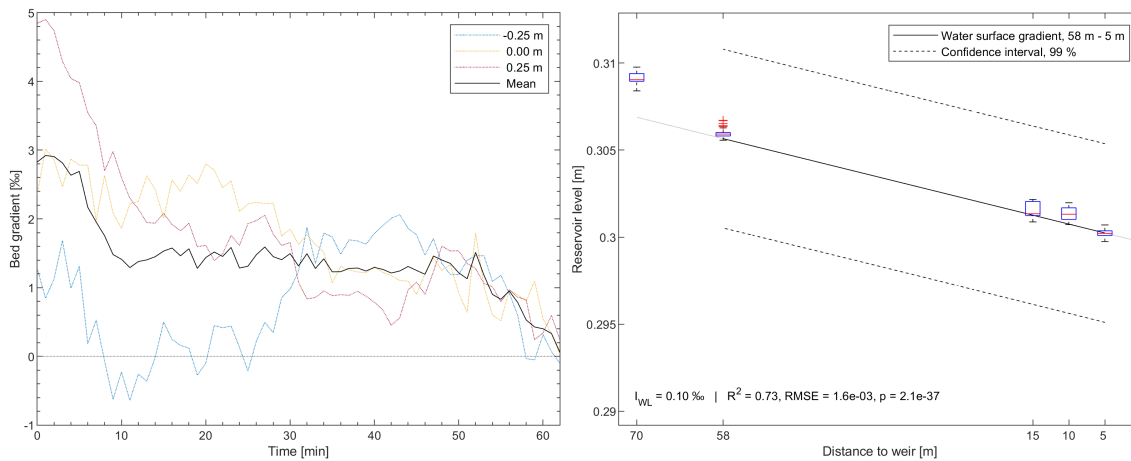
Approximate locations of the bed surface in 3 longitudinal sections after 1, 30 and 60 minutes of bed survey:



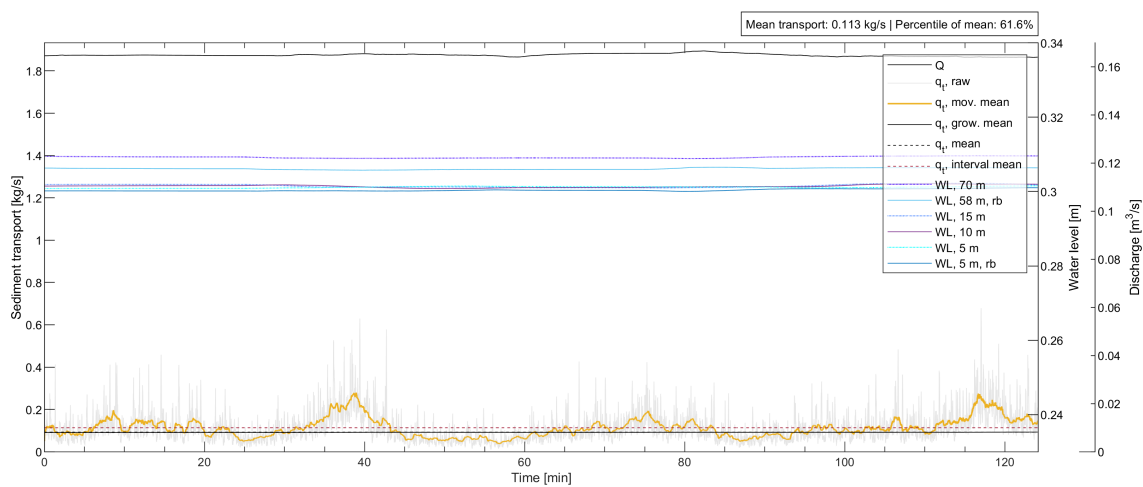
Dune lengths and heights of the reservoir bed:



Time series of the longitudinal bed gradient (left) and averaged longitudinal water surface gradient in the reservoir (right):

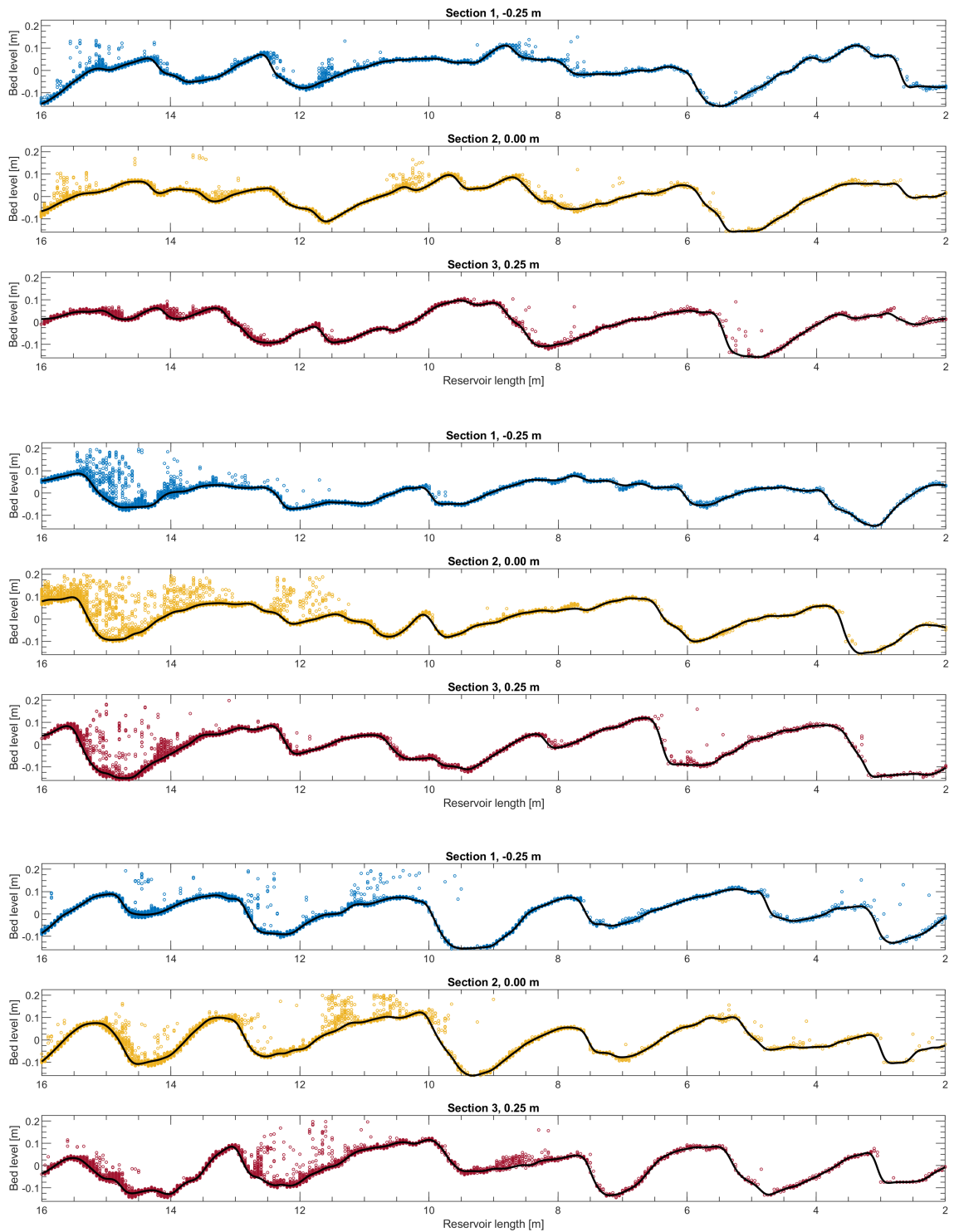


Discharge, water levels and sediment transport rate time series during the bed survey:

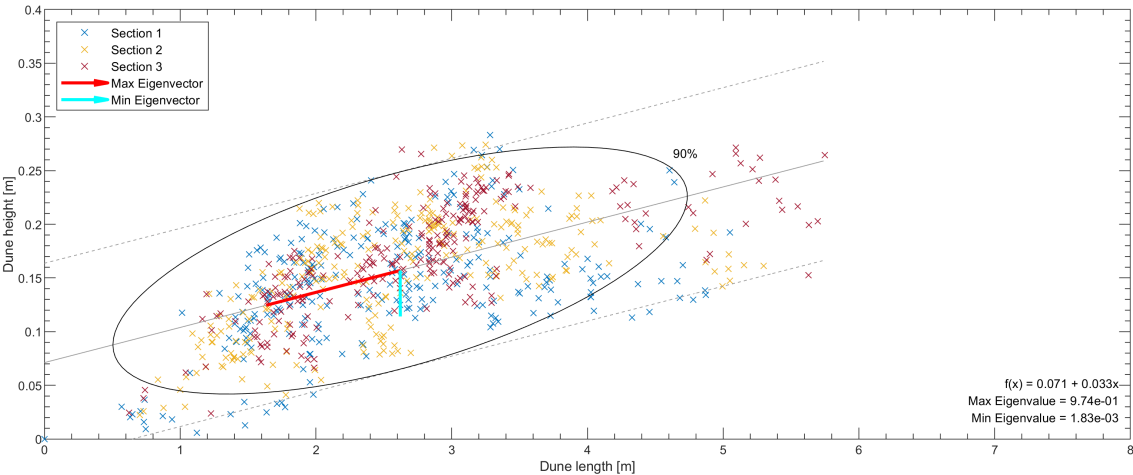


Q180-H30

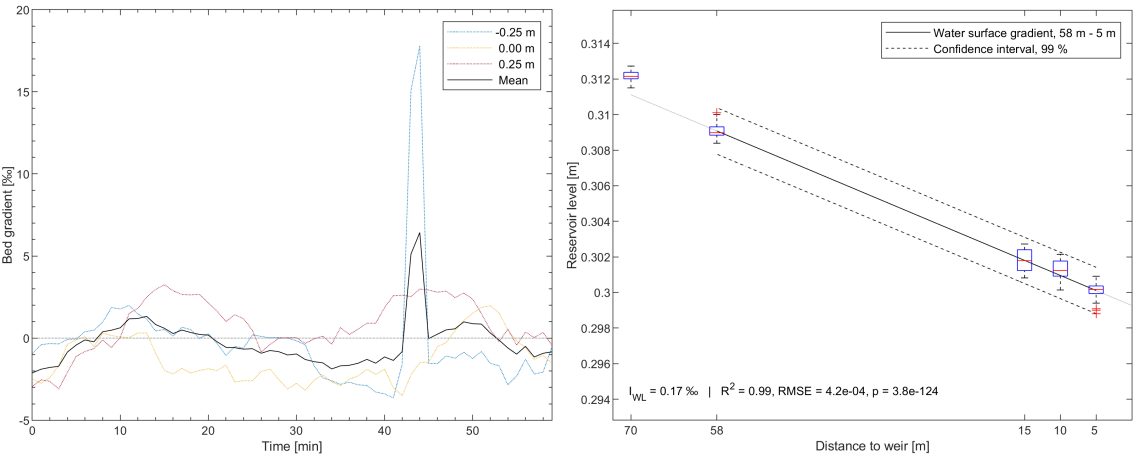
Approximate locations of the bed surface in 3 longitudinal sections after 1, 30 and 60 minutes of bed survey:



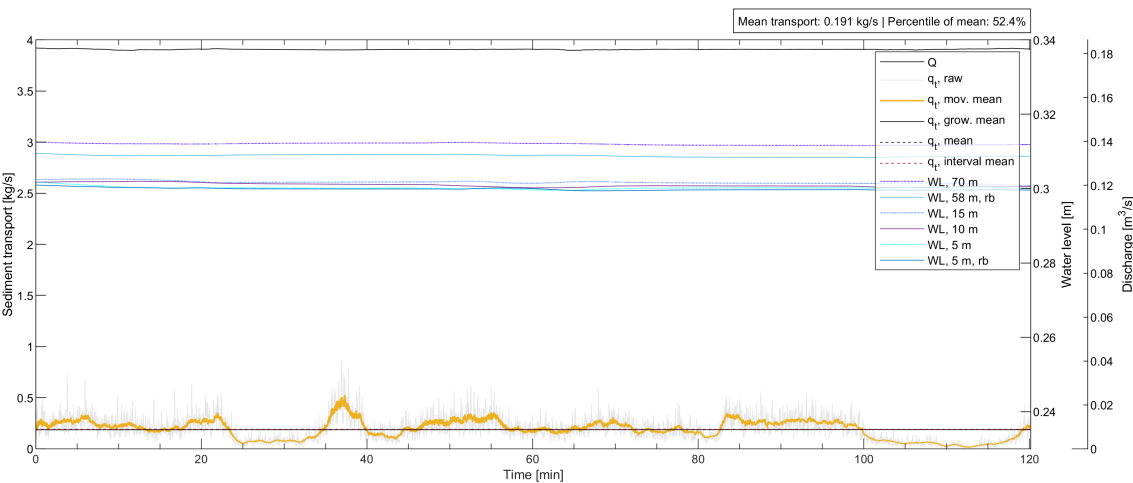
Dune lengths and heights of the reservoir bed:



Time series of the longitudinal bed gradient (left) and averaged longitudinal water surface gradient in the reservoir (right):

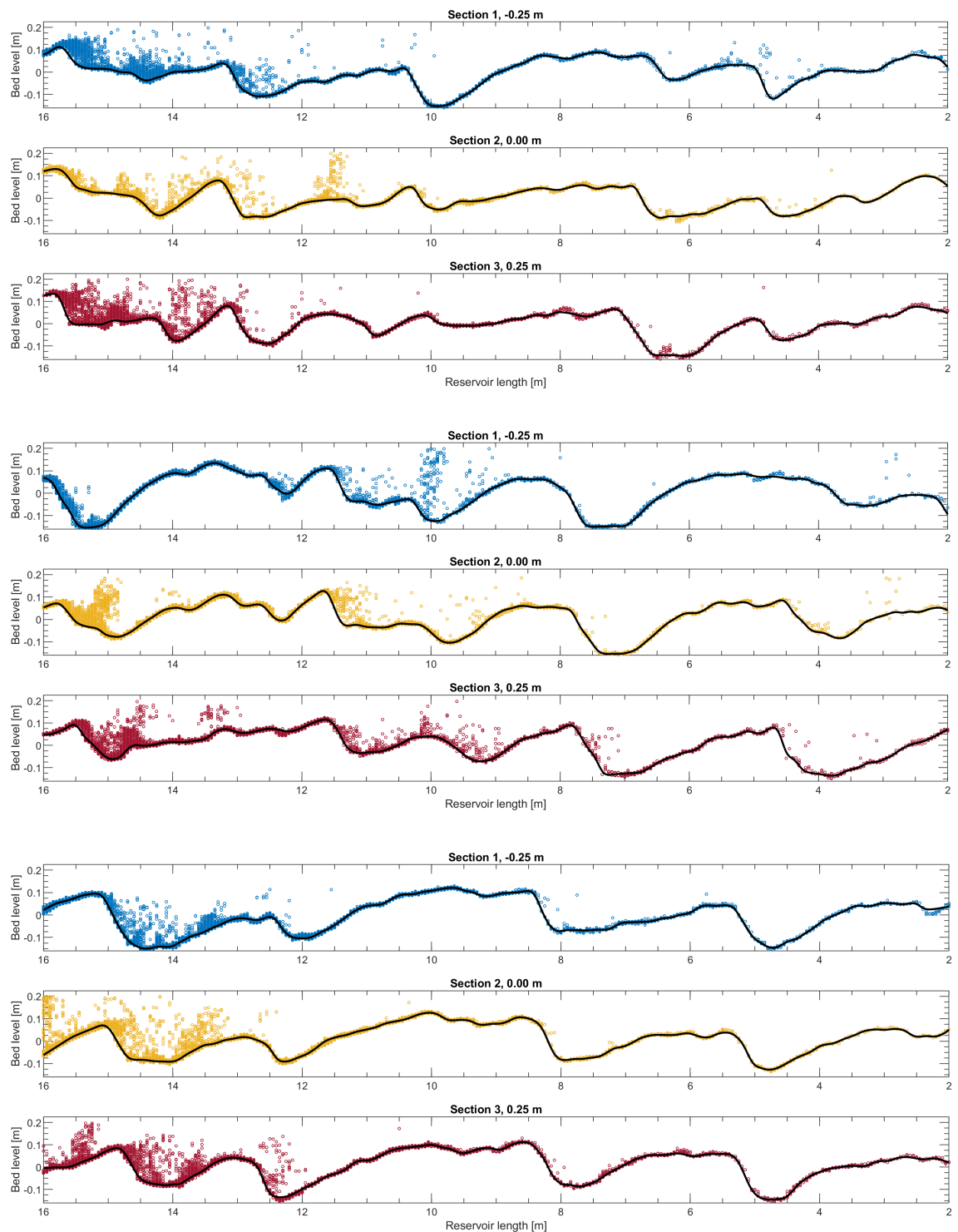


Discharge, water levels and sediment transport rate time series during the bed survey:

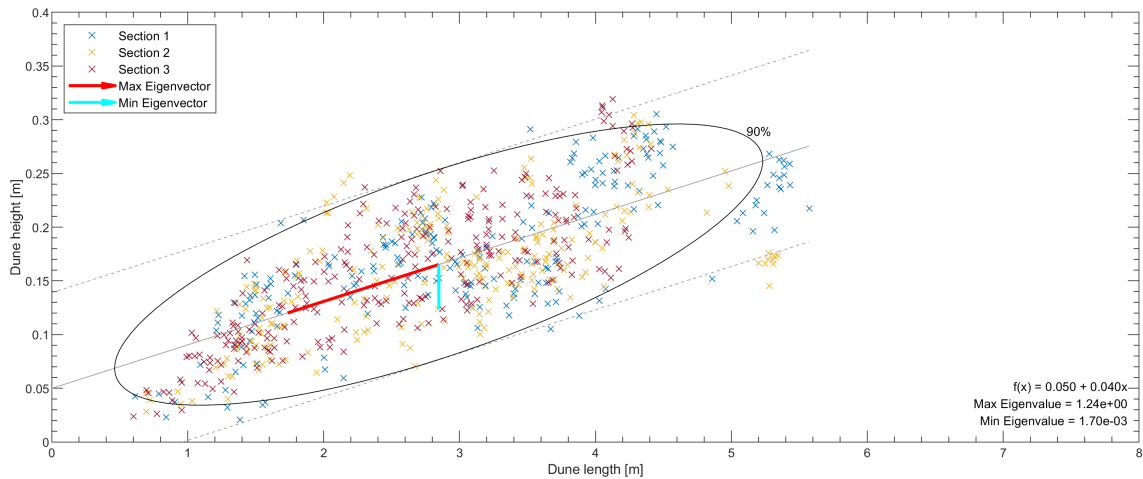


Q193-H30

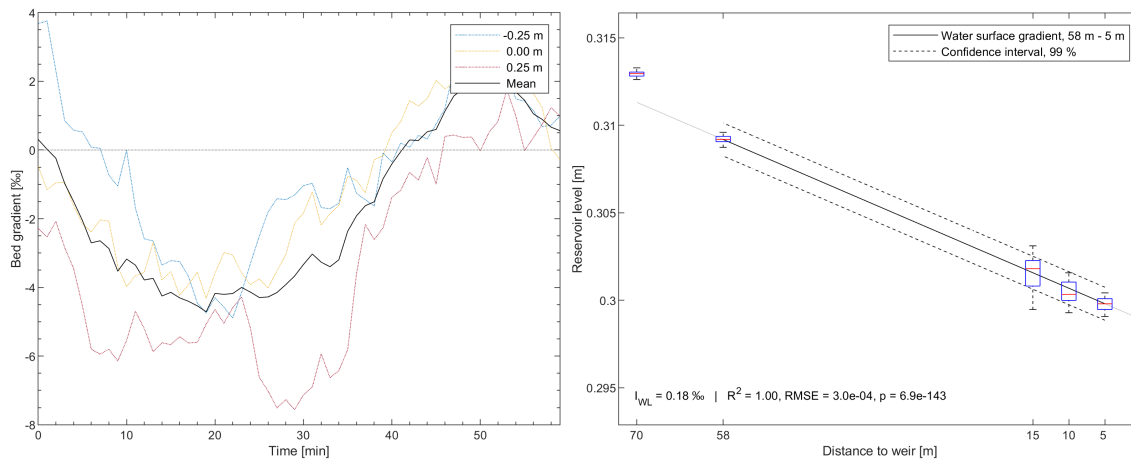
Approximate locations of the bed surface in 3 longitudinal sections after 1, 30 and 60 minutes of bed survey:



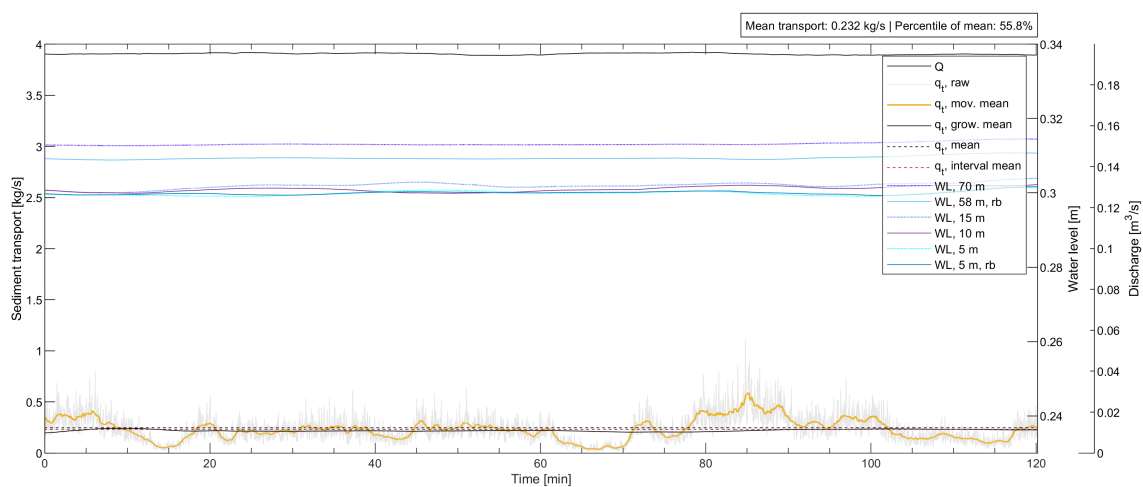
Dune lengths and heights of the reservoir bed:



Time series of the longitudinal bed gradient (left) and averaged longitudinal water surface gradient in the reservoir (right):

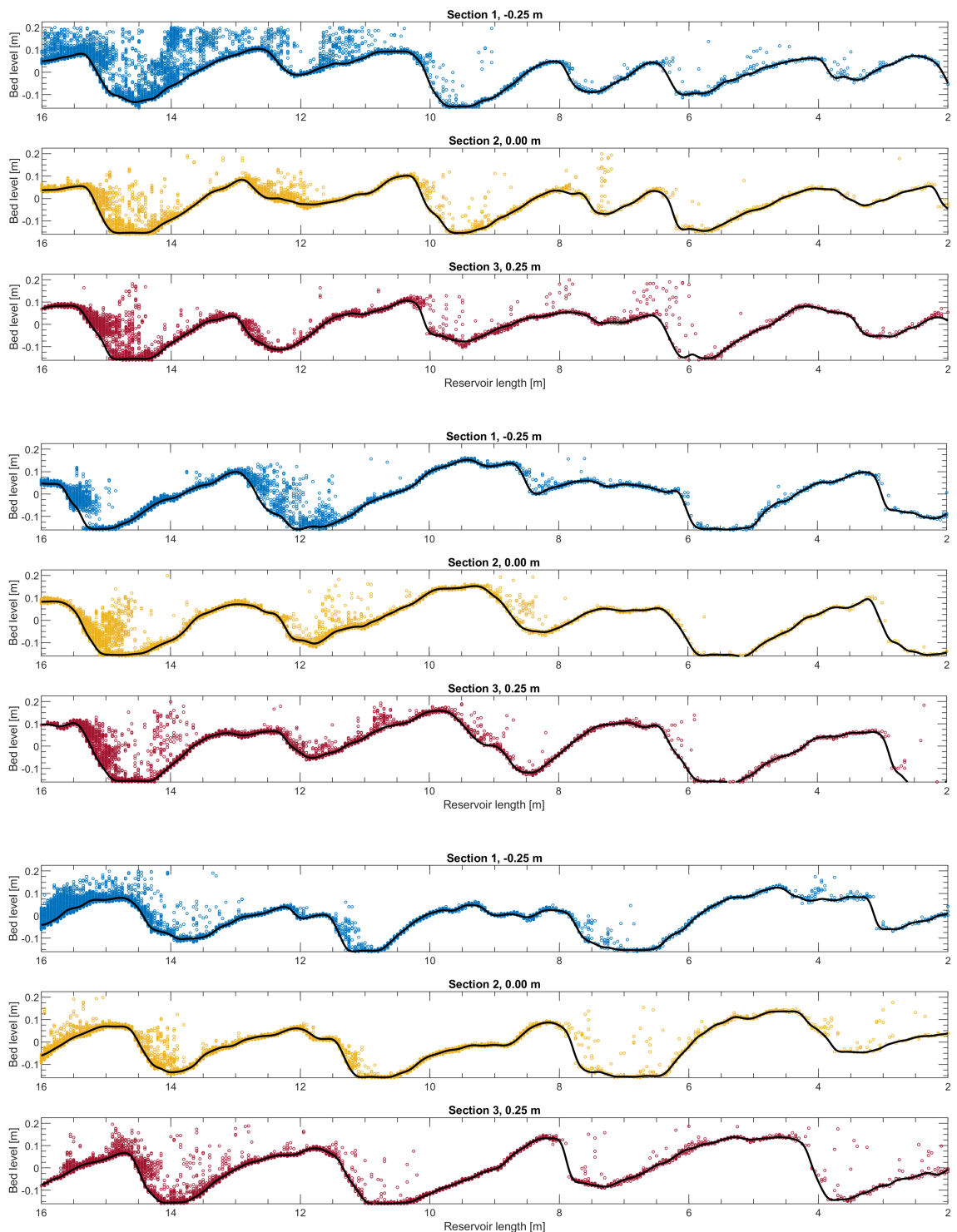


Discharge, water levels and sediment transport rate time series during the bed survey:

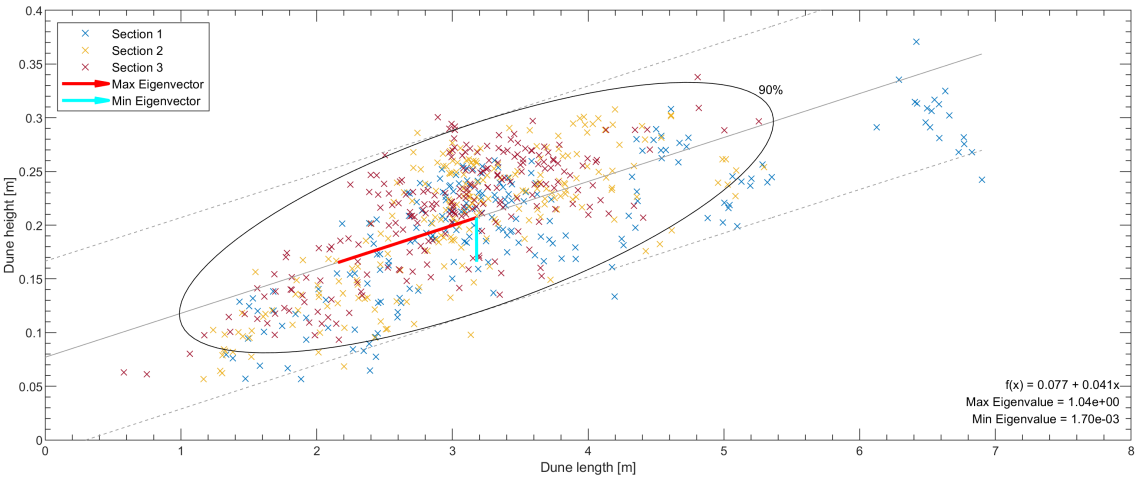


Q216-H30

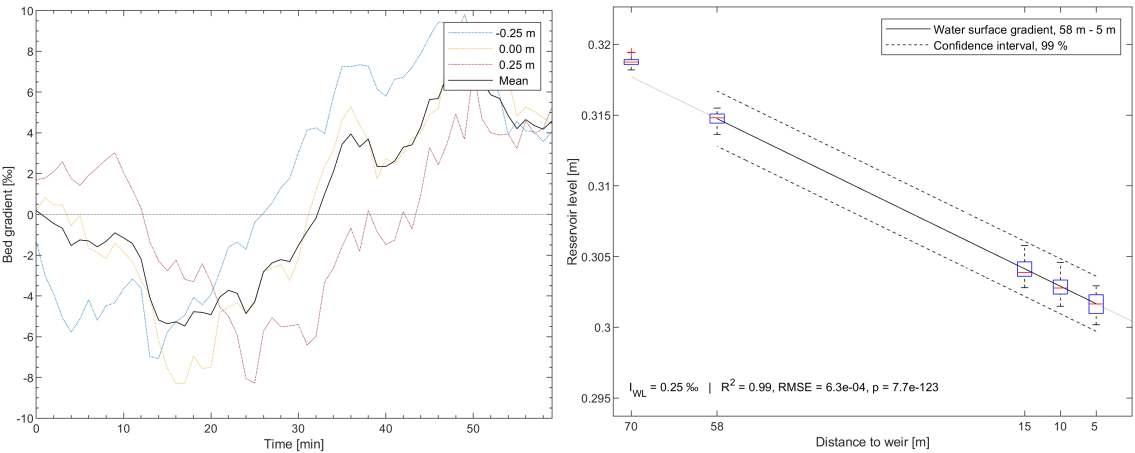
Approximate locations of the bed surface in 3 longitudinal sections after 1, 30 and 60 minutes of bed survey:



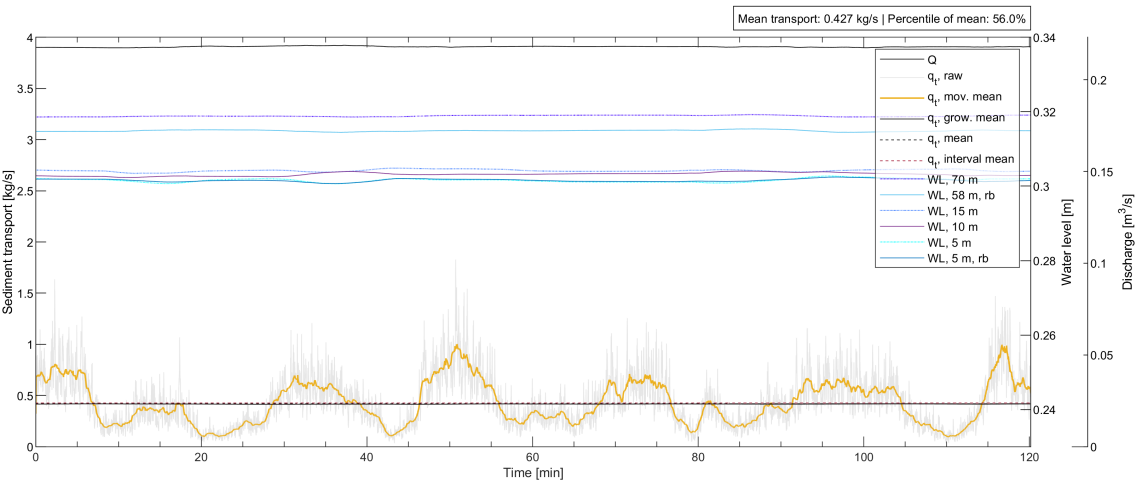
Dune lengths and heights of the reservoir bed:



Time series of the longitudinal bed gradient (left) and averaged longitudinal water surface gradient in the reservoir (right):

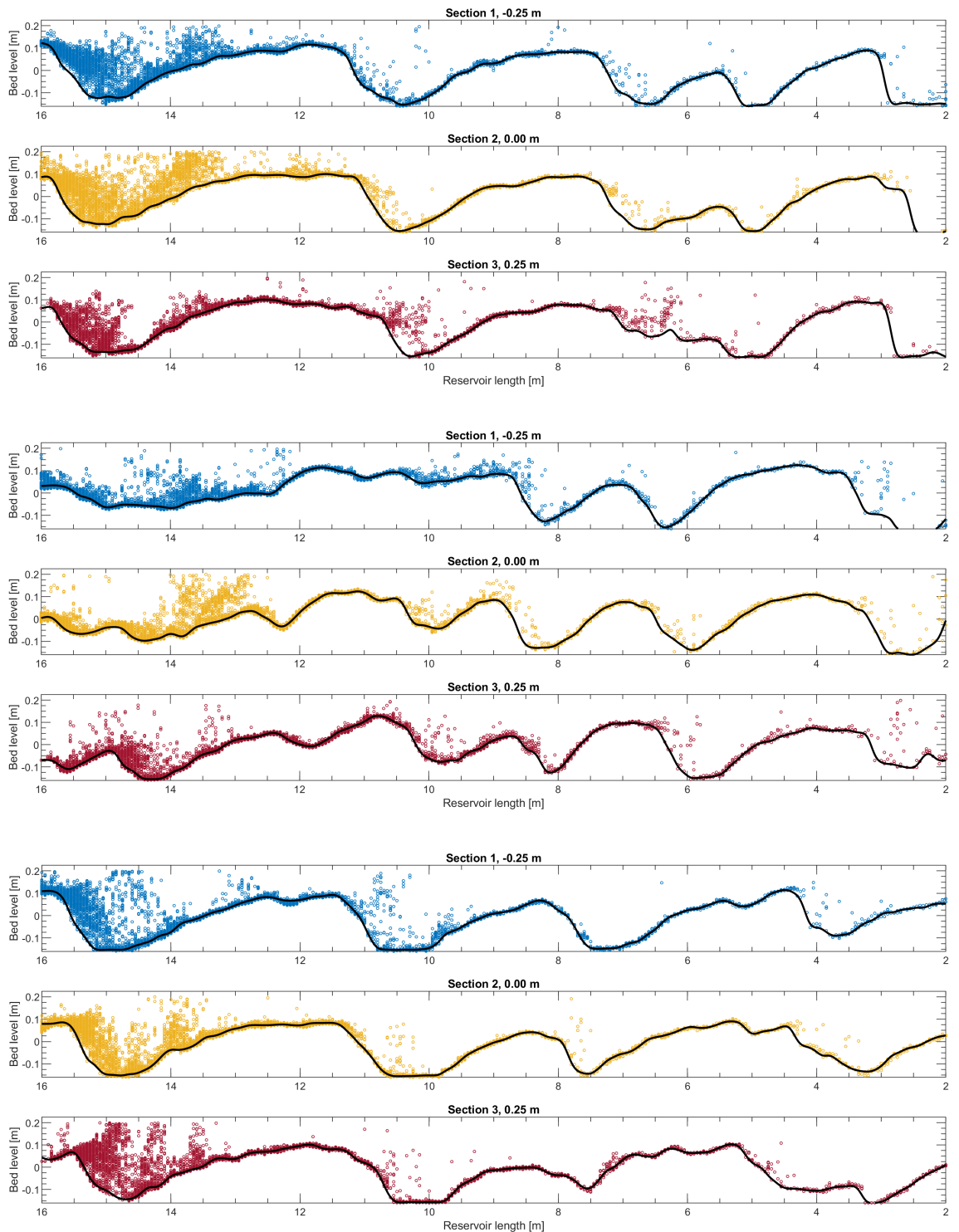


Discharge, water levels and sediment transport rate time series during the bed survey:

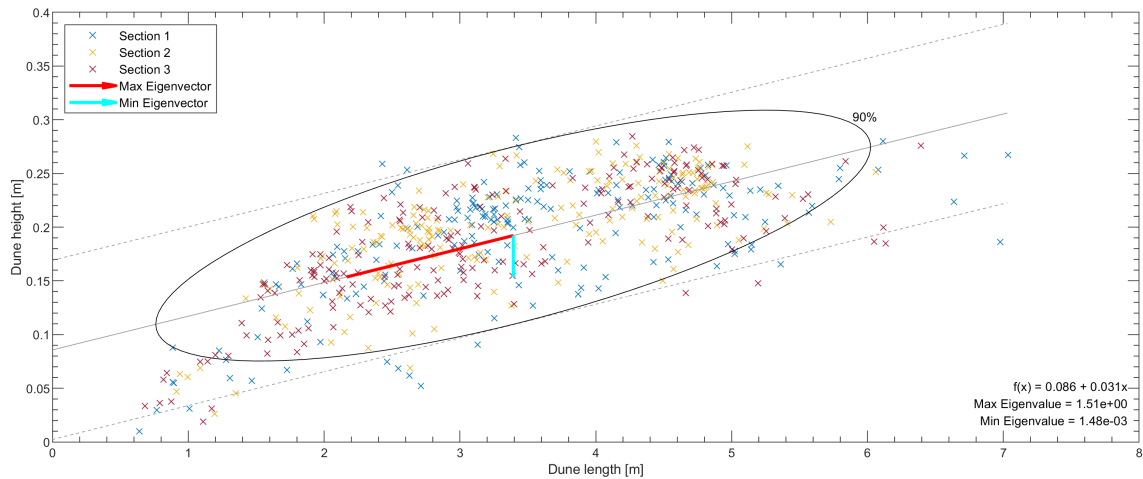


Q259-H30

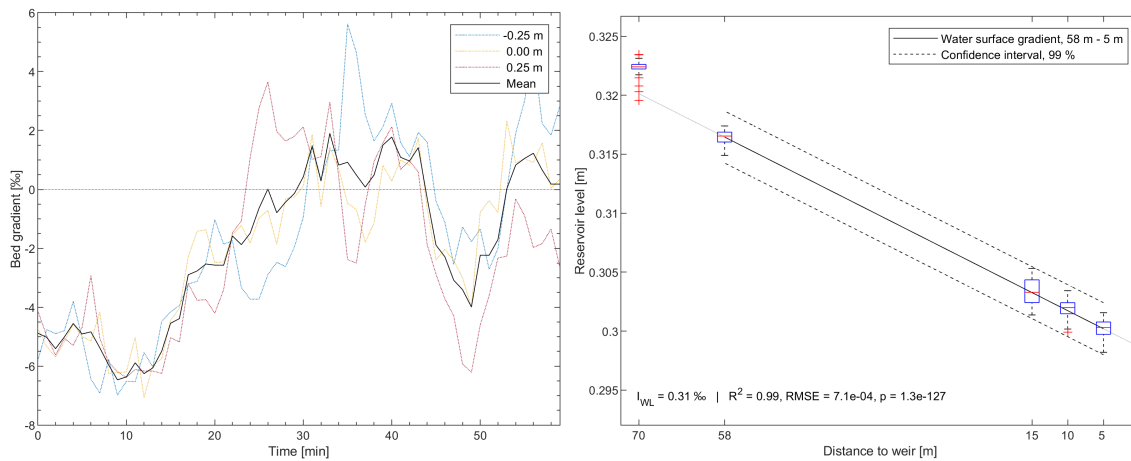
Approximate locations of the bed surface in 3 longitudinal sections after 1, 30 and 60 minutes of bed survey:



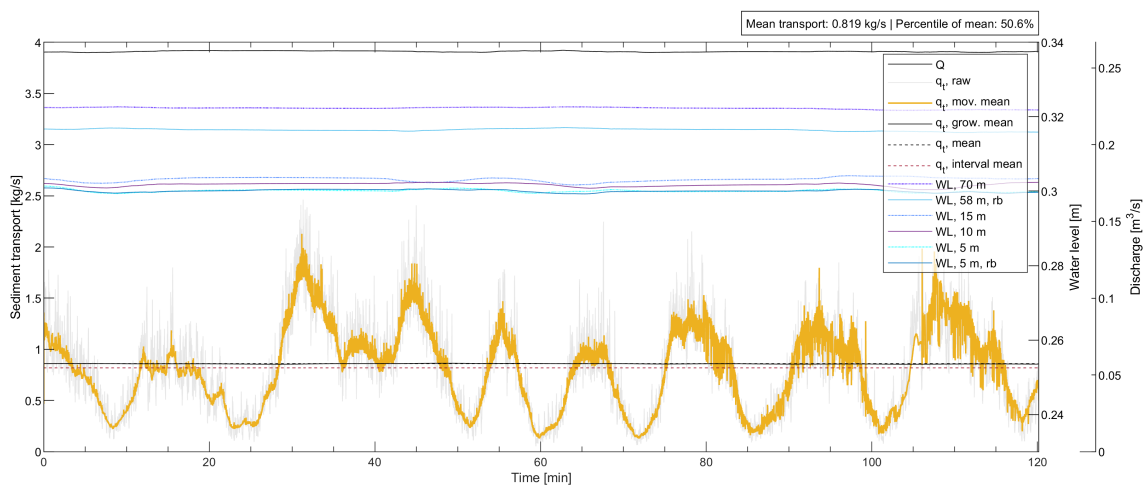
Dune lengths and heights of the reservoir bed:



Time series of the longitudinal bed gradient (left) and averaged longitudinal water surface gradient in the reservoir (right):

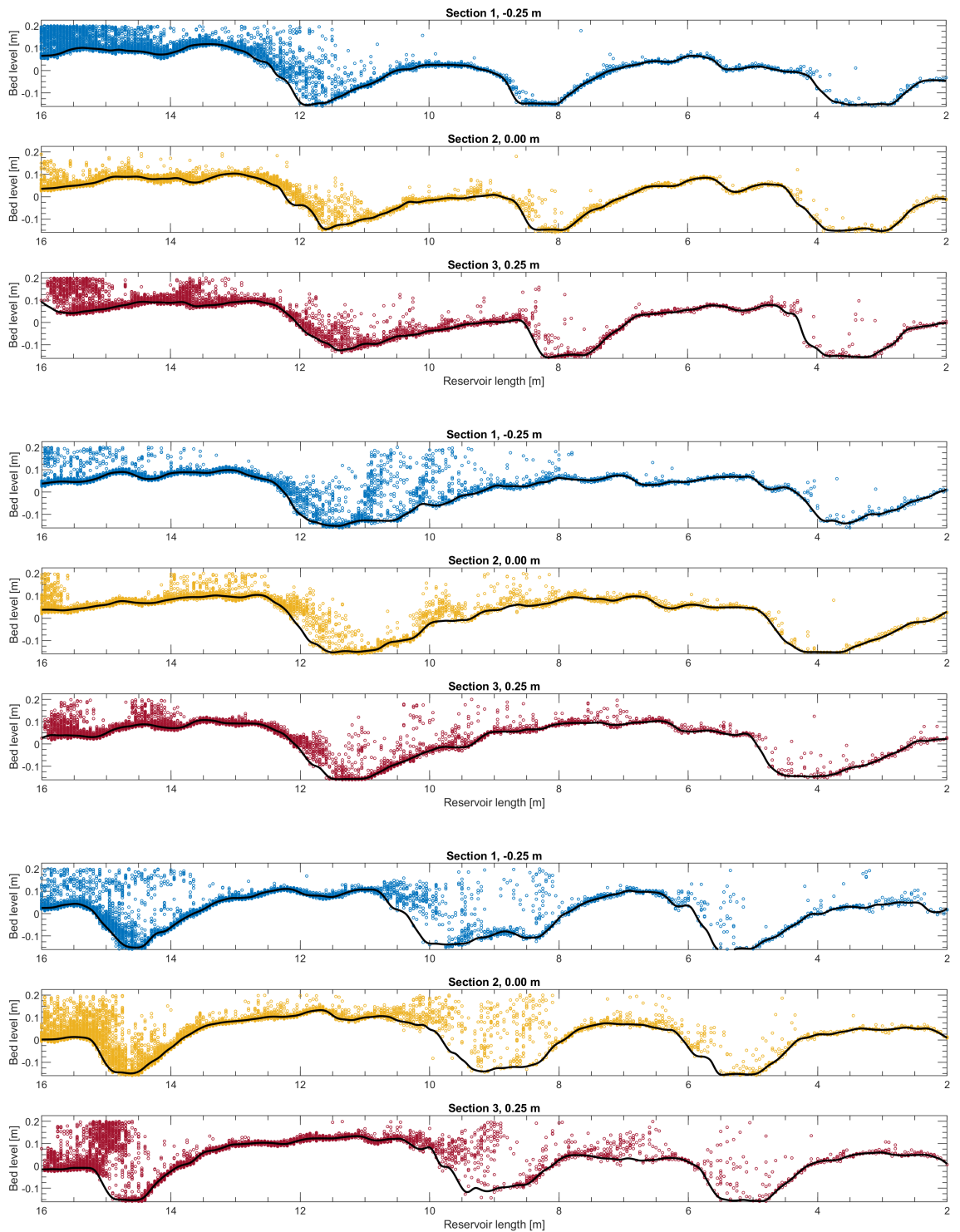


Discharge, water levels and sediment transport rate time series during the bed survey:

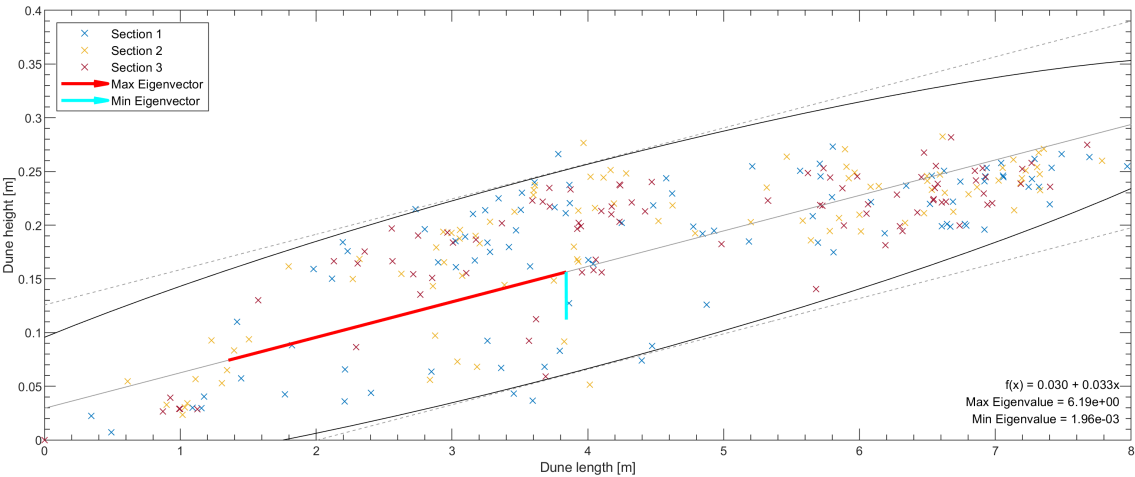


Q325-H30

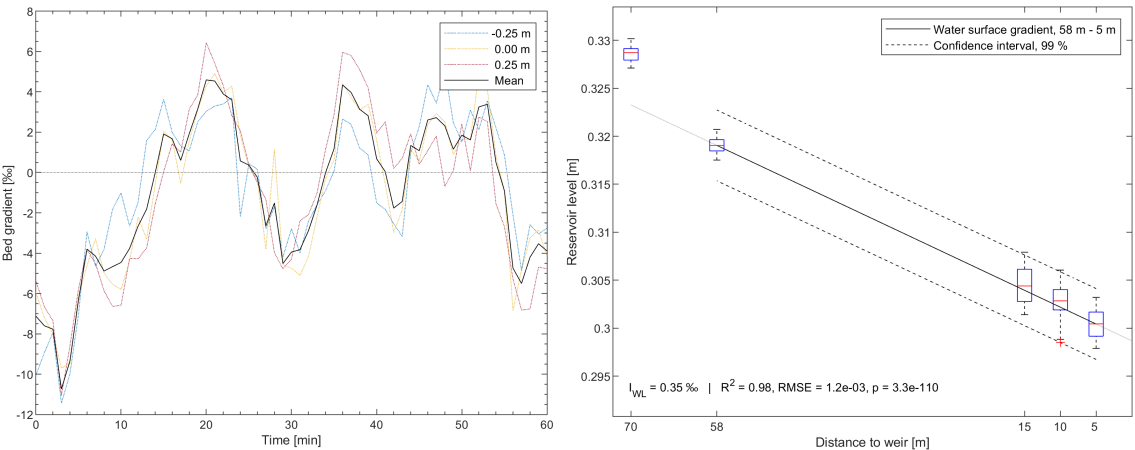
Approximate locations of the bed surface in 3 longitudinal sections after 1, 30 and 60 minutes of bed survey:



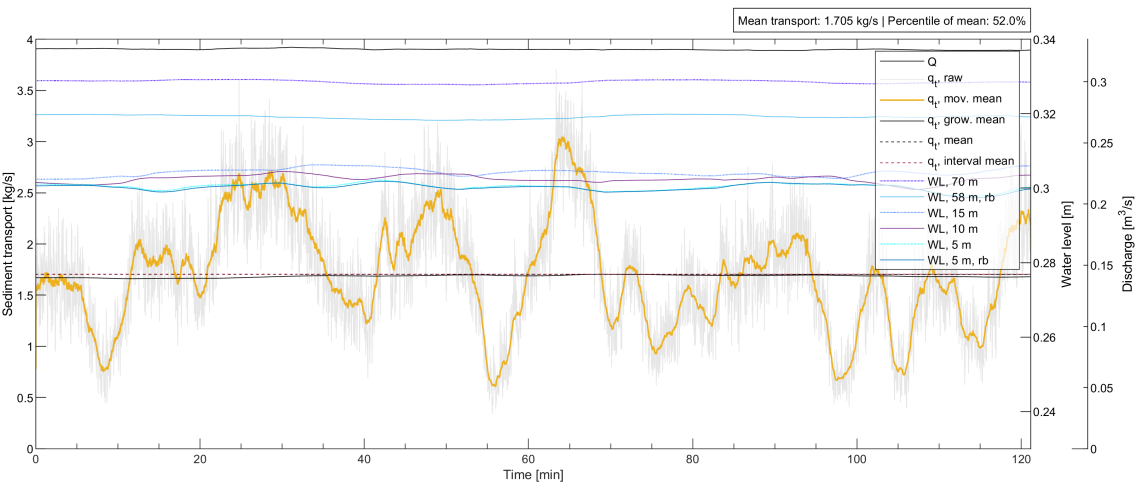
Dune lengths and heights of the reservoir bed:



Time series of the longitudinal bed gradient (left) and averaged longitudinal water surface gradient in the reservoir (right):



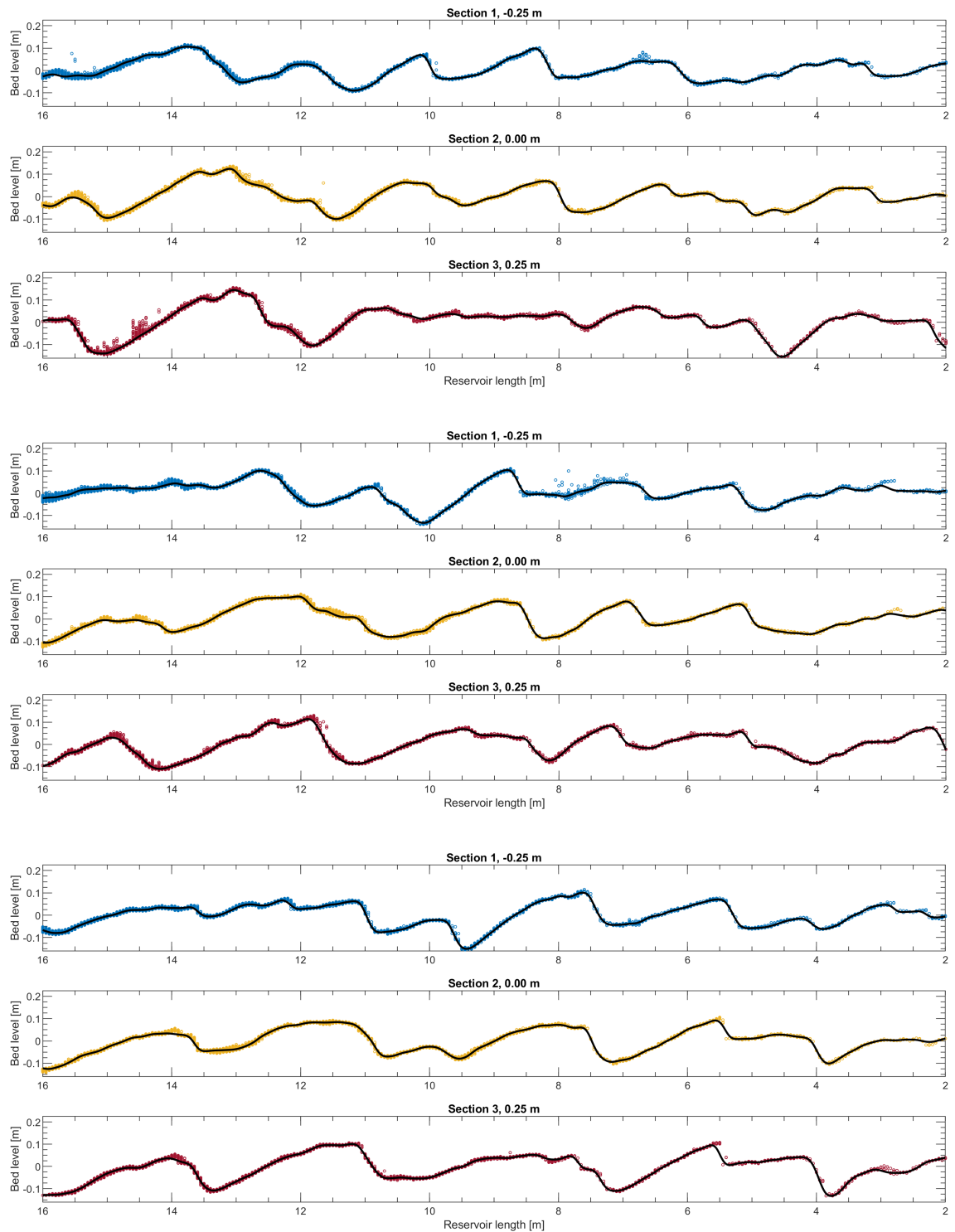
Discharge, water levels and sediment transport rate time series during the bed survey:



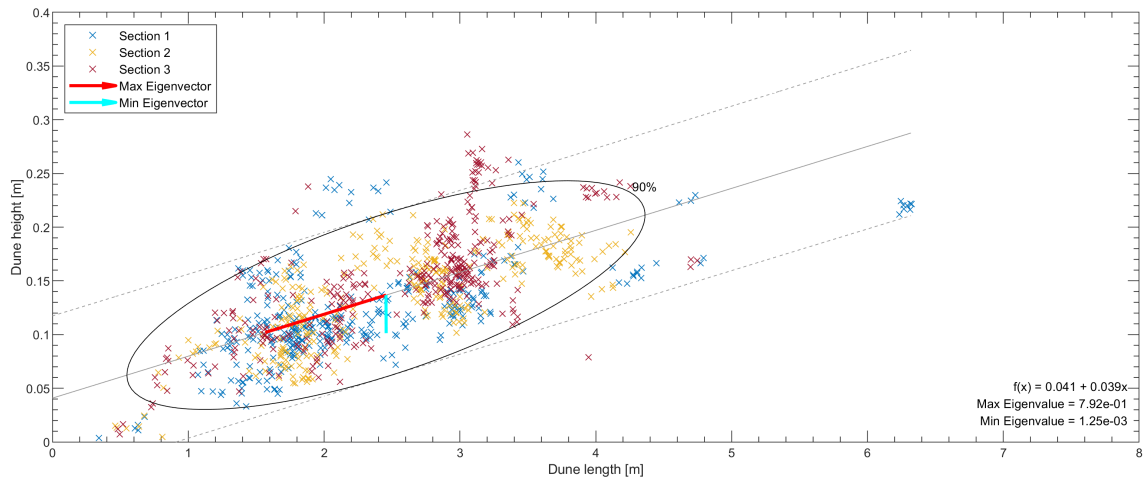
C.3. $H = 35.00$ cm

Q180-H35

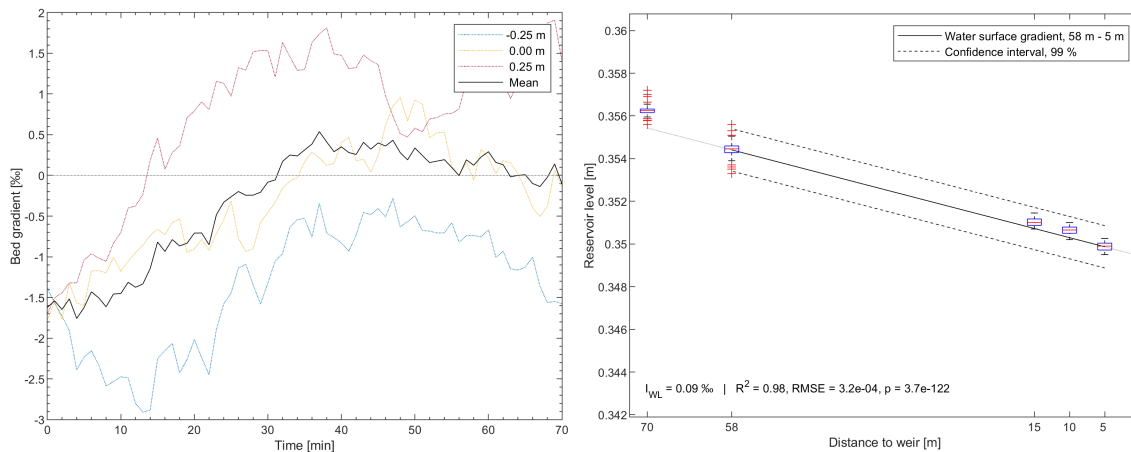
Approximate locations of the bed surface in 3 longitudinal sections after 1, 30 and 60 minutes of bed survey:



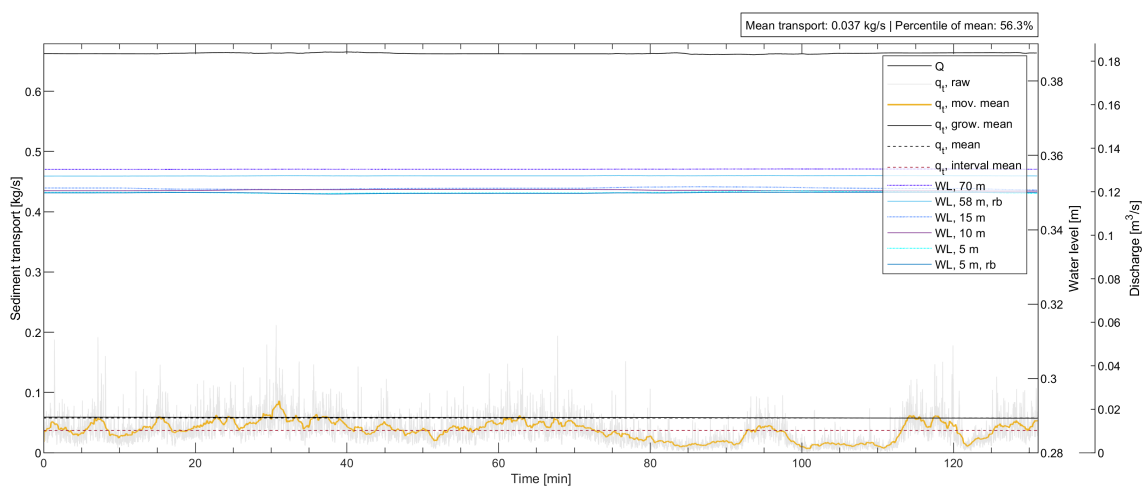
Dune lengths and heights of the reservoir bed:



Time series of the longitudinal bed gradient (left) and averaged longitudinal water surface gradient in the reservoir (right):

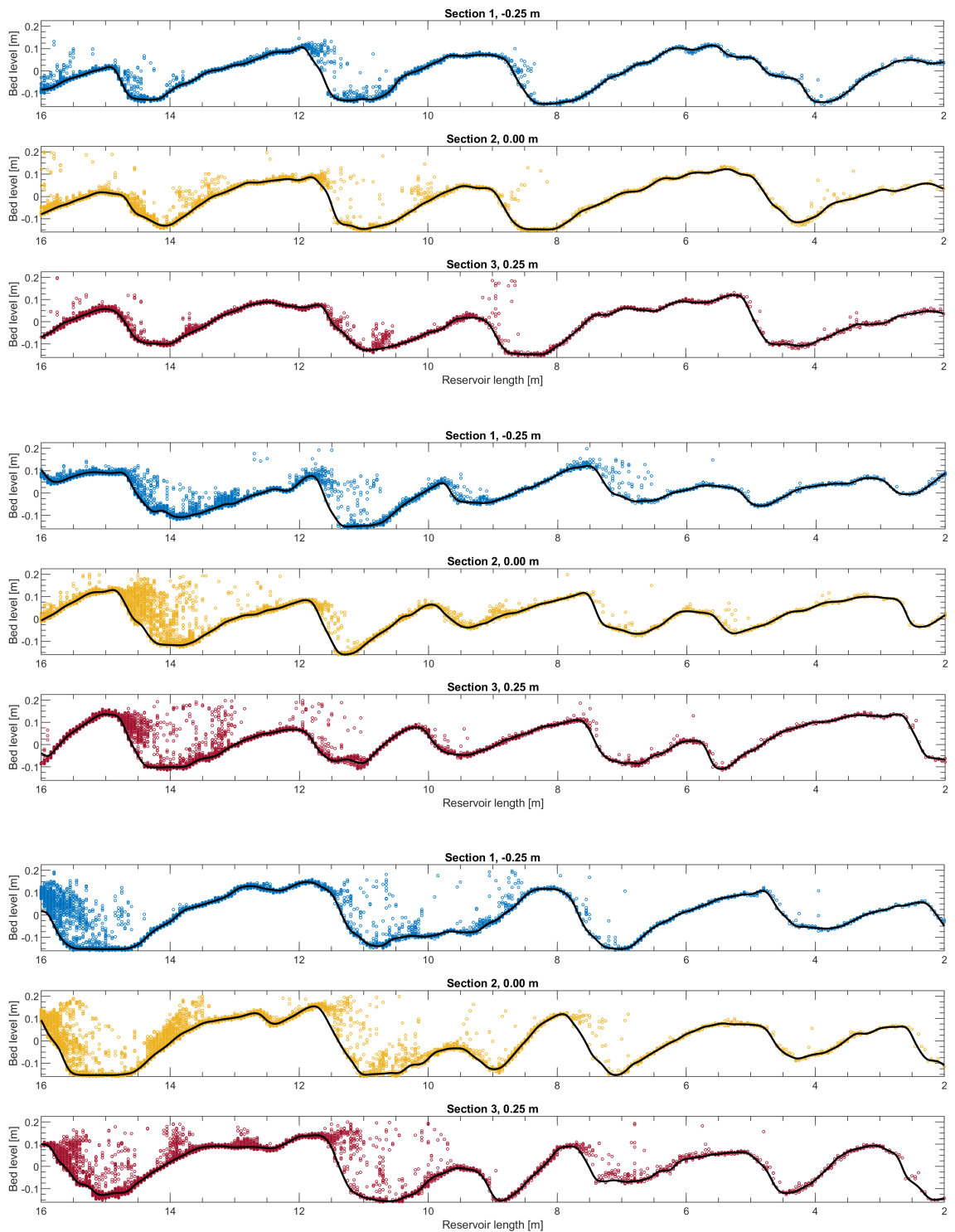


Discharge, water levels and sediment transport rate time series during the bed survey:

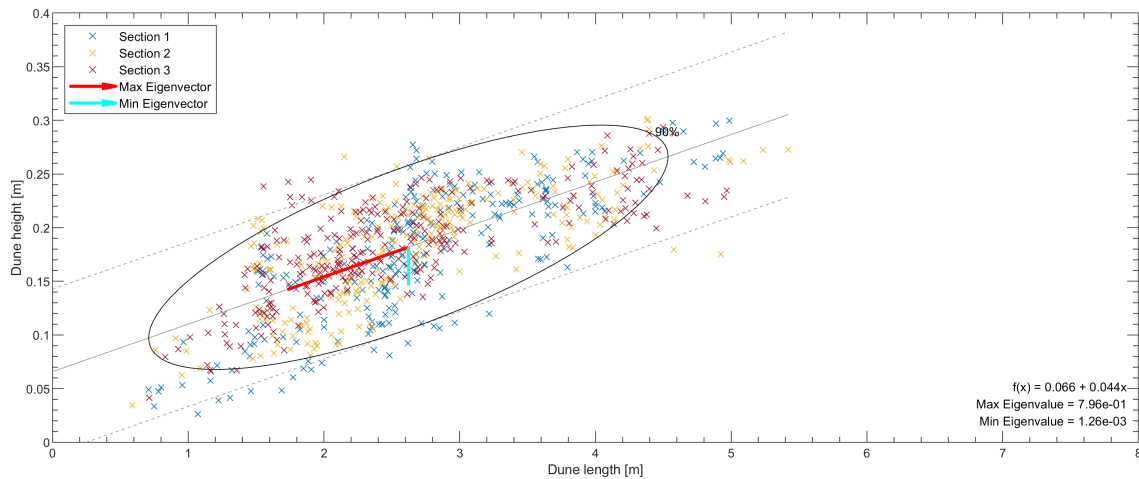


Q259-H35

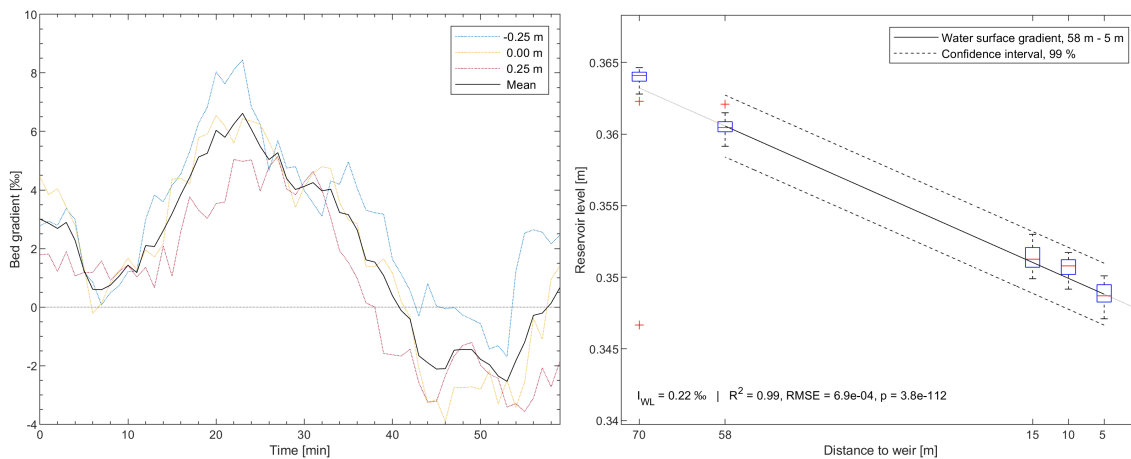
Approximate locations of the bed surface in 3 longitudinal sections after 1, 30 and 60 minutes of bed survey:



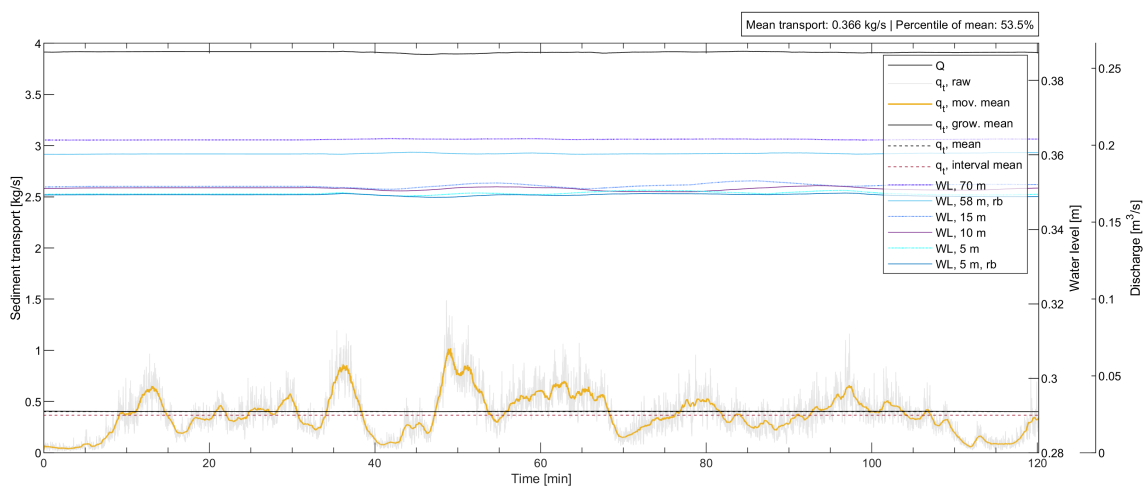
Dune lengths and heights of the reservoir bed:



Time series of the longitudinal bed gradient (left) and averaged longitudinal water surface gradient in the reservoir (right):

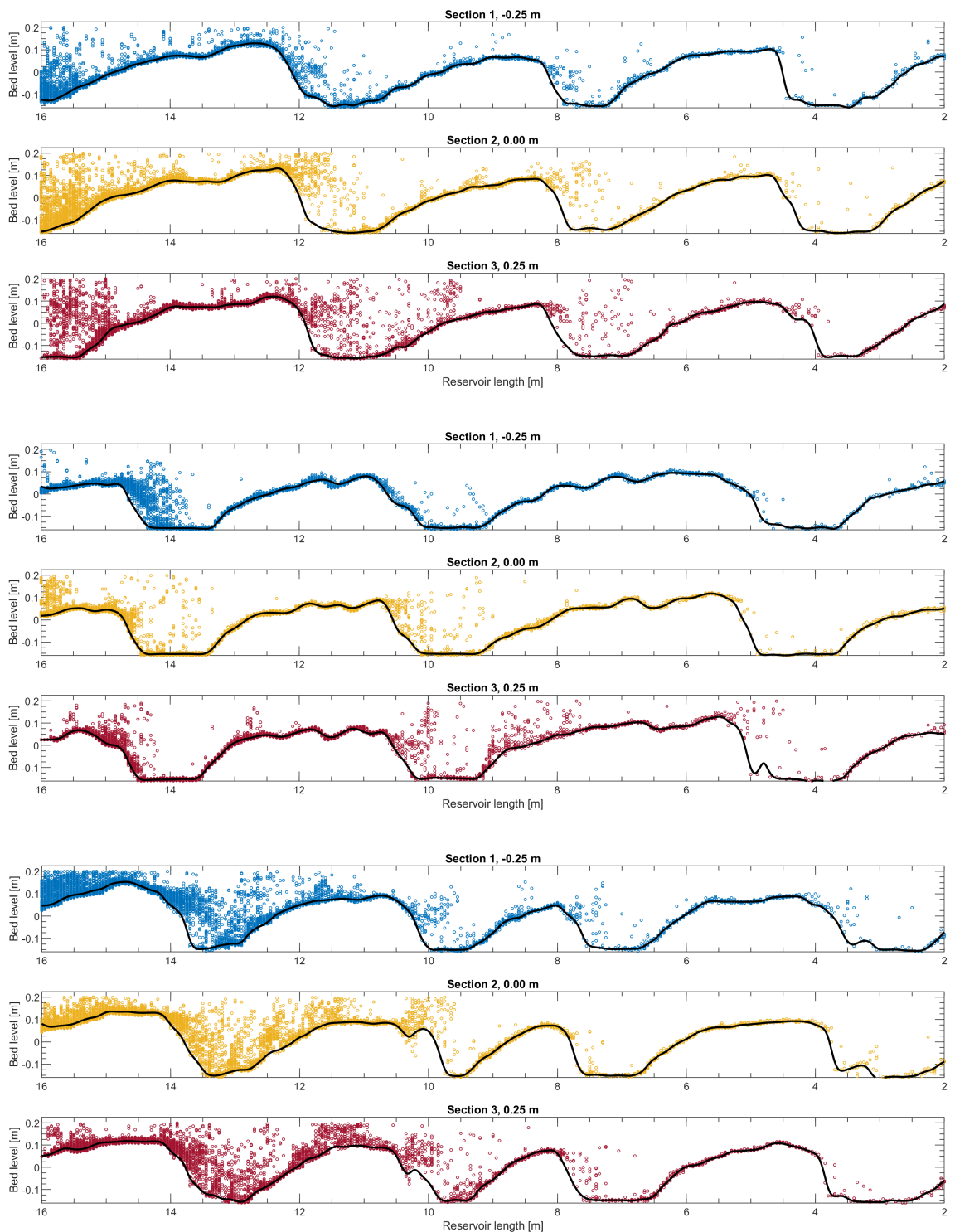


Discharge, water levels and sediment transport rate time series during the bed survey:

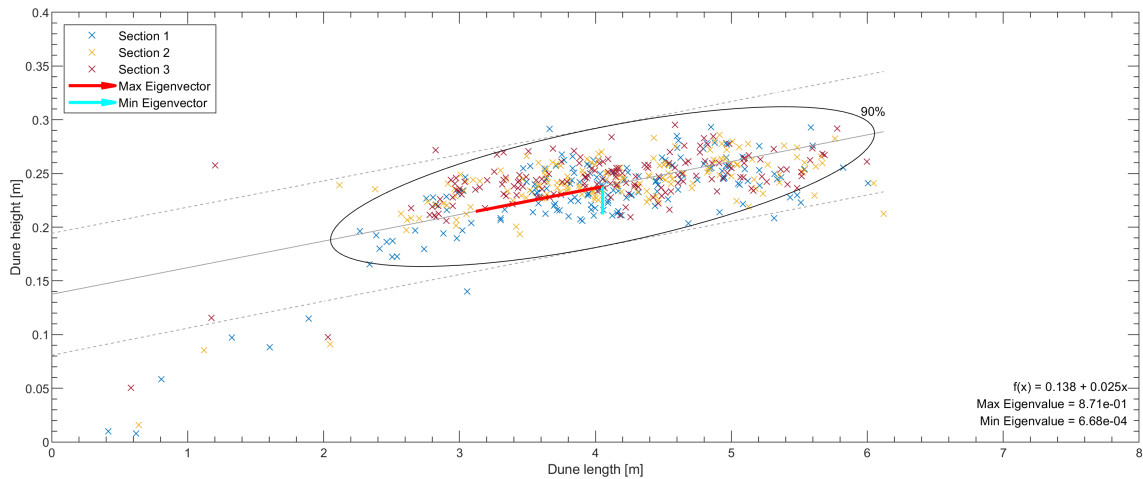


Q325-H35

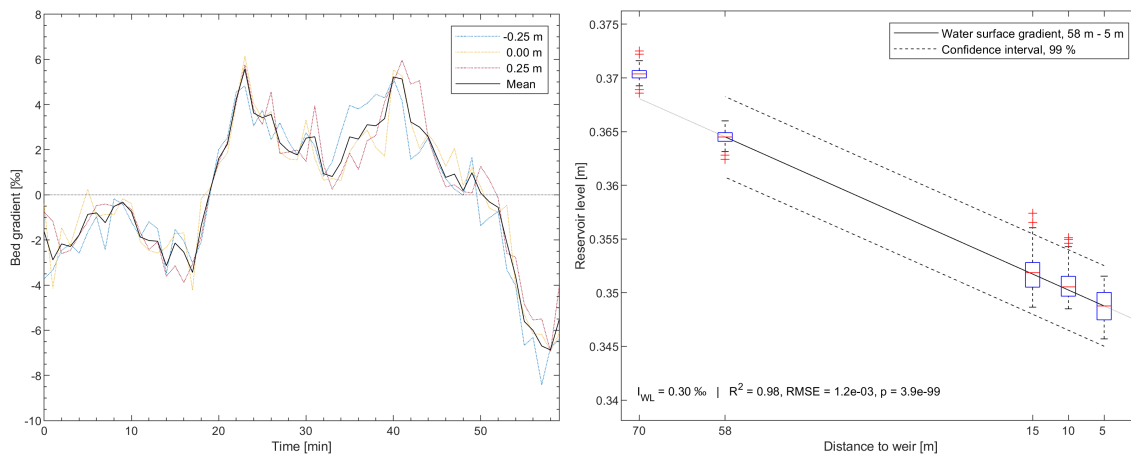
Approximate locations of the bed surface in 3 longitudinal sections after 1, 30 and 60 minutes of bed survey:



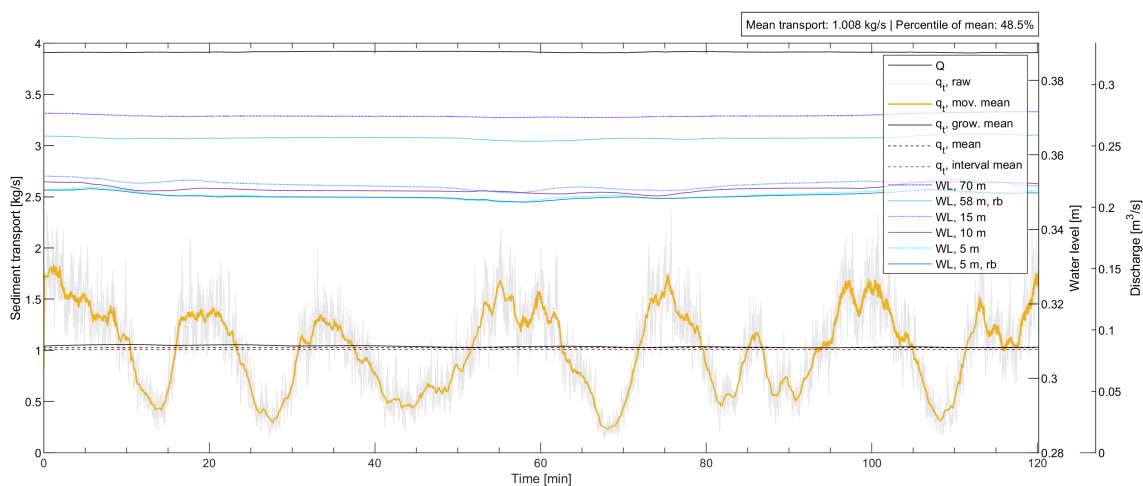
Dune lengths and heights of the reservoir bed:



Time series of the longitudinal bed gradient (left) and averaged longitudinal water surface gradient in the reservoir (right):

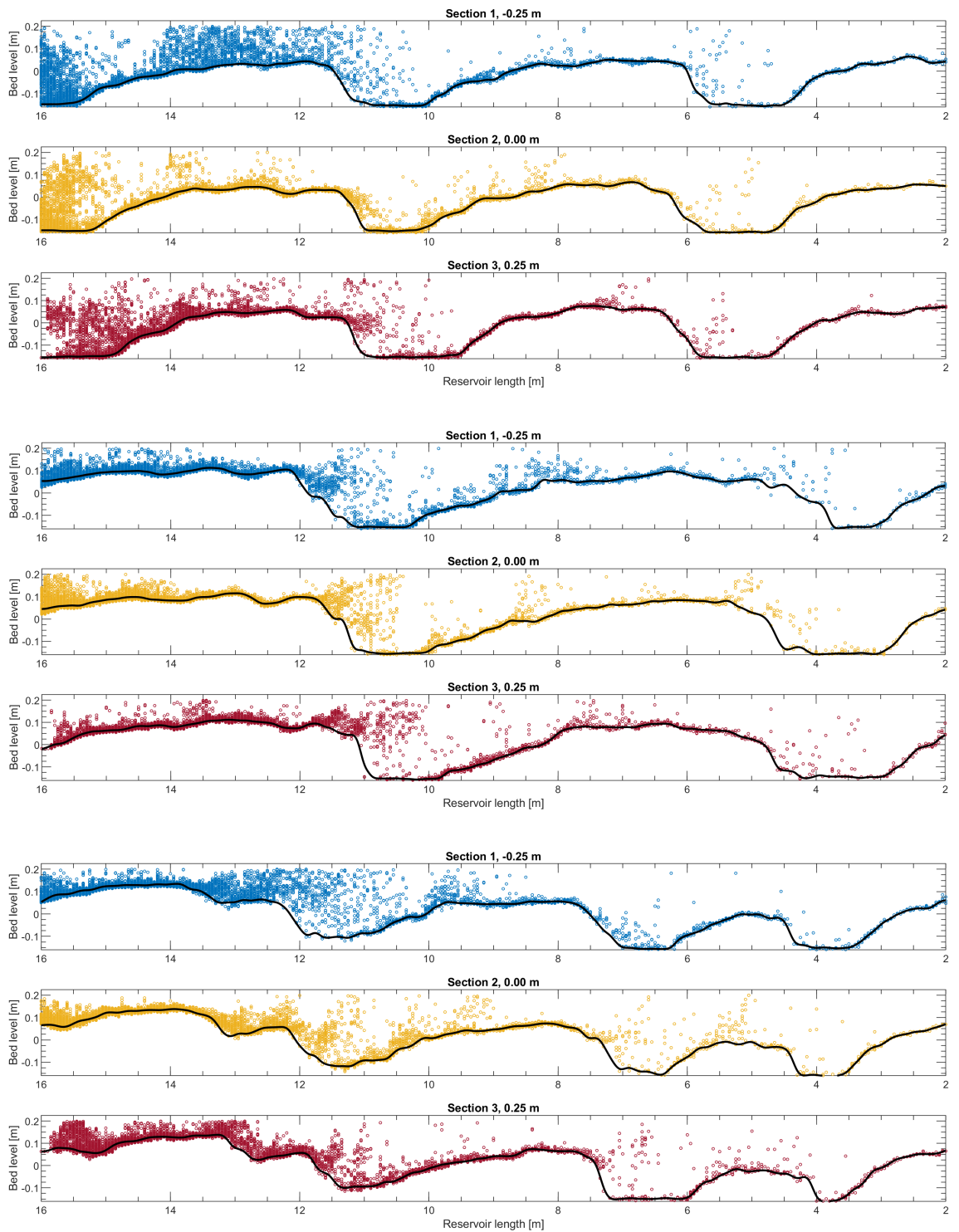


Discharge, water levels and sediment transport rate time series during the bed survey:

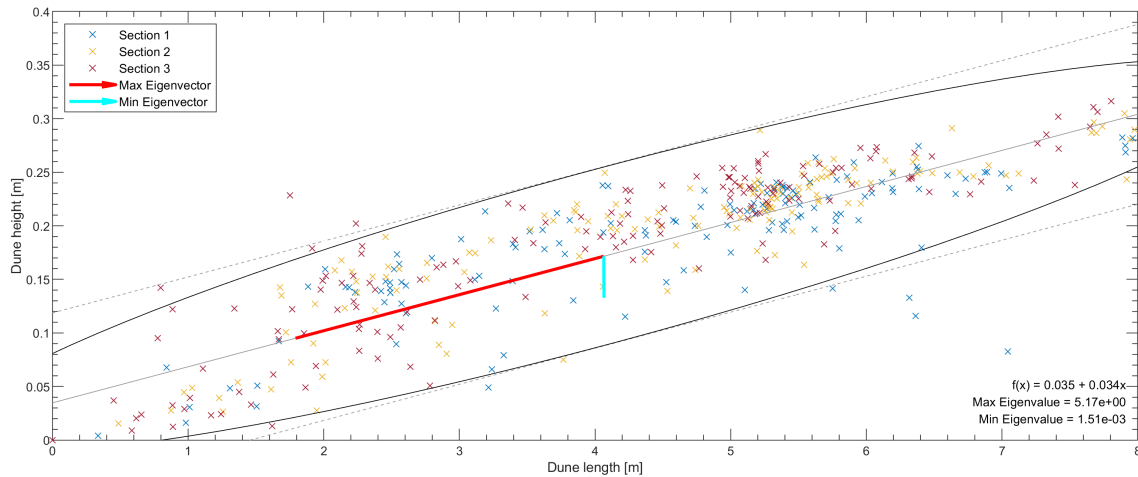


Q409-H35

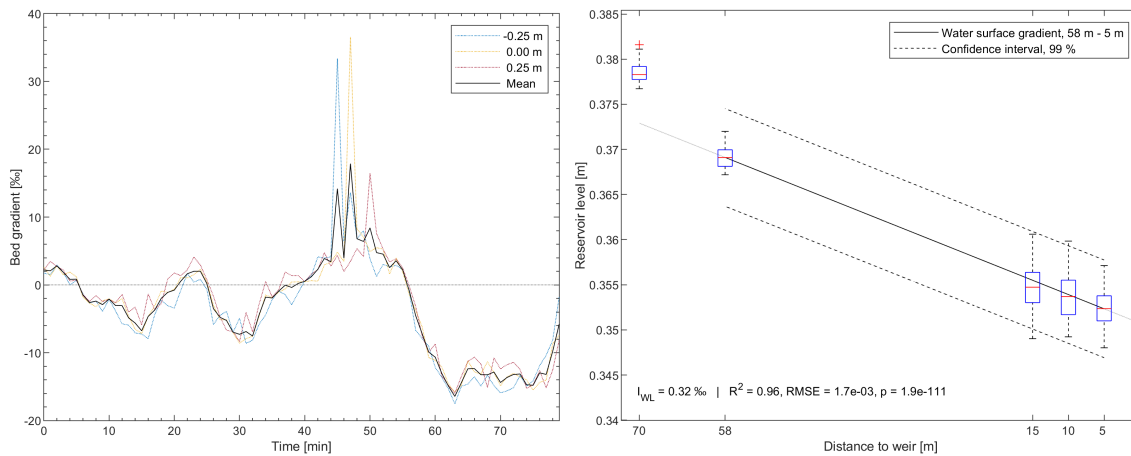
Approximate locations of the bed surface in 3 longitudinal sections after 1, 30 and 60 minutes of bed survey:



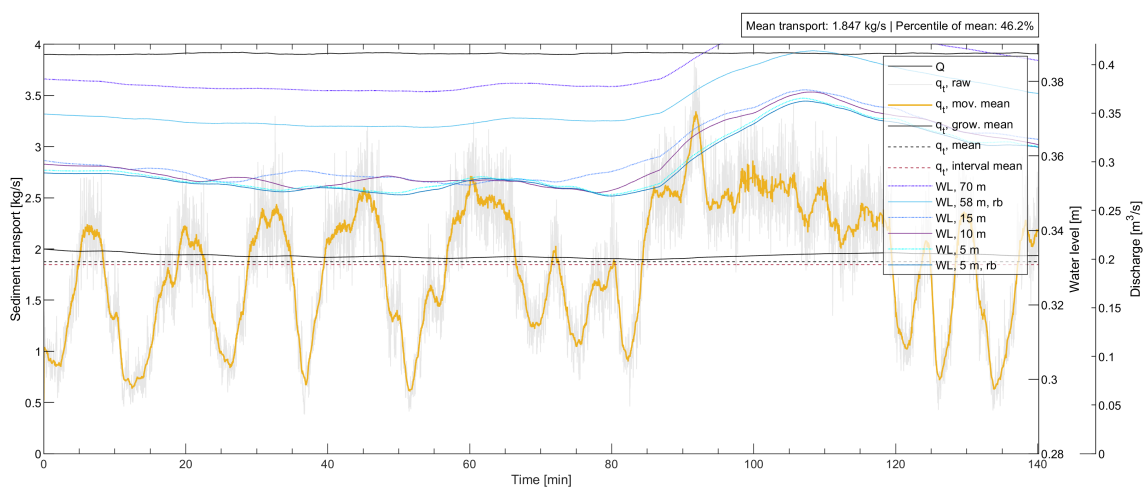
Dune lengths and heights of the reservoir bed:



Time series of the longitudinal bed gradient (left) and averaged longitudinal water surface gradient in the reservoir (right):



Discharge, water levels and sediment transport rate time series during the bed survey:



C.4. Dune velocities

Dune velocities in [m/h] from zero crossing analysis/from manually-timed measurement:

Discharge [l/s]	Water depth [cm]		
	21.25	30	35
101.7	5.6/6.0		
135.5	10.9/11.0	2.3/1.8	
162.7	18.1/20.0	3.8/3.7	
180.8		6.4/4.1	3.2/2.1
193.2	24.7/25.0	7.2/6.8	
216.9	29.3/27.5	10.2/8.9	
259.1		16.9/15.0	9.9/8.4
325.4		26.3/27.5	15.0/16.9
409.7			26.1/31.3